



**HAL**  
open science

# Cellulose nanofibers for the production of bionanocomposites

Oleksandr Nechyporchuk

► **To cite this version:**

Oleksandr Nechyporchuk. Cellulose nanofibers for the production of bionanocomposites. Chemical and Process Engineering. Université Grenoble Alpes; Instituto superior técnico (Lisbonne), 2015. English. NNT: 2015GREAI056 . tel-01244186

**HAL Id: tel-01244186**

**<https://theses.hal.science/tel-01244186>**

Submitted on 15 Dec 2015

**HAL** is a multi-disciplinary open access archive for the deposit and dissemination of scientific research documents, whether they are published or not. The documents may come from teaching and research institutions in France or abroad, or from public or private research centers.

L'archive ouverte pluridisciplinaire **HAL**, est destinée au dépôt et à la diffusion de documents scientifiques de niveau recherche, publiés ou non, émanant des établissements d'enseignement et de recherche français ou étrangers, des laboratoires publics ou privés.

## THÈSE

Pour obtenir le grade de

### DOCTEUR DE L'UNIVERSITÉ GRENOBLE ALPES

Spécialité : **Matériaux, Mécanique, Génie civil, Electrochimie**

Arrêté ministériel : le 6 janvier 2005 – 7 août 2006

et de

### DOUTOR EM ENGENHARIA DE MATERIAIS, INSTITUTO SUPERIOR TÉCNICO, UNIVERSIDADE DE LISBOA

Présentée par

## Oleksandr NECHYPORCHUK

Thèse dirigée par **Frédéric PIGNON** et **Ana Maria BOTELHO DO REGO**,  
codirigée par **Mohamed Naceur BELGACEM**

préparée au sein des **Laboratoire Rhéologie et Procédés** (Grenoble),  
**Laboratoire de Génie des Procédés Papetiers** (Grenoble) et  
**Centro de Química-Física Molecular** (Lisbonne)

dans l'**École Doctorale Ingénierie – Matériaux, Mécanique,**  
**Environnement, Energétique, Procédés, Production**

# Nanofibres de cellulose pour la production de bionanocomposites

Thèse soutenue publiquement le **2 Octobre 2015**  
devant le jury composé de :

**M. Etienne FLEURY**

Professeur, Institut national des sciences appliquées de Lyon (président du jury)

**M. Alain PONTON**

Docteur, directeur de recherche CNRS, Université Paris Diderot (rapporteur)

**Mme Ana Paula DUARTE**

Professeur, Universidade da Beira Interior (rapporteur)

**M. Philippe CASSAGNAU**

Professeur, Université Claude Bernard Lyon 1 (examineur)

**M. Albert MAGNIN**

Docteur, directeur de recherche CNRS, Université Grenoble Alpes (examineur)

**Mme Amélia ALMEIDA**

Professeur adjoint, Instituto Superior Técnico (examineur)

**Mme Ana Maria BOTELHO DO REGO**

Professeur associé, Instituto Superior Técnico (directrice de thèse)

**M. Frédéric PIGNON**

Docteur, directeur de recherche CNRS, Université Grenoble Alpes (directeur de thèse)

**M. Mohamed Naceur BELGACEM**

Professeur, Université Grenoble Alpes (codirecteur de thèse, invité)





## **DISSERTATION**

To obtain the degree of

### **DOCTOR FROM UNIVERSITÉ GRENOBLE ALPES**

Speciality: **Materials, Mechanics, Civil Engineering, Electrochemistry**

Ministerial Order: January 6, 2005 – August 7, 2006

and of

### **DOUTOR EM ENGENHARIA DE MATERIAIS, INSTITUTO SUPERIOR TÉCNICO, UNIVERSIDADE DE LISBOA**

Presented by

**Oleksandr NECHYPORCHUK**

supervised by **Frédéric PIGNON** and **Ana Maria BOTELHO DO REGO**,  
co-supervised by **Mohamed Naceur BELGACEM**

performed at **Laboratoire Rhéologie et Procédés** (Grenoble),  
**Laboratoire de Génie des Procédés Papetiers** (Grenoble) and  
**Centro de Química-Física Molecular** (Lisbon)

at the **Engineering Doctoral School – Materials, Mechanics,  
Environment, Energy, Process, Production**

# **Cellulose Nanofibers for the Production of Bionanocomposites**

Dissertation defended in public on **October 2, 2015**  
in front of the jury members:

**Mr. Etienne FLEURY**

Professor, National Institute of Applied Sciences of Lyon (jury president)

**Mr. Alain PONTON**

Doctor, CNRS Senior Scientist, Université Paris Diderot (reporter)

**Ms. Ana Paula DUARTE**

Professor, Universidade da Beira Interior (reporter)

**Mr. Philippe CASSAGNAU**

Professor, Université Claude Bernard Lyon 1 (examiner)

**Mr. Albert MAGNIN**

Doctor, CNRS Senior Scientist, Université Grenoble Alpes (examiner)

**Ms. Amélia ALMEIDA**

Assistant Professor, Instituto Superior Técnico (examiner)

**Ms. Ana Maria BOTELHO DO REGO**

Associate Professor, Instituto Superior Técnico (dissertation director)

**Mr. Frédéric PIGNON**

Doctor, CNRS Senior Scientist, Université Grenoble Alpes (dissertation director)

**Mr. Mohamed Naceur BELGACEM**

Professor, Université Grenoble Alpes (dissertation co-director, guest)





# Abstract

Due to environmental concerns the development of bio-based composite materials for different industrial applications is nowadays a frequent research subject. Many studies are performed on the use of natural fibers in composites as an alternative to conventional synthetic fillers, which are traditionally used to reinforce thermoplastic matrices. This dissertation focuses on the development of such composite materials using the bio-based and biodegradable reinforcing agent — nanofibrillated cellulose (NFC).

Thus, in this work the NFC aqueous suspensions were produced from dry bleached bisulfite softwood pulp applying enzymatic or 2,2,6,6-tetramethylpiperidine-1-oxyl (TEMPO)-mediated oxidation treatments, followed by wet grinding (using Supermasscolloider), as an ultimate fibrillation technique. Two commercial enzyme solutions: (i) cellulase (Celluclast 1.5 L), with the predominant activity of endoglucanase and exoglucanase, and (ii) monocomponent endoglucanase (FiberCare R), were compared to facilitate the nanofibrils extraction from cellulose fibers. The influence of their concentrations, as well as that of the other processing conditions, was analyzed. The oxidation of cellulose using oxygen in the presence of N-hydroxyphthalimide (NHPI) and anthraquinone at elevated pressure and temperature was studied as an alternative technique to TEMPO-mediated oxidation.

The morphology of the produced NFC was characterized using optical microscopy, atomic force microscopy (AFM), field emission gun scanning electron microscopy (FEG-SEM), and morphological fiber analyzer (MorFi). Nanofibrils with a wide size distribution were produced. The average lateral dimensions of  $12 \pm 7$  nm for the most disintegrated enzymatically hydrolyzed NFC and  $4 \pm 2$  nm for TEMPO-oxidized counterpart were established from the AFM height images. The degree of polymerization (DP) decreased and the crystallinity index (CI) increased with an increase of the concentration of the enzyme solutions. TEMPO-oxidation did not have a significant impact on the cellulose CI; however, the DP was strongly affected. The monocomponent endoglucanase solution was found to have a stronger influence on the nanofibrils isolation rather than their depolymerization.

The rheological behavior of NFC suspensions was studied since the flow and deformation are involved in the production process and can influence the performance of the final product (for instance, in coating process). The properties of enzymatically hydrolyzed and TEMPO-

oxidized NFC suspensions were investigated in harmonic oscillation and steady-state shearing modes and were compared with the morphology of the studied materials. The stronger fibrous network structures were formed when using monocomponent endoglucanase solution comparing to those of cellulase. Furthermore, TEMPO-oxidized nanofibers possessed stronger network comparing to enzymatically hydrolyzed homologues.

The issues of flow instabilities arising in NFC suspensions were particularly addressed. These instabilities are often attributed to: (i) heterogeneities in the structural organization; (ii) specific structural orientation; (iii) water release when appearing in the volume of the suspension or (iv) adhesion phenomena when appearing at the interface of the measuring tools. These flow instabilities introduce an error in the rheological measurements and have to be controlled. A slippage on the edge of geometry tools and suspension (wall-slip) as well as the flow localization within a specific volume of the sample (shear banding) were explored. These phenomena were visualized using a technique based on the introduction of titanium dioxide pigment into the specific volume of NFC suspension and monitoring its deformation. The influence of the used geometry, namely cone-plate, concentric cylinders (Couette) and vane-in-cup, on the flow fluctuations was analyzed.

A roughening of the tool surfaces was performed to overcome the aforementioned problem. Consequently, a stronger suspension response was detected for TEMPO-oxidized NFC at low shear rates with higher values of measured shear stress. However, a shear banding became more pronounced. The use of serrated tools for enzymatically-hydrolyzed NFC produced lower shear stress at the moderate shear rates, which was influenced by water release from the suspension. No significant influence of the geometry shape and the surface was found at high shear rates.

The flow instabilities appeared to be more pronounced with an increase of the NFC concentration. It was shown that the use of serrated geometry is necessary to compete with the wall-slip but is not sufficient to prevent it completely. Serrated Couette was found to be the most appropriate geometry to measure the rheological properties of NFC suspensions.

The polydispersity of the TEMPO-oxidized NFC was confirmed using small-angle X-ray scattering (SAXS) analysis. The average diameter of nanofibrils swollen in water was determined based on the scattering data and found to be in agreement with that measured by AFM. It is worth noting that when using AFM the nanofibrils are analyzed in the dry state, which can yield slightly lower diameter due to the nanofibrils shrinkage while drying.

---

However, SAXS measurements allowed determining the average diameter of nanofibrils swollen in water.

Finally, two model latexes of poly[styrene-*co*-(2-ethylhexyl acrylate)] were synthesized *via* miniemulsion polymerization comprising cationic and anionic surfactants. These latexes were characterized to determine the glass transition temperature, average particle size distribution and molar mass distribution and were further used to study the interactions between its particles and TEMPO-oxidized NFC in composites. These interactions were examined by means of the homogeneity of NFC dispersion in the matrix and the ensuing composites mechanical properties.

Stable aqueous dispersions with a solid mass fraction of around 30% and the ensuing cast composites were prepared when using latex with anionic surfactant and 1–4 wt.% of TEMPO-oxidized NFC. The good dispersion of the filler within the matrix was confirmed by FEG-SEM and was attributed to the electrostatic repulsion between the cellulose nanofibers and polymer particles. Despite these repulsive forces, the reinforcement effect was determined for all the composites, comparing to the neat matrix, as determined from tensile tests. Both elastic modulus and ultimate strength increased progressively by incorporating the NFC into anionic latex, whereas the strain at break decreased. The reinforcement of the cast composites was achieved through hydrogen bonding of the percolated NFC network.

The application of cationic surfactant in latex, used to enhance the interactions between the negatively charged NFC and positively charged matrix, resulted in non-homogeneous distribution of NFC within the matrix. It occurred due to aggregation through the creation of cross-linked structures between the NFC and latex particles, governed by ionic forces.

**Keywords:** nanocellulose, cellulose nanofibers (CNF), nanofibrillated cellulose (NFC), rheology, flow instabilities, small-angle X-ray scattering (SAXS), nanocomposites, latex, miniemulsion polymerization.



# Résumé

Etant donné les préoccupations environnementales actuelles le développement des matériaux composites biosourcés pour différentes applications industrielles est un sujet de recherche important et d'actualité. Beaucoup d'études sont réalisées sur l'utilisation de fibres naturelles dans les matériaux composites comme une alternative à des homologues minérales classiques, traditionnellement utilisées pour renforcer des matrices thermoplastiques. Cette thèse a pour but le développement de tels matériaux composites à l'aide de l'agent de renforcement biosourcé et biodégradable — nanofibrilles de cellulose (NFC).

Dans ce travail, les suspensions aqueuses de NFC ont été produites à partir de pâte bisulfite blanchie de bois résineux par voie enzymatique ou oxydation assistée par 2,2,6,6-tétraméthylpipéridine-1-oxyle (TEMPO), suivie par broyage humide (à l'aide de Supermasscolloider), comme une technique de fibrillation ultime. Deux solutions d'enzymes commerciales: (i) la cellulase (Celluclast 1.5 L), avec activité prédominante de l'endoglucanase et l'exoglucanase, et (ii) l'endoglucanase monocomposante (FiberCare R), ont été comparées pour faciliter l'extraction des nanofibrilles de cellulose à partir des fibres. L'influence de leur concentration, ainsi que celle des autres conditions de traitement, ont été analysées. L'oxydation de la cellulose par l'oxygène en présence de N-hydroxyphthalimide (NHPI) et de l'antraquinone à pression et à température élevées a été étudiée comme une technique alternative par rapport à l'oxydation assistée par le prétraitement TEMPO.

La morphologie des NFC produites a été caractérisée en utilisant la microscopie optique, la microscopie à force atomique (AMF de l'anglais : Atomic Force Microscope), la microscopie électronique à balayage (MEB) à effet de champ (FEG-SEM de l'anglais : Field Emission Gun Scanning Electron Microscopy), et un analyseur morphologique des fibres (MorFi). Des nanofibrilles avec une large distribution de taille ont été produites. A partir d'images AFM et en utilisant le critère de la hauteur, les dimensions latérales moyennes ont été déterminées :  $12 \pm 7$  nm pour les NFC désintégrées par la voie enzymatique et  $4 \pm 2$  nm pour celles oxydées par TEMPO. Le degré de polymérisation (DP) diminue et l'indice de cristallinité (CI) augmente avec une augmentation de la concentration des deux solutions enzymatiques. L'oxydation TEMPO n'a pas eu un impact significatif sur le CI de la cellulose. Toutefois, le DP a été fortement affecté. La solution d'endoglucanase monocomposante se trouve avoir une influence plus forte sur l'isolement des nanofibrilles, ainsi que sur leur dépolymérisation.

Le comportement rhéologique des suspensions NFC a été étudié étant donné que l'écoulement et les relations contraintes-déformations sont à l'origine des processus impliqués dans leur mise en forme et leur production et peuvent influencer la performance du produit final (par exemple, dans le processus de revêtement). Les propriétés des suspensions de NFC hydrolysée par la voie enzymatique et oxydée par la voie TEMPO ont été étudiées en cisaillement harmonique et en régime d'écoulement permanent et ont été mis en relation avec la morphologie des matériaux étudiés. Les structures du réseau fibreux les plus fortes ont été formées lors de l'utilisation de la solution d'endoglucanase monocomposante en comparaison à celles produites avec la cellulase. En outre, des nanofibrilles TEMPO-oxydées possèdent un réseau plus fort que les suspensions hydrolysées par voie enzymatique.

Des instabilités d'écoulement de ces suspensions de NFC ont été mises en évidence. Ces instabilités sont couramment attribuées : (i) à une hétérogénéité de l'organisation structurale ; (ii) à des orientations locales ; (iii) à des changements de concentrations locales lorsqu'elles ont lieu dans le volume des échantillons ou (iv) à des phénomènes d'adhésion lorsqu'elles ont lieu aux interfaces des parois des outils. Ces instabilités peuvent introduire une erreur dans les mesures rhéologiques et doivent être prise en compte ou contrôlées. Ces phénomènes ont été visualisés par une technique basée sur l'introduction d'un marquage de l'échantillon avec une suspension de NFC colorée par du dioxyde de titane et le suivi de la déformation de ce marquage au cours de la mise en écoulement des suspensions.

Un glissement entre le bord des outils de la géométrie et la suspension (glissement à la paroi) ainsi que la localisation de l'écoulement dans le volume spécifique de l'échantillon (bandes de cisaillement) ont été observés. L'influence de la géométrie utilisée sur la stabilité ou l'instabilité de l'écoulement ont été analysées pour des géométries de types : cône-plan, cylindres concentriques (géométrie de Couette) et scissomètre (pâles croisées dans une cuve cylindrique).

Le glissement à la paroi a été mis en évidence sur une large gamme de gradients de vitesse pour les deux types de suspensions de NFC : celles produites en utilisant soit des prétraitements enzymatiques soit le prétraitement d'oxydation TEMPO. Par conséquent, les valeurs obtenues ne sont pas représentatives des propriétés de volume intrinsèque des suspensions mais sont altérées avec une certaine erreur, introduite par le glissement à la paroi. Pour éviter ce phénomène les surfaces des outils ont été rendues rugueuses. Cela a abouti à des mesures plus précises pour les suspensions de NFC oxydé par TEMPO, bien que le phénomène de fracturation en bandes de cisaillement ait été observé. Pour les suspensions de NFC obtenues par prétraitement enzymatique l'utilisation d'outils rugueux n'a pas réussi à

empêcher le glissement à la paroi aux bas gradients de vitesse. Néanmoins aux gradients de vitesse élevés (supérieurs à environ  $10\text{ s}^{-1}$ , pour toutes les géométries étudiées), les courbes se rejoignent pour les différentes géométries d'écoulement et pour les différents états de surface (lisse ou rugueux) et l'écoulement est homogène dans l'échantillon, ce qui a permis de caractériser correctement les propriétés d'écoulement de ces suspensions.

Il a été observé que les instabilités d'écoulement sont plus prononcées à concentration en NFC croissante. Il a été montré que l'utilisation de la géométrie rugueuse est nécessaire pour lutter contre le glissement à la paroi, mais n'est pas suffisante pour l'empêcher complètement. La géométrie de Couette rugueuse a été établie comme la géométrie la plus appropriée pour mesurer les propriétés rhéologiques des suspensions de NFC.

La polydispersité de NFC TEMPO-oxydée a été confirmée par analyse de la diffusion des rayons X aux petits angles (SAXS de l'anglais : Small Angle X-rays Scattering). Le diamètre moyen des nanofibrilles, gonflées dans l'eau, a été déterminé à partir des intensités diffusées et un bon accord a été trouvé avec celui déterminé par l'AFM. Il est important de noter que lors de l'utilisation de l'AFM les nanofibrilles sont analysées à l'état sec, ce qui peut donner un diamètre légèrement inférieur en raison de rétrécissement des nanofibrilles pendant le séchage. Cependant, les mesures de SAXS permettent de déterminer le diamètre des nanofibrilles gonflées dans l'eau.

Enfin, deux types de latex de poly[styrène-*co*-(acrylate de 2-éthylhexyle)] ont été synthétisés par polymérisation en miniémulsion comprenant des agents tensioactifs anioniques et cationiques. Ces latex ont été caractérisés pour déterminer la température de transition vitreuse, la distribution moyenne de taille des particules et la distribution de masses molaires. Ces données ont ensuite été utilisées pour étudier les interactions entre les particules et NFC TEMPO-oxydées dans les composites. Ces interactions ont été étudiées sur le plan de l'homogénéité des dispersion de NFC dans la matrice et les propriétés mécaniques de composites obtenus.

Les dispersions aqueuses stables avec une fraction de masse solide de près de 30 % en poids et les composites coulés ont été préparés lors de l'utilisation de latex avec un tensioactif anionique et des NFC TEMPO-oxydés de 1–4 % en poids. La bonne dispersion de la charge dans la matrice a été confirmée par MEB à effet de champ et a été attribuée à la répulsion électrostatique entre les nanofibres de cellulose et les particules de polymère. En dépit de ces forces de répulsion, l'effet de renforcement a été mis en évidence par les essais de traction, pour tous les composites, en comparaison de la matrice pure. Le module d'élasticité et la

résistance à la traction augmentent progressivement en intégrant les NFC dans latex anionique, tandis que la déformation à la rupture diminue. Le renforcement des composites coulés a été attribué à des liaisons hydrogène du réseau percolé de NFC.

L'application de tensioactif cationique dans le latex, qui sert à améliorer les interactions entre NFC chargé négativement et la matrice chargée positivement, a donné lieu à une distribution non homogène des NFC à l'intérieur de la matrice. Ceci a eu lieu en raison de l'agrégation au travers de la création de structures réticulées entre les particules de latex et les NFC, régies par des forces ioniques.

**Mots-clés:** nanocellulose, nanofibres, nanofibrilles de cellulose (NFC), rhéologie, instabilités d'écoulement, diffusion des rayons X aux petits angles (SAXS), nanocomposites, latex, polymérisation en miniémulsion.

# Resumo

Devido às preocupações ambientais, o desenvolvimento de materiais compósitos de base biológica para diferentes aplicações industriais é um tema de investigação de importância crescente. O uso de fibras naturais em compósitos como alternativa às cargas minerais convencionais, que são tradicionalmente utilizadas para reforçar matrizes termoplásticas, é um assunto muito estudado. Esta tese de doutoramento centra-se no desenvolvimento de tais materiais compósitos usando um agente de reforço biodegradável e de origem biológica, os nanofibrilos de celulose (NFC).

Neste trabalho, as suspensões aquosas de NFC foram produzidas a partir de polpa de celulose de madeira resinosa (branqueada com bissulfito) por via enzimática ou por oxidação assistida por 2,2,6,6-tetrametilpiperidina-1-oxilo (TEMPO) a que se seguiu uma moagem por via húmida, usando o Supermasscolloider, como técnica de fibrilação principal. Foi comparada a capacidade de extração de nanofibras, a partir de fibras de celulose, de duas soluções de enzimas comerciais: (i) celulase (Celluclast 1.5 L), com atividade predominante de endoglucanase e exoglucanase, e (ii) endoglucanase de componente único (FiberCare R). Foi analisada a influência das suas concentrações, bem como de outros parâmetros de processamento. A oxidação da celulose, usando oxigénio na presença de N-hidroxiftalimida (NHPI) e de antraquinona a pressão e temperatura elevadas, foi estudada como uma técnica alternativa à oxidação assistida por TEMPO.

A morfologia dos NFC produzidos foi caracterizada por microscopia óptica, microscopia de força atómica (AFM), microscopia eletrónica de varrimento com canhão de emissão de campo (FEG-SEM) e analisador de morfologia de fibras (Morfi). Foram produzidos nanofibrilos com uma ampla distribuição de tamanhos. As dimensões laterais médias encontradas foram de  $12 \pm 7$  nm para os NFC mais desintegrados e hidrolisados com enzimas, e de  $4 \pm 2$  nm para os NFC resultantes da oxidação por TEMPO, sendo ambas determinadas a partir das imagens topográficas AFM. O aumento da concentração de enzimas diminuiu o grau de polimerização (DP) e aumentou o índice de cristalinidade (CI) da celulose nos nanofibrilos. A oxidação através do TEMPO não teve um impacto significativo sobre o CI da celulose; no entanto, o DP foi fortemente afetado. A solução de endoglucanase teve maior influência sobre o isolamento dos nanofibrilos do que na despolimerização.

O comportamento reológico das suspensões NFC foi estudado, visto que, quer o escoamento quer as relações esforço-deformação, estão envolvidos no processo de produção de materiais baseados em NFC e podem influenciar o desempenho do produto final (por exemplo, no processo de revestimento). As propriedades das suspensões de NFC, enzimaticamente hidrolisada ou oxidada por TEMPO, foram investigadas em escoamento de corte de oscilação harmónica e em estado estacionário e relacionadas com a morfologia dos materiais estudados. Quando se usou a solução de endoglucanase (de componente único) foi obtida uma estrutura de rede fibrosa mais forte do que quando se usou a solução de celulase. Além disso, os nanofibrilos oxidados via TEMPO apresentaram uma rede mais forte do que os obtidos nas suspensões hidrolisadas enzimaticamente.

Foram evidenciadas instabilidades de escoamento das suspensões de NFC. Estas instabilidades são habitualmente atribuídas: (i) a uma heterogeneidade da organização estrutural; (ii) a orientações locais; (iii) a alterações locais de concentração em volume ou (iv) a fenómenos de adesão quando ocorrem na interface com a parede do equipamento—e podem introduzir um erro nas medidas reológicas, pelo que devem ser tomadas em conta ou controladas. Essas instabilidades foram visualizadas utilizando uma técnica baseada na marcação de uma faixa específica da suspensão de NFC com um pigmento branco (dióxido de titânio) e monitorização da sua deformação. Foi observado um deslizamento entre a parede do equipamento (deslizamento de parede) e a suspensão, bem como a localização do escoamento num dado volume da suspensão (bandas de corte). Analisou-se a influência, sobre as flutuações do escoamento, da geometria usada: cone-placa, cilindros concêntricos (Couette) e palheta em cruz (vane-in-cup).

Para superar o problema acima mencionado, foi aumentada a rugosidade das superfícies da ferramenta. Foi, assim, possível obter medidas mais precisas para a suspensão de NFC oxidada via TEMPO, ainda que o fenómeno de formação de bandas de corte continuasse a ser observado. O uso de ferramentas com superfícies rugosas para NFC enzimaticamente hidrolisada não conseguiu evitar o deslizamento na parede para baixos gradientes de velocidade. No entanto, para gradientes de velocidade elevados (superiores a cerca de  $10 \text{ s}^{-1}$  para todas as geometrias estudadas), todas as curvas experimentais obtidas, para diferentes geometrias de escoamento e para diferentes estados de superfície (lisa ou rugosa), passaram a ser coincidentes e o escoamento tornou-se homogéneo na amostra o que permitiu caracterizar corretamente as propriedades de escoamento das suspensões. As instabilidades de fluxo foram mais acentuadas com o aumento da concentração de NFC. Mostrou-se que a utilização de superfícies rugosas é necessária para evitar o deslizamento na parede, mas não é suficiente

para impedi-lo por completo. Verificou-se que a geometria mais adequada para medir as propriedades reológicas das suspensões de NFC é a Couette com superfície rugosa.

A polidispersão das NFC oxidadas via TEMPO foi confirmada através da análise de difusão de raios-X a baixo ângulo (SAXS). O diâmetro médio dos nanofibrilos em água foi determinada com base nos dados de difusão de raios-X e estão de acordo com os valores obtidos por AFM. Cabe dizer, que na técnica de AFM os nanofibrilos foram analisados no estado seco e, assim, o diâmetro poderia ser ligeiramente menor devido à retração dos nanofibrilos durante a secagem.

Finalmente, dois látexes-modelo de poli[estireno-co-(2-etilhexil acrilato)] foram sintetizados via polimerização em mini-emulsão utilizando-se surfactantes catiónicos e aniônicos. Estes látexes foram caracterizados em termos de temperatura de transição vítrea, distribuição de tamanho de partícula e massa molar. Estes dados foram depois utilizados como modelo para estudo de interações entre a matriz e os NFC oxidados por TEMPO nos compósitos. Estas interações foram estudadas através da avaliação da dispersão das NFC na matriz e das propriedades mecânicas dos compósitos.

As dispersões aquosas estáveis com uma fracção de massa de sólidos de cerca de 30 % e os compósitos subsequentes foram preparados, no caso da utilização do látex, com surfactante aniônico e 1–4 % em peso de fibrilos oxidados por TEMPO. Uma boa dispersão das fibras na matriz foi confirmada por FEG-SEM e atribuída à repulsão eletrostática entre as fibras e as partículas poliméricas da matriz. Apesar destas cargas repulsivas, um efeito de reforço pode ser determinado em todos os compósitos, se comparados com a matriz, através de testes de tração. Tanto o módulo elástico como a força de rutura apresentaram um incremento progressivo com a adição dos NFC, enquanto a elongação na rutura diminuiu. O efeito de reforço encontrado nos compósitos preparados por evaporação de solvente foi alcançado devido às ligações de hidrogénio presentes na rede percolada de NFC.

A aplicação de um surfactante catiónico no látex, usado para melhorar as interações entre o NFC negativamente carregado e a matriz positivamente carregada, resultaram numa distribuição não homogénea dos fibrilos na matriz. Isso ocorreu devido à agregação causada pela criação de ligações cruzadas entre as estruturas fibrilares do NFC e as partículas de látex, ditadas por forças iónicas.

**Palavras-chave:** nanocelulose, nanofibras de celulose (CNF), nanofibrilos de celulose (NFC), reologia, instabilidades de escoamento, difusão de raios-X a baixo ângulo (SAXS), nanocompósitos, látex, polimerização por miniemulsão.



# Preface

This dissertation reports the results of the work carried out in 2012–2015 at three research units: Laboratoire Rhéologie et Procédés (LRP), France, Laboratoire de Génie des Procédés Papiers (LGP2), France, and Centro de Química-Física Molecular (CQFM), Portugal, performed within the joint doctoral program between Université Grenoble Alpes, France, and Instituto Superior Técnico, Portugal. This dissertation was established in the framework of International Doctoral Program in Functional Materials (IDS-FunMat, Erasmus Mundus), and was funded by French Ministry of Higher Education and Research.

The manuscript is organized so that it starts with Chapter 1, describing the production of NFC and focusing basically on the morphological properties of the obtained nanofibers. Chapter 2 presents the rheological and structural characterization of NFC suspensions using rheometry and small-angle X-ray scattering techniques, respectively. Chapter 3 is dedicated to the incorporation of nanofibrillated cellulose into latex matrices for the production of bionanocomposites, describing the mechanical, thermal and morphological properties of the final products.

This dissertation is the original work of the author. The field emission gun scanning electron microscopy (FEG-SEM) and X-ray diffraction (XRD) measurements were performed at the Consortium des Moyens Technologiques Communs (CMTC), Grenoble. Nuclear magnetic resonance (NMR) spectrometry was performed at Laboratoire d'Electrochimie et de Physicochimie des Matériaux et des Interfaces (LEPMI), Grenoble. The Small-angle X-ray scattering (SAXS) measurements were carried out at European Synchrotron Radiation Facility (ESRF), Grenoble. The data analyses were performed by the author. The processing of cellulose suspensions through homogenizer was carried out at Centre Technique du Papier (CTP), Grenoble. All other experiments were performed on-site in the permanent laboratories. Some figures were adapted from the original artwork with the reference to the original sources and, if required, with the permission of copyright reproduction from the appropriate right holder.

The parts of this work have been published in the following articles:

- (i) Nechyporchuk O, Belgacem MN, Pignon F (2014) Rheological properties of micro-/nanofibrillated cellulose suspensions: Wall-slip and shear banding phenomena. *Carbohydrate Polymers* 112:432–439. doi: 10.1016/j.carbpol.2014.05.092;

- (ii) Nechyporchuk O, Pignon F, Belgacem MN (2015) Morphological properties of nanofibrillated cellulose produced using wet grinding as an ultimate fibrillation process. *Journal of Materials Science* 50(2), 531–541. doi: 10.1007/s10853-014-8609-1;
  - (iii) Nechyporchuk O, Belgacem MN, Pignon F (2015) Concentration effect of TEMPO-oxidized nanofibrillated cellulose aqueous suspensions on the flow instabilities and small-angle X-ray scattering structural characterization. *Cellulose* 22(4), 2197–2210. doi: 10.1007/s10570-015-0640-0;
  - (iv) Nechyporchuk O, Pignon F, Botelho Do Rego AM, Belgacem MN (2016) Influence of ionic interactions between nanofibrillated cellulose and latex on the ensuing composite properties. *Composites Part B* 85, 188–195. doi.org/10.1016/j.compositesb.2015.09.030.
- and were presented at the following conferences:

- (i) winter training school Use of Nanopolysaccharides in Biobased Packaging, 2013, Grenoble (oral presentation);
- (ii) 9<sup>th</sup> TAPPI International Conference on Nanotechnology for Renewable Materials, 2014, Vancouver (poster presentation);
- (iii) 49<sup>th</sup> annual congress of the French Group of Rheology, 2014, Grenoble (poster presentation);
- (iv) 2<sup>nd</sup> International Conference on Natural Fibers, 2015, Ponta Delgada, Portugal (oral presentation);
- (v) three training schools of IDS-FunMat, 2013–2015 (oral presentations).

This dissertation emerged thanks to great researchers, who supervised this work: Mohamed Naceur Belgacem, Frédéric Pignon and Ana Maria Botelho do Rego. I would like to express my deep appreciation and gratitude to them for their inspiring guidance, support and encouragement within all the years of this project. I express my gratitude to the members of the dissertation committee for their time and critical comments which have helped to improve this work. I would like to thank my family, friends and colleagues for the support during these years and for the memorable moments we had.

Oleksandr Nechyporchuk



1.2.3.6	Determination of degree of polymerization (DP).....	21
1.2.3.7	X-ray diffraction (XRD).....	22
1.2.3.8	Carboxyl content determination .....	22
1.2.3.9	Fourier transform infrared (FTIR) spectroscopy.....	22
1.3	Results and discussion.....	23
1.3.1	Influence of mechanical disintegration .....	23
1.3.2	Enzymatic pretreatment.....	25
1.3.3	Oxidation pretreatment.....	30
	Conclusions .....	32
	References .....	33

<b>Chapter 2</b>	<b>Rheological and structural properties of nanofibrillated cellulose suspensions .....</b>	<b>43</b>
	Introduction .....	43
2.1	State of the art .....	44
2.1.1	Introduction to rheology .....	44
2.1.2	Rheology of NFC suspensions .....	46
2.1.3	SAXS characterization .....	48
2.2	Experimental .....	49
2.2.1	Nanofibrillated cellulose suspensions production .....	49
2.2.2	Rheological measurements.....	50
2.2.3	Visualization approach .....	51
2.2.4	SAXS measurements .....	52
2.2.5	Analysis of SAXS data.....	53
2.3	Results and discussion.....	55
2.3.1	Oscillation measurements.....	55
2.3.2	Flow properties .....	59
2.3.3	Flow instabilities visualization.....	59
2.3.4	Influence of NFC concentration on flow instabilities .....	65
2.3.5	SAXS characterization .....	73
	Conclusions .....	78
	References .....	80
<b>Chapter 3</b>	<b>Composites production from nanofibrillated cellulose and latex .....</b>	<b>85</b>
	Introduction .....	85
3.1	State of the art .....	86

---

3.1.1 Composites.....	86
3.1.2 Nanofibrillated cellulose composites .....	87
3.1.2.1 Hydrophilic matrices.....	88
3.1.2.2 Hydrophobic matrices.....	92
3.1.3 Latex/nanofibrillated cellulose composites.....	93
3.2 Experimental.....	95
3.2.1 Materials.....	95
3.2.2 Nanofibrillated cellulose production.....	95
3.2.3 Latex synthesis.....	96
3.2.4 Composites fabrication .....	97
3.2.5 Characterization techniques .....	98
3.2.5.1 Monomer to polymer conversion.....	98
3.2.5.2 Dynamic light scattering (DLS).....	98
3.2.5.3 Size-exclusion chromatography (SEC).....	98
3.2.5.4 Optical microscopy .....	99
3.2.5.5 Field emission gun scanning electron microscopy (FEG-SEM).....	99
3.2.5.6 Differential scanning calorimetry (DSC).....	99
3.2.5.7 Tensile testing .....	99
3.2.5.8 Proton nuclear magnetic resonance ( <sup>1</sup> H NMR) .....	100
3.2.5.9 X-ray photoelectron spectroscopy (XPS) .....	100
3.3 Results and discussion .....	100
3.3.1 Synthesis of model latex .....	100
3.3.2 Composites production and characterization .....	106
Conclusions.....	113
References.....	114
 General conclusions.....	 125
 Résumé substantiel (Extended Summary).....	 129
 Annex A. Supplementary material for Chapter 1 .....	 141
 Annex B. Cellulose oxidation by oxygen, catalyzed by N-hydroxyphthalimide (NHPI) .....	 143
 Annex C. Supplementary material for Chapter 2 .....	 147
 Annex D. Supplementary material for Chapter 3 .....	 149



# Symbols and Abbreviations

$\gamma$	Strain
$\dot{\gamma}$	Shear (strain) rate
$\eta$	Viscosity
$\sigma$	Shear stress
AFM	Atomic force microscopy
BNC	Bacterial nanocellulose
CI	Crystallinity index
CNC	Cellulose nanocrystals
DLS	Dynamic light scattering
DP	Degree of polymerization
DP <sub>v</sub>	Viscometric degree of polymerization
DSC	Differential scanning calorimetry
DMA	Dynamic mechanical analysis
EHA	Ethylhexyl acrylate
EVOH	Ethylene–vinyl alcohol
FEG-SEM	Field emission gun scanning electron microscopy
FTIR	Fourier transform infrared spectroscopy
$G'$	Storage modulus
$G''$	Loss modulus
<sup>1</sup> H NMR	Proton nuclear magnetic resonance
$I(q)$	Scattered intensity
MFC	Microfibrillated cellulose
$M_n$	Number-average molar mass
$M_w$	Weight-average molar mass
MorFi analyzer	Morphological fiber analyzer
MTAB	Myristyltrimethylammonium bromide
NFC	Nanofibrillated cellulose
NMR	Nuclear magnetic resonance
PCL	Polycaprolactone
PDI	Polydispersity index
PE	Polyethylene

---

PHA	Polyhydroxyalkanoates
PHBV	Poly[(3-hydroxybutyrate)- <i>co</i> -(3-hydroxyvalerate)]
PLA	Poly(lactic acid)
PP	Polypropylene
P[S- <i>co</i> -(2-EHA)]	Poly[styrene- <i>co</i> -(2-ethylhexyl acrylate)]
PVOH	Poly(vinyl alcohol)
$q$	Magnitude of scattering vector
SAXS	Small-angle X-ray scattering
SDS	Sodium dodecyl sulfate
SEC	Size-exclusion chromatography
SEM	Scanning electron microscopy
$T_g$	Glass transition temperature
TEMPO	2,2,6,6-tetramethylpiperidine-N-oxyl
THF	Tetrahydrofuran
XPS	X-ray photoelectron spectroscopy
XRD	X-ray diffraction

# Chapter 1 Nanofibrillated cellulose production and properties

## Introduction

Nowadays there is a strong demand for development of high added-value products from renewable resources, which are designated to substitute petroleum-based materials. This work demonstrates the production of nanofibrillated cellulose (NFC), the material with exceptional mechanical and optical properties, low density, renewable and biodegradable character, which makes it promising for applications in such fields as composites, packaging, adhesives, biomedicine and automotive (Klemm *et al.* 2011; Tingaut *et al.* 2011).

The production of NFC from wood pulp fibers is the dominant theme in this chapter. Cellulose nanofibrils can be extracted from cellulosic fibers using mechanical disintegration methods; however, there is a strong need of using alternative ways in order to facilitate fibers fibrillation and to reduce the energy consumption during the production process. In this context, chemical oxidation or enzymatic hydrolysis techniques are known to be applied in combination with mechanical treatment.

In this work, the influence of the mechanical disintegration, combined with enzymatic or oxidation treatment, on the nanofibrillated cellulose isolation was analyzed. Cellulose hydrolysis using: (i) cellulase solution (Celluclast 1.5 L), with the major activity of endoglucanase and exoglucanase, and (ii) monocomponent endoglucanase solution (FiberCare R) was compared in terms of nanofibrils isolation. The variation of the degree of polymerization and crystallinity index is reported. TEMPO-mediated cellulose oxidation using sodium hypochlorite is studied. The oxidation with oxygen in the presence of N-hydroxyphthalimide (NHPI) and anthraquinone at high pressure and temperature are investigated. Disintegration of cellulose suspensions using wet grinding, as an ultimate fibrillation technique, is reported.

## 1.1 State of the art

### 1.1.1 Cellulose

Cellulose is the most abundant natural polymer on Earth. It is renewable, biodegradable and non-toxic material and is a vast source for environmentally friendly and biocompatible products. The annual production of cellulose by photosynthesis is estimated to be  $10^{11}$ – $10^{12}$  ton (Klemm *et al.* 2004). It has been used for centuries as a source of heat or construction material, in paper and board, and in textile industry. Furthermore, it is a versatile source for different products obtained by cellulose chemical modification.

#### 1.1.1.1 Feedstocks

Cellulose can be derived from a variety of sources such as: wood (hardwood and softwood), seed fibers (cotton, coir *etc.*), bast fibers (flax, hemp, jute, ramie *etc.*), grasses (bagasse, bamboo *etc.*), marine animals (tunicate), algae, fungi, invertebrates and bacteria (Varshney and Naithani 2011).

Wood is currently the most important industrial source of cellulose (Siró and Plackett 2010; Stelte and Sanadi 2009). Besides cellulose, it also contains hemicelluloses and lignin and a very small content of extractives and mineral substances. Wood species can be distinguished as hard- and softwoods based on their anatomical features. Hardwood is more complex and heterogeneous in structure than softwood (Wiedenhoeft and Miller 2005). Generally, softwood fibers are 3–4 times longer than hardwood ones (Shackford 2003). However, it is known that hardwoods have more rigid structure than softwoods due to their high Runkel ratio (cell wall thickness divided by lumen radius) (Wang *et al.* 2012), which is valid for dense hardwoods (*e.g.*, *Eucalyptus*). Thus, it was reported (Stelte and Sanadi 2009) that softwood requires less mechanical treatment than hardwood to produce equivalent fibrillation.

At the same time, non-wood plants are getting increasing interest as a source of cellulose since they generally comprise less lignin. Consequently, fibers isolation and purification processes are easier and less harmful for cellulose (Siró and Plackett 2010). Moreover, the further fibrillation of such cellulose is less energy-consuming.

It should be also noted, that the use of never-dried cellulose comparing to once-dried makes the fibrillation more favorable, since drying promotes irreversible hydrogen-bonding

between microfibrils, known as hornification (Spinu *et al.* 2011). However, the dry cellulose is much easier to transport. Therefore, the research focuses also on the use of dry cellulose as a raw material for NFC production.

### 1.1.1.2 Structure and chemistry

Cellulose is the main constituent of higher (vascular) plants and is the primary structural component responsible for their mechanical strength. Cellulose can be also found in some algae, bacteria, fungi, protozoans and animal tunicates; however, the commercial cellulose production concentrates on the harvested sources such as wood, annual plants or agricultural residues. Besides cellulose, they contain hemicelluloses, lignin, and a very small amount of extractives. In such products cellulose is represented as a well-organized architecture of fibrillar elements composing the cells.

Each cell represents a fiber with the width of 10–50  $\mu\text{m}$ , consisting of cell wall layers, which have the total thickness of 1–5  $\mu\text{m}$  (Chinga-Carrasco 2011) (see Figure 1.1, related to spruce wood). The middle lamella binds the neighboring cells due to the high content of lignin. The cells surround a central cavity called lumen. The cell wall is composed of three

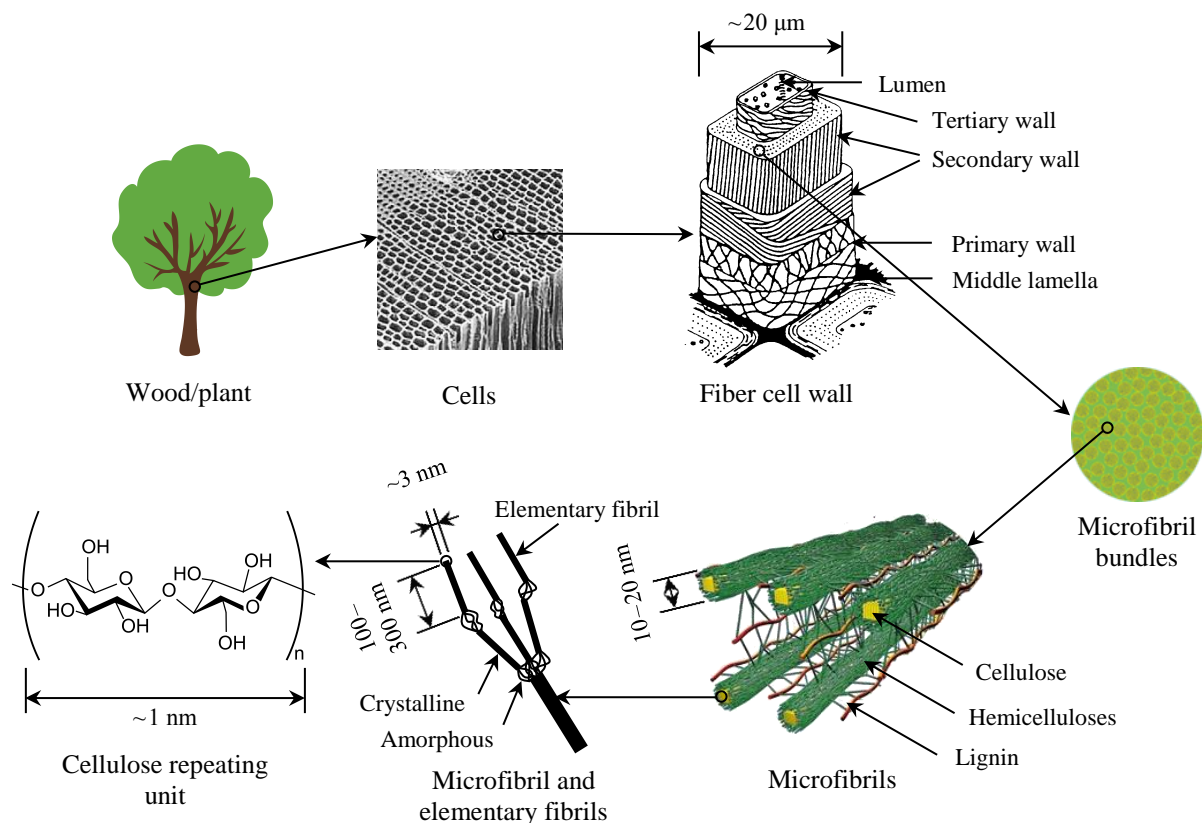


**Figure 1.1** Schematic diagram of the structural composition of spruce wood (adapted from Fengel and Wegener 1983; and Ritter 2008)

cell wall layers: primary, secondary and tertiary wall. Each region contains three main components: cellulose microfibrils (with characteristic distributions and organization), hemicelluloses, and a matrix, typically, pectin in primary walls and lignin in secondary walls.

The primary cell wall is approximately 0.03–1.0  $\mu\text{m}$  thick and also contains a high percentage of lignin. The microfibrils in the primary wall are located crosswise, forming a layer of 50 nm. The secondary cell wall consists of two layers with a thickness from about 100 nm (cotton) to 300 nm (spruce pulp). The secondary cell wall contains most of the cellulose mass. Within this layer the microfibrils are aligned parallel and packed densely in a flat helix. The inner layer closest to the fiber lumen is the tertiary layer, which is rather thin and has the microfibrils aligned in a flat helix as well (Klemm *et al.* 1998).

As described above, cellulose is present in the fibers in form of the microfibrils. For instance, in the spruce wood the microfibrils have a diameter of 10–20 nm. These microfibrils are in turn made of the elementary fibrils, which are considered as the smallest morphological units in the fiber (Frey-Wyssling and Mühlethaler 1963). The diameter of elementary fibrils varies from 3 to 35 nm depending on the cellulose source (Klemm *et al.* 2005), and is in the range of 2.2–3.6 nm for spruce wood (Fernandes *et al.* 2011), as shown in Figure 1.1.

Cellulose is a semicrystalline polymer comprising the crystalline (ordered) and amorphous (disordered) regions within microfibril, where the individual cellulose molecule is considered to pass through several crystalline and amorphous parts according to fringe micelle theory (Shmulsky and Jones 2011). The degree of crystallinity is usually in the range of 40–60% and depends on the origin of cellulose and the isolation method.

The building blocks of cellulose polymer chain are D-glucopyranose (glucose) molecules. When linked together by  $\beta$ -1,4-glucosidic bonds they turn to anhydroglucose units. Two anhydroglucose units compose cellobiose, which is the repeating unit of cellulose polymer (see Figure 1.2). Each anhydroglucose unit has six carbon atoms with three hydroxyl groups (at C2, C3, and C6 atoms) giving a high degree of functionality to cellulose molecule. There are three types of anhydroglucose units: (i) reducing end with free hemiacetal or aldehyde

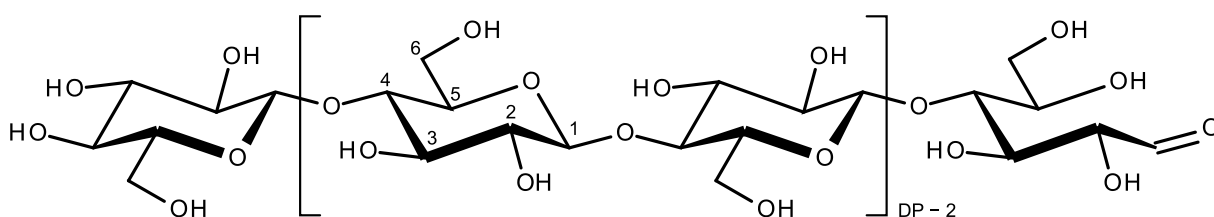


**Figure 1.2** Molecular structure of cellulose polymer

group at C1 atom, (ii) non-reducing end with free hydroxyl group at C4 atom, and (iii) internal rings. Due to its molecular structure, cellulose bears such properties as hydrophylicity, insolubility in water and most organic solvents, degradability and chirality.

The degree of polymerization (DP) of cellulose varies depending on the cellulose source (*e.g.*, 10 000 in native wood, 20 000 in cotton, 44 000 in *Valonia*) and the isolation or purification method (*e.g.*, 200–500 in regenerated cellulose and 1000 in bleached kraft pulps) (Fengel and Wegener 1983; Wertz *et al.* 2010).

### 1.1.2 Nanocellulose

The individual cellulose elements with a diameter in nanometer range (<100 nm) is referred to nanocellulose. Depending on the production conditions, which influence the dimensions, composition, and properties, the nanocellulose can be divided into three main categories (Klemm *et al.* 2011): (i) cellulose nanocrystals (CNC) or whiskers; (ii) nanofibrillated cellulose (NFC) or microfibrillated cellulose (MFC), or cellulose nano-/microfibrils and (iii) bacterial nanocellulose (BNC). However, the terminology of cellulose nanomaterials has not been standardized yet.

CNC and NFC are produced by disintegration of cellulose fibers to the nanomaterial (see Figure 1.3). On the contrary, BNC is generated by a buildup from low molecular weight sugars by aerobic bacteria. Regardless of the nanocellulose type, it exhibits hydrophilic character, relatively large specific surface area, broad potential of surface chemical modification *etc.*

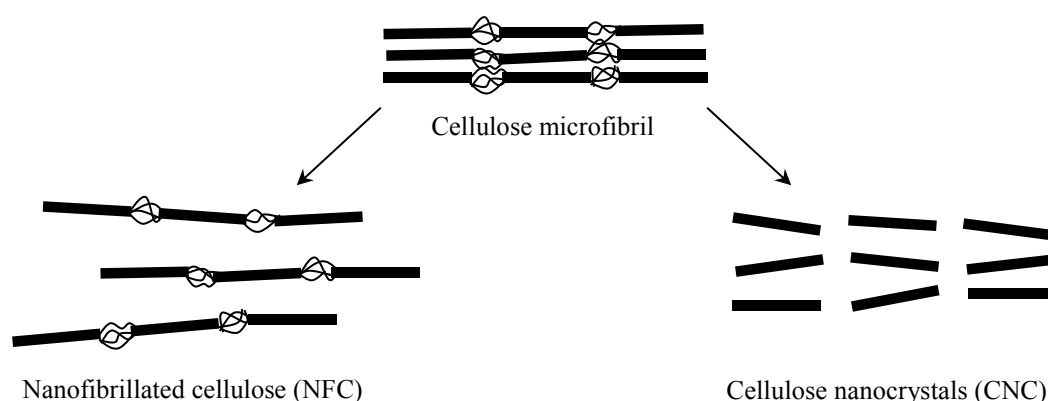


**Figure 1.3** Schematic representation of nanofibrillated cellulose and cellulose nanocrystals individualization from cellulose microfibrils

### 1.1.2.1 Cellulose nanocrystals

CNC, otherwise known as cellulose whiskers, were first produced by Rånby (1949) using acid hydrolysis of cellulose fibers in aqueous suspensions. In this method, the concentrated sulfuric acid ( $\text{H}_2\text{SO}_4$ ) is commonly used, which degrades amorphous regions of cellulose and leaves crystalline ones. By such a treatment, rod-like CNC with sulfate groups at their surface are produced. Their morphology generally depends on the source of cellulose. Typically, nanocrystals with diameters of 3–35 nm and lengths of 0.05–4  $\mu\text{m}$  are produced (Moon *et al.* 2011).

### 1.1.2.2 Nanofibrillated cellulose

NFC as a new cellulosic material was introduced by Turbak *et al.* (1983a, b) who produced cellulose with the lateral dimensions in nanometer range by passing softwood pulp aqueous suspension through a high-pressure homogenizer. During such treatment, strongly entangled networks of nanofibrils, having both crystalline and amorphous domains, are produced due to high shearing forces. They possess high aspect ratio and gel-like behavior in water with pseudoplastic and thixotropic properties (Klemm *et al.* 2011). Depending on the processing conditions, cellulose fibers can be disintegrated to NFC with the lateral dimensions from  $\sim 3$  nm, representing elementary fibrils, to tens of nanometers, which corresponds to microfibrils. Typically, NFC has a diameter of 5–50 nm and a length of few micrometers (Isogai 2013, Lavoine *et al.* 2012). The in-depth review of NFC production techniques and properties is presented in Section 1.1.3.

### 1.1.2.3 Bacterial nanocellulose

BNC, or simply bacterial cellulose (BC), is high-purity cellulose generated by *Gluconacetobacter* bacterial strains in aqueous culture media containing sugar source. The time of such process ranges from days up to two weeks (Gatenholm and Klemm 2010). BNC has the same chemical composition as plant cellulose; however, it is free of functional groups other than hydroxyl, *e.g.*, carboxyl or carbonyl, which are usually introduced to wood or plant-derived cellulose during the purification process. BNC is also free from the other polymers, *e.g.*, lignin, hemicelluloses or pectin. BNC is assembled into hierarchical structures of nanofibrils with a width of 10 nm and a length of more than 2  $\mu\text{m}$  (Stevanic *et al.* 2011). It has a DP in the range of 3000–9000 and a crystallinity index of 80–90%.

### 1.1.3 Nanofibrillated cellulose

Last years have become a real breakthrough in commercial production of nanofibrillated cellulose (NFC) and this progress seems only to expand. Today NFC is already available in the market as a commercial product and gains much interest for industrial application in such areas as papermaking, paints and coatings, composites, pharmaceuticals and cosmetics, food. Such interest in the NFC is supported as well by growing annual number of scientific publications, as shown in Figure 1.4.

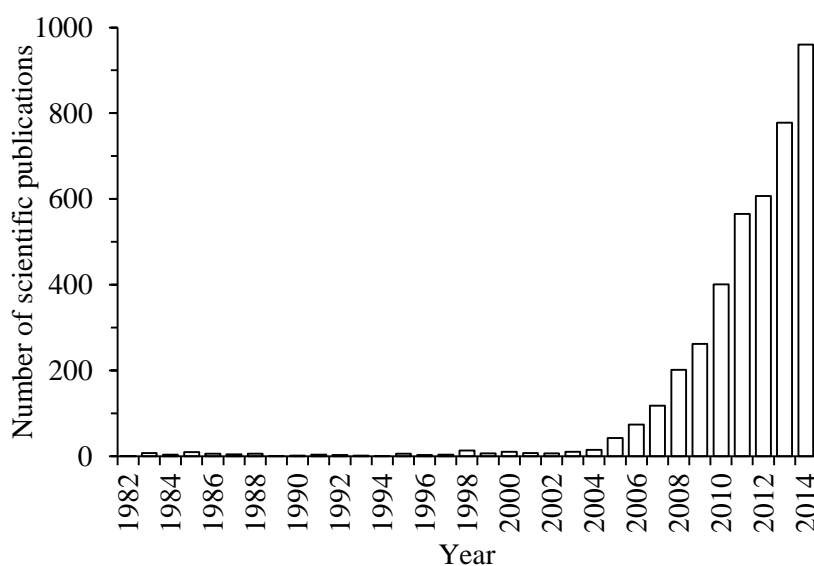


**Figure 1.4** Annual number of scientific publications and patents using the keywords: nanofibrillated cellulose, microfibrillated cellulose, cellulose nanofibers and cellulose nanofibrils. Data analysis performed using SciFinder database in February, 2015

During the last decades the isolation of cellulose nanofibrils was a challenge due to the high energy demanded by mechanical disintegration process. However, by introducing the pretreatment methods, *e.g.*, TEMPO-mediated oxidation (Saito *et al.* 2006) or enzymatic hydrolysis (Henriksson *et al.* 2007; Pääkkö *et al.* 2007), which facilitate the mechanical disintegration, NFC became more attractive for commercial application.

#### 1.1.3.1 Disintegration techniques

Dry cellulose fibers can be disintegrated to small fragments using mechanical methods. However, it leads to shredding of the fibers, rather than splitting of the elementary fibrils, resulting in low degree of polymerization and aspect ratio, and hence relatively poor mechanical properties. This occurs due to strong hydrogen bonding between cellulose molecular chains. The interfibrillar hydrogen bonding energy should be exceeded to

individualize the elementary fibrils or microfibrils. Moreover, to benefit from the disintegrated fibrils, the reverse coalescence should be prevented. For this reason, NFC is commonly produced by disintegration of cellulose fibers in aqueous medium, which loosen the interfibrillar hydrogen bonds. Cellulose is usually dispersed at low concentrations (~2 wt.%) due to its high water retention capacity.

**Refining.** The refining process, commonly used in papermaking industry, is used prior to major operations of NFC production in order to swell and peel the fiber cell walls. Refining increases fibers specific surface and volume (Carrasco *et al.* 1996) and makes the microfibrils more accessible for chemicals or enzymes. Refining increases also the amount of fines and decreases fibers length through cutting. Several refining devices are used to refine cellulose pulp at the initial stages of NFC production: disk refiners (Hamada *et al.* 2012; Nakagaito and Yano 2004), PFI mills (Henriksson *et al.* 2007; Janardhnan and Sain 2007; Turbak *et al.* 1983b), Valley beaters (Joseleau *et al.* 2012; Spence *et al.* 2010) and grinders (Hassan *et al.* 2011; Stelte and Sanadi 2009). The laboratory PFI mill and Valley beater are shown in Figure 1.5.



**Figure 1.5** Laboratory refiners used for pulp fibrillation: PFI mill (a) and Valley beater (b)

**Homogenization.** During homogenization, cellulose suspension is forced at high pressure through specific assemblies, where fibrillation occurs. In this context, there are two types of equipment employed: homogenizers (Henriksson *et al.* 2007; Nakagaito and Yano 2004; Turbak *et al.* 1983a, b; Svagan *et al.* 2007) and microfluidizers (Henriksson *et al.* 2007; Pääkkö *et al.* 2007; Zimmermann *et al.* 2004), as illustrated in Figure 1.6. These devices are commonly used in several industries, *e.g.*, food, cosmetic, pharmacy, biotechnology.

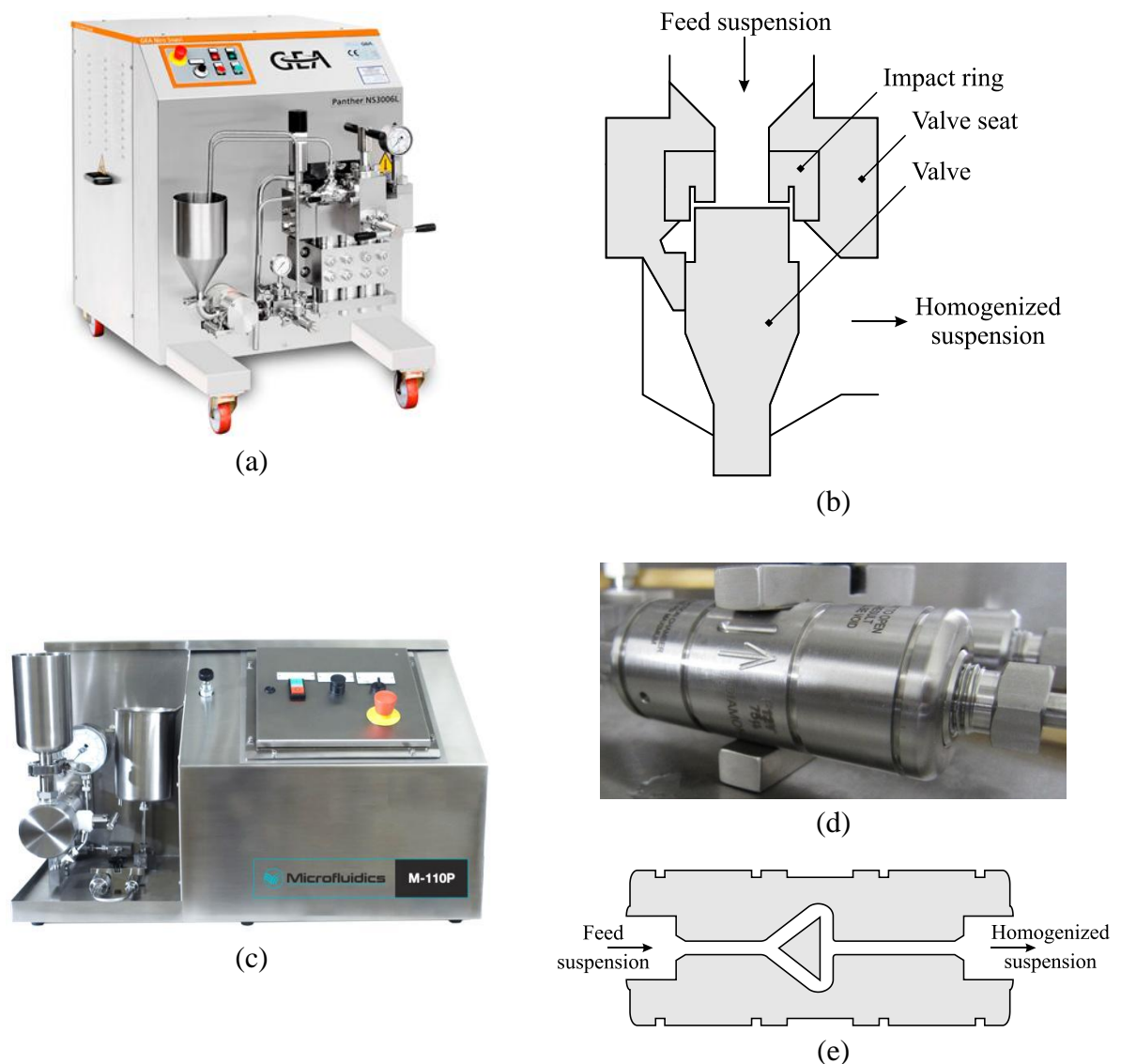


**Figure 1.6** The photograph of homogenizer Panther NS3006L, GEA Niro Soavi S.p.A., Italy (a), reproduced from [www.niro-soavi.com](http://www.niro-soavi.com); and the schematic diagram of its homogenizing valve (b), reproduced from [wikipedia.org](http://wikipedia.org); the photograph of microfluidizer processor M-110P, Microfluidics, USA (c), reproduced from [www.microfluidicscorp.com](http://www.microfluidicscorp.com); and the photograph (d) and schematic diagram (e) of its interaction chamber, reproduced from [www.labx.com](http://www.labx.com)

Turbak *et al.* (1983a, b) and Herrick *et al.* (1983) reported the production of NFC by passing water suspension of refined wood pulp through Manton-Gaulin homogenizer. As a result they obtained individualized microfibrils with diameters less than 100 nm. Before the homogenization, cellulose was refined with PFI mill up to 10 000 revolutions and passed through homogenizer at a pressure of 8000 psi with water cooling to maintain stable temperature of 70–80 °C. (Turbak *et al.* 1983b). During such a treatment, the cellulose slurry is fed through a spring-loaded valve assembly which opens and closes rapidly subjecting the fibers to large pressure drops with shear and impact forces, which ensure cellulose fibrillation (Nakagaito and Yano 2004).

As an alternative for homogenizer, Zimmermann *et al.* (2004) reported the use of microfluidizer (Microfluidics Inc., USA) for cellulose fibrillation. Sulphite pulp suspensions were passed through M-100Y microfluidizer at a pressure of 1000 bar for 60 min. As a result, microfibrils of 20–100 nm in diameter and several tens of micrometers in length were obtained. When cellulose is passed through thin chamber of microfluidizer (*e.g.*, Z- or Y-shape, orifice width of 100–400  $\mu\text{m}$ ), very high velocities are achieved with strong shear forces and impacts against the channel walls. It was also reported that the NFC was produced by 5 passes of cellulose suspension through the chamber of 100  $\mu\text{m}$  at a pressure of 2200 bar (Da Silva Perez *et al.* 2010).

For a long period of time the main barrier for commercial success of homogenization process was the high energy consumption reaching 70 000 kW h/ton (Eriksen *et al.* 2008). However, with the development of pretreatments methods (*e.g.* enzymatic or oxidation) this value decreased drastically and can be around 2000 kW h/ton (Lindström 2011). Another disadvantage of homogenization technique is often clogging of the system when using long fibers (Spence *et al.* 2011).

**Grinding.** An ultra-fine friction grinding is another technique used for the production of nanofibrillated cellulose applying Supermasscolloider grinder (Masuko Sangyo Co. Ltd., Japan) (see Figure 1.7). Taniguchi and Okamura (1998) described the production of NFC by passing 5–10 wt.% natural fibers suspensions from different sources through grinder for

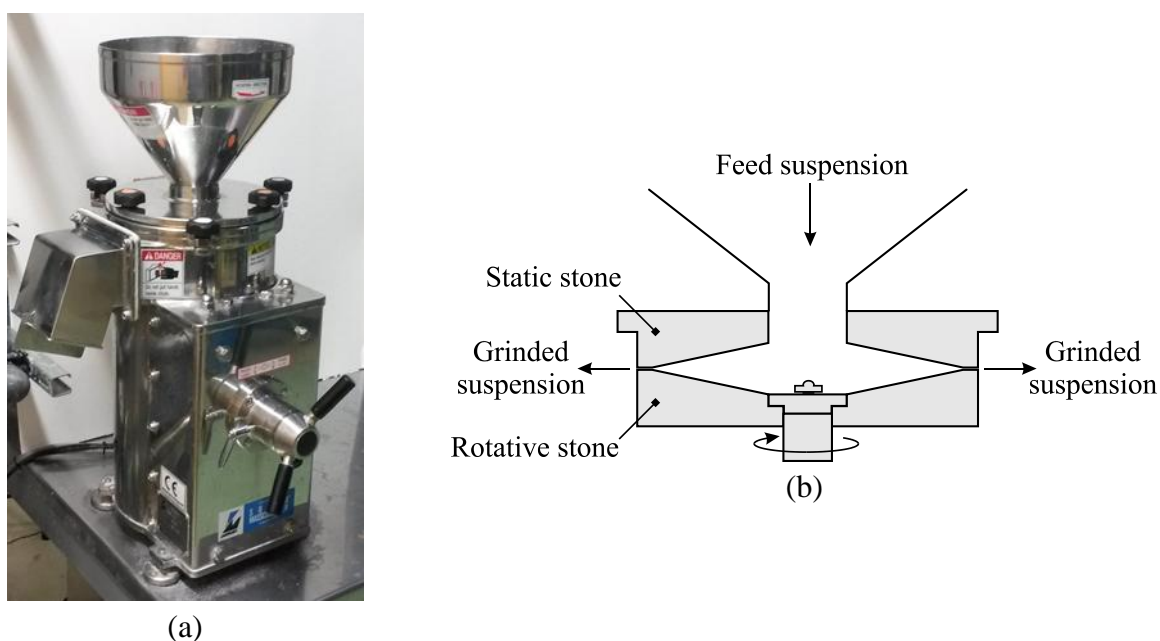


**Figure 1.7** The photograph of grinder Supermasscolloider MKCA6-2, Masuko Sangyo Co. Ltd., Japan (a) and the schematic diagram of its working principle (b)

10 times and obtained NFCs with diameter in the range of 20–90 nm. During such process the cellulose slurry is passed between a static and rotating grinding stones. By the shearing forces generated between the stones the cell wall is delaminated and the nanofibrils are individualized. Other researchers (Bulota *et al.* 2012; Jonoobi *et al.* 2012; Iwamoto *et al.* 2007) reported the production of NFC by such method, but all of them used never-dried cellulose as a raw material, which is much easier to be fibrillated.

**Extrusion.** Twin-screw extrusion can be used for NFC fibrillation from cellulose fibers. With such technique cellulose pulp is disintegrated by two intermeshing, co-rotating screws mounted in a closed barrel. The production of NFC from never-dried refined needle-leaf bleached kraft pulp by twin-screw extrusion was showed by Ho *et al.* (2015). A combination of kneading and feeding screws was used and the operating temperature of 0 °C was set. The pulp was fed in the extruder at the concentration of 28 wt.% and was fibrillated up till 14 passes. The further processing was not performed since the temperature exceeded 40 °C. By increasing the passes number, the evaporation of the moisture in the pulp occurred. Finally, the solid content of 45 wt.% was obtained and NFC was in the form of humid powder. Scanning electron microscopy (SEM) revealed the production of nanofibers by extrusion process.

Extrusion has several advantages comparing to homogenization or grinding techniques. First, NFC at high solid content, *e.g.*, 25–40 wt.% (Ho *et al.* 2015), can be processed, which can be a significant benefit for transportation as well as storage and production itself. Second, cellulose *in situ* fibrillation can be performed while melt compounding of composites. The remaining challenge of this technique is optimization of the screw profile and other processing conditions to achieve the sufficient shear forces necessary to delaminate the fibers along with preventing the cellulose degradation.

### 1.1.3.2 Enzymatic pretreatments

The production of NFC using mechanical disintegration requires high energy costs (Spence *et al.* 2011; Tejado *et al.* 2012). Therefore, an intensive research has been performed over the last decades to facilitate fibrillation and reduce energy demand. Recent production methods of NFC involve mainly enzymatic and chemical pretreatments.

It has been known for a long time that some enzymes catalyse the hydrolysis of cellulose and enhance its fibrillation. In 1962 Bolaski *et al.* patented the use of cellulase to improve cellulose fibrillation in papermaking process. Since then, an extensive investigation has been carried out ranging from mild enzymatic hydrolysis in order to facilitate refining process till strong hydrolysis to convert cellulose into glucose for further production of bioethanol

(Tangnu 1982). Only recently the production of NFC by mild enzymatic hydrolysis of the previously refined bleached softwood pulp, followed by homogenization treatment, was reported (Henriksson *et al.* 2007; Pääkkö *et al.* 2007). In both works a monocomponent endoglucanase Novozym 476 (Novozymes A/S, Denmark) was used as an enzyme.

Fungi are the main microorganisms producing cellulases, although some bacteria and actinomycetes have also been reported to yield cellulase activity (Jayant *et al.* 2011). Generally, cellulases can be divided into three classes: (i) endoglucanases (endocellulases), which hydrolyse amorphous regions of cellulose; (ii) cellobiohydrolases (exoglucanases), which progressively cleave the ends of cellulose crystalline or amorphous regions, producing disaccharides (cellobiose) and tetrasaccharides, and (iii)  $\beta$ -glucosidases (cellobiases), which hydrolyze the di- and tetrasaccharides into glucose (Zhou and Ingram 2000). Two cellobiohydrolases occur in natural cellulases: cellobiohydrolase I and cellobiohydrolase II, which hydrolyze reducing and non-reducing ends of the cellulose molecular chain, respectively (Väljamäe *et al.* 1998). A schematic representation of each enzyme activity on cellulose is shown in Figure 1.8. In the process of enzymatic hydrolysis cellulases can be irreversibly bound to lignin; hereby, it is necessary to remove the latter before the hydrolysis (Andersen 2007).

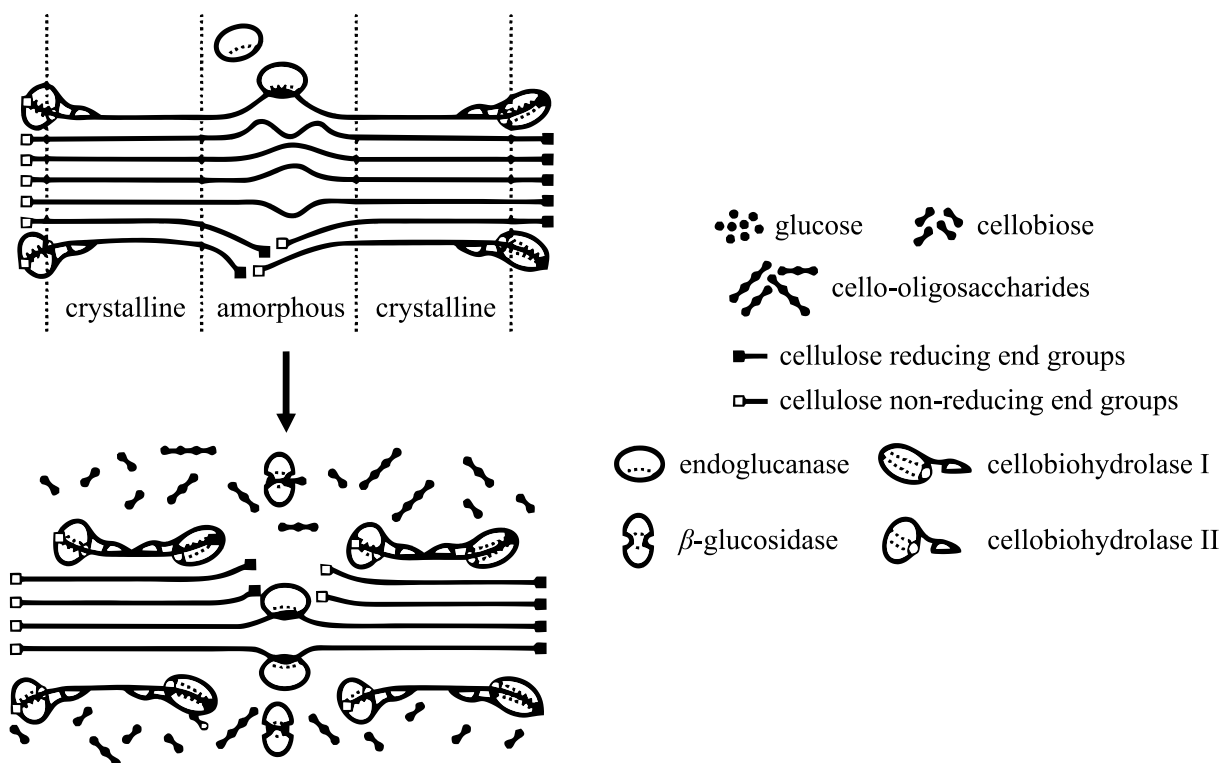


**Figure 1.8** Schematic diagram of the cellulase types activity: endoglucanase, cellobiohydrolase I and II and  $\beta$ -glucosidase (adapted from Lynd *et al.* (2002) with permission of American Society for Microbiology)

Some studies (Siqueira *et al.* 2010; Qing *et al.* 2013) reported the use of cellulase solution Celluclast 1.5 L (Novozym A/S, Denmark), which is a mixture of endoglucanase, exoglucanase and cellobiase (Turon *et al.* 2008) with the major activity of endoglucanase and exoglucanase (Rosgaard *et al.* 2007). The comparison of cellulase solutions: Celluclast 1.5 L and Ecopulp Energy (AB Enzymes, Germany) was also reported for the production of NFC (Siqueira *et al.* 2010). The latter enzyme solution has the major activity of exoglucanase.

Qing *et al.* (2013) compared the use of endoglucanase solution FiberCare (the grade was not specified) and the mixture of FiberCare and Celluclast 1.5 L for the production of NFC. They did not find a significant difference between these treatments. In our study, the use of cellulase solution Celluclast 1.5 L and endoglucanase solution FiberCare R apart is compared for the production of NFC. Enzymatic pretreatment is a very promising method for industrial application and large-scale production. It was reported to be used at first pilot plant for production of NFC by Innventia (Lindström 2011), and at pilot scale within SUNPAP project (2012).

### 1.1.3.3 Chemical pretreatments

**Carboxymethylation.** The introduction of charged groups (*e.g.*, carboxymethyl and carboxyl) into cellulosic fibers is known to improve delamination of the microfibrils. This happens due to electrostatic repulsion formed between the negatively charged cellulose microfibrils (Bäckström *et al.* 2012). Based on the same principle, it is known that sulfite pulps are easier to delaminate than kraft homologues.

Carboxymethyl cellulose was first prepared in 1918, and was already produced commercially in the early 1920s in Germany (Heinze and Koschella 2005). A schematic diagram of cellulose carboxymethylation is shown in Figure 1.9. The production of NFC from carboxymethylated cellulose as a new type material was reported by Wågberg *et al.* in 2008. It has been produced using the high-pressure homogenization of carboxymethylated

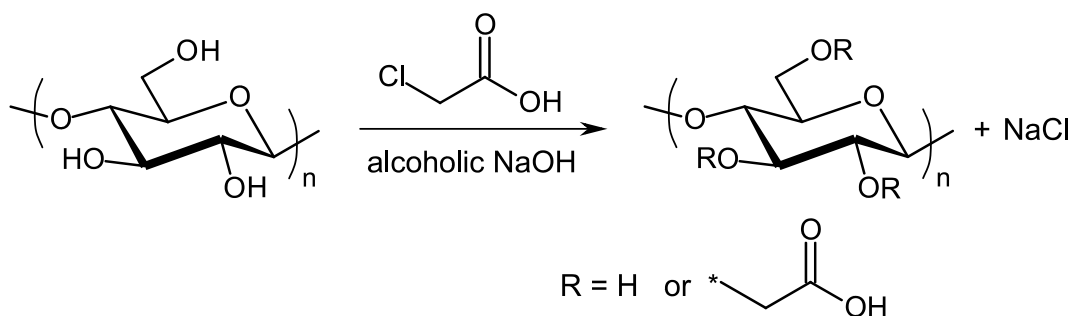


**Figure 1.9** Schematic diagram of cellulose carboxymethylation

cellulose fibers followed by ultrasonication and centrifugation to remove the partially fibrillated fibers. The nanofibrillated cellulose had cylindrical cross section with a diameter of 5–15 nm and a length of up to 1  $\mu\text{m}$ .

**Carboxylation using TEMPO-mediated oxidation.** Since 1993, when Davis and Flitsch reported the use of 2,2,6,6-tetramethylpiperidine-N-oxyl (TEMPO) radical for selective oxidation of the primary hydroxyl groups of monosaccharides, this process has become one of the most studied topics in the field of selective oxidation of cellulose. A novel way of the introduction of carboxylate groups to cellulosic materials through TEMPO-mediated oxidation and further NFC preparation was reported in 2006 by Saito *et al.* In their work never-dried celluloses (bleached sulfite wood pulp, cotton, tunicin, and bacterial cellulose) were disintegrated into individual microfibrils with regular width of 3–5 nm using TEMPO-mediated oxidation and the further homogenization.

The basic principle of such treatment (TEMPO/NaBr/NaClO system) is the oxidation of cellulose fibers by nitrosonium cation, generated *in situ* through the reaction of TEMPO radical with oxidants, such as hypobromide ions, which in turn are generated from bromide salts and sodium hypochlorite (see Figure 1.10). In the procedure reported by Saito *et al.* (2006) TEMPO/NaBr/NaClO system was used at pH 10. Later, the same research group reported (Saito *et al.* 2009) the oxidation of cellulose with TEMPO/NaClO/NaClO<sub>2</sub> system under neutral or weakly acidic conditions was reported (see Figure 1.11).

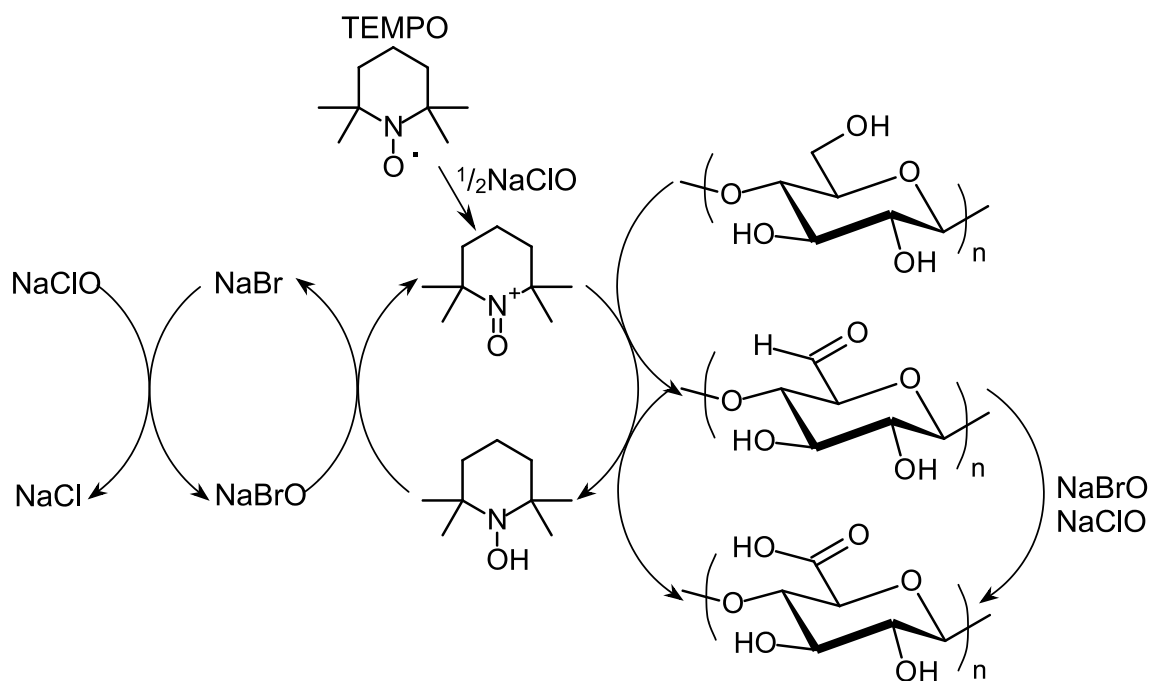


**Figure 1.10** Schematic diagram of the regiospecific oxidation of cellulose primary hydroxyl groups by TEMPO/NaBr/NaClO system in water at basic pH

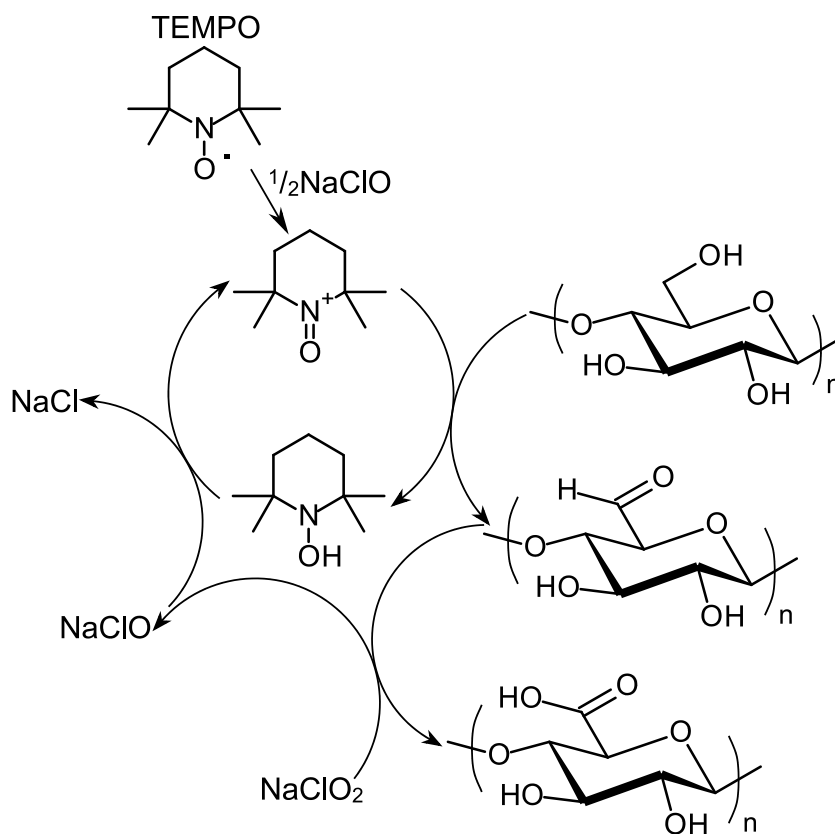


**Figure 1.11** Schematic diagram of the regiospecific oxidation of cellulose primary hydroxyl groups by TEMPO/NaClO/NaClO<sub>2</sub> system in water at neutral or slightly acidic pH

It has been found that the depolymerization of cellulose during TEMPO-mediated oxidation takes place. This phenomenon was attributed to the presence of sodium hypochlorite in the system, which causes 2,3-scissions of glucose units, forming dialdehyde and dicarboxylic groups (de Nooy *et al.* 1994). The key factors controlling the depolymerization of cellulose are the amount of added TEMPO, oxidation time and temperature (Isogai and Kato 1998). It was also reported (Bäckström *et al.* 2012) that through microfibrils surface oxidation the reduction in the network strength is observed due to decrease of the coefficient of friction between the fibers.

**Carboxylation using periodate–chlorite oxidation.** Liimatainen *et al.* (2012) reported a method of regiospecific periodate–chlorite oxidation pretreatment to enhance the further fibrillation of cellulose. In their work this method was demonstrated on hardwood cellulose pulp, which was further converted to NFC through homogenization. The oxidized cellulose with the carboxyl content up till 1.75 mmol/g was reported. It should be noted that using such method, secondary alcohols of cellulose molecule are converted to carboxylates, which leads to breaking of the glucopyranose ring (see Figure 1.12).

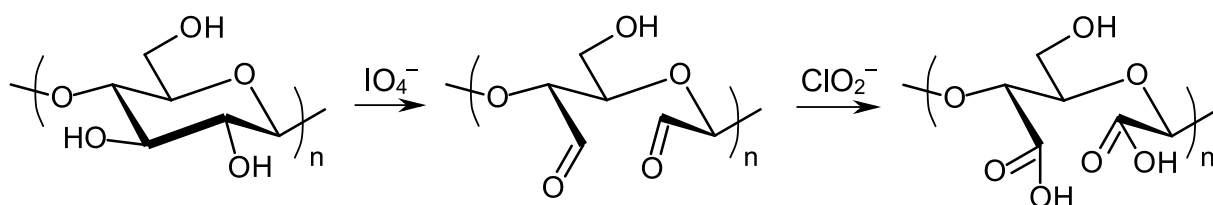


**Figure 1.12** Schematic diagram of the regioselective oxidation of cellulose C2 and C3 hydroxyl groups by periodate and chlorite

**Quaternization.** Ho *et al.* (2011) reported the use of quaternization pretreatment to obtain trimethylammonium-modified cellulose and further homogenization to produce NFC. Oat straw cellulose pulp was quaternized and further disintegrated using microfluidizer. The quaternization facilitates nanofibrils separation due to positive charge on their surfaces.

#### 1.1.3.4 Other production techniques

**Cryocrushing.** Another method for production of NFC was proposed by Dufresne *et al.* (1997) and is called cryocrushing. In this method cellulose is frozen using liquid nitrogen and the ensuing glassy solid is subjected to high shear forces. Under mechanical shear ice crystals exert pressure on the cell walls, causing their breaking and releasing cell wall fragments. This process was proposed (Dufresne *et al.* 1997) for the production of NFC from hydrated and cryocrushed raw sugar beet pulp, which was further passed through Manton-Gaulin homogenizer at 500 bar for 2 h. Cryocrushing is not very popular; however, it is often used by Sain's research group (Bhatnagar and Sain 2005; Wang *et al.* 2007; Janardhnan and Sain 2007; Alemdar and Sain 2008) mostly for fibrillation of agricultural crops.

**Electrospinning.** Recently, the electrospun nanofibers from cellulose and its derivatives have gained an evident interest. In electrospinning a stable jet of solubilized cellulose is ejected from the cone tip. Solvent evaporates as the jet passes through the air, forming an ultrafine filament collected on an electrically grounded target (Lim *et al.* 2010). This method can be used to prepare fibres with the diameter of several tens of nanometers (Doshi and Reneker 1993). Currently, a lot of studies in this field are devoted to investigation of appropriate solvents for cellulose (Park *et al.* 2007; Konwarh *et al.* 2013; Ghorani *et al.* 2013).

#### 1.1.3.5 Properties

The properties of NFC can be distinguished depending on the form in which it is present: as a single nanofibril or fibrous network, in aqueous medium (NFC suspension or hydrogel) or in dry state (film or aerogel).

**Individual nanofibrils.** The dimensions of single cellulose nanofibrils are generally 3–50 nm in diameter and few micrometers in length, as already discussed in Section 1.1.2.2. However, these dimensions are commonly measured in dry state. Thus, the nanofibrils are expected to shrink while drying and have slightly lower dimensions comparing to those observed in wet state.

The elastic modulus of single nanofibrils prepared from tunicate cellulose by TEMPO-oxidation was measured by Iwamoto *et al.* (2009) during three-point bending test using AFM. It was reported to be  $145.2 \pm 31.3$  GPa for the NFC with cross sectional dimensions of  $8 \times 20$  nm and  $150.7 \pm 28.8$  GPa for the same NFC further hydrolyzed by sulfuric acid. Such values are very close to the elastic modulus of 143 GPa reported by Šturcová *et al.* (2005) for tunicate cellulose nanocrystals, measured using Raman spectroscopy.

**Films.** Dry NFC film, also called nanopaper, possesses specific mechanical, optical and barrier properties, which are worth to be emphasized. As shown by Siró and Plackett (2010), elastic modulus of NFC films may approach 20 GPa and their strength can reach 240 MPa. However, in general, values of 10 GPa and 100 MPa are obtained for elastic modulus and tensile strength, respectively, with a strain at break of 5%. NFC films are not redispersible in water which is due to strong hydrogen bonding between nanofibrils. Henriksson and Berglund (2007) reported that the mechanical properties of NFC films were reduced when immersed in water but the major part of the structure was retained.

NFC has a diameter less than one tenth of visible light wavelength. Thus, when the nanofibrils are densely packed it does not induce light scattering (Nogi *et al.* 2009). Consequently, NFC films exhibit high level of transparency. For instance, Fukuzumi *et al.* (2009) reported 78% and 90% of light transmittance for TEMPO-oxidized NFC films from hardwood and softwood, respectively. The lower light transmittance of hardwood NFC was related to the presence of xylan as the main constituent in hemicellulose comparing to softwood samples.

NFC films are known to have high oxygen and water vapor barrier properties. Syverud and Stenius (2009) reported the values of  $17.75 \pm 0.75$  cm<sup>3</sup> m<sup>-2</sup> day<sup>-1</sup> for oxygen transmission rate (OTR) at 23 °C and 0% of relative humidity, which fulfils the requirements for OTR in modified atmosphere packaging. Aulin *et al.* (2012) reported the OTR of 9.2 cm<sup>3</sup> m<sup>-2</sup> d<sup>-1</sup> at 23 °C and 50% of relative humidity. However, this value was increased till 454 cm<sup>3</sup> m<sup>-2</sup> d<sup>-1</sup> at 80% of relative humidity. Aulin *et al.* (2012) also measured water vapor transmission rate (WVTR) of 70.3 g m<sup>-2</sup> d<sup>-1</sup> and >2000 g m<sup>-2</sup> d<sup>-1</sup> at relative humidity of 50% and 80%, respectively.

**Suspensions.** NFC is typically produced in the form of aqueous suspensions, which possess shear-thinning, thixotropic and gel-like behavior. The properties of NFC suspensions are extensively discussed in Chapter 1.

**Hydrogels.** NFC suspensions at low concentrations exhibited high viscosity but still possessed fluidity. They can be converted into stiff “hydrogels” that are freestanding with a water content of 99.9%, having no (or negligible) fluidity (Saito *et al.* 2011; Abe and Yano 2011). Saito *et al.* (2011) prepared such hydrogels by acid treatment of TEMPO-oxidized NFC suspensions at pH of ~2 for 6 h. Abe and Yano (2011) produced NFC hydrogels by soaking of grinded NFC suspension in NaOH for 12 h and further neutralization for 6 h using acid.

**Aerogels.** NFC aerogels are porous sponge-like structures with very low density ( $<0.03 \text{ g cm}^{-3}$ ), high porosity (98%) (Aulin *et al.* 2010) and specific surface area of  $20 \text{ m}^2 \text{ g}^{-1}$  (Aulin *et al.* 2010, Pääkkö *et al.* 2008). Such aerogels are prepared by freeze-drying of NFC aqueous suspensions. When prepared from cellulose derivatives, the surface areas can increase up to  $250 \text{ m}^2 \text{ g}^{-1}$ – $389 \text{ m}^2 \text{ g}^{-1}$  (Pääkkö *et al.* 2008). However, lower porosity (41–82%) and higher density ( $0.15$ – $0.85 \text{ g cm}^{-3}$ ) are obtained. NFC aerogels have a wide variety of applications in selective delivery/separation, tissue-engineering, nanocomposites upon impregnation by polymers, and other medical and pharmaceutical applications (Pääkkö *et al.* 2008).

## 1.2 Experimental

### 1.2.1 Materials

Bleached softwood bisulfite pulp (Quality 2100, Domsjö Fabriker AB, Sweden) was used as a source of cellulose. The alpha-cellulose content of 93 % and the DP of 780 were specified by the supplier. The pulp was stored at the controlled temperature of 23 °C and humidity of 50%. The commercial enzyme solutions: Celluclast 1.5 L (cellulase, a mixture of endoglucanase, exoglucanase and cellobiase (Turon *et al.* 2008) with the major activity of endoglucanase and exoglucanase (Rosgaard *et al.* 2007), with the declared activity of  $700 \text{ EGU g}^{-1}$  (endoglucanase units per gram of solution), and FiberCare R (monocomponent endoglucanase)— $4700 \text{ ECU g}^{-1}$  (endocellulase units per gram of solution) were used for cellulose hydrolysis (both products of Novozymes A/S, Denmark). Since endoglucanase and endocellulase are synonyms, the solutions can be compared in terms of such a specific activity. Sodium acetate trihydrate, acetic acid, TEMPO, sodium bromide, sodium hypochlorite solution (13%) and the other chemicals were of laboratory grade and used without further purification.

### 1.2.2 Production methods

The processing conditions for the production of NFC using enzymatic and TEMPO-mediated oxidation pretreatments are summarized in Table 1.1.

**Table 1.1** Processing parameters for the production of NFC from once-dried bisulfite softwood pulp

Sample name	Processing conditions			
	Refining <sup>a</sup>	Pretreatment <sup>b</sup>	Grinding <sup>c</sup>	Homogenization <sup>d</sup>
enz-C2.1	Yes	Celluclast 1.5 L; 2.1 EGU g <sup>-1</sup>	Yes	No
enz-C10.5	Yes	Celluclast 1.5 L; 10.5 EGU g <sup>-1</sup>	Yes	No
enz-C21.0	Yes	Celluclast 1.5 L; 21.0 EGU g <sup>-1</sup>	Yes	No
enz-F21	Yes	FiberCare R; 21.0 ECU g <sup>-1</sup>	Yes	No
enz-F21-H	Yes	FiberCare R; 21.0 ECU g <sup>-1</sup>	Yes	Yes
enz-F210	Yes	FiberCare R; 210.0 ECU g <sup>-1</sup>	Yes	No
enz-F315	Yes	FiberCare R; 315.0 ECU g <sup>-1</sup>	Yes	No
ox-TEMPO	No	TEMPO/NaBr/NaClO	Yes	No

<sup>a</sup> beating in PFI mill for 40 000 revolutions;

<sup>b</sup> EGU g<sup>-1</sup> stands for endoglucanase units per gram of cellulose; ECU g<sup>-1</sup> stands for endocellulase units per gram of cellulose; TEMPO/NaBr/NaClO — 0.1/1/5 millimol per gram of cellulose, respectively;

<sup>c</sup> disintegration in the grinder (Supermasscolloider MKZA6-2) for 60 passes except for enz-F21-H, where the cellulose suspension of 6 L was passed continuously through the grinder, using recirculation pump, for 1 h;

<sup>d</sup> passing in the homogenizer (Panther NS3006L) for 2 times at the pressure of 1000 and 1500 bar, sequentially.

#### 1.2.2.1 Refining

Cellulose was soaked in water for 4 h and dispersed in a standard disintegrator according to ISO 5263-1:2004 standard. The obtained cellulose suspension was filtered till 10 wt. % on a Büchner funnel using a nylon sieve with the mesh size of 1 µm and beaten in PFI mill according to the procedure described in ISO 5264-2:2011, for a given number of revolutions, typically 40 000.

#### 1.2.2.2 Enzymatic hydrolysis

The enzymatic hydrolysis was performed using cellulase Celluclast 1.5 L and endoglucanase FiberCare R enzyme solutions at different concentrations. The reactions were performed under a mild stirring of 2 wt.% cellulose suspensions at a temperature of 50 °C during 2 h in acetate buffer solution of 50 mM and pH of 5, prepared using sodium acetate trihydrate and acetic acid. The enzymatic activity was stopped by heating the suspension at 80 °C for 15 min. Chloroform at 0.01 wt.% was used as a biocide. The used concentrations of enzyme solutions and the other processing conditions of each experiment are specified in Table 1.1.

### 1.2.2.3 TEMPO-mediated oxidation

TEMPO-mediated oxidation was performed using the non-refined cellulose fibers. The reaction protocol was based on (Saito *et al.* 2007). TEMPO/NaBr/NaClO system was used with 0.1/1/5 millimol of the reactants per gram of cellulose (mmol/g), respectively. TEMPO, ground using a mortar and pestle, and NaBr were mixed with the cellulose suspension before the addition of NaClO water solution with the adjusted pH till 10 using HCl. For the pH adjustments, 3 M HCl and 3 M NaOH were used. The concentration of the obtained cellulose suspension was 1 wt.%. The reaction was carried out at 25 °C at a controlled pH of  $10 \pm 0.1$ . The stable pH during the reaction was acquired by the continuous addition of NaOH. When the pH no longer decreased, indicating that no longer creation of carboxyl groups is occurring any more, the reaction was quenched by lowering the pH till 7. The TEMPO-oxidized cellulose was filtered on a Büchner funnel using a nylon sieve with a mesh size of 1  $\mu\text{m}$  and washed until the filtrate conductivity reached a value below 5  $\mu\text{S cm}^{-1}$ . Chloroform at 0.01 wt.% was used as a biocide.

### 1.2.2.4 Mechanical disintegration

The cellulose suspensions were fibrillated using ultrafine friction grinder Supermasscolloider (model MKZA6-2, disk model MKG-C 80, Masuko Sangyo Co., Ltd., Japan) and for one sample (enz-F21-H) additionally with homogenizer Panther (model NS3006L, GEA Niro Soavi S.p.A., Italy). Supermasscolloider was used at 2500 rpm; 60 passes of cellulose suspension were performed except for enz-F21-H, where the cellulose suspension of 6 L was passed continuously through the grinder, using recirculation pump, for 1 h. 2 passes through homogenizer were carried out at 1000 and 1500 bar, sequentially.

## 1.2.3 Characterization techniques

### 1.2.3.1 MorFi analysis

The size distribution of cellulose fibers and the fines content was determined using MorFi LB-01 fiber analyzer (Techpap, France), hereinafter MorFi analysis. The fiber threshold length and diameter were set in the software to 80  $\mu\text{m}$  and 2  $\mu\text{m}$ , respectively. The fines content was measured as: (i) % in length, indicating the percentage of the fines length *versus* the total length of all the objects, both fibers and fines; (ii) fines/g, representing a number of fines per gram of all the cellulosic elements in the suspension.

### 1.2.3.2 Schopper-Riegler method

The drainability (freeness) of pulp suspension in water was determined in terms of Schopper-Riegler degree (°SR) according to ISO 5267-1:1999.

### 1.2.3.3 Optical microscopy

The optical microscopy images were taken using Carl Zeiss Axio Imager M1m optical microscope in a transmission mode. The cellulose suspensions were diluted to a concentration of 0.2 wt.% and a drop was placed between the glass slide and a coverslip. The images were captured by AxioCam MRc 5 digital camera.

### 1.2.3.4 Atomic force microscopy (AFM)

The AFM was performed in a tapping mode using Dimension Icon Atomic Force Microscope with an OTESPA cantilever. The cellulose samples were diluted to a concentration of  $10^{-3}$  wt.% and a droplet of suspension was placed on a mica disc and dried at room temperature. Nanoscope III software was used for the evaluation of the nanofibrils diameter from the height profiles of AFM height images (see Figure A.1 in Annex A). At least four different areas of the sample were scanned and 200 heights were measured for each sample.

### 1.2.3.5 Field emission gun scanning electron microscopy (FEG-SEM)

The FEG-SEM was performed using a ZEISS Ultra 55 microscope, equipped with In-Lens secondary electron detector. An accelerating voltage of 3 kV was used. The samples were deposited on a double-sided adhesive carbon tape, dried under vacuum and sputtered with Au/Pd layer of 2–3 nm before the analysis.

### 1.2.3.6 Determination of degree of polymerization (DP)

The DP of cellulose was measured using the capillary viscometer method according to ISO 5351:2010 from the intrinsic viscosities ( $\eta_{\text{int}}$ ) of cellulose, dissolved in copper(II) ethylenediamine (CED) solution. The viscometric average degree of polymerization ( $DP_v$ ) was calculated from the intrinsic viscosity using the Mark-Houwink-Sakurada equation:

$$DP_v^{0.905} = 0.75 \eta_{\text{int}}. \quad (1.1)$$

For the preparation of cellulose solution in CED the produced NFC suspensions in water were used directly without drying.

### 1.2.3.7 X-ray diffraction (XRD)

The crystallinity index (CI) of cellulose samples was determined from wide-angle XRD spectra (see Figure A.2 in Annex A). The samples were placed into zero-background Si holder and the measurements were performed using PANalytical X'Pert PRO MPD diffractometer, equipped with an X'celerator detector. The operating conditions were: Copper Ka radiation with a wavelength of 1.5418 Å, double Bragg angle ( $2\theta$ ) of 5–56°, step of 0.067° and the counting time of 360 s. The cellulose CI was determined according to the peak height method (Segal *et al.* 1959):

$$\text{CI (\%)} = (I_{002} - I_{\text{am}})/I_{002} \times 100, \quad (1.2)$$

where:  $I_{002}$  is the diffraction intensity of the main crystalline peak at  $2\theta \sim 22.5^\circ$  and  $I_{\text{am}}$  represents the intensity at the minimum taken at  $2\theta \sim 18^\circ$  both after subtraction of the background signal.

### 1.2.3.8 Carboxyl content determination

The carboxyl content of cellulose was determined using the conductometric titration method according to SCAN-CM 65:02. After the protonization, cellulose suspension was titrated with sodium hydroxide solution using the addition step of 400  $\mu\text{L}$ . The titration curves were then plotted (see Figure A.3 in Annex A) showing three characteristic regions with two intersection points ( $V_1$  and  $V_2$ ) corresponding to the volume (L) of NaOH required to neutralize the strong acidic and carboxylic groups, respectively. Carboxyl content ( $X_{\text{COOH}}$ , mmol/g) was calculated from the following equation:

$$X_{\text{COOH}} = [(V_2 - V_1) c]/w, \quad (1.3)$$

where:  $c$  is the concentration (mmol/L) of the sodium hydroxide solution;  $w$  is the oven-dried weight (g) of cellulose.

### 1.2.3.9 Fourier transform infrared (FTIR) spectroscopy

The FTIR spectroscopy was performed to characterise the chemical modification of the cellulose samples. The cellulose suspensions were oven-dried at 105 °C. 2 mg of dry cellulose was mixed with 200 mg of potassium bromide powder and pressed to prepare pellets with diameter of 13 mm. The absorption spectra were obtained in transmission mode using FTIR spectrometer PerkinElmer Spectrum 65 in the spectral range of 600–4000  $\text{cm}^{-1}$  with the resolution of 4  $\text{cm}^{-1}$  during 8 scans. The baselines were corrected using ParkinElmer Spectrum v.10.02 software for all the recorded spectra.

## 1.3 Results and discussion

### 1.3.1 Influence of mechanical disintegration

The optical microscope image of the raw bisulfite softwood pulp is shown in Figure 1.13, where the kinked fibers, as well as much smaller elements, *i.e.*, fines, are observed. The morphology of this pulp was quantitatively characterized using MorFi analysis, as shown in Table 1.2. The average length of  $969.7 \pm 16.0 \mu\text{m}$  and the average diameter of  $28.0 \pm 0.1 \mu\text{m}$  were detected.

Some preliminary experiments were carried out to determine the sufficient levels of refining (beating) in PFI mill and the final grinding in Supermasscolloider. The refining stage disintegrates the fibers, increases their specific surface area and makes them more accessible for enzymatic activity. Figure 1.14 presents the influence of the refining in PFI mill on the fines content of the beaten raw cellulose pulp. The most significant increase of the fines content

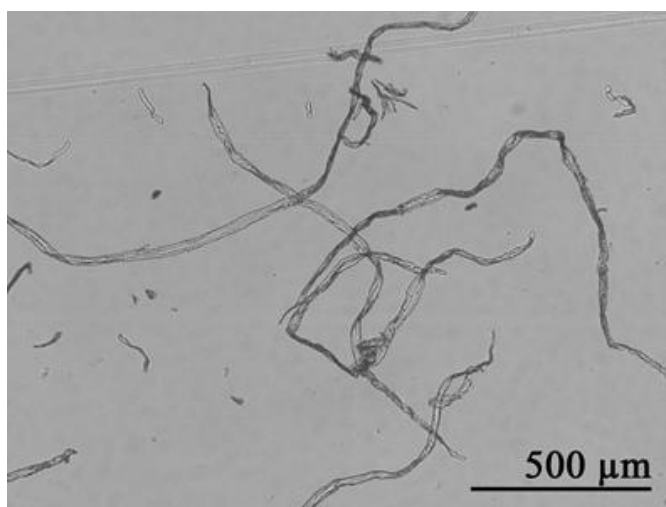
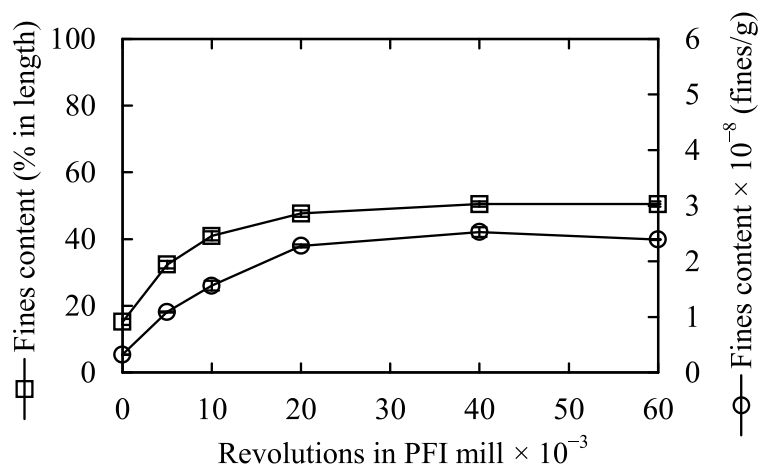


**Figure 1.13** Optical microscope image of the raw bisulfite softwood pulp

**Table 1.2** MorFi analysis of the raw bisulfite softwood pulp

Property	Average value
Length ( $\mu\text{m}$ )	$969.7 \pm 16.0$
Diameter ( $\mu\text{m}$ )	$28.0 \pm 0.1$
Kinks angle ( $^\circ$ )	$124 \pm 1$
Curvature (%)	$18.1 \pm 0.1$
Fines content <sup>1</sup> (%)	$7.38 \pm 0.09$

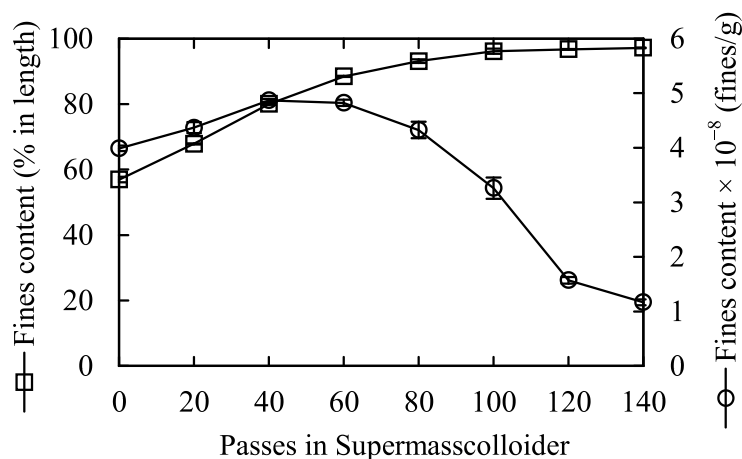
<sup>1</sup> the percentage of fines length *versus* the length of both fibres and fines



**Figure 1.14** Dependence of the fines content on the number of revolutions in PFI mill for the raw pulp

occurs for the first 20 000 revolutions, reaching a plateau at 40 000. The further fibrillation did not influence much the measured parameters. Thereby, refining for 40 000 revolutions in PFI mill was performed for all the rest of the samples. However, in terms of efficient energy consumption, 20 000 revolutions can be more favorable.

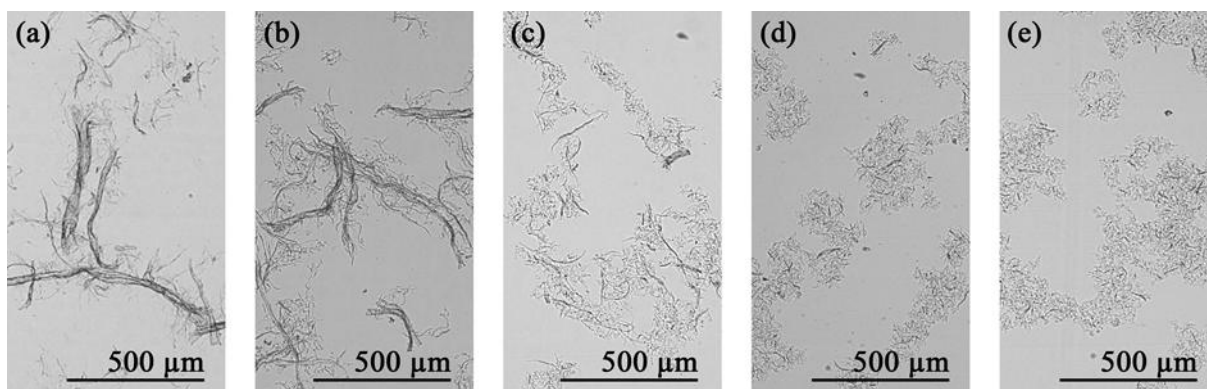
The raw cellulose pulp was beaten using PFI mill for 40 000 revolutions and enzymatically-treated with endoglucanase solution FiberCare R at 210.0 ECU g<sup>-1</sup>. It was further used to study the influence of the grinding operation. Figure 1.15 shows the dependence of the fines content on the number of passes through Supermasscolloider for this sample. The curves show that during all the grinding process the cellulose fibrillation occurs. The percentage of the fines increases progressively reaching a plateau at ~ 97 %. The growth of the fines content indicates the conversion of the fibers to fines and nanofibrils. The number of the fines per gram of cellulose reaches a peak at 40–60 passes and declines with the further



**Figure 1.15** Dependence of the fines content on the number of passes through the grinder for the pulp, previously beaten in PFI mill for 40,000 revolutions and enzymatically treated with endoglucanase solution FiberCare R, 210.0 ECU g<sup>-1</sup>

grinding. The decline occurs since the nanofibrils production dominates the conversion of the fibers into fines. Since the nanofibrils are not detected by MorFi analyzer due to their small dimensions, the decrease of the fines content is observed. The fiber dimensions reduce progressively within the multiple processing conditions applied, such as beating in PFI-mill, enzymatic hydrolysis and grinding, as seen from the optical microscopy images in Figure 1.16. However, some non-fibrillated flocculated structures remained even with increasing the number of passes through the grinder. Therefore, the grinding operation for 60 passes was chosen for all the next samples in order to study the effect of the enzymatic treatment.

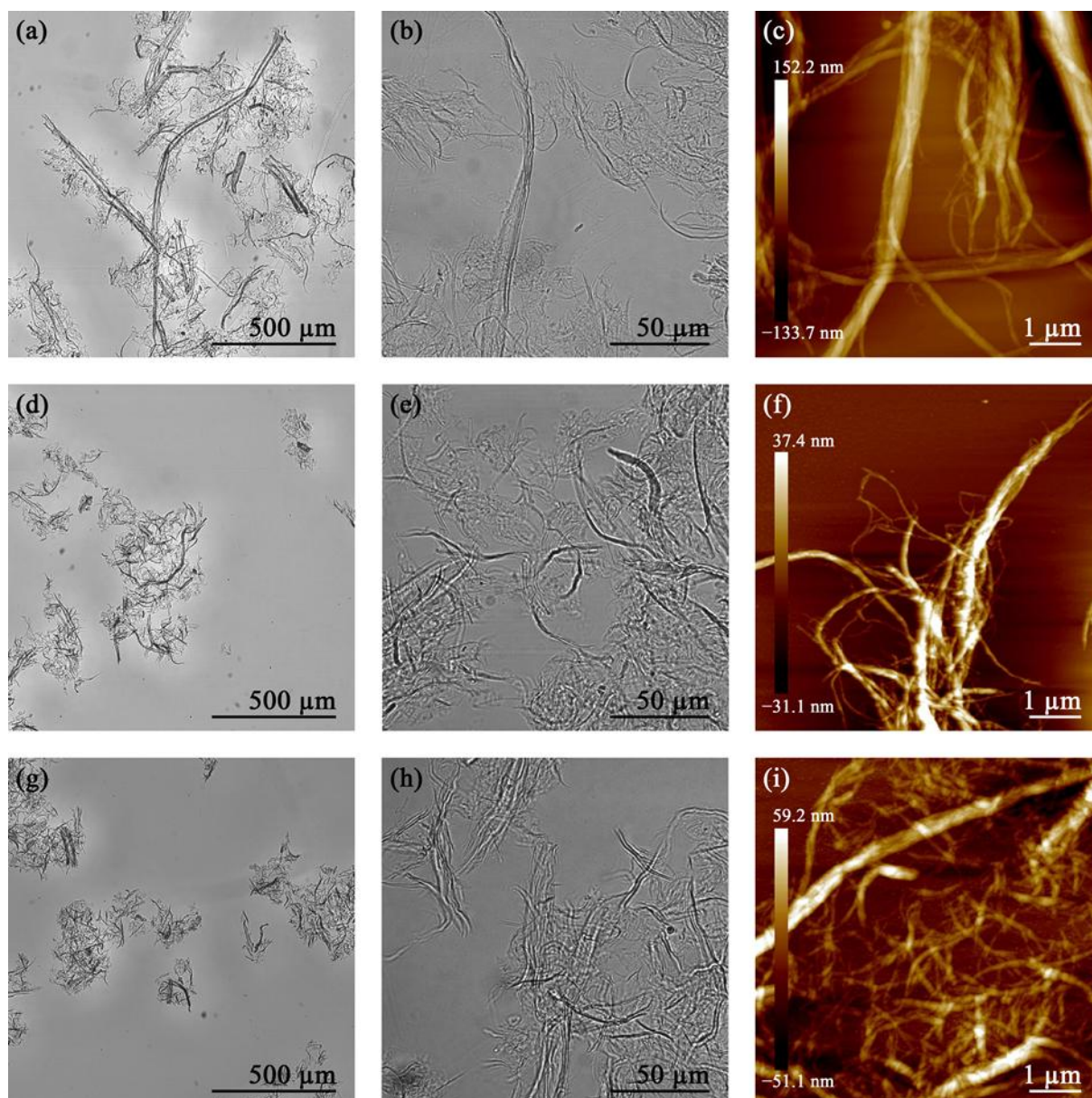
The enzymatic hydrolysis, performed to facilitate the NFC isolation, using two enzyme solutions, namely Celluclast 1.5 L and FiberCare R, was compared. The difference between the enzyme solutions resides in their composition: Celluclast 1.5 L is a cellulase mixture with the major activity of endoglucanase and exoglucanase, whereas FiberCare R contains a monocomponent endoglucanase.



**Figure 1.16** Optical microscopy images of bisulfite wood pulp: (a) beaten in PFI-mill for 40,000 revolutions; (b) refined and enzymatically-treated with endoglucanase solution FiberCare R at  $210.0 \text{ ECU g}^{-1}$ ; refined, enzymatically-treated and grinded using Supermasscolloider for: (c) 40 passes; (d) 80 passes; and (e) 120 passes

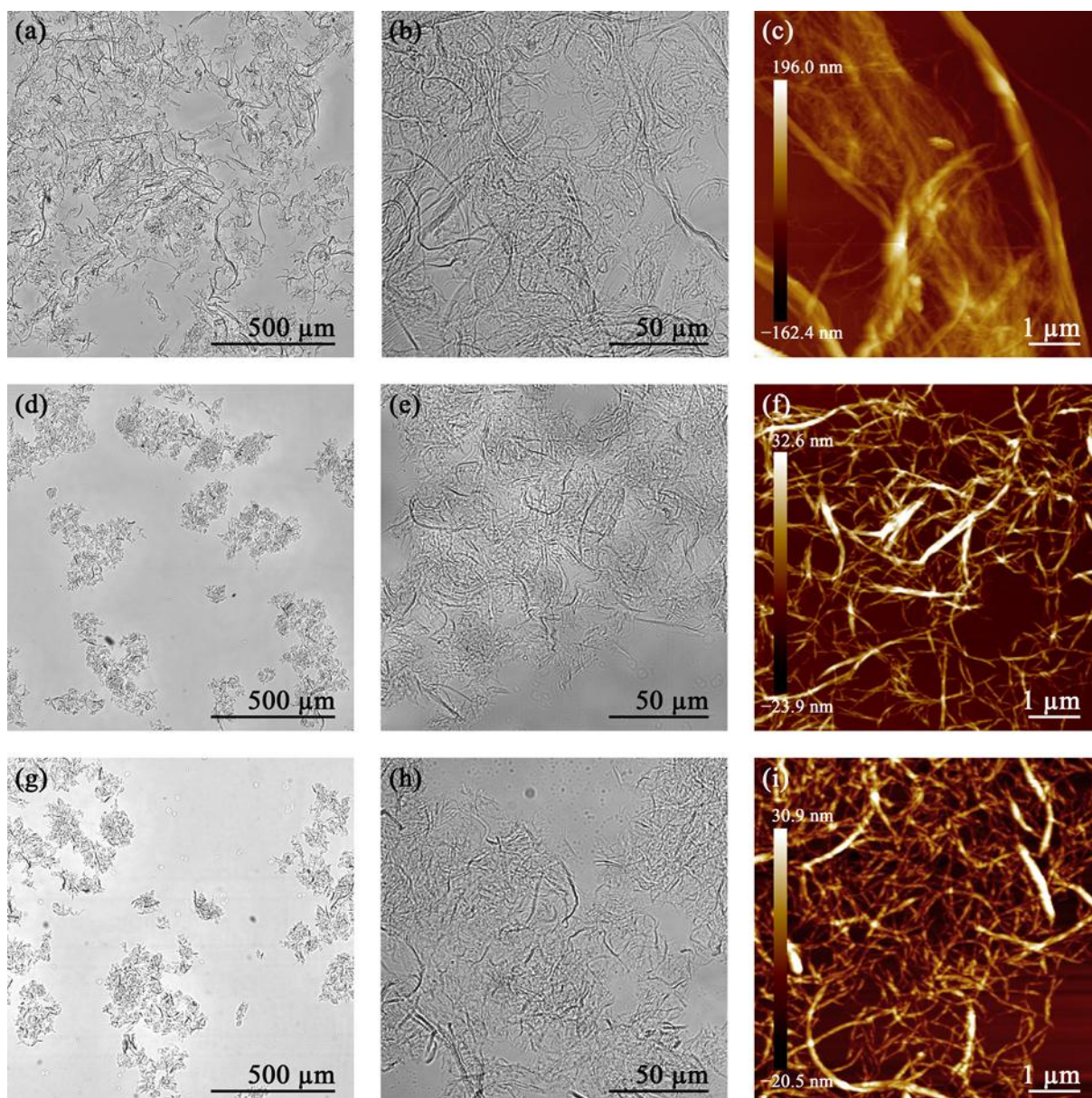
### 1.3.2 Enzymatic pretreatment

Figure 1.17 shows the optical microscopy and atomic force microscopy images of the produced NFC suspensions, treated with different concentrations of cellulase solution Celluclast 1.5 L. Obviously, the increase of the enzymatic concentration results in the stronger cellulose fibrillation in the grinder. The minimal concentration of the applied enzyme produced fibers, which are partly disintegrated in nanofibrils. The enz-C21.0 sample, despite some non-fibrillated flocculated residuals, comprises nanofibrils with lateral dimensions of  $29 \pm 25 \text{ nm}$ , measured from the height profile of AFM height sensor images as shown in Figure A.1 (see Annex A).



**Figure 1.17** Optical microscopy (*left and middle*) and AFM height sensor (*right*) images of: (a–c) enz-C2.1; (d–f) enz-C10.5 and (g–i) enz-C21.0 samples at different magnifications

The optical microscopy and AFM height sensor images of NFC samples, produced when applying endoglucanase solution FiberCare R, are shown in Figure 1.18. The better dissociation of cellulose in enz-F21 (Figure 1.18a), comparing to enz-C21.0 (Figure 1.17g), is observed from the optical microscopy images, despite the equivalent concentrations of endoglucanase (endocellulase) applied. The further increase of FiberCare R concentration enhances the hydrolysis, which is revealed by the presence of smaller cellulose objects, detected in the microscopy images. The enz-F210 and enz-F315 samples possess lateral dimensions of  $18 \pm 10$  nm and  $18 \pm 13$  nm, respectively, as deduced from the AFM height sensor images. However, some residuals still remain, as detected using optical microscopy.



**Figure 1.18** Optical microscopy (*left and middle*) and AFM height sensor (*right*) images of: (a–c) enz-F21; (d–f) enz-F210 and (g–i) enz-F315 samples at different magnifications

The DP and CI of enzymatically hydrolyzed and TEMPO-oxidized NFC before the grinding operation, as well as of the raw cellulose pulp, are compared in Figure 1.19a and b. The XRD patterns, measured to determine the CI, are shown in Figure A.2 (see Annex A). The DP decreases drastically as the enzymatic concentration increases, which is in agreement with other studies (Siqueira *et al.* 2010; Qing *et al.* 2013, Zhu *et al.* 2011). As seen from Figure 1.19a, enz-C21.0 has lower DP comparing to enz-F21 ( $290 \pm 1$  vs.  $361 \pm 5$ ) when applying the equivalent endoglucanase activity. Apparently, the stronger depolymerization of enz-C21.0 occurs due to the presence of the other active enzymes, *e.g.*, exoglucanase.

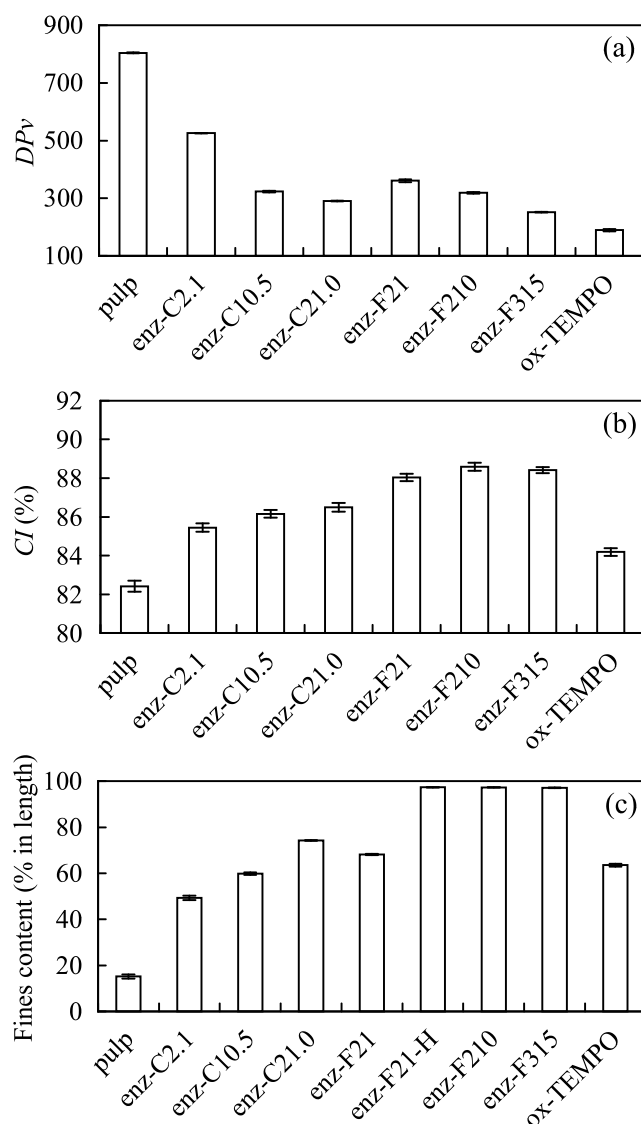


**Figure 1.19** Comparison of the raw cellulose pulp and the NFC suspensions: (a) degrees of polymerization and (b) crystallinity indexes before grinding and (c) fines content of the final NFC suspensions

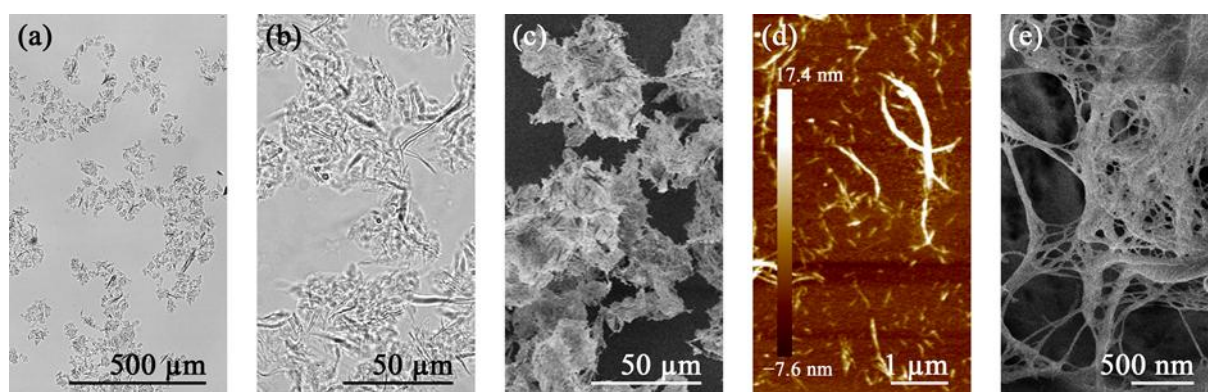
The cellulose CI was reported to vary significantly depending on the measurement method (Park *et al.* 2010). The peak height method based on XRD spectra, used in this work, is known to produce higher values of crystallinity comparing to the other methods. However, it is used here basically to analyze the crystallinity variation, rather than to determine the absolute CI values of cellulose samples.

Figure 1.19b shows that the cellulose CI raises with the increase of enzymatic charge, as previously reported (Qing *et al.* 2013). The raw cellulose pulp has a CI of 82.4% and this value increases till 86.5% for the highest concentration of Celluclast 1.5 L applied (enz-C21.0 sample). It is likely to occur due to the hydrolysis of cellulose amorphous regions by endoglucanase. Moreover, the enzymatic hydrolysis rate of amorphous cellulose is around 30 times higher than that of crystalline ones (Zhu *et al.* 2011). The CI of enz-F21 was found to be slightly higher comparing to that of enz-C21.0 (88.0 vs. 86.5), which means that

FiberCare R attacks the amorphous domains of cellulose more strongly comparing to Celluclast 1.5 L. The crystallinity indexes of enz-F210 and enz-F315 are almost at the same level. Thus, the saturation of the enzyme may occur, as reported elsewhere (Gama and Mota 1997). It can be illustrated as well from the similar microscopy images for these samples. However, the decrease of DP for enz-F315, comparing to enz-F210, is still observed. The fines content of the produced NFC suspensions is presented in Figure 1.19c. The increase of the enzymatic load enhances the fines content. For enz-F210 and enz-F315 samples the fines content reaches the value of  $\sim 97\%$  indicating the strong fibrillation level of cellulose.

Comparing to enz-C21.0, the enz-F210 was treated with the higher concentration of endoglucanase, and lower depolymerization of this sample is observed ( $290 \pm 1$  vs.  $319 \pm 3$ , respectively, see Figure 1.19a). At the same time, much higher fines content for enz-F210 was observed (Figure 1.19c), as well as smaller residual aggregates (as seen from Figure 1.18). We have also reported (see Section 2.3.1) much stronger viscoelastic properties of the NFC samples, hydrolyzed using FiberCare R, comparing to that treated with Celluclast 1.5 L, while performing the rheological measurements. This indicates stronger networks of nanofibrils produced when using FiberCare R enzyme. The foregoing suggests that the use of endoglucanase solution FiberCare R allows increasing the enzymatic load, comparing to cellulase solution Celluclast 1.5 L, preserving cellulose from the depolymerization and producing better fibrillated cellulose suspensions.

One sample (enz-F21-H) was mildly hydrolyzed by FiberCare R applying  $21 \text{ ECU g}^{-1}$ , grinded in Supermasscolloider equipped with a recirculation pump for 1 h (by processing the suspension of 6 L) and finally passed through Panther homogenizer for two times (at 1000 and 1500 bar, respectively). The homogenizer was applied to examine whether it would be effective to disintegrate the residual fibers in the NFC suspension. Figure 1.20 shows that in



**Figure 1.20** Optical microscopy (a, b), FEG-SEM (c, e) and AFM height sensor (d) images of enz-F21-H sample at different magnifications

the enz-F21-H sample much lower amount of the residual aggregates is present, comparing to all the other enzymatically treated samples. However, the optical microscopy (Figure 1.20b) and FEG-SEM (Figure 1.20c) both demonstrate the presence of flocks of  $\sim 50 \mu\text{m}$  in diameter. These flocks consist of highly entangled NFC. The individual nanofibrils with diameter of  $12 \pm 7 \text{ nm}$  are present, as deduced from AFM height sensor images.

### 1.3.3 Oxidation pretreatment

As a result of TEMPO-mediated oxidation, the NFC (ox-TEMPO sample) with carboxyl content of  $1.75 \pm 0.05 \text{ mmol g}^{-1}$  was produced, as determined from conductometric titration curves (see Figure A.3 in Annex A). Few passes of the suspension in the grinder were sufficient to obtain a translucent gel; however, with the increase of the passes number till 60 the gel became more viscous.

A strong decrease of the DP was observed after TEMPO-oxidation (see Figure 1.19), which is in agreement with the previous studies (Saito *et al.* 2009, Shinoda *et al.* 2012). This occurs due to the presence of sodium hypochlorite in the system, which causes 2,3-scissions of glucose units, forming dialdehyde and dicarboxyl groups (Puangsin *et al.* 2013), which leads to the further cellulose chain depolymerization. The CI of ox-TEMPO was not much influenced, which is also in agreement with the previous works (Saito *et al.* 2007, Shinoda *et al.* 2012).

The microscopy observations of ox-TEMPO (see Figure 1.21) show the produced nanofibrils at different magnifications. The lateral dimensions of  $4 \pm 2 \text{ nm}$  were determined from the AFM height sensor images (see Figure 1.21d). The FEG-SEM image (see Figure 1.21e) shows some nanofibrils with a similar width and some larger elements, which may be agglomerations formed while drying. Some residual non-fibrillated fibers were detected by

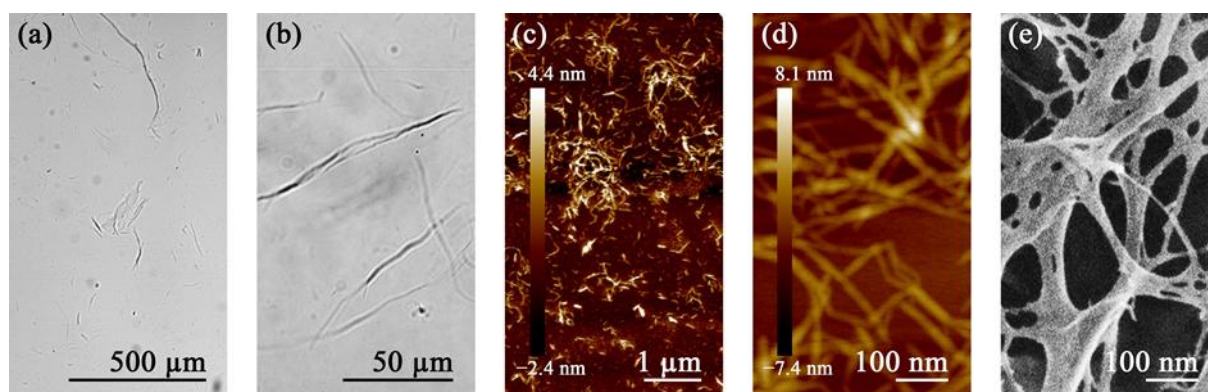


**Figure 1.21** Optical microscopy (a, b), AFM height sensor (c, e) and FEG-SEM (d) images of ox-TEMPO sample at different magnifications

optical microscopy (see Figure 1.21a and b), which justify the relatively low amount of fines content for this sample (63.5 %, as seen from Figure 1.19c).

The oxidation of cellulose pulp using oxygen in the presence of NHPI was performed (see Annex B) as an alternative to TEMPO-mediated oxidation in order to facilitate the nanofibrils separation. The reaction was not useful to provide similar or higher levels of oxidation. Consequently, this method of cellulose oxidation in aqueous medium without using toxic chemicals should be revised to improve its efficiency.

## Conclusions

The NFC suspensions were successfully produced from dry bleached bisulfite softwood pulp using enzymatic and TEMPO-oxidation pretreatments followed by wet grinding. The increase of the enzymatic concentration resulted in a stronger hydrolysis and hence efficient fibrillation, which was accompanied by the decrease of the DP and the increase of the CI.

The enzymatic hydrolysis using endoglucanase solution FiberCare R was found to be more favourable for the NFC production since it led to lower depolymerization with better dissociation of the nanofibrils comparing to cellulase solution Celluclast 1.5 L, which has the major activity of endoglucanase and exoglucanase. Grinding of TEMPO-oxidized suspensions produced nanofibrils with lower lateral dimensions, as well as reduced length, comparing to that associated with enzymatically prehydrolyzed pulp. All the enzymatically treated NFC samples possessed highly entangled flocculated structures.

It was also shown that the morphology of the produced NFC suspensions depends on the applied processing conditions, which influence the material properties. More intensive fibrillation results in smaller nanofibrils. Consequently, different NFC grades can be produced. The exact processing conditions should be adapted according to the requirements for the specific application. Efficient energy consumption during the NFC production is still an important issue.

## References

- Abe K, Yano H (2011) Formation of hydrogels from cellulose nanofibers. *Carbohydrate Polymers* 85:733–737. doi: 10.1016/j.carbpol.2011.03.028
- Alemdar A, Sain M (2008) Isolation and characterization of nanofibers from agricultural residues – Wheat straw and soy hulls. *Bioresource Technology* 99:1664–1671. doi: 10.1016/j.biortech.2007.04.029.
- Andersen N (2007). *Enzymatic Hydrolysis of Cellulose: Experimental and Modeling Studies*. Doctoral dissertation. Technical University of Denmark.
- Aulin C, Netrval J, Wågberg L, Lindström T (2010) Aerogels from nanofibrillated cellulose with tunable oleophobicity. *Soft Matter* 6:3298–3305. doi: 10.1039/C001939A.
- Aulin C, Salazar-Alvarez G, Lindström T (2012) High strength, flexible and transparent nanofibrillated cellulose–nanoclay biohybrid films with tunable oxygen and water vapor permeability. *Nanoscale* 4:6622. doi: 10.1039/c2nr31726e.
- Bäckström M, Bolivar S, Paltakari J (2012) Effect of ionic form on fibrillation and the development of the fibre network strength during the refining of the kraft pulps. *O PAPEL* 73:57–65.
- Bhatnagar A, Sain M (2005) Processing of Cellulose Nanofiber-reinforced Composites. *Journal of Reinforced Plastics and Composites* 24:1259–1268. doi: 10.1177/0731684405049864.
- Bolaski W, Gallatin A, Gallatin JC (1962) Enzymatic conversion of cellulosic fibers. Patent U.S. 3041246.
- Bulota M, Kreitsmann K, Hughes M, Paltakari J (2012) Acetylated microfibrillated cellulose as a toughening agent in poly(lactic acid). *J Appl Polym Sci* 126:E449–E458. doi: 10.1002/app.36787.
- Carrasco F, Mutjé P, Pèlach MA (1996) Refining of bleached cellulosic pulps: characterization by application of the colloidal titration technique. *Wood SciTechnol* 30:227–236. doi: 10.1007/BF00229345.

- Chinga-Carrasco G (2011) Cellulose fibres, nanofibrils and microfibrils: The morphological sequence of MFC components from a plant physiology and fibre technology point of view. *Nanoscale Res Lett* 6:1–7. doi: 10.1186/1556-276X-6-417.
- Davis NJ, Flitsch SL (1993) Selective oxidation of monosaccharide derivatives to uronic acids. *Tetrahedron Lett* 34:1181–1184. doi:10.1016/S0040-4039(00)77522-8.
- de Nooy AEJ, Besemer AC, van Bekkum H (1994) Highly selective TEMPO mediated oxidation of primary alcohol groups in polysaccharides. *Recl Trav Chim Pays-Bas* 113:165–166. doi: 10.1002/recl.19941130307.
- Doshi J, Reneker DH (1993) Electrospinning process and applications of electrospun fibers. Conference Record of the 1993 IEEE Industry Applications Society Annual Meeting. pp 1698–1703 vol.3.
- Dufresne A, Cavallé J-Y, Vignon MR (1997) Mechanical behavior of sheets prepared from sugar beet cellulose microfibrils. *J Appl Polym Sci* 64: 1185–1194. doi: 10.1002/(SICI)1097-4628(19970509)64:6<1185::AID-APP19>3.0.CO;2-V.
- Eriksen Ø, Syverud K, Gregersen Ø (2008) The use of microfibrillated cellulose produced from kraft pulp as strength enhancer in TMP paper. *Nordic Pulp and Paper Research Journal* 23:299–304. doi: 10.3183/NPPRJ-2008-23-03-p299-304.
- Fengel D, Wegener G (1983) *Wood: chemistry, ultrastructure, reactions*. Walter de Gruyter.
- Fernandes AN, Thomas LH, Altaner CM, *et al.* (2011) Nanostructure of cellulose microfibrils in spruce wood. *Proc Natl Acad Sci USA* 108:E1195–E1203. doi: 10.1073/pnas.1108942108.
- Frey-Wyssling VA, Mühlethaler K (1963) Die elementarfibrillen der cellulose. *Makromol Chem* 62:25–30. doi: 10.1002/macp.1963.020620103.
- Fukuzumi H, Saito T, Iwata T, *et al* (2009) Transparent and High Gas Barrier Films of Cellulose Nanofibers Prepared by TEMPO-Mediated Oxidation. *Biomacromolecules* 10:162–165. doi: 10.1021/bm801065u.
- Gama FM, Mota M (1997) Enzymatic hydrolysis of cellulose (I): relationship between kinetics and physico-chemical parameters. *Biocatal Biotransform* 15:221–236. doi:10.3109/10242429709103511

- Gatenholm P, Klemm D (2010) Bacterial Nanocellulose as a Renewable Material for Biomedical Applications. *MRS Bulletin* 35:208–213. doi: 10.1557/mrs2010.653.
- Ghorani B, Russell SJ, Goswami P (2013) Controlled Morphology and Mechanical Characterisation of Electrospun Cellulose Acetate Fibre Webs. *International Journal of Polymer Science* 2013:e256161. doi: 10.1155/2013/256161.
- Hamada H, Tahara K, Uchida A (2012) The effects of nano-fibrillated cellulose as a coating agent for screen printing. 12th TAPPI Advanced Coating Fundamentals Symposium.
- Hassan ML, Hassan EA, Oksman KN (2011) Effect of pretreatment of bagasse fibers on the properties of chitosan/microfibrillated cellulose nanocomposites. *J Mater Sci* 46:1732–1740. doi: 10.1007/s10853-010-4992-4.
- Heinze T, Koschella A (2005) Carboxymethyl Ethers of Cellulose and Starch—A Review. *Macromolecular Symposia* 223:13–40.
- Henriksson M, Berglund LA (2007) Structure and properties of cellulose nanocomposite films containing melamine formaldehyde. *J Appl Polym Sci* 106:2817–2824. doi: 10.1002/app.26946.
- Henriksson M, Henriksson G, Berglund LA, Lindström T (2007) An environmentally friendly method for enzyme-assisted preparation of microfibrillated cellulose (MFC) nanofibers. *European Polymer Journal* 43:3434–3441. doi: 10.1016/j.eurpolymj.2007.05.038.
- Herrick FW, Casebier RL, Hamilton JK, Sandberg KR (1983) Microfibrillated Cellulose: Morphology, and Accessibility. In Sarko A (ed.) *Proceedings of the Ninth Cellulose Conference*. Applied Polymer Symposia 37. N.Y.: Wiley. pp. 797–813.
- Ho TTT, Abe K, Zimmermann T, Yano H (2015) Nanofibrillation of pulp fibers by twin-screw extrusion. *Cellulose* 22:421–433. doi: 10.1007/s10570-014-0518-6.
- Ho TTT, Zimmermann T, Hauert R, Caseri W (2011) Preparation and characterization of cationic nanofibrillated cellulose from etherification and high-shear disintegration processes. *Cellulose* 18:1391–1406. doi: 10.1007/s10570-011-9591-2.
- Isogai A, Kato Y (1998) Preparation of Polyuronic Acid from Cellulose by TEMPO-mediated Oxidation. *Cellulose* 5:153–164. doi: 10.1023/A:1009208603673.
- Isogai A (2013) Wood nanocelluloses: fundamentals and applications as new bio-based nanomaterials. *J Wood Sci* 59:449–459. doi: 10.1007/s10086-013-1365-z.

- Iwamoto S, Kai W, Isogai A, Iwata T (2009) Elastic Modulus of Single Cellulose Microfibrils from Tunicate Measured by Atomic Force Microscopy. *Biomacromolecules* 10:2571–2576. doi: 10.1021/bm900520n.
- Iwamoto S, Nakagaito AN, Yano H (2007) Nano-fibrillation of pulp fibers for the processing of transparent nanocomposites. *Appl Phys A* 89:461–466. doi: 10.1007/s00339-007-4175-6.
- Janardhnan S, Sain MM (2007) Isolation of cellulose microfibrils—An enzymatic approach. *BioResources* 1:176–188.
- Jayant M, Rashmi J, Shailendra M, Deepesh Y (2011) Production of cellulase by different co-culture of *Aspergillus niger* and *Penicillium chrysogenum* from waste paper, cotton waste and baggase. *Journal of Yeast and Fungal Research* 2(2):24–27.
- Joseleau J-P, Chevalier-Billosta V, Ruel K (2012) Interaction between microfibrillar cellulose fines and fibers: influence on pulp qualities and paper sheet properties. *Cellulose* 19:769–777. doi: 10.1007/s10570-012-9693-5.
- Jonoobi M, Mathew AP, Oksman K (2012) Producing low-cost cellulose nanofiber from sludge as new source of raw materials. *Industrial Crops and Products* 40:232–238. doi: 10.1016/j.indcrop.2012.03.018.
- Klemm D, Heublein B, Fink H-P, Bohn A (2005) Cellulose: Fascinating Biopolymer and Sustainable Raw Material. *Angewandte Chemie International Edition* 44:3358–3393. doi: 10.1002/anie.200460587.
- Klemm D, Kramer F, Moritz S, *et al.* (2011) Nanocelluloses: A New Family of Nature-Based Materials. *Angew Chem Int Ed* 50:5438–5466. doi: 10.1002/anie.201001273.
- Klemm D, Philipp B, Heinze T, *et al.* (1998) Fundamentals and Analytical Methods, *Comprehensive Cellulose Chemistry*, vol 1. Wiley-VCH, Weinheim ; New York, pp 9–21.
- Klemm D, Schmauder H-P, Heinze T (2004) Cellulose. In: de Baets S, Vandamme E, Steinbüchel A (eds) *Biopolymers*, vol 6. Polysaccharides II: polysaccharides from eukaryotes. Wiley-VCH, Weinheim, pp 275–319.
- Konwarh R, Karak N, Misra M (2013) Electrospun cellulose acetate nanofibers: The present status and gamut of biotechnological applications. *Biotechnology Advances* 31:421–437. doi: 10.1016/j.biotechadv.2013.01.002.

- Lavoine N, Desloges I, Dufresne A, Bras J (2012) Microfibrillated cellulose—Its barrier properties and applications in cellulosic materials: A review. *Carbohydrate Polymers* 90:735–764. doi: 10.1016/j.carbpol.2012.05.026.
- Liimatainen H, Visanko M, Sirviö JA, Hormi OEO, Niinimäki J (2012) Enhancement of the Nanofibrillation of Wood Cellulose through Sequential Periodate–Chlorite Oxidation. *Biomacromol* 13:1592–1597. doi: 10.1021/bm300319m.
- Lim Y-M, Gwon H-J, Pyo J, Nho Y-C (2010) Preparation of Cellulose-based Nanofibers Using Electrospinning. In: Kumar A (ed) *Nanofibers*. InTech.
- Lindström T. (2011) NanoCellulose Research and Developments at Innventia. TAPPI International Conference on Nanotechnology for Renewable Materials. Washington D.C., USA.
- Lynd LR, Weimer PJ, Zyl WH van, Pretorius IS (2002) Microbial Cellulose Utilization: Fundamentals and Biotechnology. *Microbiol Mol Biol Rev* 66:506–577. doi: 10.1128/MMBR.66.3.506-577.2002.
- Moon RJ, Martini A, Nairn J, et al (2011) Cellulose nanomaterials review: structure, properties and nanocomposites. *Chem Soc Rev* 40:3941–3994. doi: 10.1039/C0CS00108B
- Nakagaito AN, Yano H (2004) The effect of morphological changes from pulp fiber towards nano-scale fibrillated cellulose on the mechanical properties of high-strength plant fiber based composites. *Appl Phys A* 78:547–552. doi: 10.1007/s00339-003-2453-5.
- Nogi M, Iwamoto S, Nakagaito AN, Yano H (2009) Optically Transparent Nanofiber Paper. *Adv Mater* 21:1595–1598. doi: 10.1002/adma.200803174.
- Qing Y, Sabo R, Zhu JY, *et al.* (2013) A comparative study of cellulose nanofibrils disintegrated via multiple processing approaches. *Carbohydr Polym* 97:226–234. doi: 10.1016/j.carbpol.2013.04.086.
- Pääkkö M, Ankerfors M, Kosonen H, Nykänen A, Ahola S, Österberg M, Ruokolainen J, Laine J, Larsson PT, Ikkala O, Lindström T (2007) Enzymatic Hydrolysis Combined with Mechanical Shearing and High-Pressure Homogenization for Nanoscale Cellulose Fibrils and Strong Gels. *Biomacromolecules* 8:1934–1941. doi: 10.1021/bm061215p.
- Pääkkö M, Vapaavuori J, Silvennoinen R, Kosonen H, Ankerfors M, Lindström T, Berglund L, Ikkala O (2008) Long and entangled native cellulose I nanofibers allow flexible

aerogels and hierarchically porous templates for functionalities. *Soft Matter* 4:2492. doi: 10.1039/b810371b.

Park JY, Han BW, Lee IH (2007) Preparation of electrospun porous ethyl cellulose fiber by THF/DMAc binary solvent system. *J Ind Eng Chem* 13:1002–1008.

Park S, Baker JO, Himmel ME et al (2010) Cellulose crystallinity index: measurement techniques and their impact on interpreting cellulase performance. *Biotechnol Biofuels* 3:10. doi:10.1186/1754-6834-3-10

Puangsin B, Fujisawa S, Kuramae R, Saito T, Isogai A (2013) TEMPO-Mediated Oxidation of Hemp Bast Holocellulose to Prepare Cellulose Nanofibrils Dispersed in Water. *J Polym Environ* 21:555–563. doi: 10.1007/s10924-012-0548-9.

Rånby BG (1949) Aqueous Colloidal Solutions of Cellulose Micelles. *Acta Chem Scand* 3: 649-650. doi: 10.3891/acta.chem.scand.03-0649.

Ritter SK (2008) Sustainability. *Chemical & Engineering News* 86:59-68.

Rosgaard L, Pedersen S, Langston J, Akerhielm D, Cherry JR, Meyer AS (2007) Evaluation of Minimal *Trichoderma reesei* Cellulase Mixtures on Differently Pretreated Barley Straw Substrates. *Biotechnol Progress* 23:1270–1276. doi: 10.1021/bp070329p.

Saito T, Hirota M, Tamura N, Kimura S, Fukuzumi H, Heux L, Isogai A (2009) Individualization of Nano-Sized Plant Cellulose Fibrils by Direct Surface Carboxylation Using TEMPO Catalyst under Neutral Conditions. *Biomacromolecules* 10:1992–1996. doi: 10.1021/bm900414t.

Saito T, Nishiyama Y, Putaux J-L, Vignon M, Isogai A (2006) Homogeneous Suspensions of Individualized Microfibrils from TEMPO-Catalyzed Oxidation of Native Cellulose. *Biomacromolecules* 7:1687–1691. doi: 10.1021/bm060154s.

Saito T, Kimura S, Nishiyama Y, Isogai A (2007) Cellulose nanofibers prepared by TEMPO-mediated oxidation of native cellulose. *Biomacromol* 8:2485–2491. doi:10.1021/bm0703970.

Saito T, Uematsu T, Kimura S, Enomae T, Isogai A (2011) Self-aligned integration of native cellulose nanofibrils towards producing diverse bulk materials. *Soft Matter* 7:8804. doi: 10.1039/c1sm06050c.

- Segal L, Creely JJ, Martin AE, Conrad CM (1959) An empirical method for estimating the degree of crystallinity of native cellulose using the X-Ray diffractometer. *Text Res J* 29:786–794. doi: 10.1177/004051755902901003.
- Shackford LD (2003) A Comparison of Pulping and Bleaching of Kraft Softwood and Eucalyptus Pulps. 36th International pulp and paper congress and exhibition. São Paulo, Brazil.
- Shinoda R, Saito T, Okita Y, Isogai A (2012) Relationship between Length and Degree of Polymerization of TEMPO-Oxidized Cellulose Nanofibrils. *Biomacromol* 13:842–849. doi: 10.1021/bm2017542.
- Shmulsky R, Jones PD (2011) *Forest Products and Wood Science*. John Wiley & Sons.
- Siqueira G, Tapin-Lingua S, Bras J, da Silva Perez D, Dufresne A (2010) Morphological investigation of nanoparticles obtained from combined mechanical shearing, and enzymatic and acid hydrolysis of sisal fibers. *Cellul* 17:1147–1158. doi: 10.1007/s10570-010-9449-z.
- Siró I, Plackett D (2010) Microfibrillated cellulose and new nanocomposite materials: a review. *Cellulose* 17:459–494. doi: 10.1007/s10570-010-9405-y.
- Spence KL, Venditti RA, Habibi Y, Rojas OJ, Pawlak JJ (2010) The effect of chemical composition on microfibrillar cellulose films from wood pulps: Mechanical processing and physical properties. *Bioresource Technology* 101:5961–5968.
- Spence KL, Venditti RA, Rojas OJ, Habibi Y, Pawlak JJ (2011) A comparative study of energy consumption and physical properties of microfibrillated cellulose produced by different processing methods. *Cellulose* 18:1097–1111. doi: 10.1007/s10570-011-9533-z.
- Spinu M, Santos ND, Moigne NL, Navard P (2011) How does the never-dried state influence the swelling and dissolution of cellulose fibres in aqueous solvent? *Cellulose* 18:247–256. doi: 10.1007/s10570-010-9485-8.
- Stelte W, Sanadi AR (2009) Preparation and Characterization of Cellulose Nanofibers from Two Commercial Hardwood and Softwood Pulps. *Ind Eng Chem Res* 48:11211–11219. doi: 10.1021/ie9011672.
- Stevanic JS, Joly C, Mikkonen KS, Pirkkalainen K, Serimaa R, Rémond C, Toriz G, Gatenholm P, Tenkanen M, Salmén L (2011) Bacterial nanocellulose-reinforced arabinoxylan films. *J Appl Polym Sci* 122:1030–1039. doi: 10.1002/app.34217.

- Šturcová A, Davies GR, Eichhorn SJ (2005) Elastic Modulus and Stress-Transfer Properties of Tunicate Cellulose Whiskers. *Biomacromolecules* 6:1055–1061. doi: 10.1021/bm049291k.
- SUNPAP project—Final Conference (2012) <http://sunpap.vtt.fi/finalconference2012.htm>. Accessed 10 May 2015.
- Svagan AJ, Azizi SMA, Berglund LA (2007) Biomimetic Polysaccharide Nanocomposites of High Cellulose Content and High Toughness. *Biomacromolecules* 8:2556–2563. doi: 10.1021/bm0703160.
- Syverud K, Stenius P (2009) Strength and barrier properties of MFC films. *Cellulose* 16:75–85. doi: 10.1007/s10570-008-9244-2.
- Tangnu SK (1982) Process Development for Ethanol Production based on Enzymatic Hydrolysis of Cellulosic Biomass. *Process Biochemistry*:36–49.
- Taniguchi T, Okamura K (1998) New films produced from microfibrillated natural fibres. *Polymer International* 47:291–294. doi: 10.1002/(SICI)1097-0126(199811)47:3<291::AID-PI11>3.0.CO;2-1.
- Tejado A, Alam MN, Antal M, Yang H, van de Ven TGM (2012) Energy requirements for the disintegration of cellulose fibers into cellulose nanofibers. *Cellulose* 19:831–842. doi: 10.1007/s10570-012-9694-4.
- Tingaut P, Eyholzer C, Zimmerm T (2011) Functional Polymer Nanocomposite Materials from Microfibrillated Cellulose. In: Hashim A (ed) *Advances in Nanocomposite Technology*. InTech. doi: 10.5772/20817.
- Turbak AF, Snyder FW, Sandberg KR (1983a) Microfibrillated Cellulose, a New Cellulose Product: Properties, Uses, and Commercial Potential. In Sarko A (ed) *Proceedings of the Ninth Cellulose Conference*. *Applied Polymer Symposia* 37. N.Y.: Wiley. pp. 815–827.
- Turbak AF, Snyder FW, Sandberg KR (1983b) Microfibrillated cellulose. Patent U.S. 4374702.
- Turon X, Rojas OJ, Deinhammer RS (2008) Enzymatic Kinetics of Cellulose Hydrolysis: A QCM-D Study. *Langmuir* 24:3880–3887. doi: 10.1021/la7032753.
- Väljamäe P, Sild V, Pettersson G, Johansson G (1998) The initial kinetics of hydrolysis by cellobiohydrolases I and II is consistent with a cellulose surface – erosion model.

- European Journal of Biochemistry 253:469–475. doi: 10.1046/j.1432-1327.1998.2530469.x.
- Varshney VK, Naithani S (2011) Chemical Functionalization of Cellulose Derived from Nonconventional Sources. In: Kalia S, Kaith BS, Kaur I (eds) Cellulose Fibers: Bio- and Nano-Polymer Composites. Springer Berlin Heidelberg, pp 43–60.
- Wang B, Sain M, Oksman K (2007) Study of Structural Morphology of Hemp Fiber from the Micro to the Nanoscale. *Appl Compos Mater* 14:89–103. doi: 10.1007/s10443-006-9032-9
- Wang QQ, Zhu JY, Gleisner R, Kuster TA, Baxa U, McNeil SE (2012) Morphological development of cellulose fibrils of a bleached eucalyptus pulp by mechanical fibrillation. *Cellulose* 19:1631–1643. doi: 10.1007/s10570-012-9745-x.
- Wågberg L, Decher G, Norgren M, *et al.* (2008) The build-up of polyelectrolyte multilayers of microfibrillated cellulose and cationic polyelectrolytes. *Langmuir* 24:784–795. doi: 10.1021/la702481v.
- Wertz J-L, Bédoué O, Mercier JP (2010) Cellulose Science and Technology. EPFL Press. p. 21.
- Wiedenhoef AC, Miller RB (2005) Structure and function of wood. In Rowell RM (ed) Handbook of wood chemistry and wood composites. CRC Press, pp 9–33.
- Zhou S, Ingram LO (2000) Synergistic hydrolysis of carboxymethyl cellulose and acid-swollen cellulose by two endoglucanases (CelZ and CelY) from *Erwinia chrysanthemi*. *J Bacteriol* 182: 5676–5682. doi: 10.1128/JB.182.20.5676-5682.2000.
- Zhu JY, Sabo R, Luo X (2011) Integrated production of nanofibrillated cellulose and cellulosic biofuel (ethanol) by enzymatic fractionation of wood fibers. *Green Chem* 13:1339–1344. doi:10.1039/C1GC15103G.
- Zimmermann T, Pöhler E, Geiger T (2004) Cellulose Fibrils for Polymer Reinforcement. *Advanced Engineering Materials* 6:754–761. doi: 10.1002/adem.200400097.



# Chapter 2 Rheological and structural properties of nanofibrillated cellulose suspensions

## Introduction

NFC is commonly produced in the form of aqueous suspensions. The rheology of such suspensions becomes a key issue, since the flow is involved in the production process and can affect the properties of the final product. Therefore, the control of the flow behavior of NFC suspensions is highly desirable. Moreover, the rheological properties give an insight into the structural organization of these rather complex biphasic materials. For instance, Ishii *et al.* (2011) reported a method for the determination of the average length of 2,2,6,6-tetramethylpiperidine-1-oxyl (TEMPO)-oxidized NFC based on the rheological measurements. A more comprehensive analysis of the structural properties of NFC suspensions can be performed using scattering techniques, *e.g.*, small-angle X-ray scattering (SAXS).

In this chapter the rheological behavior of enzymatically hydrolyzed and TEMPO-oxidized NFC aqueous suspensions is reported. The problems of flow instabilities (wall-slip and shear banding), which introduce an error in the measured suspension response, are particularly addressed. These phenomena are investigated through visualization technique using different rheometer geometries. SAXS was used to provide supplementary information about the structural organization of NFC in aqueous medium. The statistical average diameter was determined for the NFC swollen in water from the scattering data using unified fit (Beaucage) function approach.

## 2.1 State of the art

### 2.1.1 Introduction to rheology

Rheology investigates the properties of materials determined by their response to deformation and flow (Malkin *et al.* 2006). Materials, in this context, can possess the properties of fluids (liquids or gases), solids or both. Ideal fluids deform irreversibly and are referred to as Newtonian (named after Isaac Newton). For such materials there is a linear relationship between the rate of deformation and the magnitude of the applied force to achieve this deformation. On the contrary, ideal solids, often referred to as Hookean (named after Robert Hooke), deform elastically (with reversible deformation). For such materials, comparing to ideal fluids, there is a linear relationship between the deformation, rather than deformation rate, and the magnitude of the applied force. The majority of materials is neither ideal solids nor ideal fluids and has a rheological behavior representative of both solids and fluids. Thus, they possess both elastic and viscous behavior and may therefore be named as viscoelastic (or as plastic in some specific cases).

The simplest way to illustrate the rheological measurements is a parallel-plate system (see Figure 2.1). The examined material is placed between two plates, mounted at a distance  $l$  [m], each with the surface of  $A$  [m<sup>2</sup>]. If the upper plate is moved with the tangential force  $F$  [N = kg m s<sup>-2</sup>], a plate displacement  $x$  [m] will result, accompanied by sample flow.

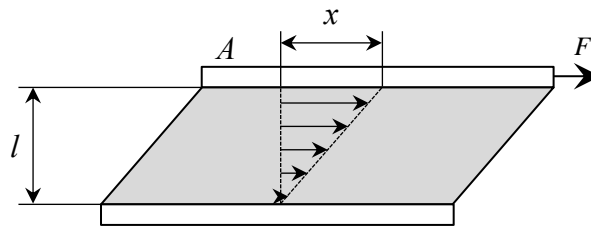


**Figure 2.1** Schematic diagram of the parallel plate geometry for rheological measurements

In the shear flow experiment the force is applied to the upper plate continuously in one direction. If the sample in this case deforms laminary (as layers parallel to the plates) a strain  $\gamma$  can be defined as a ratio of plate displacement to sample thickness:

$$\gamma = \frac{x}{l} \left[ \frac{m}{m} \right]. \quad (2.1)$$

The strain, in this case, is constant within the sample thickness and is also called a gradient of the shear. Since the strain increases while the sample is continuously sheared, the constant value of velocity gradient  $\dot{\gamma}$ , otherwise referred to as shear rate, can be determined:

$$\dot{\gamma} = \frac{dy}{dt} \text{ [s}^{-1}\text{]}. \quad (2.2)$$

A measure of the friction force from the sample acting on the upper plate is called shear stress  $\sigma$  and is defined as:

$$\sigma = \frac{F}{A} \left[ \frac{\text{N}}{\text{m}^2} = \text{Pa} \right]. \quad (2.3)$$

A measure of the resistance to flow is called viscosity  $\eta$ :

$$\eta = \frac{\sigma}{\dot{\gamma}} \text{ [Pa s]}. \quad (2.4)$$

When a periodic sinusoidal shear is applied to the sample, and its response is in-phase with the deformation, the materials behavior is fully elastic:

$$\sigma = G \gamma, \quad (2.5)$$

where  $G$  is the elastic modulus. When the sample response is out-of-phase with the deformation (a phase shift of  $90^\circ$ ), the material has purely viscous behavior. Viscoelastic materials have a phase shift between  $0$  and  $90^\circ$  and the elastic modulus has both in-phase and out-of-phase components, corresponding to elastic and viscous contributions, respectively. The values of these contributions are denoted as the storage modulus ( $G'$ ) and loss modulus ( $G''$ ), respectively.

Coming back to the shear flow experiment, it should be noted that such characterization is valid if the strain is constant at any point of the sample volume within the geometry gap, as shown in Figure 2.2a. Typically, at the beginning of the experiment only a small portion of fluid very close to the top plate will start moving, while the rest of the sample is at rest. Only in the long time limit the velocity becomes a linear function, thus the shear viscosity is measured in this steady state. However, flow instabilities, like flow localization in a specific volume of the sample, called shear banding (see Figure 2.2b), or interfacial slippage on the interface between the shearing tools and the sample, called wall-slip (see Figure 2.2c), occur in a variety of systems even at long time experiments. The flow instabilities are known to take

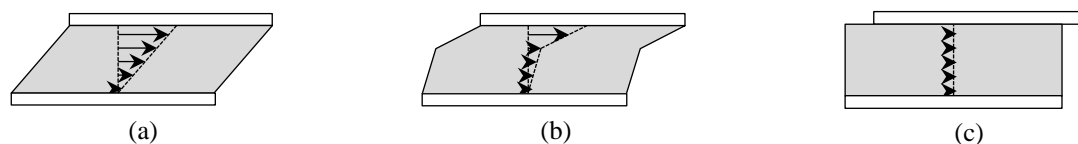


**Figure 2.2** Schematic diagram of sample subjected to deformation in plate-plate geometry: laminar flow (a); flow localization within specific volume of the sample (shear banding) (b); wall-slip (absence of the flow) (c)

place in: wormlike micellar solutions, emulsions, clay suspensions, granular materials, foams, telechelic polymers, colloidal gels *etc.* (Fardin and Lerouge 2012).

The wall-slip is known to occur in fibrous suspensions. It originates from the displacement of a disperse phase from solid boundaries, which creates a lubrication effect (Barnes 1995). As a result, a very narrow layer of the suspension (typically 0.1–10  $\mu\text{m}$ ) at the boundary is subjected to flow. Thereby, it is considered sometimes as shear banding. Since this layer of the suspension is very thin, it is almost imperceptible and appears as a wall-slip.

The shear banding phenomenon usually takes place in complex fluids with structure that relaxes on slow time scales (Olmsted 2008). When an applied shear rate exceeds a characteristic structural relaxation time, the system can acquire a nonequilibrium state with the structure qualitatively different from that of at rest. Thus, the fluid flow is inhomogeneous with coexistence of shear bands with different apparent viscosities separated along the flow gradient direction.

### 2.1.2 Rheology of NFC suspensions

The rheological properties of NFC suspensions were first presented by Herrick *et al.* (1983), who reported the gel-like and shear thinning behavior of NFC at 2 wt.%, produced by mechanical disintegration of cellulose fibers using a Manton-Gaulin homogenizer (Turbak *et al.* 1983). Since then, the various methods have been investigated to facilitate the nanofibrils separation and the rheological properties of the resulting NFC suspensions were studied. The modern methods involve mainly enzymatic or chemical pretreatments followed by the mechanical disintegration.

The research has been conducted on the rheology of suspensions, produced using: mechanical disintegration (Agoda-Tandjawa *et al.* 2010; Karppinen *et al.* 2012; Pahimanolis *et al.* 2011; Saarinen *et al.* 2009), enzymatic treatment (Charani *et al.* 2013; Pääkkö *et al.* 2007), TEMPO-mediated oxidation (Benhamou *et al.* 2014; Lasseuguet *et al.* 2008; Saito *et al.* 2007), carboxymethylation (Naderi *et al.* 2014), ultrasonication (Chen *et al.* 2013) *etc.*

Various sources of cellulose fibers were used in these studies: hardwood (Chen *et al.* 2013; Karppinen *et al.* 2012; Pahimanolis *et al.* 2011; Saarinen *et al.* 2009; Saito *et al.* 2007), softwood (Pääkkö *et al.* 2007), sugar beet (Agoda-Tandjawa *et al.* 2010; Lowys *et al.* 2001), kenaf (Charani *et al.* 2013) *etc.* These studies have mostly focused on the determination of storage and loss moduli from the linear viscoelastic regions during oscillatory measurements and viscosity and shear stress during the flow measurements.

It was often reported that NFC suspensions exhibit gel-like properties ( $G' \gg G''$ ) even at low concentrations, *e.g.* 0.125 wt.% (Pääkkö *et al.* 2007), and have a shear-thinning and thixotropic behavior (Dinand *et al.* 1996; Klemm *et al.* 2011; Pääkkö *et al.* 2007; Saito *et al.* 2007). A strong influence of the concentration (Chen *et al.* 2013; Pääkkö *et al.* 2007; Shogren *et al.* 2011) and the effect of pH (Pääkkö *et al.* 2007) on the rheological properties were also described. The higher viscosities are acquired with more intense fibrillation (Lasseguette *et al.* 2008).

NFC is known to have a complex entangled network and in several works the flocculation in flow was studied (Karppinen *et al.* 2012; Saarinen *et al.* 2009). Some researchers observed the flow curves containing two shear-thinning regions with a viscosity plateau between them (Agoda-Tandjawa *et al.* 2010; Iotti *et al.* 2011), which was supposed to occur due to structural changes of NFC suspension. Such behavior was confirmed by Karppinen *et al.* (2012) when using a visualization approach. They observed a breakdown of the uniform NFC network and formation of relatively large individualized flocculi at the intermediate shear rates caused by the shearing. The formation and breakdown of shear-induced structures in NFC suspensions was also examined by Iotti *et al.* (2011), who have studied a hysteresis loop in the shear rate–viscosity dependence. Martoia *et al.* (2015) examined TEMPO-oxidized and enzymatically hydrolyzed NFC suspensions using Couette rheometer geometry combined with optical observations and ultrasonic speckle velocimetry. It was shown that the flow was heterogeneous and exhibited complex behavior with the coexistence of multiple flow bands, wall slippage and possibly multidimensional effects.

Rheological studies of different NFC-based products have been published. For instance, the properties of NFC suspensions from sugar beet pulp mixed with polyelectrolytes, as potential thickening systems for food applications, were studied by Lowys *et al.* (2001). A melt rheology of nanofibrillated cellulose/acrylic polymer nanocomposites was examined by Besbes *et al.* (2011). Dimic-Misic *et al.* (2013) characterized the papermaking furnishes containing NFC during the dewatering process. The rheological behavior of NFC/acrylate systems for wood coatings has been studied by Grüneberger *et al.* (2014).

The continuous research in this field revealed the problems of flow instabilities, which cause a distortion of the rheological measurements. NFC suspensions tend to slip against smooth walls of the rheometer rotor or stator. Moreover, during flow measurements the deformation can be localized within a specific volume of the sample, called shear banding. The problems of the wall-slip and shear banding in NFC suspensions were mentioned in several works (Saarinen *et al.* 2009; Saarikoski *et al.* 2012; Puisto *et al.* 2012; Mohtaschemi *et al.* 2014). In order to compete with the wall-slip in NFC suspensions, Iotti *et al.* (2011) used parallel plate geometry with a roughened base plate; Charani *et al.* (2013) applied roughened rotor and stator plates; Naderi *et al.* (2014) used serrated bob and cup; Mohtaschemi *et al.* (2014) described the use of wide-gap vane geometry. These were believed to minimize the slip on the contact surface between the geometry tools and the NFC suspension. However, to the best of our knowledge, no work was reported to study the efficiency of these instruments to prevent the flow instabilities in NFC suspensions.

In this work, the rheological behavior of the NFC suspensions was studied in oscillatory and steady-flow regimes. The influence of the used enzymes and their concentrations, oxidation treatment, as well as that of the other process conditions was analyzed. To study the flow instabilities, *e.g.*, wall-slip and shear banding phenomena, the strain field of the samples was monitored using the visualization technique where TiO<sub>2</sub> pigment was implemented in cone-plate, concentric cylinder (Couette) and vane-in-cup geometries. Since TiO<sub>2</sub> possesses a very high refractive index ( $\sim 2.7$ ), it was used to impart white opacity to a certain volume of the sample and to monitor its deformation. The advantage of Couette geometry is the possibility of studying dilute suspensions, as well as testing suspensions with large size of particles. Vane-in-cup geometry induces a minimal disturbance of the sample when inserting the tool. Moreover, a recent study (Mohtaschemi *et al.* 2014) claimed that the wall-slip can be avoided when using wide-gap vane-in-cup geometry for testing NFC suspensions.

### 2.1.3 SAXS characterization

During the rheological measurements, the complex entangled structure of NFC suspensions is the main reason of the flow instabilities occurrence. The structural properties of NFC suspensions are determined particularly by cellulose nanofibrils morphology, which is commonly studied using microscopy techniques, *e.g.*, atomic force microscopy (AFM), transmission electron microscopy (TEM). However, these techniques are based on a selective analysis of some portion of the sample. Moreover, the cellulose samples are commonly used in a dry state for such analyses. To evaluate the size, shape and orientation of particles in

suspension, SAXS can be used. This technique is based on a statistical average over a large amount of scattering objects constituting the suspension under investigation.

The SAXS studies were reported for the suspensions of cellulose nanocrystals (Terech *et al.* 1999; Bonini *et al.* 2002; Elazzouzi-Hafraoui *et al.* 2008) as well as for NFC homologues (Leppänen *et al.* 2010; Penttilä *et al.* 2013; Su *et al.* 2014). Leppänen *et al.* (2010) analyzed the NFC suspension at 10 wt.% concentration, as well as in dry and re-wetted states. Penttilä *et al.* (2013) have focused their studies on the structural changes of NFC during enzymatic hydrolysis. Su *et al.* (2014) studied TEMPO-oxidized NFC produced by homogenization and recovered from the supernatant after centrifugation. The dilute suspensions of such NFC were examined using SAXS and a ribbon model with near rectangular cross section was applied to determine the NFC cross section dimensions.

In this work SAXS measurements on TEMPO-oxidized NFC aqueous suspensions, produced by grinding, were performed. The dilute suspensions of 0.1 and 0.5 wt.% were used for minimizing the interparticle interferences in order to determine the dimensions of cellulose nanofibrils and examine their structural organization using a unified fit function modeling (Beaucage 1995). Such approach was used to distinguish the scattering signal from individual nanofibers and their aggregates or residual non-fibrillated fibers, which can give a perspective for further studies in the field of MFC/NFC fractionation.

## 2.2 Experimental

### 2.2.1 Nanofibrillated cellulose suspensions production

The tested NFC suspensions were produced as reported in Section 1.2. Briefly, two approaches were used comprising enzymatic and TEMPO-mediated oxidation treatments. For the first one, the pulp was extensively refined in the PFI mill for 40 000 revolutions, enzymatically treated (at 50 °C, in 0.05 M acetate buffer, pH 5, during 2 h) and finally grinded using Masuko Supermasscolloider (model MKZA6-2, disk model MKG-C 80) at 2 500 rpm for 60 passes. Two enzymes were employed apart: (i) Celluclast 1.5 L (Novozymes A/S, Denmark; 700 endoglucanase units (EGU)/g) using concentrations of 2.1; 10.5 and 21.0 EGU/g of cellulose (enz-C2.1; enz-C10.5 and enz-C21.0 samples, respectively), and (ii) FiberCare R (Novozymes A/S, Denmark; 4 700 endocellulase units (ECU)/g) using concentrations of 21; 210 and 315 ECU/g of cellulose (enz-F21; enz-F210 and enz-F315 samples, respectively). The suspensions were heated at 80 °C for 15 min to stop the enzymatic activity, cooled down to 25 °C and the pH was adjusted to 7 using 3 M NaOH. The

samples were prepared with a concentration of 2.00 wt.%. Chloroform at 0.01 wt.% was used as a biocide.

One sample (enz-F21-H) was refined in PFI mill, treated with FiberCare R applying 21 ECU/g of cellulose, grinded for 1 h through Masuko Supermasscolloider (6 L of suspension), equipped with recirculation pump, and then passed two times through homogenizer GEA Panther NS3006L (1000 and 1500 bar, respectively). Due to some water remaining in the homogenizer before the processing, the NFC suspension was slightly diluted. The resulting concentration was measured and found to be 1.75 wt.%.

For TEMPO-mediated oxidation TEMPO/NaBr/NaClO system (0.1, 1 and 5 mmol/g of cellulose respectively) was used (ox-TEMPO sample). The oxidized cellulose was filtered on a Büchner funnel using a nylon sieve with a mesh size of 1  $\mu\text{m}$  and washed with deionized water until the filtrate conductivity value was below 5  $\mu\text{S}/\text{cm}$ . Finally, to study the concentration effect on the flow instabilities, cellulose was redispersed in deionized water at 1.50 wt.% and ground with Masuko Supermasscolloider for 60 passes. For all the other measurements, cellulose suspension of 1.00 wt.% concentration was prepared and was ground similarly.

To study the effect of concentration on dynamic moduli, the NFC suspensions were concentrated using centrifuge (Sigma 6-16KS) at 10 000 rpm for 15 min, some portion of the supernatant was removed till the desired concentration and the sediment was homogenized with the remaining supernatant using disperser (T 25 Digital Ultra-Turrax). All the samples were stored in a fridge at 4  $^{\circ}\text{C}$  and left overnight at room temperature ( $\sim 23$   $^{\circ}\text{C}$ ) before the measurements.

### 2.2.2 Rheological measurements

The measurements were carried out using stress-controlled rheometer DHR-3 (TA Instruments), equipped with smooth or serrated (roughened) geometries. The roughened surfaces were made by attaching sandpaper (roughness of  $\sim 120$   $\mu\text{m}$ ) to the available geometries with smooth surfaces (roughness of  $\sim 0.8$   $\mu\text{m}$ ), as shown in Figure C.2 in Annex C.

The following geometries were used: (i) cone-plate with smooth surfaces (truncation gap of 130  $\mu\text{m}$ ; angle of  $4^{\circ} 21' 30''$ ; diameter of 49 mm); (ii) serrated cone-plate (truncation gap of 570  $\mu\text{m}$ ); (iii) Couette with smooth surfaces (recessed concentric cylinders; cup diameter of 37 mm; bob diameter of 28 mm; operating gap of 4 mm); (iv) serrated Couette (cup diameter of 36.2 mm; bob diameter of 28.8 mm); and (v) vane-in-cup (cup diameter of 37 mm; four-blade vane: diameter of 10 mm, height of 19 mm; operating gap of 37 mm).

Before starting the experiments, the samples were kept overnight at room temperature. After the insertion into the rheometer they were allowed to rest for 5 min to minimize the shear history arising from the sample loading. The samples were not presheared in the rheometer which is sometimes used to eliminate the thixotropy effect, since the high shearing forces fracture the sample creating bands of stagnating and flowing suspensions, especially for highly concentrated suspensions. Moreover, at low shear rates wall-slip appears. Thus, the initial NFC structure can be distorted before the measurements.

Oscillation strain sweeps from 0.01 to 10 % at angular frequency of  $1 \text{ rad s}^{-1}$  were performed to detect the linear viscoelastic regions. Then, the oscillation frequency sweeps in these linear viscoelastic regions were performed in the range of  $0.1\text{--}100 \text{ rad s}^{-1}$  to measure the dynamic (storage and loss) moduli ( $G'$  and  $G''$ ). The apparent viscosity measurements were carried out at stepped shear rate ramps typically in the range of  $0.001\text{--}1000 \text{ s}^{-1}$ . To eliminate the thixotropy, the sufficient shearing time was applied until a steady state was reached. All the measurements were carried out at controlled temperature of  $23 \text{ }^\circ\text{C}$ . The measurements were performed in triplicate and an average value was calculated and used for the data analysis.

### 2.2.3 Visualization approach

To study the flow instabilities occurring during the flow measurements, the visualization of the strain field within the sample was performed according to the method proposed by Pignon *et al.* (1996). According to this method, the cone was pierced at a distance of 3 mm from the edge and a vertical filament of the suspension, colored with titanium dioxide, was introduced into the volume of the sample (see Figure 2.3). A transparent cover was used to prevent the

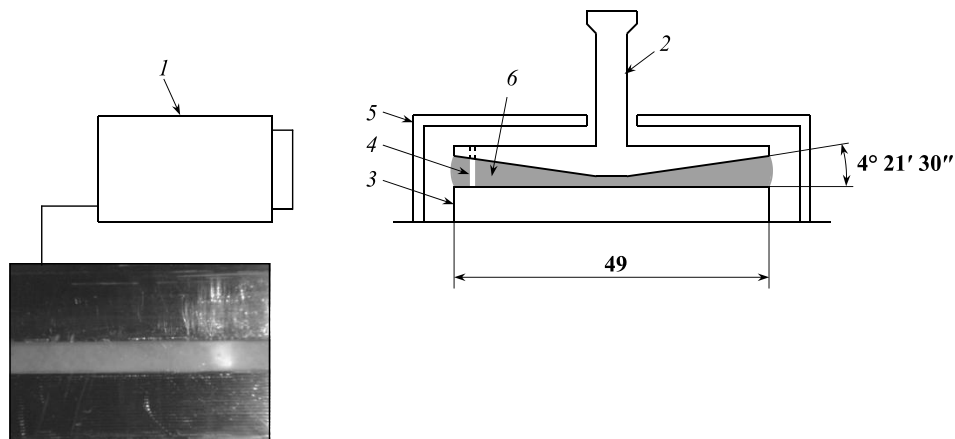


**Figure 2.3** Schematic diagram of cone-plate setup for the rheological measurements combined with the visualization of the sample deformation: (1) video camera; (2) truncated cone; (3) plate; (4) filament of the NFC suspension, colored with titanium dioxide; (5) transparent cover to prevent water evaporation; (6) studied NFC suspension. The dimensions (mm) are shown in *bold*

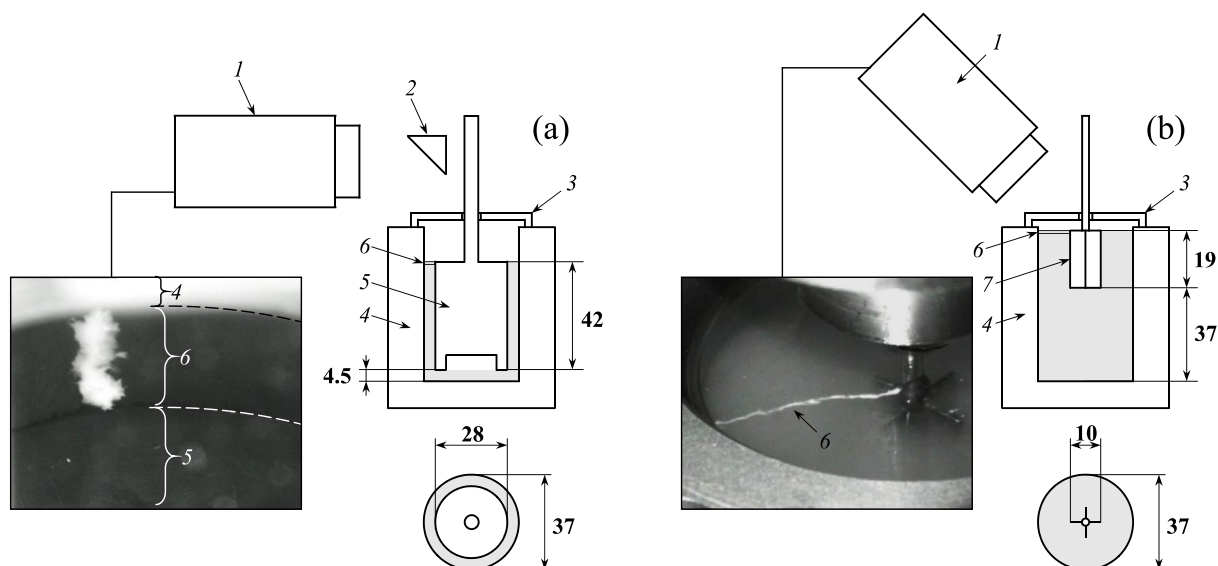


**Figure 2.4** Schematic diagrams of Couette (a) and vane-in-cup (b) setups for the rheological measurements combined with the visualization of the sample deformation: (1) video camera; (2) mirror; (3) transparent cup to prevent water evaporation; (4) cup; (5) bob; (6) filament of NFC suspension colored with titanium dioxide pigment; (7) vane. The dimensions (mm) are shown in *bold*

water evaporation. Displacement of the colored vertical filament was monitored outside using video camera.

The method was extended for Couette and vane-in-cup geometries, where the filament of the  $\text{TiO}_2$  colored suspension was introduced as shown in Figure 2.4. For the interpretation of the shear flow in the vane-in-cup geometry, it was assumed that: (i) the stress distribution is uniform over the cylindrical sheared surface, described by the outer edges of the blades; (ii) the NFC suspension trapped between the blades of vane geometry behaves as a rigid material and there is no secondary flow between the blades. Therefore, the sample was analyzed similarly to the one tested using Couette geometry. Despite the various methods reported to improve the accuracy of the shear flow measurements from vane-in-cup geometry (Baravian *et al.* 2002; Estellé *et al.* 2008), here the main purpose was to investigate the possible flow instabilities using visualization approach.

### 2.2.4 SAXS measurements

The measurements were performed on ID2 high brilliance beamline at European synchrotron radiation facility (Grenoble, France). Dilute TEMPO-oxidized NFC suspensions (0.1 and 0.5 wt.%) were analyzed under controlled temperature ( $25 \pm 1$  °C). The samples were introduced in a flow-through capillary cell (diameter of  $\sim 2$  mm) and were further measured at rest. The enzymatically hydrolyzed NFC was not studied since it possesses highly flocculated morphology. An incident monochromatic X-ray beam with a wavelength of  $0.995$  Å was

used. Scattered intensities were recorded on a two-dimensional CCD detector at sample-to-detector distances of 1 and 10 m.

The scattering intensity distribution was obtained by radial integration of 2D scattering pattern, as a function of scattering vector. The scattering data of cell filled with water was subtracted as a background from the intensity of the suspension yielding information about the NFC. The scattering curves at different sample-to-detector distances were superimposed. The unified fit function (Beaucage 1995) was modeled using Irena software (Ilavsky and Jemian 2009).

### 2.2.5 Analysis of SAXS data

During SAXS experiment the sample was irradiated by X-rays and the intensity of scattered beam at low angular range was analyzed (see Figure C.1 in Annex C). The magnitude of the scattering vector ( $q$ ), is related to the scattering angle, as follows:

$$q = \left( \frac{4\pi}{\lambda} \right) \sin \theta, \quad (2.6)$$

where:  $\lambda$  is the wavelength of X-rays and  $\theta$  is a half of the scattering angle.

When plotting the scattered intensity ( $I$ ) as a function of scattering vector at logarithmic scales, a power-law dependence (Eq. 2.7) yields the fractal dimensions ( $D$ ) of the scattering objects at the particular length scale, yielding the information about the particle shape.

$$I(q) \propto q^{-D}. \quad (2.7)$$

If there is no interparticle interference (*e.g.*, in very dilute suspensions), Guinier approximation (Glatter and Kratky 1982) can be applied for the size determination of the scattering objects:

$$I(q) = I_0 \exp\left(\frac{-R_g^2 q^2}{3}\right), \quad (2.8)$$

where  $R_g$  is a radius of gyration, which represents an effective size of the scattering object.  $R_g$  can be determined by plotting  $\ln[I(q)]$  vs.  $q^2$ , the so-called Guinier plot. When yielding a linear behavior, the slope is equal to  $-R_g^2/3$ . The Guinier approximation is valid for  $qR_g \leq 1$ , indicating that the objects are smaller than the probed range. Thus, the objects constituting one structural level (*e.g.*, non-aggregated spherical particles) can be described by Guinier and a power-law regime.

Individualized elongated particles exhibit two structural levels: there is a scattering arising from the whole particle, and another one associated with the particle cross section. Thus, two Guinier laws and two power laws describe the structure of the scattering objects. In this case Guinier laws appear as: (i) Guinier approximation at lower  $q$ , representing the scattering resulting from the particle, as described by (Eq. 2.8) and (ii) Guinier approximation at higher  $q$ , relative to the particle cross section, described as follows:

$$I(q) = \frac{I_0}{q} \exp\left(\frac{-R_{gc}^2 q^2}{2}\right), \quad (2.9)$$

where  $R_{gc}$  is a radius of gyration of the particle cross section.  $R_{gc}$  can be determined by plotting  $\ln[qI(q)]$  vs.  $q^2$ , where the slope of the curve is equal to  $-R_{gc}^2/2$ . Here, when multiplying the  $I(q)$  by  $q$ , the factor of the particle length is eliminated and the obtained curve represents the information associated with the cross section only (Glatter and Kratky 1982). From the  $R_{gc}$  the particle radius ( $r$ ) can be calculated as follows:

$$R_{gc}^2 = \frac{r^2}{2}. \quad (2.10)$$

For the rod-like particles the length ( $l$ ) can be calculated from the  $R_g$  as follows:

$$R_g^2 = \frac{l^2}{12} + \frac{r^2}{2}. \quad (2.11)$$

For complex hierarchical systems, consisting of overlapped structural levels (e.g., polydisperse aggregated particles) a unified fit function approach (Beaucage 1995; 1996) can be used to analyze the small-angle scattering data. The unified function (Eq. 2.12) consists of the scattering functions from  $n$  structural levels, each containing a Guinier regime representing the  $R_g$ , and a power-law regime reflecting the type of the analyzed structure:

$$I(q) = \sum_{i=1}^n \left( G_i \exp\left(-\frac{q^2 R_{g,i}^2}{3}\right) + B_i \exp\left(-\frac{q^2 R_{g,i-1}^2}{3}\right) \left( \frac{[\operatorname{erf}(kqR_{g,i}/\sqrt{6})]^3}{q} \right)^{P_i} \right), \quad (2.12)$$

where  $G$  is a Guinier prefactor;  $B$  is a power-law prefactor;  $\operatorname{erf}()$  is the error function,  $k = 1$  for  $P > 3$  or  $k = 1.06$  for  $1.5 \lesssim P \lesssim 3$  and  $P$  is an exponent reflecting the power-law scattering (Beaucage 1996). The function describes a system, where  $i = 1$  is a primary structural level composed of the smallest scattering objects at high  $q$ ; and  $i = n$  at low  $q$  represents the largest

scattering objects, which can be composed from the elements from the previous structural levels.

For the rod-like particles the radius ( $r$ ) and length ( $l$ ) can be calculated from the radii of gyration at the first and second structural levels (Beaucage 2012):

$$R_{g,1}^2 = \frac{3}{4} r^2; \quad (2.13)$$

$$R_{g,2}^2 = \frac{l^2}{12} + \frac{r^2}{2}. \quad (2.14)$$

## 2.3 Results and discussion

### 2.3.1 Oscillation measurements

Figure 2.5 shows the storage and loss moduli as a function of oscillation strain. The  $G'$  and  $G''$  were plotted while the raw phase was below  $90^\circ$  indicating that there is no influence of the inertial effects. During the oscillation strain sweeps, the rheological properties of the NFC suspensions are almost independent of strain up to a critical strain level. Beyond this critical strain level, the suspensions behavior becomes non-linear, which occurs due to disruption of the material structure. The suspensions become progressively more fluid-like while  $G''$  approaches the level of  $G'$ . It is evident that the critical strain level is much higher for ox-TEMPO (strain of  $\sim 1\%$ ) to compare with all the enzymatically treated samples (strain of  $\sim 0.1\%$ ), for which it was almost independent of the enzymes types and their concentrations.

The NFC suspensions were further analyzed during a frequency sweep at a strain below the critical level. Figure 2.6 shows the storage and loss moduli as a function of oscillation frequency. As for the oscillation strain, the  $G'$  and  $G''$  were plotted while the raw phase was below  $90^\circ$ . It is evident that all the suspensions exhibit gel-like properties ( $G' \gg G''$ ) in a large range of frequencies. Surprisingly, with the increase of enzymatic concentration, the dynamic moduli decrease despite the higher fibrillation and, hence, the higher specific surface of fibrous elements. However, it can be explained by depolymerization of cellulose as a result of enzymatic hydrolysis, as shown in Section 1.3.2.

The NFC suspensions treated with endoglucanase solution FiberCare R (Figure 2.6a) yielded stronger networks comparing to that of cellulase solution Celluclast 1.5 L (Figure 2.6b) despite the higher enzymatic concentration applied in the former case. Comparing

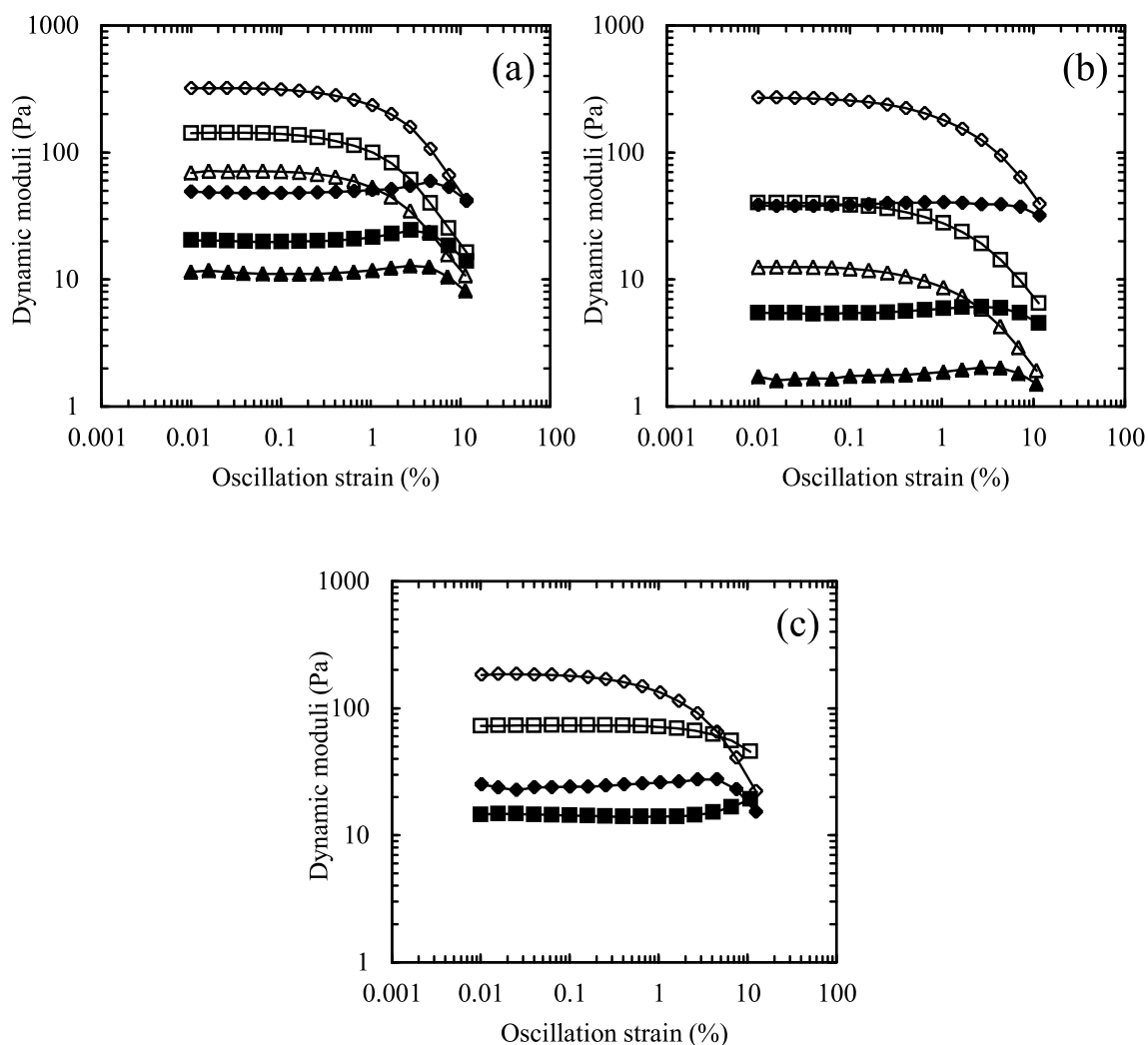


**Figure 2.5** Storage (*empty symbols*) and loss moduli (*filled symbols*) as a function of oscillation strain of: (a) enz-F21 ( $\diamond$ ,  $\blacklozenge$ ), enz-F210 ( $\square$ ,  $\blacksquare$ ), enz-F315 ( $\triangle$ ,  $\blacktriangle$ ); (b) enz-C2.1 ( $\diamond$ ,  $\blacklozenge$ ), enz-C10.5 ( $\square$ ,  $\blacksquare$ ), enz-C21 ( $\triangle$ ,  $\blacktriangle$ ) (all the samples at 2.00 wt.% concentration); (c) enz-F21-H ( $\diamond$ ,  $\blacklozenge$ ) of 1.75 wt.% and ox-TEMPO ( $\square$ ,  $\blacksquare$ ) of 1.00 wt.%. Performed using concentric cylinders geometry

two types of the applied enzymes, it should be noticed that Celluclast 1.5 L is an enzyme mixture composed of *Trichoderma reesei* fungus containing endoglucanases, exoglucanases, cellobiohydrolases, and  $\beta$ -glucosidases, while FiberCare R is a monocomponent endoglucanase. Thereby, the former degrades cellulose to elementary sugars in a stronger manner due to its composition. Consequently, the use of Celluclast 1.5 L decreases more the viscoelasticity of the NFC suspension.

The dynamic moduli of enz-F21-H are practically equal to enz-F21. However, the concentrations of the samples are 1.75 vs. 2.00 wt.%, respectively, indicating the stronger fibrous network of the former suspension. The storage and loss moduli of ox-TEMPO (1.00 wt.%) are similar to that of enz-F315 (2.00 wt.%).

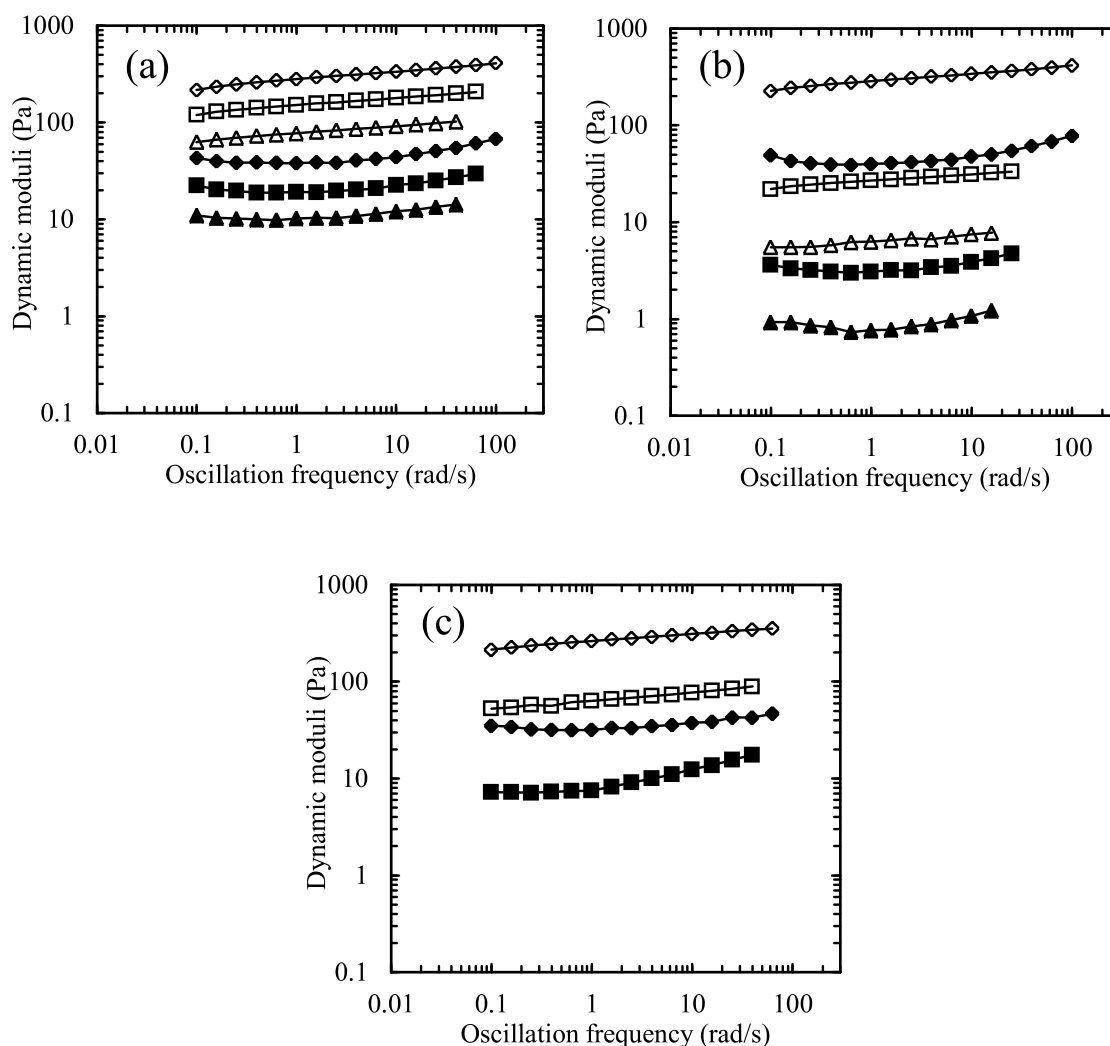


**Figure 2.6** Storage (*empty symbols*) and loss moduli (*filled symbols*) as a function of oscillation frequency of: (a) enz-F21 ( $\diamond$ ,  $\blacklozenge$ ), enz-F210 ( $\square$ ,  $\blacksquare$ ), enz-F315 ( $\triangle$ ,  $\blacktriangle$ ); (b) enz-C2.1 ( $\diamond$ ,  $\blacklozenge$ ), enz-C10.5 ( $\square$ ,  $\blacksquare$ ), enz-C21 ( $\triangle$ ,  $\blacktriangle$ ) (all the samples at 2.00 wt.% concentration); (c) enz-F21-H ( $\diamond$ ,  $\blacklozenge$ ) of 1.75 wt.% and ox-TEMPO ( $\square$ ,  $\blacksquare$ ) of 1.00 wt.%. Performed using concentric cylinders geometry

Viscoelastic properties of ox-TEMPO (Figure 2.7a) and enz-F21-H (Figure 2.7b) were investigated at different cellulose concentrations. The storage and loss moduli increased dramatically with the increase of cellulose concentration. By changing the mass fraction of ox-TEMPO from 0.75 to 1.25 wt.% the storage modulus increased by one order of magnitude. In the case of enz-F21-H, at the oscillation frequency of 1 rad/s,  $G'$  changed from 34 to 6 023 Pa by varying the concentration from 1 to 3 wt.%. The drastic change of the dynamic moduli with a slight variation of cellulose concentration is in agreement with other studies (Agoda-Tandjawa *et al.* 2010; Charani *et al.* 2013; Dimic-Misic *et al.* 2013; Iotti *et al.* 2011; Lowys *et al.* 2001; Pääkkö *et al.* 2007).

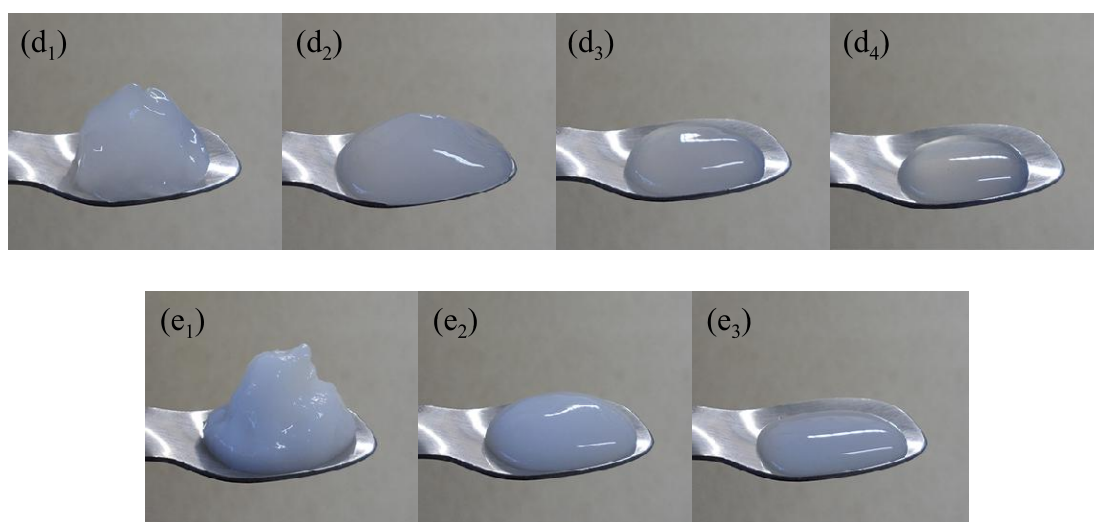
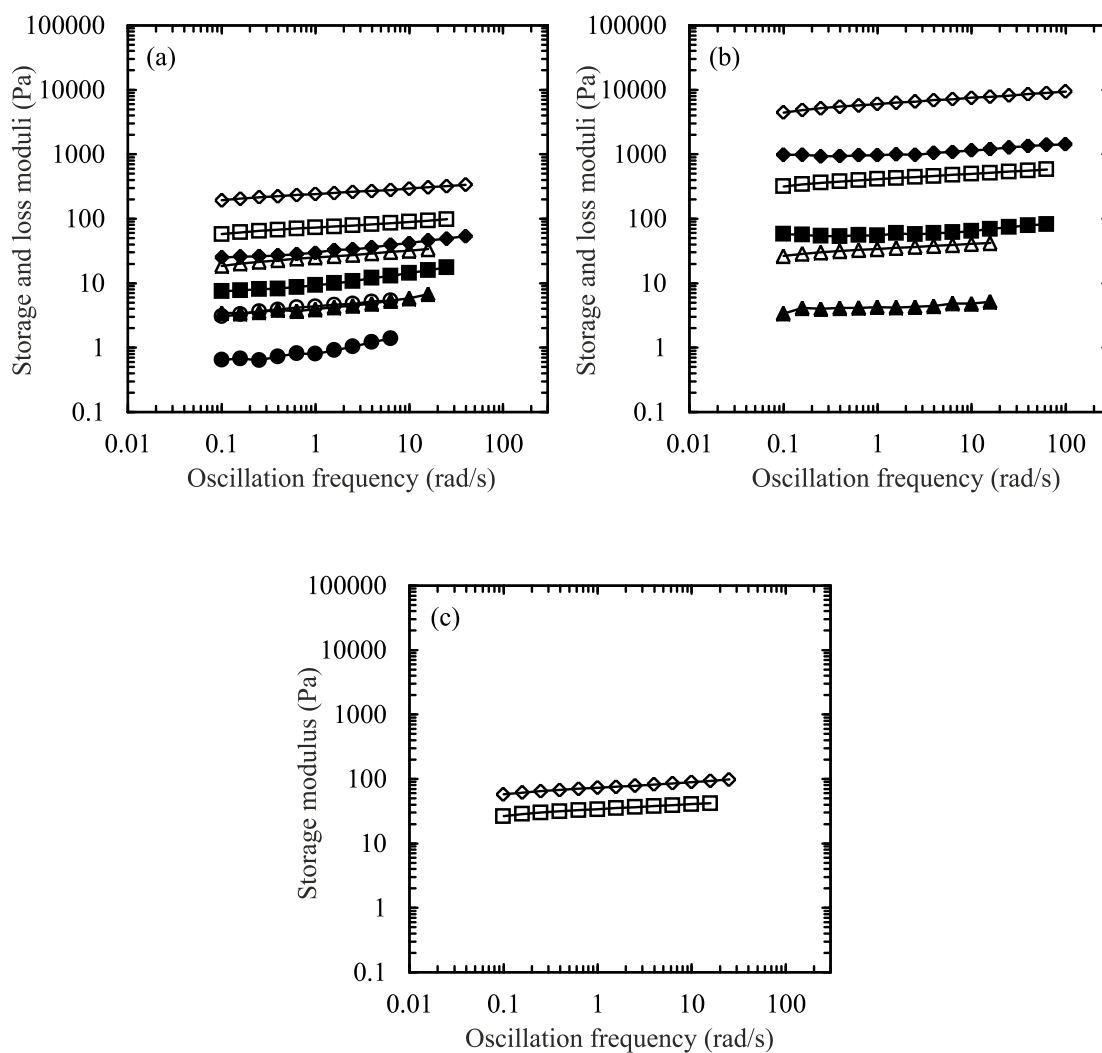


**Figure 2.7** Viscoelastic properties and digital camera photographs of the NFC suspensions at different concentrations. Storage (*empty symbols*) and loss moduli (*filled symbols*) as a function of oscillation frequency of: ox-TEMPO NFC sample (a) at 1.25 wt.% (◇, ◆); 1.00 wt.% (□, ■); 0.75 wt.% (△, ▲); 0.50 wt.% (○, ●); enz-F21-H NFC sample (b) at 3 wt.% (◇, ◆), 2 wt.% (□, ■) and 1 wt.% (△, ▲); and ox-TEMPO (◇) and enz-F21-H (□) NFC samples (c) both at 1.00 wt.%. Photographs of: ox-TEMPO at 1.25 wt.% (d<sub>1</sub>), 1.00 wt.% (d<sub>2</sub>), 0.75 wt.% (d<sub>3</sub>), 0.50 wt.% (d<sub>4</sub>) and enz-F21-H at 3 wt.% (e<sub>1</sub>), 2 wt.% (e<sub>2</sub>) and 1 wt.% (e<sub>3</sub>)

Figure 2.7c shows  $G'$  of ox-TEMPO and enz-F21-H both at 1 wt.% for comparison. It is seen, that the former has a stronger fibrous network which can be explained by lower dimensions of the nanofibrils, as shown in Section 1.3.2. In a colloidal suspension, the smaller are the particles, the higher is the volume fraction, which is a relevant parameter.

### 2.3.2 Flow properties

All the studied NFC suspensions exhibit a shear-thinning behavior, as seen from the flow curves in Figure 2.8. A decrease of the apparent viscosity is observed as the shear rate ( $\dot{\gamma}$ ) increases and for some samples a Newtonian plateau can be noticed at shear rates of 10–100  $\text{s}^{-1}$ . A similar behavior was reported in previous studies (Agoda-Tandjawa *et al.* 2010; Iotti, Gregersen, Moe, & Lenes, 2011; Pääkkö *et al.* 2007). The apparent shear stress decreases slightly till intermediate shear rates (0.1–10  $\text{s}^{-1}$ ) and is followed by a strong increase for the range of 10–1000  $\text{s}^{-1}$ . The difference between the flow behavior of the studied samples is similar with that of the storage and loss moduli described in Section 2.3.1.

Similar behavior was previously reported by Karppinen *et al.* (2012) when using the visualization approach. They observed the breakdown of the uniform NFC network and formation of relatively large individualized flocculi at intermediate shear rates caused by the shearing. The formation and breakdown of shear-induced structures in NFC suspensions was also examined by Iotti *et al.* (2011), who have studied a hysteresis loop in the shear rate–viscosity dependence.

### 2.3.3 Flow instabilities visualization

To study the strain field inside the bulk of the NFC suspensions, the truncated cone and plate geometry in combination with visual observations using video camera were applied. The introduced vertical filament of the suspension, colored with  $\text{TiO}_2$  (as shown in Figure 2.3), illustrated very well the occurring phenomena.

It is apparent from Figure 2.9 (see photographs below the graph) that when using non-serrated (smooth) cone-plate geometry at low shear rates (0.001–0.1  $\text{s}^{-1}$ ) the ox-TEMPO sample remained almost not deformed, since the wall-slip occurred. Initially, a small deformation happened at the beginning of the experiment which is seen from a slight deviation from the vertical position of the colored rod. The further shear forces did not induce the deformation, producing the wall-slip on the boundary of the NFC and the cone (see Figure 2.9b).

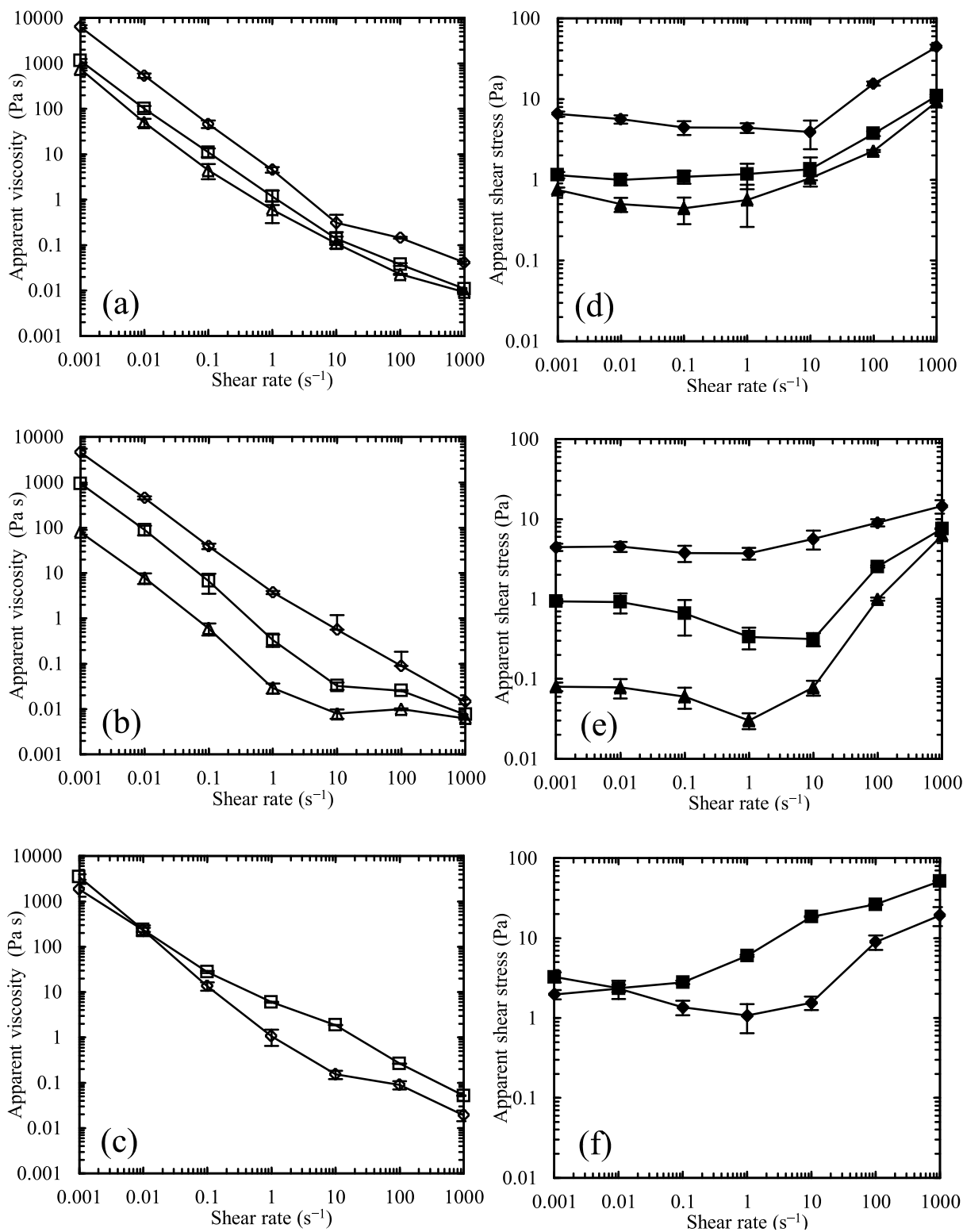


**Figure 2.8** Apparent viscosity (a, b, c) and apparent shear stress (d, e, f) as a function of shear rate for: (a, d) enz-F21 (◇, ◆), enz-F210 (□, ■), enz-F315 (△, ▲); (b, e) enz-C2.1 (◇, ◆), enz-C10.5 (□, ■), enz-C21 (△, ▲); (c, f) enz-F21-H (◇, ◆), ox-TEMPO (□, ■). Performed using concentric cylinders geometry

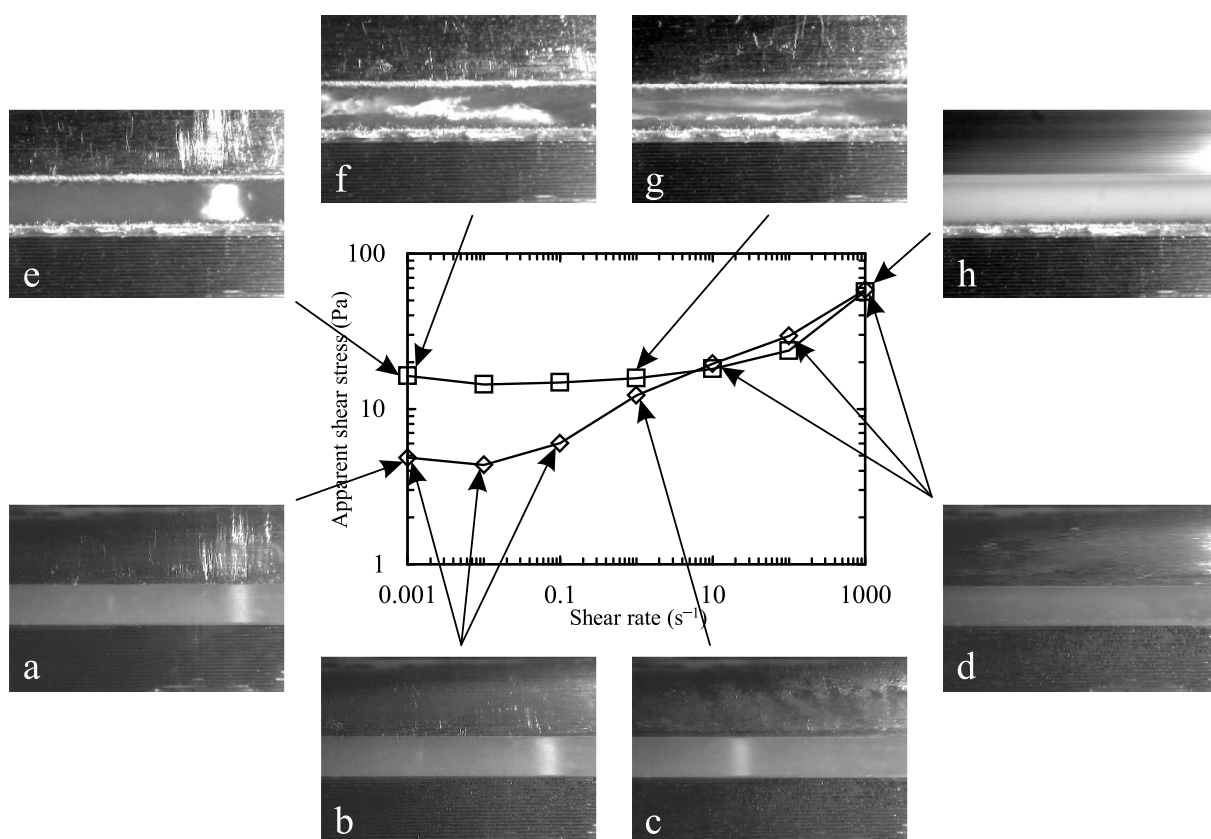


**Figure 2.9** Apparent shear stress as a function of shear rate together with visualization of the flow behavior of ox-TEMPO NFC sample using serrated ( $\square$ ) and non-serrated (smooth) ( $\diamond$ ) cone-plate geometries. Illustration of the occurred phenomena applying non-serrated geometries: initial position before the measurement (**a**), wall-slip on the boundary of the NFC suspension and the cone (**b**); wall-slip on the boundaries of the NFC suspension and both cone and plate (**c**); sample flow, shear banding detected (not noticeable from the photograph) (**d**). Occurred phenomena applying serrated geometries: initial position before the measurement (**e**) sample flow (**f**); shear banding with a fracture between the moving and stagnant NFC suspension parts (**g**); sample flow (**h**)

At the shear rate of  $1 \text{ s}^{-1}$  the slippage on the edge between the suspension and both cone and plate occurred (Figure 2.9c). Moreover, no deformation of the bulk took place so that the NFC rotated preserving the colored rod shape. Only when reaching a shear rate of  $10 \text{ s}^{-1}$  the bulk deformation started to occur (Figure 2.9d). Nevertheless, the suspension did not flow uniformly: fast and slow flowing regions were observed, which is known as shear banding phenomenon. At higher shear rates, above  $10 \text{ s}^{-1}$ , the suspension flows within all the gap of the tools geometry, which is more relevant as a volume property of the sample.

The shape of the apparent shear stress *vs.* shear rate dependence of ox-TEMPO sample measured using smooth cone-plate geometry (Figure 2.9) is similar to that measured using concentric cylinders (Figure 2.8f). Thereby, it is assumed that in the latter case the wall-slip and shear banding phenomena could also take place.

Saarinen *et al.* (2009) showed the influence of the geometry gap on the viscoelastic properties of the NFC suspensions. They associated the results divergence with the wall-slip.

To hinder the wall-slip phenomena while studying different kinds of materials the roughening of the geometry surfaces has been sufficiently applied, *e.g.* by sandblasting (Buscall *et al.* 1993) or attaching sandpaper (Pignon *et al.* 1996). Iotti *et al.* (2011) used plate-plate geometry with roughened base plate in order to prevent the wall-slip while studying the NFC suspensions. However, in their work no results were reported showing whether it was efficient or not to hinder the slippage.

In this work sandpaper was used to form the rough surfaces on the cone and plate as described in Section 2.1.2. The use of serrated geometries prevented the slip while testing the ox-TEMPO, as shown in Figure 2.9 (the photographs above the graph). The resulted values of the shear stress at low shear rates are notably higher comparing to that of non-serrated geometry and can be considered as more accurate since the sample is subjected to the deformation. However, the fracture of the bulk was observed; it was especially evident at the shear rate of  $1 \text{ s}^{-1}$  (Figure 2.9g). It resulted into the localization of the flow within a fine layer in the middle of the bulk.

Figure 2.10 (the photographs above the graph) shows that the wall-slip occurred for enz-F21-H sample as well when applying the smooth geometry. It was observed that the suspension remained not deformed even at a shear rate of  $1 \text{ s}^{-1}$  (Figure 2.10b). At  $10 \text{ s}^{-1}$  the slippage at two boundaries took place without causing the deformation of the bulk (Figure 2.10c), similarly to that described above for ox-TEMPO at  $1 \text{ s}^{-1}$ . The flow of the sample was detected at  $100 \text{ s}^{-1}$  when the shear rate started to increase as a function of shear rate (Figure 2.10d).

The use of serrated cone and plate (see Figure 2.10, photographs below the graph) increased slightly the values of the shear stress at low shear rates. However, then a drastic decrease was observed, since the sand granules were likely to alter the structure of the NFC, squeezing water from the NFC suspension and creating the lubrication layer, localized between the NFC and the cone (Figure 2.10f). As a result, the flow was localized in the top layer of the suspension. At this range of shear rates ( $0.001\text{--}10 \text{ s}^{-1}$ ) the shear stress level corresponds to the stress in a thin top layer of the bulk and it is not representative of a volume property of the sample. By a further increase of shear rate (above  $100 \text{ s}^{-1}$ ) the flow of the all volume of the enz-F21-H sample was achieved (Figure 2.10g) and the shear stress reached the same values, as those obtained with non-serrated tools.

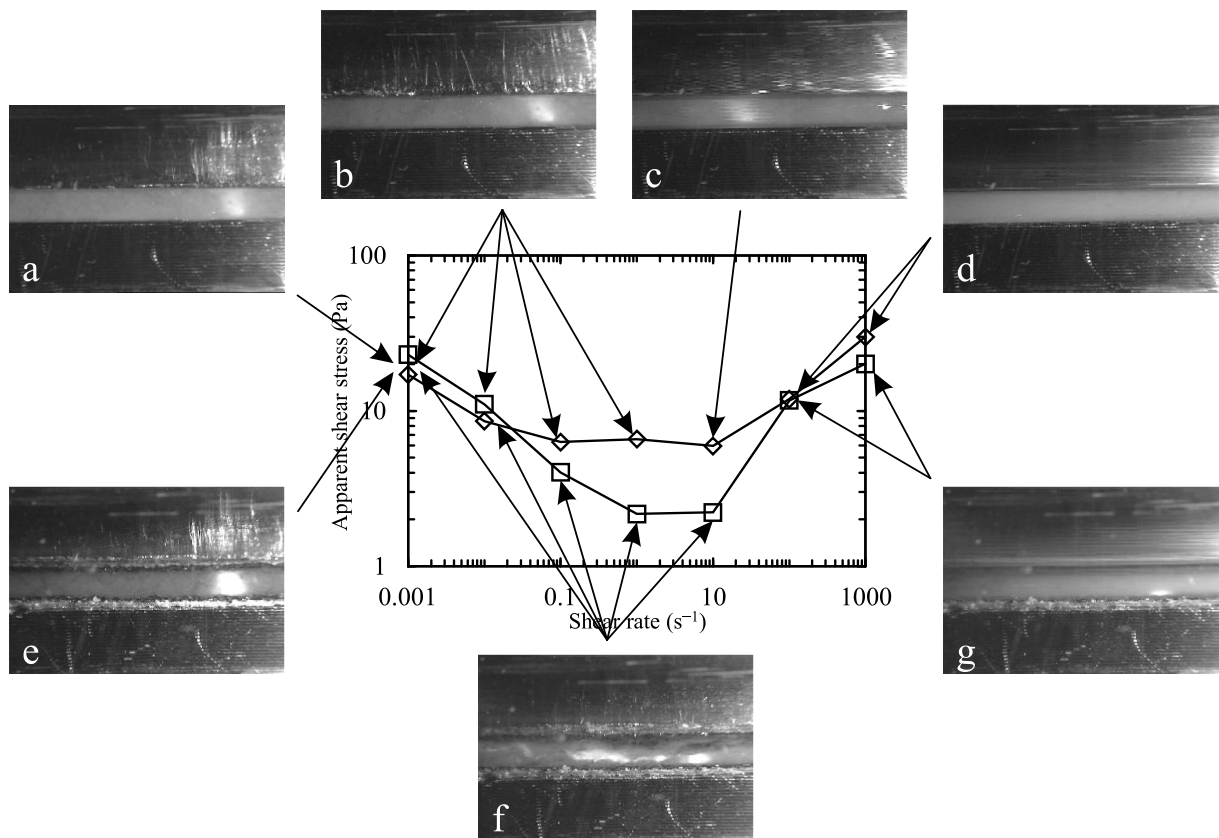


**Figure 2.10** Shear stress as a function of shear rate together with visualization of the flow behavior of enz-F21-H NFC sample using serrated ( $\square$ ) and non-serrated (smooth) ( $\diamond$ ) cone-plate geometries. Illustration of the occurred phenomena applying non-serrated geometries: initial position before the measurement (**a**), wall-slip on the boundary of the NFC suspension and the cone (**b**); wall-slip on the boundaries of the NFC suspension and both cone and plate (**c**); sample flow (**d**). Occurred phenomena applying serrated geometries: initial position before the measurement (**e**), wall-slip at the boundary of the NFC suspension and the cone, the lubrication layer was noticeable due to water release from the sample (**f**); sample flow (**g**)

Figure 2.11 shows the ox-TEMPO suspension analyzed at different characteristic shear rates. For each test a new portion of the sample was placed and the shear stress was analyzed as a function of step time. Subjecting the sample to the shear, the colored rod passed from the vertical to slightly inclined position till the yield stress, corresponding to the maximum of the stress–time curve (*e.g.* in Figure 2.11a at time of 2.6 s). After this, at different shear rates: a wall slip at upper boundary (Figure 2.11a); a wall slip at both upper and lower boundaries (Figure 2.11b) and the flow within all the sample volume (Figure 2.11c) occurred. Figure 2.11d represents the use of serrated geometry and the changes of ox-TEMPO structure at different times. After reaching the yield stress a fracture of the sample bulk occurred. The time of the image capturing from the beginning of the test is indicated in the top left position on the photograph.

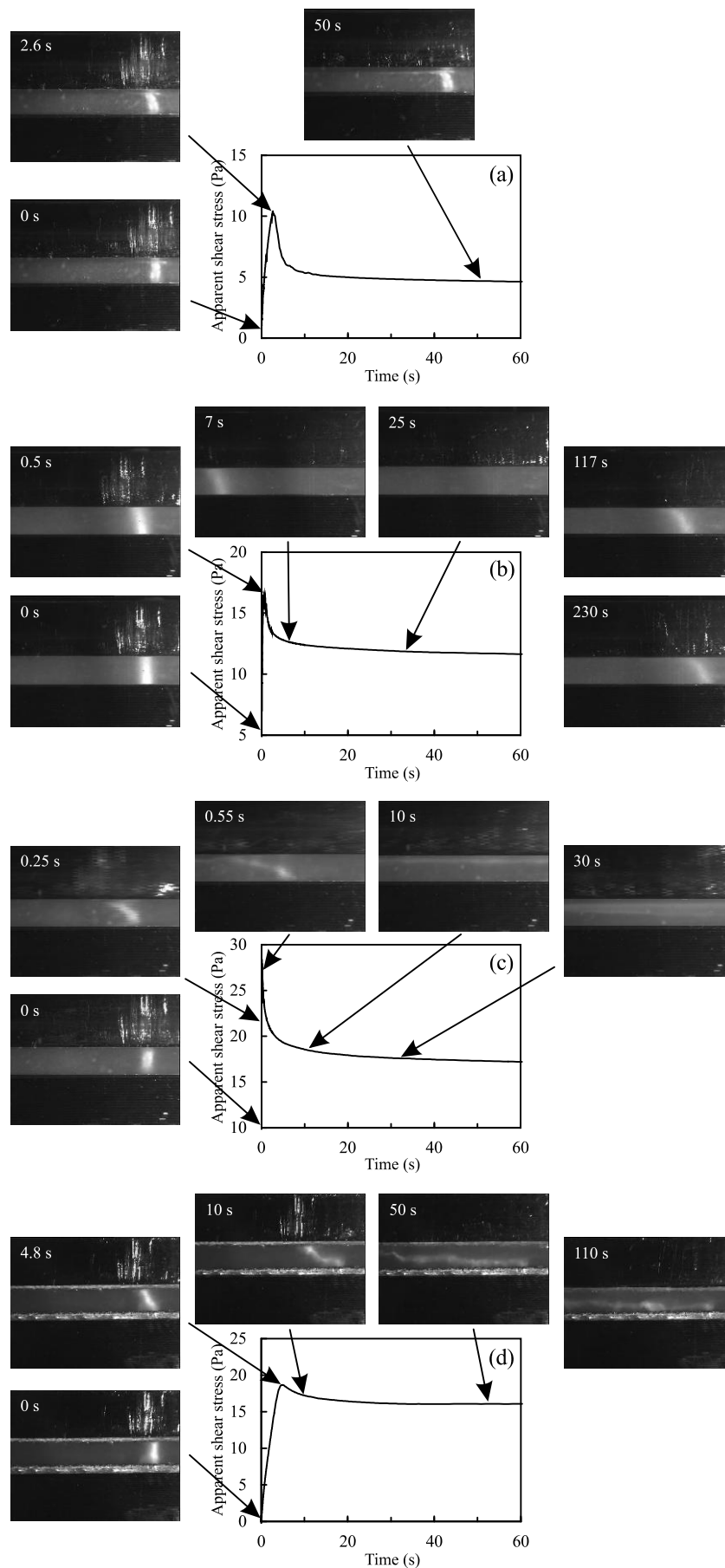


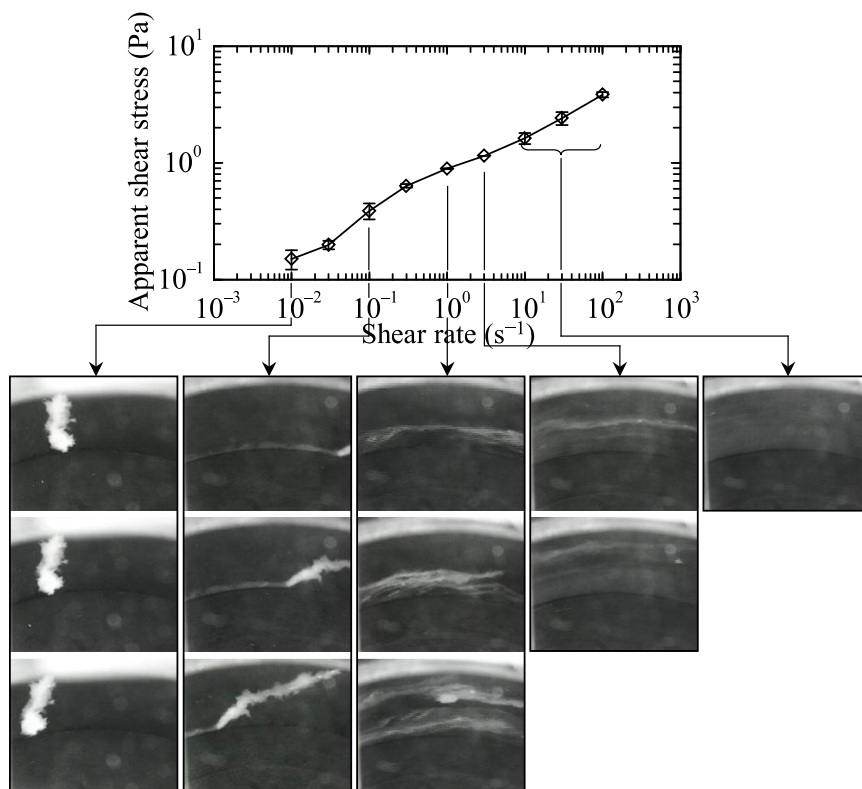
**Figure 2.11** Shear stress as a function of time of ox-TEMPO NFC sample measured at shear rate of:  $0.1 \text{ s}^{-1}$  (a, d);  $1 \text{ s}^{-1}$  (b) and  $10 \text{ s}^{-1}$  (c) using non-serrated (a, b, c) and serrated (d) cone-plate geometries. The time when picture was taken is indicated in the top left part of the photograph

### 2.3.4 Influence of NFC concentration on flow instabilities

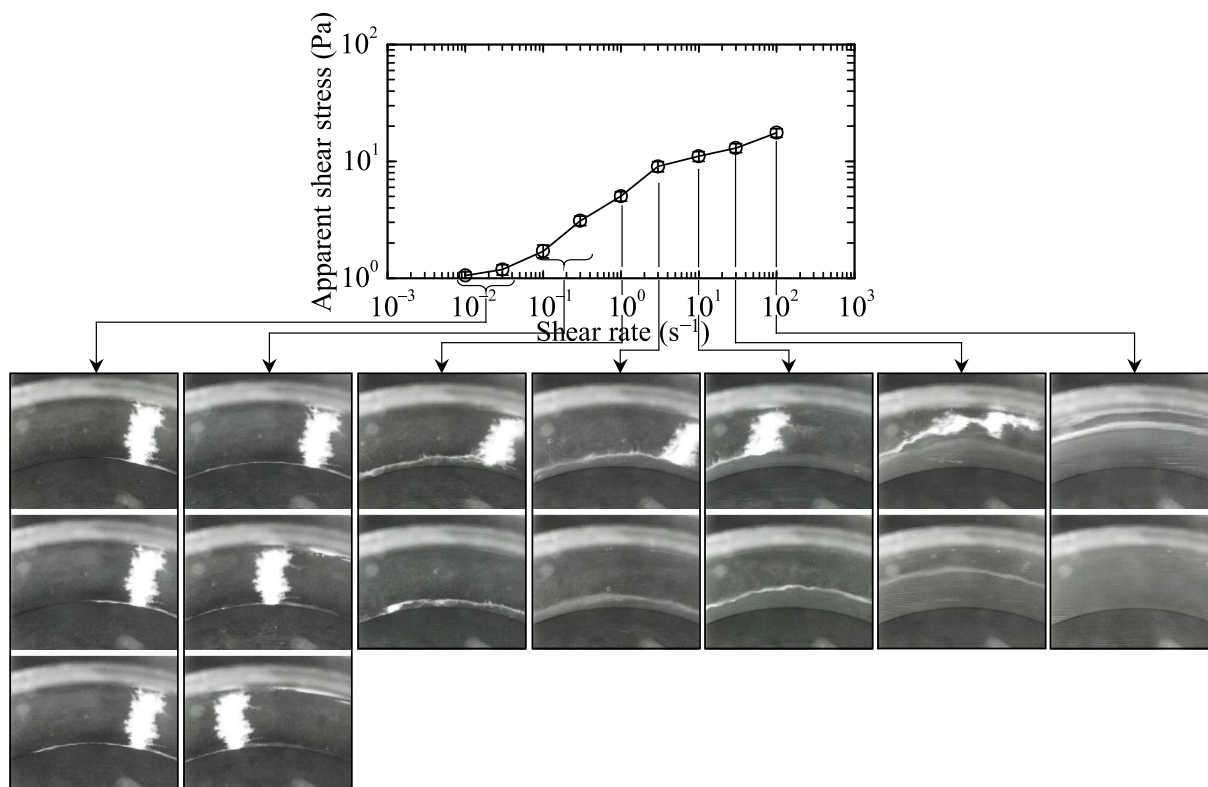
Couette geometry with smooth surfaces was used in combination with the visual monitoring of the strain field inside the sample, as illustrated above in Figure 2.4a, to study the occurrence of flow instabilities in TEMPO-oxidized NFC suspensions, when submitted to a steady shear. Figures 2.12, 2.13 and 2.14 show the apparent shear stress *vs.* shear rate curves for the suspensions at the concentrations of 0.5, 1.0 and 1.5 wt.%, respectively. Each column of photographs represents the characteristic behavior of the sample at a constant shear rate while the strain increases. The photographs of the samples were taken as a function of strain/time. The lower photograph position indicates the higher strain applied. The typical nonlinear rheology of the NFC suspensions is observed. The shear stress increases within all the range of shear rates applied for the three tested concentrations.

Figure 2.12 shows that at the concentration of 0.5 wt.% the deformation of the colored filament takes part within all the range of shear rates. However, at  $\dot{\gamma} = 0.1 \text{ s}^{-1}$ , even if the deformation took place, it is evident that a depletion of the NFC suspension adjacent to the shearing surfaces of the bob happens thus inducing a wall-slip (white margin at the bob-suspension contact seen in Figure 2.13). Thus, the local strain of the sample is lower than that applied by the rheometer. With an increase of the shear rate, the suspension undergoes a shear banding transition. At  $\dot{\gamma} = 1$  and  $3 \text{ s}^{-1}$ , the sample flows non-homogeneously with a separation of the suspension into regions with different shear rates. The shear banding is characterized by a homogeneous flow near the bob and a non-homogeneous flow near the cup boundary. At higher shear rates ( $10\text{--}100 \text{ s}^{-1}$ ) the flow appears homogeneous within all the gap of the Couette geometry.

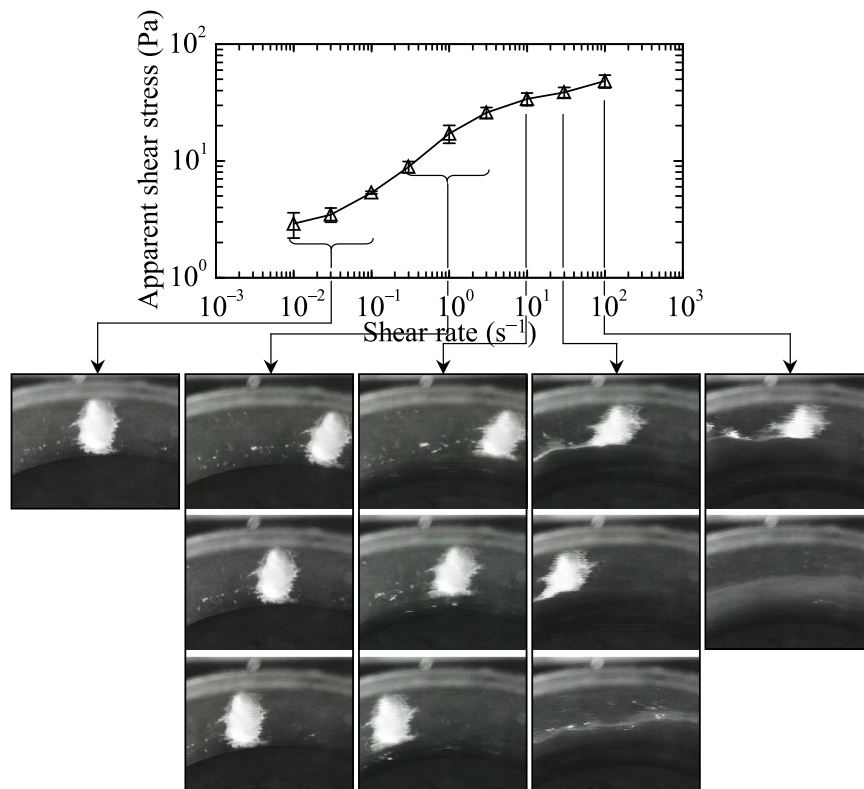
The flow instabilities became more pronounced for the NFC suspension at a concentration of 1.0 wt.%, as shown in Figure 2.13. At  $\dot{\gamma} = 0.01$  and  $0.03 \text{ s}^{-1}$  a slip at the boundary of the bob and suspension is significant, which impedes the suspension flowing. At  $\dot{\gamma} = 0.1$  and  $0.3 \text{ s}^{-1}$  no deformation of the color filament is observed, but two slips occur at the contact of the NFC suspension with bob and cup. The subsequent increase of the shear rate produces a shear banding effect. The magnitude of the flowing volume of the suspension enhances with the increase of shear rate. The total deformation of the sample results from a combination of flow and stagnation of some volume of the sample, which slips over the cup surface.



**Figure 2.12** Flow curves together with strain visualization of TEMPO-oxidized NFC suspensions at the concentrations of 0.5 wt.% examined using Couette geometry. Each column of photographs represents the characteristic behavior of the sample at a constant shear rate while the strain increases. The lower photograph position indicates the higher strain applied



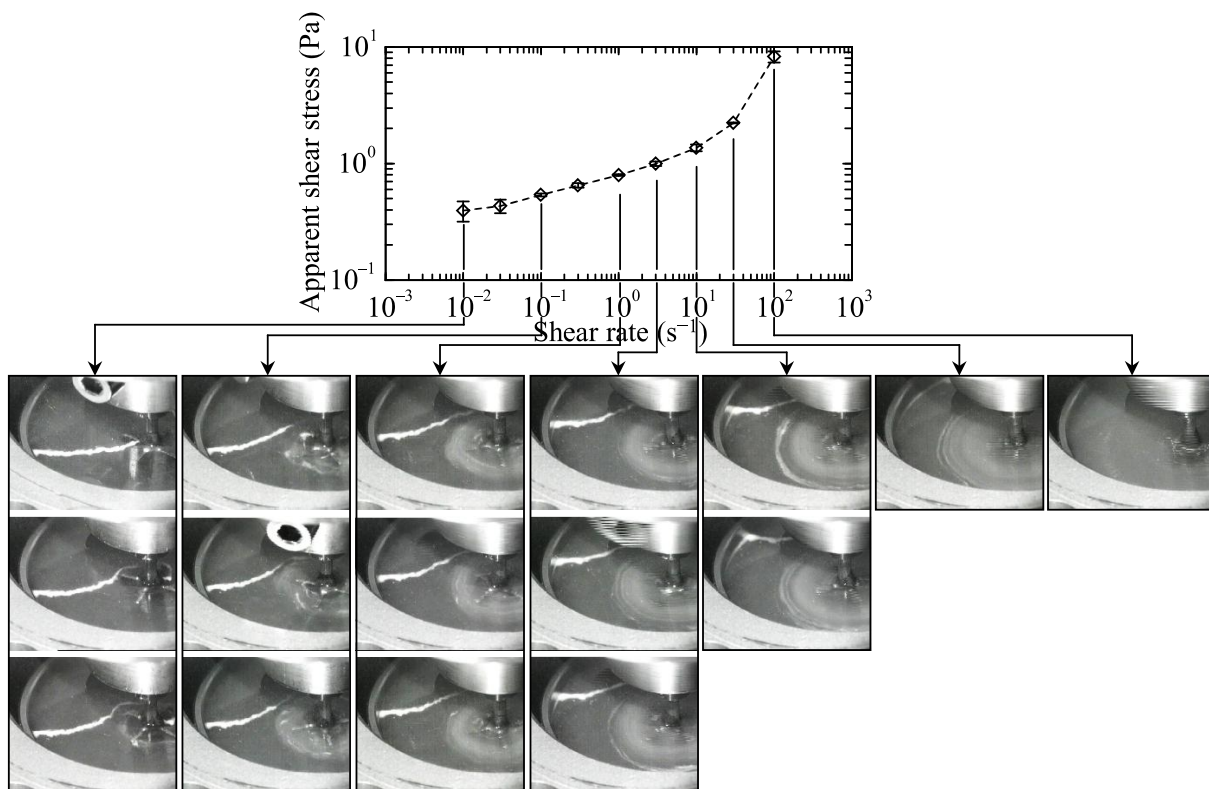
**Figure 2.13** Flow curves together with strain visualization of TEMPO-oxidized NFC suspensions at the concentrations of 1.0 wt.% examined using Couette geometry



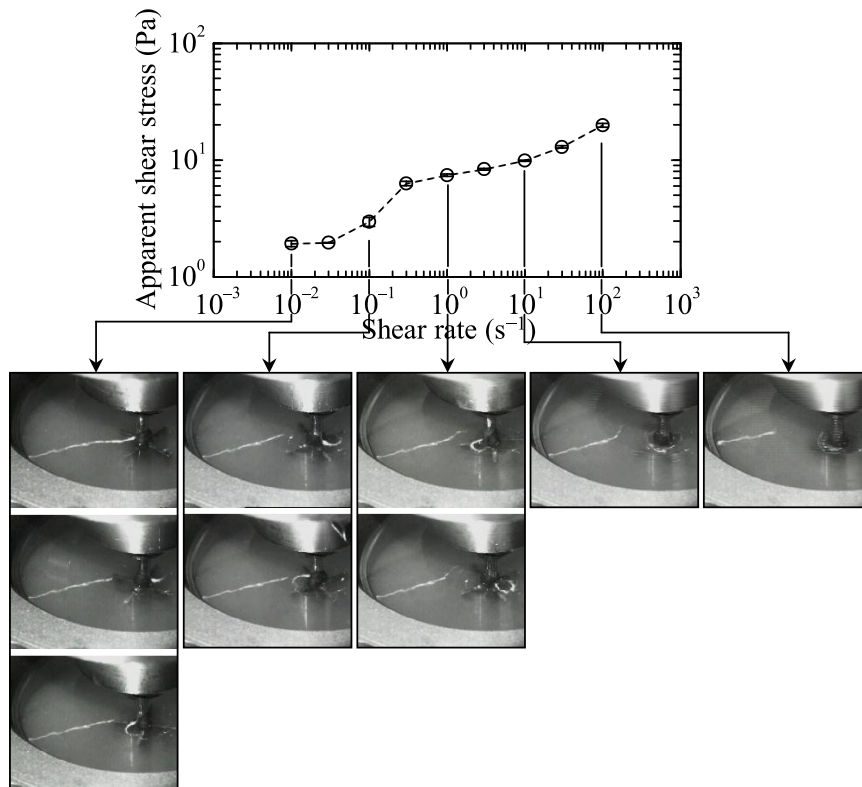
**Figure 2.14** Flow curves together with strain visualization of TEMPO-oxidized NFC suspensions at the concentrations of 1.5 wt.% examined using Couette geometry

Figure 2.14 presents the flow experiments of the NFC suspension at 1.5 wt.%. At low shear rates ( $\dot{\gamma} = 0.01\text{--}0.1\text{ s}^{-1}$ ), a slip at the boundary of the bob and the suspension appears. At higher shearing forces ( $\dot{\gamma} = 0.3\text{--}3\text{ s}^{-1}$ ), a slip against smooth walls of both bob and cup took place preserving the NFC sample flow. The higher shear rates produced the bands, consisting of the flowing and stagnating portions of the suspension.

Obviously, such flow instabilities have a significant impact with regard to the measured rheological properties. To avoid these instabilities, different methods can be used. In Section 2.3.3 the roughening of the cone and plate surfaces was performed to prevent the wall-slip. Another way to avoid the wall-slip is to use a wide-gap vane-in-cup geometry, as proposed by Mohtaschemi *et al.* (2014). When using vane geometry, the NFC suspension is sheared by the blades and the suspension trapped between them, which is believed to avoid the slip at the edge of vane blades and the sample. A wide gap between the vane and cup is necessary to avoid the wall-slip at the cup surface due to the low stress arising at the cup edge (Mohtaschemi *et al.* 2014).



**Figure 2.15** Flow curves together with strain visualization of TEMPO-oxidized NFC suspensions at the concentrations of 0.5 wt.% examined using vane-in-cup geometry



**Figure 2.16** Flow curves together with strain visualization of TEMPO-oxidized NFC suspensions at the concentrations of 1.0 wt.% examined using vane-in-cup geometry

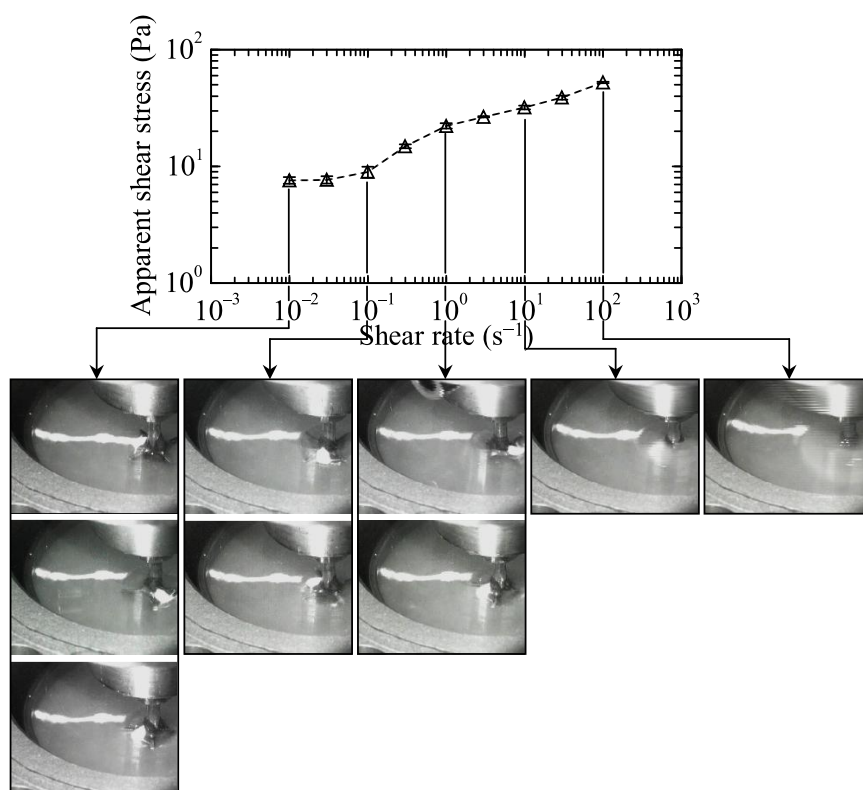


**Figure 2.17** Flow curves together with strain visualization of TEMPO-oxidized NFC suspensions at the concentrations of 1.5 wt.% examined using vane-in-cup geometry

Figures 2.15, 2.16 and 2.17 show the apparent shear stress *vs.* shear rate curves combined with the photographs of the sample deformation for the wide-gap vane-in-cup experiments at different NFC concentration. The use of such geometry was efficient to avoid a slip at vane-sample contact for suspension at a concentration of 0.5 wt.%. However, at low shear rates the flow appears only in a thin volume of the sample close to the vane blades. Only at the shear rate of 100 s<sup>-1</sup> the deformation within all the gap of the geometry was achieved, as seen from Figure 2.15. Therefore, the measurements are representative of the volume property of the sample only after reaching this shear rate.

Similarly to that of Couette geometry, the flow instabilities became more apparent as the NFC concentration increased. Figure 2.16 shows that at a concentration of 1.0 wt.% the stagnating volume of the sample increases for the equivalent strain applied. At low shear rates ( $\dot{\gamma} = 0.01\text{--}0.1\text{ s}^{-1}$ ) an effect resembling a slip occurs. It appears despite the cohesive forces between the NFC suspension, trapped between the blades, and the suspension in the geometry gap (between the edge of the blades and the walls of the cup). The sample fractures at the edge of the vane blades and is not subjected to flowing in the gap of the geometry. With an increase of shear rate, the shear banding transition occurs producing the stationary and flowing portions of the sample.

Figure 2.17 shows the flow curves and the deformation visualization of the NFC suspension at a concentration of 1.5 wt.%. Similar flow instabilities occur as for the suspension at a concentration of 1.0 wt.%; however, the slip is observed for a higher range of shear rates. At the shear rates of 10 and 100 s<sup>-1</sup> only slight volume of the sample is subjected to flow.

It is important to emphasize that these flow instabilities, observed for Couette and vane-in-cup geometries, introduce a strong error in the rheological measurements. The use of wide-gap vane-in-cup geometry prevented the slip effect only for the suspension at a concentration of 0.5 wt.% and was not efficient for 1.0 and 1.5 wt.%. Moreover, strong flow localization occurs affecting the rheological measurements at all the concentrations. Consequently, these measurements should be corrected regarding the true strain of the sample. At the same time, such behavior illustrates the ability of the examined TEMPO-oxidized NFC to slip over the smooth shearing surfaces and to fracture at the specific regions where the strain is accumulated.

The obtained results using vane-in-cup geometries are in contradiction with those reported by Mohtaschemi *et al.* (2014) who tested the TEMPO-oxidized NFC suspensions at the concentrations of 1.0–2.3 wt.%, avoiding the wall-slip. However, the comparisons and speculations in this context appear to be difficult since the visual observations of the sample flow were not reported in the aforementioned work. Moreover, the cellulose sources and the production processes of TEMPO-oxidized NFC are different between the two works, as well as the dimensions of the used geometries.

Roughening of the bob and cup surfaces was performed to compete with the wall-slip by attaching sandpaper. Figures 2.18, 2.19 and 2.20 show the flow curves of the NFC suspensions at different concentrations examined using serrated Couette geometry. As seen from Figure 2.18, this approach was efficient to prevent the slip at the boundary of bob and the suspension at the concentration of 0.5 wt.% due to the cohesive contact. However, some volume of the sample remains undeformed during the experiment and it decreases with the increase of shear rate. At higher NFC concentrations (Figures 2.19 and 2.20) the flow instabilities become more pronounced, similarly to the previous experiments.

The flow curves obtained using Couette and vane-in-cup geometries are compared in Figure 2.21. The measured shear stresses differ significantly at low shear rates and vary less at high ones. The highest stress response at low shear rates is observed when using serrated Couette geometry due to the strong cohesion between the NFC suspension and the geometry tools. The slightly lower stress is measured for the vane-in-cup geometry, which is achieved

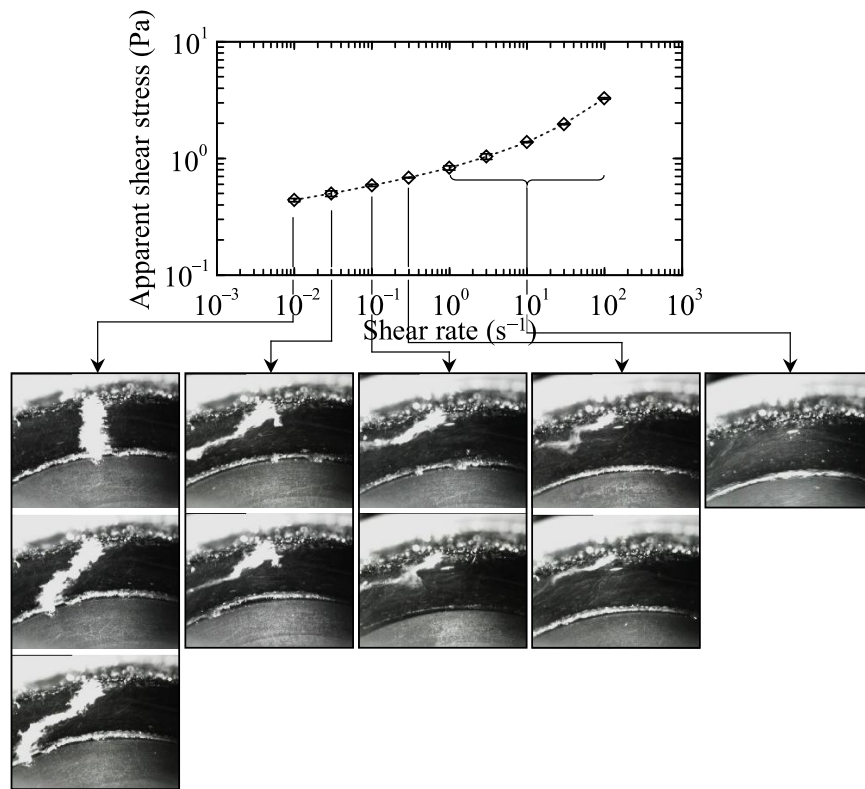


**Figure 2.18** Flow curves together with strain visualization of TEMPO-oxidized NFC suspensions at the concentrations of 0.5 wt.% examined using serrated (roughened) Couette geometry

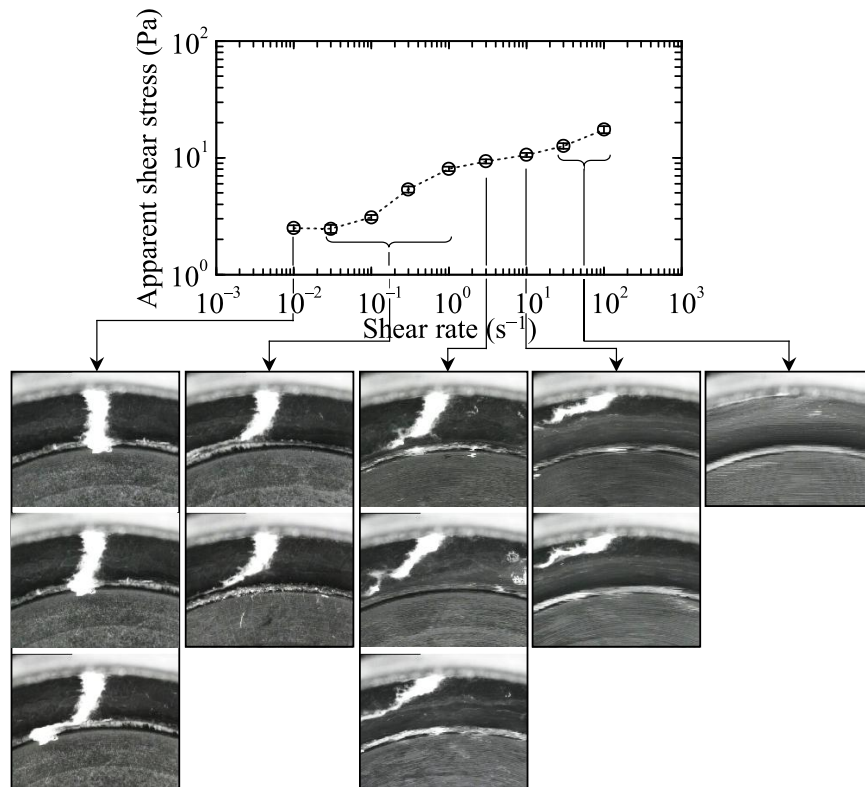


**Figure 2.19** Flow curves together with strain visualization of TEMPO-oxidized NFC suspensions at the concentrations of 1.0 wt.% examined using serrated (roughened) Couette geometry

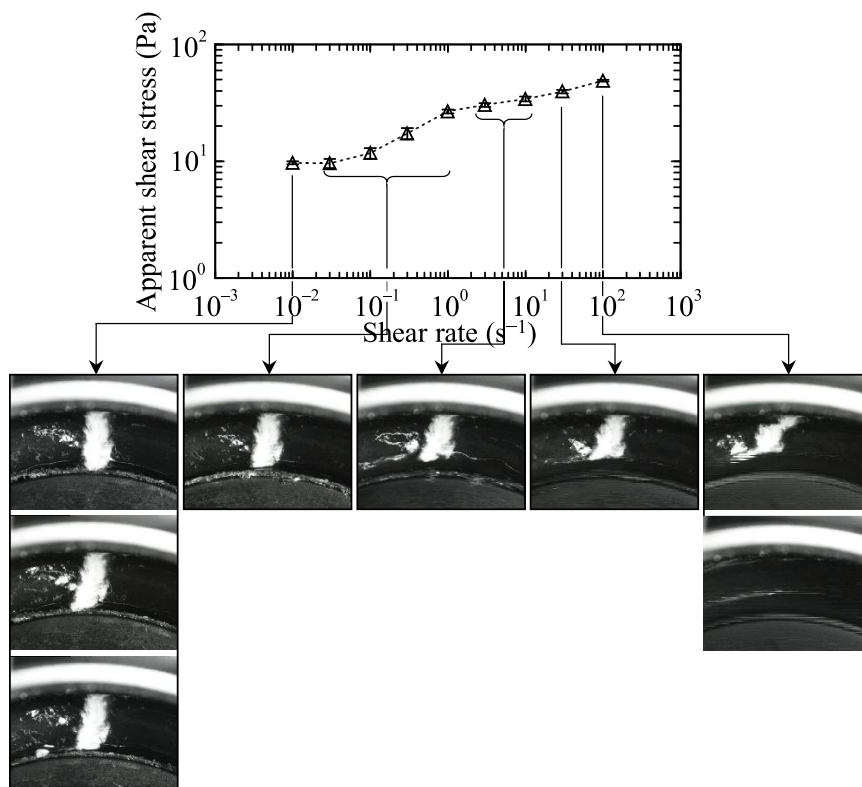


**Figure 2.20** Flow curves together with strain visualization of TEMPO-oxidized NFC suspensions at the concentrations of 1.5 wt.% examined using serrated (roughened) Couette geometry

by the contact at the surface between the suspension located in the gap of the geometry and the one trapped between the blades.

In smooth Couette geometry, the sample is in contact with a smooth bob surface, which makes its slipping easier and results in much lower level of the shear stress. A conspicuous deviation from the other measurements is observed for the 0.5 wt.% NFC suspension measured using vane geometry at a shear rate of  $100 \text{ s}^{-1}$ . Such dramatic increase of the shear stress can occur due to the secondary flows, which are more significant at high shear rates, caused by the specificity of the vane geometry. Such effect can also take place due to the appearance of Taylor-Couette instabilities (Philippe *et al.* 2012) or turbulent flow (Beaumont *et al.* 2013).

Comparing the above results at low shear rates with those of obtained in Section 2.3.3, lower values of shear stress are obtained. This could be explained by the wider geometry gap in Couette and vane-in-cup geometries. At higher shear rates, similar levels of shear stress are achieved for Couette and vane-in-cup, as well as for cone-plate, geometries. In this shear rates range, the samples start to flow; however, the measured stress level is still influenced by the shear banding in the bulk of the sample, which becomes more significant with an increase of NFC concentration.

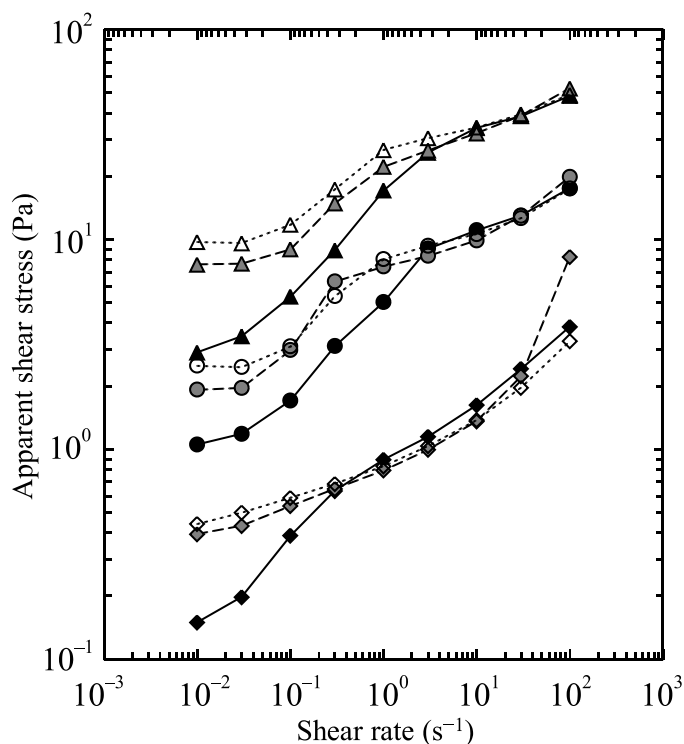


**Figure 2.21** Comparison of the flow curves of TEMPO-oxidized NFC suspensions obtained using smooth Couette (*filled symbols*), roughened Couette (*empty symbols*) and vane-in-cup (*half-filled symbols*) geometries at 0.5 wt.% (*diamonds*); 1.0 wt.% (*circles*) and 1.5 wt.% (*triangles*)

### 2.3.5 SAXS characterization

Figure 2.22a shows the radial average experimental scattering curves of the TEMPO-oxidized NFC suspensions at the concentrations of 0.1 and 0.5 wt.% with the subsequent subtraction of water signal. The curves are obtained by radial integration of two-dimensional (2D) SAXS patterns, as shown in Figure 2.22b. The scattering intensities display a decline on the whole range of scattering vector. No influence of the NFC concentration on the shape of the curves is observed. Thus, there might be no influence on the interparticle interactions within the analyzed concentration range. The curves represent the scattering information about the suspension elements at different magnifications: at low  $q$  the signal arises from the whole scattering objects and at high  $q$  it reflects their interfacial features.

The linear domains can be detected from the scattering curves, where the scattering intensity can fit the power law as specified in Eq. 2.7, which can give information about the structural organization of nanofibrils in the suspension.  $D = 3$  is a characteristic fractal dimension coming from rough surfaces, indicating that large objects are detected, *e.g.*, partially disintegrated fibers, with aggregated or entangled structure (Duijneveldt *et al.* 2005). At higher scattering vector there is a slope where  $D = 5/3$ , which is a characteristic fractal dimension of swollen worm-like elements. It may represent the individual nanofibrils and

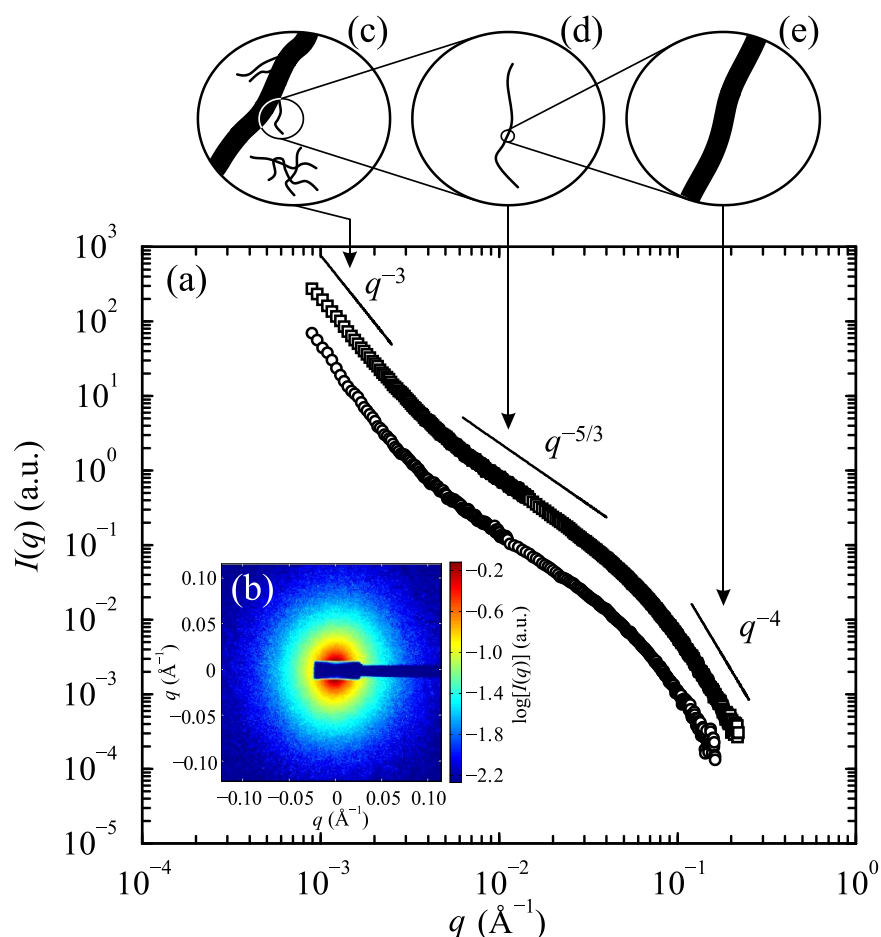


**Figure 2.22** SAXS characterization of TEMPO-oxidized NFC suspensions: (a) scattering intensity as a function of scattering vector for suspensions at the concentrations of: 0.5 wt.% ( $\square$ ) and 0.1 wt.% ( $\circ$ ); (b) typical two-dimensional SAXS pattern of the examined NFC suspensions; (c–e) schematic representation of the structures yielding the scattering signal

determine their curvature.  $D = 4$  (Porod law) indicates the non-fractal objects with smooth and well-defined interfaces, which is likely to appear from nanofibril interfaces. Each linear domain is preceded by a “shoulder”, representing the Guinier regime, which yields the size of the scattering objects. The Guinier regime located prior to the power-law regime with  $D = 3$  is out of the measured range of scattering vector and is not represented on Figure 2.22.

Thus, three structural levels can be determined from the experimental scattering data: (i) the first, originates from nanofibril surfaces, as shown in Figure 2.22e; (ii) the second, appears from individual nanofibrils, Figure 2.22d, and (iii) the third level, arises from partly disintegrated fibers or entanglements of the nanofibrils, Figure 2.22c. Each structural level consists of Guinier and power-law regimes.

Two Guinier approximations can be verified at the first two structural levels as indicated in Figure 2.22e and Figure 2.22d. By drawing the Guinier plots,  $R_{gc}$  and  $R_g$  may be deduced from the linear dependencies. Figure 2.23 does not show explicit linear regimes at Guinier

plots, which makes it impossible to extract the information concerning the size of nanofibrils from Guinier approximations. This indicates that the system is polydisperse with continuous size distribution of particles diameter and length. The polydispersity of the examined NFC can also be confirmed by microscopic measurements, which indicated the presence of the residual non-fibrillated fibers, as previously reported in Section 1.3.3. The aggregation of the nanofibrils is also expected due to hydrogen bonding. Moreover, the experiments were performed at pH of 7.0. Therefore, by increasing the pH, the concentration of carboxylate ions can be increased which would result in stronger electrostatic repulsion between the nanofibrils and possible decrease of aggregation.

The above Guinier approximation approach is applied when the interparticle interactions can be neglected. Otherwise, other methods should be used, *e.g.*, generalized indirect Fourier transformation (GIFT), which allow the separation of inter- and intraparticle effects (Fritz *et al.* 2000). Such approach was already reported for suspensions of cellulose nanocrystals (Ehmann *et al.* 2013).

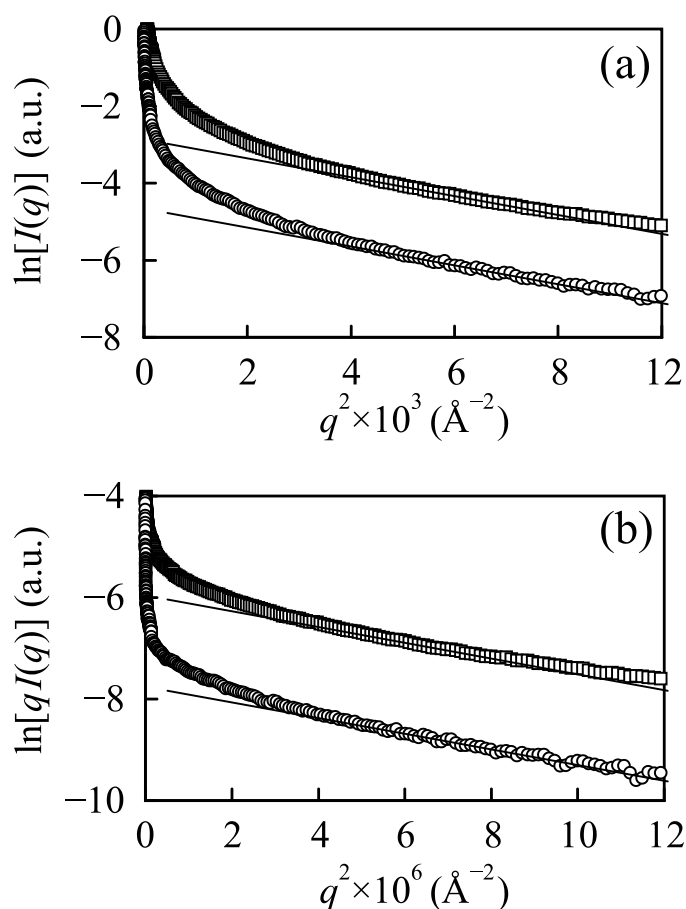


**Figure 2.23** Guinier approximations at (a) the second structural level representing the information arising from the individual nanofibrils in suspension and (b) the first structural level representing the scattering from the nanofibril cross sections, at the concentrations of: 0.5 wt.% ( $\square$ ) and 0.1 wt.% ( $\circ$ ). Straight lines are presented to show the non-linearity of the Guinier plots

In this work, the unified fit function approach was used to characterize NFC suspensions at different structural levels and to extract the average diameter of nanofibrils. Figure 2.24 shows the unified fit to the experimental data for the NFC suspension at the concentration of 0.5 wt.% and the scattering functions from the local levels. The unified fit allows distinguishing the Guinier regions where considerable overlapping with power-law regions takes place. At the first structural level, the power-law region is quite short to perform the accurate analysis and to determine the exact power law decay. Thus, the  $q$  range should be increased for more accurate analysis. Nevertheless, knowing that the analyzed material is fibrous, we can reasonably expect the power law decay with  $P_1 = 4$ . The third structural level is represented only by the power-law regime with  $P_3 = 2.937$ . To detect the Guinier regime at this level, the measurements at lower  $q$ , hence, higher sample-to-detector distance, should be performed.

The analyzed system consists of the nanofibrils that are flexible and curved, differing from the rod-like elements. Thus, the length of the nanofibrils cannot be extracted according to the Eq. 2.14. However, based on the scattering intensity originating from the nanofibrils cross section, using Eq. 2.13, the nanofibrils diameter ( $d = 2r$ ) was calculated as 4.8 nm. This value represents the statistical average diameter of nanofibrils swollen in water and is in the

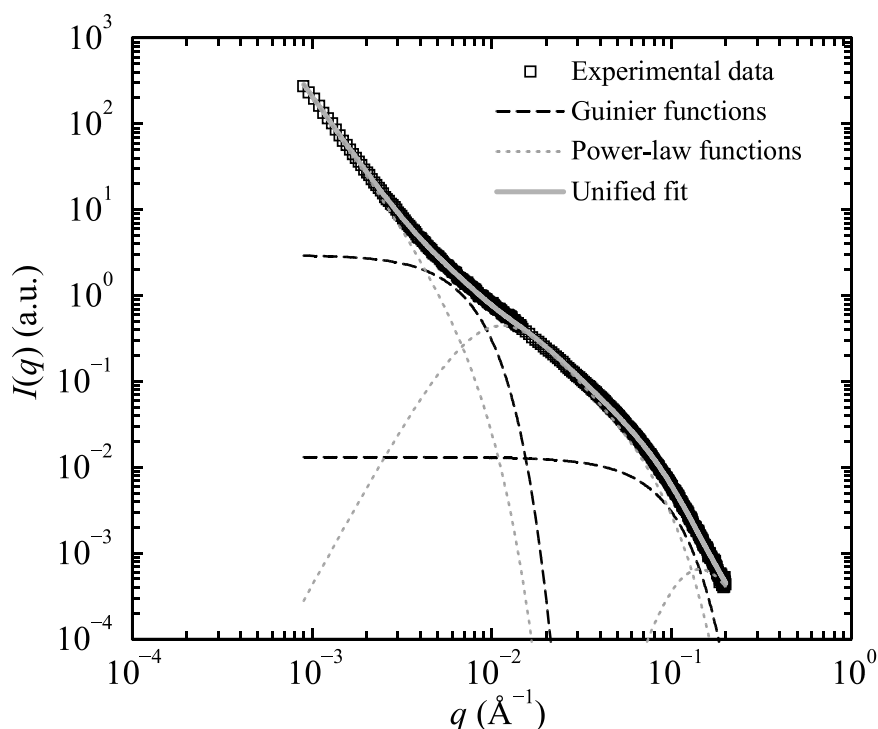


**Figure 2.24** The unified fit function (*bold solid gray line*) to the experimental scattering data ( $\square$ ) of the NFC suspension at the concentration of 0.5 wt.% and the local scattering laws (*dashed lines*). The parameters of the local laws:  $G_1 = 0.01312$ ;  $G_2 = 2.977$ ;  $R_{g,1} = 21.01 \text{ \AA}$ ;  $R_{g,2} = 262.4 \text{ \AA}$ ;  $B_1 = 7.68 \times 10^{-7}$ ;  $B_2 = 1.46 \times 10^{-4}$ ;  $B_3 = 3.27 \times 10^{-7}$ ;  $P_1 = 4$ ;  $P_2 = 1.912$ ;  $P_3 = 2.937$ .

---

range of  $4 \pm 2$  nm, as established previously based on AFM height images (see Section 1.3.3). It is worth noting that using AFM the nanofibrils are analyzed in the dry state, which can yield slightly lower diameter due to the nanofibrils shrinkage while drying. However, SAXS measurements allow determining the average diameter of nanofibrils swollen in water.

## Conclusions

This chapter focuses on the characterization of the NFC aqueous suspensions using rheometry and SAXS techniques. An extensive rheological study of the NFC suspensions in oscillation and steady-state flow modes was performed. All the suspensions exhibited gel-like, shear-thinning properties. It was shown that the concentration and the type of applied enzymes have an influence on the rheological behavior of the tested suspensions. The dynamic moduli as well as the apparent viscosity and shear stress decreased with the increase of enzymatic charge which is likely to occur due to cellulose saccharification together with nanofibril separation. The NFC obtained from TEMPO-mediated oxidation resulted into stronger fibrous network, which was confirmed by smaller nanofibril dimensions, as observed using microscopy techniques in Section 1.3.3.

As far as the authors of this work are aware, it is the first study devoted to the investigation of the wall-slip and shear banding phenomena in NFC suspensions using visualization approach. When using the smooth cone-plate geometries, the flow instabilities were detected by flow observation. A wall-slip took place at wide range of shear rates for two types of NFC suspensions: those produced using enzymatic and those resulting from TEMPO-mediated oxidation pretreatments. Therefore, the obtained values are considered to comprise an error, introduced by the wall-slip. To prevent this phenomenon the roughening of the geometry tools was performed. It resulted in more accurate measurements for TEMPO-oxidized NFC suspension. The use of serrated tools did not prevent the wall-slip of enzymatically-pretreated NFC.

TEMPO-oxidized NFC suspensions at different concentrations were studied using rheometry and SAXS techniques. The flow instabilities were demonstrated for Couette and vane-in-cup geometries when using the visualization technique. The experiments performed using Couette geometry showed that the use of serrated geometry surfaces is necessary to compete with the wall-slip but it is not sufficient to prevent it completely. These findings were compared to other data previously obtained with cone-plate geometries. The use of vane provokes a fracture of the suspension at the edge of the blades resembling to the slip. It is obvious, that the slip is more crucial with an increase of the solid content in the suspension. The flow behavior depends strongly on the used geometry at low shear rates, where the wall-slip plays a significant role. However, at high shear rates the influence of the used geometry is neutralized, resulting in similar values of shear stress. Serrated Couette appeared as the most

---

suitable geometry (among the tested ones) for the rheological measurements of NFC suspensions.

The polydispersity of the studied NFC was confirmed using SAXS analysis. It was shown that Guinier approximation is not effective to extract the size characteristics. However, the average diameter of nanofibrils in water was determined based on the scattering data using unified fit function approach.

## References

- Agoda-Tandjawa G, Durand S, Berot S, Blassel C, Gaillard C, Garnier C, Doublier JL (2010) Rheological characterization of microfibrillated cellulose suspensions after freezing. *Carbohydr Polym*, 80:677-686. doi: 10.1016/j.carbpol.2009.11.045.
- Baravian C, Lalante A, Parker A (2002) Vane rheometry with a large, finite gap. *Appl Rheol* 12:81-87. doi: 10.3933/ApplRheol-12-81.
- Barnes HA (1995) A review of the slip (wall depletion) of polymer solutions, emulsions and particle suspensions in viscometers: Its cause, character, and cure. *Journal of Non-Newtonian Fluid Mechanics* 56:221–251. Doi: 10.1016/0377-0257(94)01282-M.
- Beaucage G (1995) Approximations Leading to a Unified Exponential/Power-Law Approach to Small-Angle Scattering. *J Appl Cryst* 28:717–728. doi: 10.1107/S0021889895005292.
- Beaucage G (1996) Small-Angle Scattering from Polymeric Mass Fractals of Arbitrary Mass-Fractal Dimension. *J Appl Cryst* 29:134–146. doi: 10.1107/S0021889895011605.
- Beaucage G (2012) Combined Small-Angle Scattering for Characterization of Hierarchically Structured Polymer Systems over Nano-to-Micron Meter: Part II Theory. In: Matyjaszewski K and Möller M (eds.) *Polymer Science: A Comprehensive Reference*, Vol 2, pp. 399–409. Amsterdam: Elsevier BV.
- Beaumont J, Louvet N, Divoux T, Fardin M-A, Bodiguel H, Lerouge S, Manneville S, Colin A (2013) Turbulent flows in highly elastic wormlike micelles. *Soft Matter* 9:735. doi: 10.1039/c2sm26760h.
- Benhamou K, Dufresne A, Magnin A, Mortha G, Kaddami H (2014) Control of size and viscoelastic properties of nanofibrillated cellulose from palm tree by varying the TEMPO-mediated oxidation time. *Carbohydr Polym* 99:74–83. doi: 10.1016/j.carbpol.2013.08.032.
- Besbes I, Magnin A, Boufi S (2011) Rheological behavior of nanofibrillated cellulose/acrylic polymer nanocomposites: Effect of melt extrusion. *Polym Compos* 32:2070–2075. doi: 10.1002/pc.21232.
- Bonini C, Heux L, Cavallé J-Y, Lindner P, Dewhurst C, Terech P (2002) Rodlike Cellulose Whiskers Coated with Surfactant: A Small-Angle Neutron Scattering Characterization. *Langmuir* 18:3311–3314. doi: 10.1021/la015511t.

- Buscall R, McGowan JI, Morton-Jones AJ (1993) The rheology of concentrated dispersions of weakly attracting colloidal particles with and without wall slip. *Journal of Rheology* (1978-Present), 37:621–641. doi: 10.1122/1.550387.
- Charani PR, Dehghani-Firouzabadi M, Afra E, Shakeri A (2013) Rheological characterization of high concentrated MFC gel from kenaf unbleached pulp. *Cellulos* 20:727–740. doi: 10.1007/s10570-013-9862-1.
- Chen P, Yu H, Liu Y, Chen W, Wang X, Ouyang M (2013) Concentration effects on the isolation and dynamic rheological behavior of cellulose nanofibers via ultrasonic processing. *Cellulose* 20:149–157. doi: 10.1007/s10570-012-9829-7.
- Dimic-Misic K, Puisto A, Gane P, Nieminen K, Alava M, Paltakari J, Maloney T (2013) The role of MFC/NFC swelling in the rheological behavior and dewatering of high consistency furnishes. *Cellulos* 20:2847–2861. doi: 10.1007/s10570-013-0076-3.
- Dinand E, Chanzy H, Vignon MR (1996) Parenchymal cell cellulose from sugar beet pulp: preparation and properties. *Cellulose* 3:183–188. doi:10.1007/BF02228800.
- Duijneveldt JS van, Klein S, Leach E, Pizzey C, Richardson RM (2005) Large scale structures in liquid crystal/clay colloids. *J Phys: Condens Matter* 17:2255. doi: 10.1088/0953-8984/17/15/001.
- Ehmann HMA, Spirk S, Doliška A, et al (2013) Generalized Indirect Fourier Transformation as a Valuable Tool for the Structural Characterization of Aqueous Nanocrystalline Cellulose Suspensions by Small Angle X-ray Scattering. *Langmuir* 29:3740–3748. doi: 10.1021/la303122b.
- Elazzouzi-Hafraoui S, Nishiyama Y, Putaux J-L, Heux L, Dubreuil F, Rochas C (2008) The Shape and Size Distribution of Crystalline Nanoparticles Prepared by Acid Hydrolysis of Native Cellulose. *Biomacromol* 9:57–65. doi: 10.1021/bm700769p.
- Estellé P, Lanos C, Perrot A, Amziane S (2008) Processing the vane shear flow data from Couette analogy. *Appl Rheol* 18:34037–34481. doi: 10.3933/ApplRheol-18-34037.
- Fardin M-A, Lerouge S (2012) Instabilities in wormlike micelle systems. *Eur Phys J E* 35:1–29. doi: 10.1140/epje/i2012-12091-0.
- Fritz G, Bergmann A, Glatter O (2000) Evaluation of small-angle scattering data of charged particles using the generalized indirect Fourier transformation technique. *J Chem Phys* 113:9733–9740. doi: 10.1063/1.1321770.

- Glatter O and Kratky O (1982) *Small-angle X-ray Scattering*. Academic Press, London. Chapters 2.IV; 8.III.
- Grüneberger F, Künniger T, Zimmermann T, Arnold M (2014) Rheology of nanofibrillated cellulose/acrylate systems for coating applications. *Cellul* 21:1313–1326. doi: 10.1007/s10570-014-0248-9.
- Herrick FW, Casebier RL, Hamilton JK, Sandberg KR (1983) Microfibrillated Cellulose: Morphology, and Accessibility. In Sarko A (ed) *Proceedings of the Ninth Cellulose Conference*, Appl Polym Symp, 37. Wiley, New York, pp 797–813.
- Ilavsky J, Jemian PR (2009) Irena: tool suite for modeling and analysis of small-angle scattering. *J Appl Cryst* 42:347–353. doi: 10.1107/S0021889809002222.
- Iotti M, Gregersen ØW, Moe S, Lenes M (2011) Rheological Studies of Microfibrillar Cellulose Water Dispersions. *J Polym Environ* 19:137–145. doi:10.1007/s10924-010-0248-2.
- Ishii D, Saito T, Isogai A (2011) Viscoelastic Evaluation of Average Length of Cellulose Nanofibers Prepared by TEMPO-Mediated Oxidation. *Biomacromol* 12:548–550. doi: 10.1021/bm1013876.
- Karppinen A, Saarinen T, Salmela J, Laukkanen A, Nuopponen M, Seppälä J (2012) Flocculation of microfibrillated cellulose in shear flow. *Cellulose* 19:1807–1819. doi: 10.1007/s10570-012-9766-5.
- Klemm D, Kramer F, Moritz S, *et al.* (2011) Nanocelluloses: A New Family of Nature-Based Materials. *Angew Chem Int Ed* 50:5438–5466. doi: 10.1002/anie.201001273.
- Lasseguette E, Roux D, Nishiyama Y (2008) Rheological properties of microfibrillar suspension of TEMPO-oxidized pulp. *Cellul* 15:425–433. doi: 10.1007/s10570-007-9184-2.
- Leppänen K, Pirkkalainen K, Penttilä P, Sievänen J, Kotelnikova N, Serimaa R (2010) Small-angle x-ray scattering study on the structure of microcrystalline and nanofibrillated cellulose. *J Phys: Conf Ser* 247:012030. doi: 10.1088/1742-6596/247/1/012030.
- Lowys M-P, Desbrières J, Rinaudo M (2001) Rheological characterization of cellulosic microfibril suspensions. Role of polymeric additives. *Food Hydrocolloids* 15:25–32. doi: 10.1016/S0268-005X(00)00046-1.

- Malkin AI, Malkin AY, Isayev AI (2006) *Rheology: Concepts, Methods & Applications*. ChemTec Publishing.
- Martoia F, Perge C, Dumont PJJ, Orgéas L, Fardin MA, Manneville S, Belgacem MN (2015) Heterogeneous flow kinematics of cellulose nanofibril suspensions under shear. *Soft Matter* 11:4742–4755. doi: 10.1039/C5SM00530B.
- Mohtaschemi M, Dimic-Misic K, Puisto A, Korhonen M, Maloney T, Paltakari J, Alava MJ (2014) Rheological characterization of fibrillated cellulose suspensions via bucket vane viscometer. *Cellul* 21:1305-1312. doi: 10.1007/s10570-014-0235-1.
- Naderi A, Lindström T, Sundström J (2014) Carboxymethylated nanofibrillated cellulose: rheological studies. *Cellul* 21:1561–1571. doi: 10.1007/s10570-014-0192-8.
- Olmsted PD (2008) Perspectives on shear banding in complex fluids. *Rheol Acta* 47:283–300. doi: 10.1007/s00397-008-0260-9.
- Pääkkö M, Ankerfors M, Kosonen H, Nykänen A, Ahola S, Österberg M, Ruokolainen J, Laine J, Larsson PT, Ikkala O, Lindström T (2007) Enzymatic Hydrolysis Combined with Mechanical Shearing and High-Pressure Homogenization for Nanoscale Cellulose Fibrils and Strong Gels. *Biomacromol* 8:1934–1941. doi: 10.1021/bm061215p.
- Pahimanolis N, Hippi U, Johansson L-S, Saarinen T, Houbenov N, Ruokolainen J, Seppälä J (2011) Surface functionalization of nanofibrillated cellulose using click-chemistry approach in aqueous media. *Cellulose* 18:1201–1212. doi: 10.1007/s10570-011-9573-4.
- Penttilä PA, Várnai A, Fernández M, Kontro I, Liljeström V, Lindner P, Siika-aho M, Viikari L, Serimaa R (2013) Small-angle scattering study of structural changes in the microfibril network of nanocellulose during enzymatic hydrolysis. *Cellul* 20:1031–1040. doi: 10.1007/s10570-013-9899-1.
- Philippe AM, Baravian C, Jenny M, Meneau F, Michot LJ (2012) Taylor-Couette Instability in Anisotropic Clay Suspensions Measured Using Small-Angle X-ray Scattering. *Phys Rev Lett* 108:254501. doi: 10.1103/PhysRevLett.108.254501.
- Pignon F, Magnin A, Piau J-M (1996) Thixotropic colloidal suspensions and flow curves with minimum: Identification of flow regimes and rheometric consequences. *Journal of Rheology*, 40(4), 573–587. doi:10.1122/1.550759.
- Puisto A, Illa X, Mohtaschemi M, Alava M (2012) Modeling the rheology of nanocellulose suspensions. *Nord Pulp Pap Res J* 27:277–281.

- Saarikoski E, Saarinen T, Salmela J, Seppälä J (2012) Flocculated flow of microfibrillated cellulose water suspensions: an imaging approach for characterisation of rheological behaviour. *Cellul* 19:647–659. doi: 10.1007/s10570-012-9661-0.
- Saarinen T, Lille M, Seppälä J (2009) Technical Aspects on Rheological Characterization of Microfibrillar Cellulose Water Suspensions. *Annu Trans Nord Rheol Soc* 17:121–130.
- Saito T, Kimura S, Nishiyama Y, Isogai A (2007) Cellulose Nanofibers Prepared by TEMPO-Mediated Oxidation of Native Cellulose. *Biomacromol* 8:2485–2491. doi: 10.1021/bm0703970.
- Shogren RL, Peterson SC, Evans KO, Kenar JA (2011) Preparation and characterization of cellulose gels from corn cobs. *Carbohydr Polym* 86:1351–1357. doi: 10.1016/j.carbpol.2011.06.035.
- Su Y, Burger C, Hsiao BS, Chu B (2014) Characterization of TEMPO-oxidized cellulose nanofibers in aqueous suspension by small-angle X-ray scattering. *Journal of Applied Crystallography* 47:788–798. doi: 10.1107/S1600576714005020.
- Terech P, Chazeau L, Cavaille JY (1999) A Small-Angle Scattering Study of Cellulose Whiskers in Aqueous Suspensions. *Macromol* 32:1872–1875. doi: 10.1021/ma9810621.
- Turbak AF, Snyder FW, Sandberg KR (1983) Microfibrillated Cellulose, a New Cellulose Product: Properties, Uses, and Commercial Potential. In Sarko A (ed) *Proceedings of the Ninth Cellulose Conference*. *Appl Polym Symp* 37. N.Y.: Wiley. pp. 815–827.

# Chapter 3 Composites production from nanofibrillated cellulose and latex

## Introduction

Nowadays, the development of bio-based composite materials for different industrial applications is a frequent research subject. Much research has been performed on the use of natural fibers in composites as an alternative to synthetic organic and inorganic fillers (*e.g.*, aramid, carbon or glass fibers), which are widely used to reinforce thermoplastic matrices. Numerous reviews on the progress in this field are available (Saheb and Jog 1999; George *et al.* 2001; Kalia *et al.* 2009). Comparing to conventional composites, the nanocomposite materials have a number of advantages, *e.g.*, their better thermal, mechanical and barrier characteristics at low filler content, as well as their low weight and transparency (in the absence of chromophores in its chemical structure) (Oksman *et al.* 2006; Moon *et al.* 2011).

This chapter describes the production and characterization of bionanocomposite materials based on latex matrix and cellulose nanofibers filler. The composites were produced by incorporating TEMPO-oxidized nanofibrillated cellulose (NFC) into the poly[styrene-*co*-(2-ethylhexyl acrylate)] latex, synthesized *via* miniemulsion polymerization, to achieve the reinforcement effect. The role of cationic and anionic surfactants was analyzed in order to have a clear-cut evidence of the homogeneity of the NFC dispersion within the latex and the quality of the NFC/matrix interface after film casting. The quality of NFC dispersion in the matrix was analyzed using FEG-SEM. The mechanical properties of the ensuing composites were particularly addressed.

## 3.1 State of the art

### 3.1.1 Composites

Composites are materials made from two or more constituents, which in spite of remaining distinct when combined form a single component. There are two types of such constituents: matrix and filler. Fillers are commonly used to impart the specific properties (*e.g.*, mechanical, barrier) to the surrounding matrix, as well as to reduce the composite price. The filler is often considered as reinforcement when it is a stiff component embedded in a relatively soft matrix. Consequently, the composite possesses mechanical properties between those of the filler and the matrix (Dufresne 2008).

Composites can be distinguished into 3 categories according to the matrix type: (i) polymer matrix composites, (ii) metal matrix composites and (iii) ceramic matrix composites. In polymer matrix composites the typical objective of the filler incorporation is to achieve the reinforcement effect, while in metal matrix composites, the issues of high-temperature performance and tribological properties are often addressed. Regarding ceramic matrix composites, the main goal of the reinforcement is to improve the toughness of the matrix, which is brittle (Miao and Hamad 2013). This dissertation deals with polymer matrix composites only.

The reinforcing elements used in composites can be divided into the following types based on their structural aspect: woven, continuous fibers, short fibers and particles. Morphologically they can be classified as macroscopic, microscopic or nanoscopic according to their physical size (Miao and Hamad 2013). Comparing to classical composite materials, where macro- and microscopic reinforcement is used, the nanocomposites have at least one constituent phase with at least one dimension in the nanometer scale (lower than 100 nm; thus, smaller than the wavelength range of visible light). Typically, reinforcing nanofibers with high aspect ratio are used. This particular feature provides nanocomposites with unique and outstanding properties never found in the conventional composites (Siqueira *et al.* 2010).

The mechanical properties of polymer composites depend on several factors: (i) matrix properties, (ii) filler properties, (iii) matrix-filler interactions and (vi) quality of filler dispersion within the matrix for fiber-reinforced systems. The most common matrix-filler interactions are van der Waals forces; however, others include: covalent bonds, electrostatic forces, molecular entanglement and mechanical interlocking (Miao and Hamad 2013).

### 3.1.2 Nanofibrillated cellulose composites

Due to specific properties of nanocellulose, *e.g.*, high stiffness, low density, abundant feedstocks, optical properties, biodegradability and renewability, this family of nanomaterials is getting much interest for their use as filler in polymer composites. Regarding the wood-derived nanocellulose, CNC has much higher mechanical properties comparing to NFC, as discussed in Section 1.1.3.5. However, its production yield is much lower than that of NFC due to the dissolution of cellulose amorphous domains during the production process. Thereby, the use of NFC in polymer matrix composites was selected as the scope of this dissertation.

NFC can be employed in composites with large variety of polymer matrices. Figure 3.1 shows the classification of the composites produced from NFC based on the used matrix (adapted and complemented from Siró and Plackett 2010). However, this list may be incomplete, due to the obvious complexity to cover all the publications relative to this field.

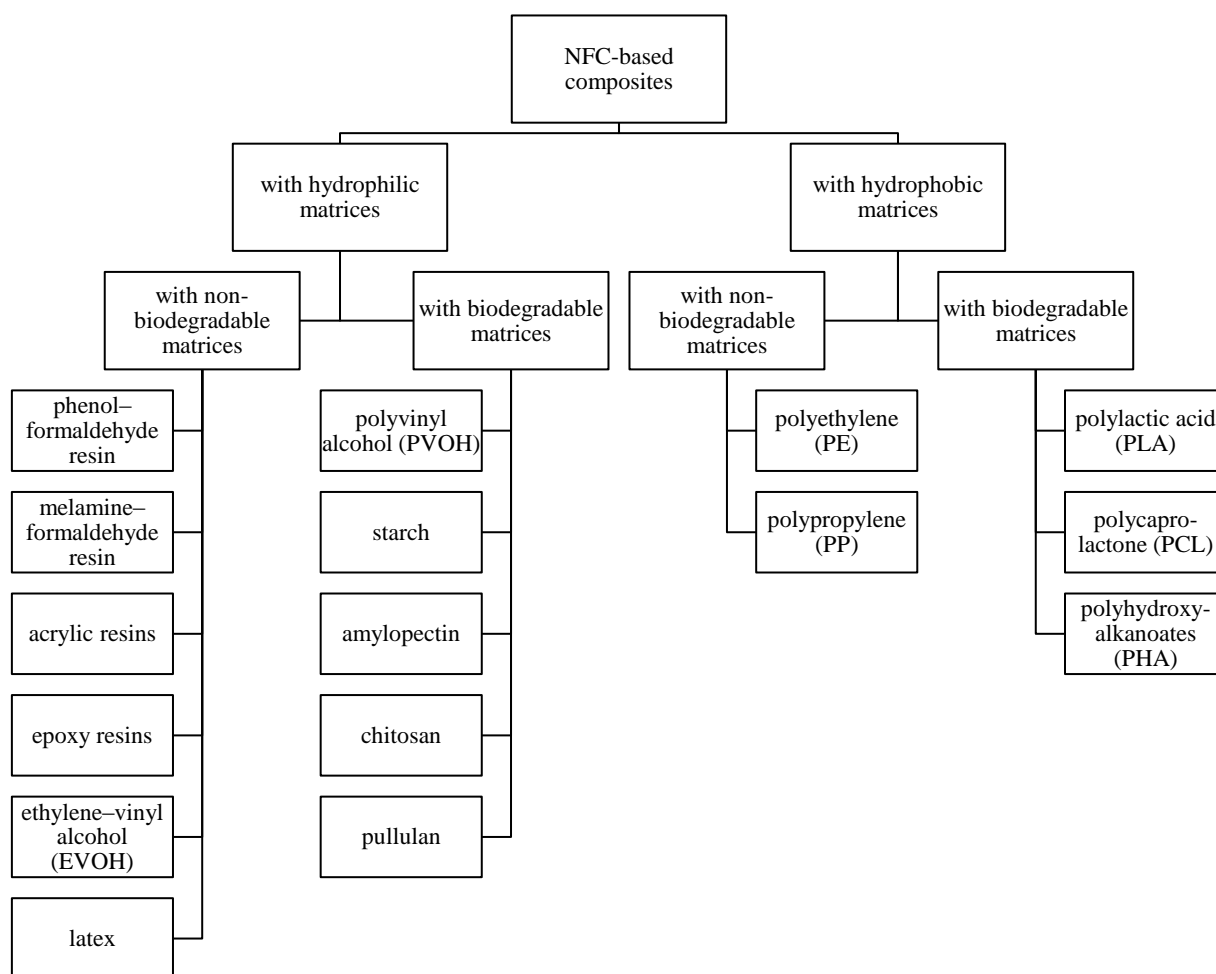


**Figure 3.1** Classification of composites produced from NFC depending on the used matrix

One of the NFC properties is its hydrophilic character, which makes it compatible with hydrophilic matrices but poorly compatible with hydrophobic ones. Cellulose has also some other drawbacks, *e.g.*, sensitivity to moisture and limited processing temperature of around 200 °C. However, due to the high ability of cellulose surface modification, these disadvantages can be overcome to some extent. Different methods of cellulose surface chemical modification have been reported, *e.g.*, silylation, esterification, cationisation, TEMPO-mediated oxidation, polymer grafting (Hubbe *et al.* 2008; Siqueira *et al.* 2010; Missoum *et al.* 2012; Ben Mabrouk *et al.* 2013; Kalia *et al.* 2014).

### 3.1.2.1 Hydrophilic matrices

**Phenol–formaldehyde resin.** As indicated above, many studies were devoted to composites with hydrophilic matrices due to the hydrophilicity of NFC. Nakagaito and Yano (2004) studied the mechanical properties of phenol–formaldehyde resin reinforced with kraft wood pulp/NFC at different degrees of fibrillation, achieved using refining and high pressure homogenization treatments. In order to produce the composites, the cellulose suspensions were vacuum filtered, dried and subsequently impregnated with the selected resin followed by drying and hot pressing. The increase of composite mechanical properties (bending strength) was reported while increasing the degree of fibrillation after certain level of refining (16 passes). Till this point, refining treatment did not improve the composite strength as compared to that based on non-refined pulp. After progressive high pressure homogenization of cellulose suspensions, the composite strength increased linearly and reached maximum values at 14 passes.

Later, Nakagaito and Yano (2008) reported the use of sodium hydroxide-treated NFC in phenol–formaldehyde resin to enhance the toughness of composites comparing to that of untreated NFC and cellulose pulp. Leitner *et al.* (2007) used NFC from sugar beet pulp and Qing *et al.* (2012, 2013) employed TEMPO-oxidized NFC from wood in phenol–formaldehyde resin composites.

**Melamine–formaldehyde resin.** Henriksson and Berglund (2007) prepared composites of NFC and melamine–formaldehyde resin. NFC suspensions were vacuum filtered, dried and impregnated into water solutions of melamine–formaldehyde at different concentrations to vary the matrix content in the NFC mat. Finally, the composites were dried and cured by hot pressing. It was shown that by controlling the composition, nanocomposites with elastic modulus as high as 16.6 GPa and tensile strength as high as 142 MPa can be obtained. Such composite has a potential for use in loudspeaker membranes.

**Acrylic and epoxy resins.** Iwamoto *et al.* (2005) described the use of NFC and BNC as a reinforcement agent for optically transparent (translucent) acrylic resin composites. Such optical properties were achieved even at high nanocellulose contents, *e.g.*, 70 wt.%. The use of NFC was shown to have reinforcing effect as well as to reduce the value of thermal expansion coefficient of the composite to one-fifth of that of the neat acrylic resin. The low coefficient of thermal expansion combined with high mechanical properties makes NFC favorable for the use in roll-to-roll production technologies (*e.g.*, manufacturing of flexible displays, solar cells, electronic paper and panel sensors) (Nogi and Yano 2008; Nakagaito *et al.* 2010).

The preparation of composites based on NFC from vegetable pulp (swede root) and different types of acrylic and epoxy resins was reported by Bruce *et al.* (2005). All the produced composites possessed higher stiffness and strength comparing to neat matrix. Lee *et al.* (2012) compared the use of NFC and BNC for the reinforcement of epoxy resin. No significant difference between NFC and BNC composites was observed. An elastic modulus and strength of  $\sim 8$  GPa and  $\sim 100$  MPa, respectively, were obtained at fiber volume fraction of 60 vol.% comparing to 3 GPa and 70 MPa of the neat matrix.

Other works were published on the use of acrylic resins (Uetani and Yano 2011; Okahisa *et al.* 2011) or epoxy resins (Shimazaki *et al.* 2007, Masoodi *et al.* 2012) as a matrix in NFC-based composites.

**Ethylene vinyl alcohol.** Fernández *et al.* (2008) reported the production of composites by casting of ethylene vinyl alcohol copolymers (EVOH29 and EVOH44) dissolved in isopropanol/water (70/30) and NFC dispersed therein. The addition of NFC preserved the transparency of EVOH-based composite films but resulted in the decrease of water barrier properties. NFC was not distinguished in the matrix using SEM, indicating the good nanofibrils dispersion within the matrix, which was also confirmed by optical microscopy and AFM.

**Latex.** As an alternative to water soluble polymer matrixes, NFC can be incorporated into waterborne latexes (stable dispersions of polymer particles in an aqueous medium). The production and properties of composites from NFC and latex are reviewed in Section 3.1.3.

**Polyvinyl alcohol.** A number of studies on reinforcing of polyvinyl alcohol (PVOH) with NFC have been reported (Zimmermann *et al.* 2004; Bhatnagar and Sain 2005; Leitner *et al.* 2007; Wang and Sain 2007a; Lu *et al.* 2008; Srithep *et al.* 2012; Virtanen *et al.* 2014; Zhai *et al.* 2015). Zimmermann *et al.* (2004) produced the composites by mixing NFC aqueous

suspensions with PVOH followed by casting. The nanocomposites with cellulose content up till 10 wt.% were produced. An increase of both elastic modulus up to 2.5 times and tensile strength up to 5 times was reported comparing to the neat matrix. Bhatnagar and Sain (2005) described the use of NFC produced from various sources, such as flax bast fibers, hemp fibers, kraft pulp, and rutabaga, to reinforce PVOH polymer. Films with NFC content of 10% were obtained. Both tensile strength and elastic modulus were improved compared to the neat matrix.

Virtanen *et al.* (2014) described the use of surface-modified NFC as reinforcement in PVOH. They also worked with epoxy-NFC with different degrees of substitution. The results showed the favorable effect of NFC surface modification on the improvement of composite mechanical properties compared to the unmodified NFC.

**Starch.** Native starch or thermoplastic starch (plasticized, e.g., with water, glycerol and sorbitol, and subjected to heat and shear) is a bio-based and biodegradable polymer. Comparing to conventional polymers, starch suffers from high water uptake and poor mechanical properties. To overcome these disadvantages, NFC was reported to be incorporated into starch matrixes (Siró and Plackett 2010).

Dufresne and Vignon (1998) reported the incorporation of potato NFC and glycerol in potato starch matrix in order to improve its thermomechanical properties and to decrease its water sensitivity, preserving its biodegradability. The elastic modulus of 7 GPa at 50 wt.% NFC content was obtained for the composite comparing to 2 GPa for the neat starch matrix. However, such reinforcing effect was strongly reduced after composites conditioning at high relative humidity (70% RH). Moreover, the addition of NFC resulted in the decrease of both equilibrium water uptake and water diffusion coefficient.

Alemdar and Sain (2008) described the production of bionanocomposites from wheat straw NFC and thermoplastic starch by solution casting method. The tensile strength and elastic modulus of the composites increased significantly comparing to that of the pure thermoplastic starch. A lot of other works were devoted to NFC/starch composites (Dufresne *et al.* 2000; Chakraborty *et al.* 2007; Mondragón *et al.* 2008; Takagi and Asano 2008; Savadekar and Mhaske 2012; Hietala *et al.* 2013).

**Amylopectin.** One of two components which compose starch is amylopectin (70–80%). López-Rubio *et al.* (2007) described the use of NFC to reinforce amylopectin. It was reported that neat amylopectin films were brittle unless 38 wt% of glycerol was added as a plasticizer. However, the incorporation of NFC gave possibility to produce stiff and strong composite

films without glycerol. Consequently, NFC acted both as a reinforcing agent and as a plasticizer because of the presence of some moisture in the fibers.

Svagan *et al.* (2007) produced the composites of amylopectin plasticized by glycerol and NFC (10–70 wt.%). An elastic modulus of 6200 MPa, a tensile strength of 160 MPa and a strain-to-failure of 8.1% were observed at 70 wt.% of NFC load comparing with 1.6 MPa, 0.35 MPa and 80%, respectively, for the neat matrix (amylopectin/glycerol with the mass ratio of 50/50). Later, Svagan *et al.* (2009) showed that the use of NFC (up till 70%) in amylopectin matrix reduces strongly the moisture diffusivity and slightly the maximum moisture uptake. Plackett *et al.* (2010) studied the influence of two types of NFC (produced from sulfite pulp with high amount of hemicellulose or carboxymethylated dissolving pulp) on the mechanical behavior of amylopectin-based composites. It was shown that the films containing NFC with higher content of hemicellulose possessed higher elastic modulus; however, they had lower ductility.

**Chitosan.** Hosokawa *et al.* (1990) reported the production of composite films from chitosan and NFC with high oxygen barrier properties and biodegradable character. The obtained composite was hydrophilic but insoluble in water. The addition of chitosan to NFC films enhanced their mechanical properties. Low moisture-sensitive high barrier composite films from chitosan and NFC were produced by Gällstedt and Hedenqvist (2006). The shrinkage of chitosan-acetic acid salt sheets, buffered in an alkaline solution, was effectively reduced by the NFC addition.

Nordqvist *et al.* (2007) studied the properties of wet composites produced from chitosan–acetic acid salt and NFC. Fernandes *et al.* (2010) reported the production of transparent chitosan composite films reinforced with high contents (up to 60%) of NFC. Two different chitosan samples were used. The composites showed better thermo-mechanical properties comparing to that of neat chitosan films.

**Pullulan.** Trovatti *et al.* (2012) reported the production of bionanocomposite films by casting water-based suspensions of pullulan and nanofibrillated cellulose. The incorporation of NFC into the pullulan matrix increases considerably the thermal stability and the mechanical properties of the nanocomposite films comparing to the neat matrix. The tensile strengths and elastic modulus of the composites plasticized with glycerol was found to be lower than those of the unplasticized counterparts. However, the plasticized ones had a clear advantage in terms of flexibility.

### 3.1.2.2 Hydrophobic matrices

**Polyethylene (PE) and polypropylene (PP).** High processing temperature limits the compounding of NFC with major engineering plastics, *e.g.*, polyethylene (PE), polypropylene (PP), polystyrene and polyvinyl chloride (Miao and Hamad 2013). However, Wang and Sain (2007a, b) reported the production of composites from NFC and PE or polypropylene (PP) using solid phase compounding method. The NFC, coated with ethylene–acrylic oligomer emulsion as a dispersant, was added to molten PE or PP and the composites were compression molded. The mechanical properties of the composites increased slightly comparing to pure matrixes. However, based on microscopy analysis, the degradation of NFC during processing was suggested.

**Polylactic acid (PLA).** Polylactic acid is biobased and biodegradable commercially available polymer with properties similar to those of fossil fuel-based commodity plastics. However, there are some weaknesses which limit its application, *e.g.*, inherent brittleness, low thermal stability and relatively high price and low gas and water vapor barrier properties for some applications (Siró and Plackett 2010). In order to overcome these limitations PLA-based composites can be produced.

Chakraborty *et al.* (2005) reported the production of NFC with further incorporation into PLA matrix. The NFC aqueous suspension was added into the PLA matrix, molten at 190 °C, and mixed using a twin screw Brabender mixer. The composite films were made by compression molding. Calcofluor dye was used as a marker to impart fluorescence to cellulose, in order to deduce the quality of NFC dispersion in the matrix. A uniform dispersion of NFC in PLA was accomplished, as observed by laser confocal microscopy. The mechanical properties of the obtained composites were not reported. Okubo *et al.* (2005) described the improvement of the interfacial adhesion between PLA and bamboo fibers by adding NFC (up to 20 wt.%). MFC, bamboo fibers and PLA were suspended and mixed in water, vacuum filtered, oven dried and finally hot pressed. As a result, the bending strength and fracture toughness of the composite were improved.

Mathew *et al.* (2006) produced composites by pumping an aqueous suspension of NFC and CNC into PLA during twin screw extrusion. The fast water evaporation during the processing led to reaggregation of cellulose. Thus, no significant improvement of composite mechanical properties was observed due to poor dispersion of nanocellulose in PLA. The addition of polyethylene glycol did not improve the filler dispersion. Iwatake *et al.* (2008) prepared the composites by mixing NFC with PLA using a twin rotary roller mixer at 140 °C. The homogeneously dispersed NFC in the matrix increased the elastic modulus and tensile

strength of PLA by 40% and 25%, respectively, without decrease of yield strain at a fiber content of 10 wt.%.

A number of other publications on preparation of NFC–PLA composites is available (Wang and Sain 2007c; Nakagaito *et al.* 2009; Suryanegara *et al.* 2009; Boissard *et al.* 2012; Tanpichai *et al.* 2012).

**Polycaprolactone (PCL).** Poly( $\epsilon$ -caprolactone), referred to as polycaprolactone or PCL, is a biodegradable polyester derived from the chemical synthesis of crude oil. Lönnberg *et al.* (2008) grafted NFC with different molecular weight PCL to improve the compatibility between cellulose and PCL in composites. Siqueira *et al.* (2009b) applied N-octadecyl isocyanate as a grafting agent to modify the surface of NFC which improved the dispersion of nanofillers in organic solvents. The mechanical properties of ensuing nanocomposite films were enhanced dramatically both in terms of stiffness and ductility.

**Polyhydroxyalkanoates (PHA).** Polyhydroxyalkanoates is a family of bacteria-synthesized polyesters from saturated and unsaturated hydroxyalkanoic acids. They exist either as homopolymers (*e.g.*, poly(3-hydroxybutyrate), referred to as P(3HB) or PHB; poly(3-hydroxyvalerate), named as P(3HV) or PHV) or as copolymers (poly[(3-hydroxybutyrate)-*co*-(3-hydroxyvalerate)]), abbreviated as P[(3-HB)-*co*-(3-HV)] or simply PHBV).

Srithep *et al.* (2013) produced bionanocomposites from NFC as reinforcement and PHBV as a matrix. PHBV was dispersed in NFC aqueous suspension, and freeze-dried. The resulting masterbatch was used further to produce composites by melt compounding process. The results showed that incorporation of NFC increased the elastic modulus of the nanocomposites nearly twofold comparing to that of the neat matrix. However, the addition of NFC reduced the toughness and caused the thermal degradation of PHBV, probably due to residual moisture in the NFC.

### 3.1.3 Latex/nanofibrillated cellulose composites

The main challenge of using NFC in composites is associated with cellulose polar nature and the non-polar characteristics of most thermoplastics, which causes difficulties in composites compounding and achieving acceptable dispersion of nanocellulose filler within the matrix. An alternative way to increase the range of applied polymer matrices is to use polymers in latex form. Latex is a stable dispersion of polymer particles in aqueous medium. It can be found in nature or synthesized from monomer emulsions — monomer droplets dispersed in

water. This production process is known as emulsion polymerization. Since NFC is typically produced in the form of aqueous suspensions, one of the options for composite production is mixing these suspensions with waterborne latexes and further casting evaporation.

In conventional emulsion polymerization water-insoluble monomer is polymerized in surfactant micelles, localized in water. The monomer in this case needs to travel through aqueous phase to reach the micelles. The polymerization of very hydrophobic monomers is thus difficult (Mittal 2010). The other possible process to synthesize latex is *via* miniemulsion polymerization. Within such process, high shear forces are primarily applied to split the emulsion into nanometric/submicron monomer droplets. Surfactant and costabilizer are used to retard monomer diffusion into larger droplets. In such system, the droplet surface area is very large due to small droplet size. Thus, most of the surfactant is adsorbed at the droplet surface and little surfactant is present in the form of micelles. Consequently, the polymerization reaction proceeds directly in the monomer droplets, which can yield faster kinetics and therefore lower polymerization times (Bunker *et al.* 2003).

Azizi *et al.* (2004) reported the production of composites by incorporating sugar beet-derived NFC and CNC into poly(styrene-*co*-butyl acrylate) latex. Films were prepared with 6 wt.% cellulose content by solvent casting. The elastic modulus of 114 MPa and tensile strength of 6.3 MPa were found for NFC-reinforced composites, comparing to 0.2 MPa and 0.18 MPa, respectively, for the neat matrix. Similar reinforcing effect was shown by Malainine *et al.* (2005) for the composites from cactus-derived NFC and the same matrix.

Dalmas *et al.* (2007) incorporated NFC from sugar beet pulp into the same latex and studied two methods for composite processing: casting or freeze-drying with further hot pressing. High mechanical properties and thermomechanical stability was achieved for the cast composites, which was explained by the formation of strong hydrogen bonds between cellulose nanofibrils. On the contrary, freeze-dried and hot pressed composites had limited reinforcement effect, assumedly because the creation of strong interactions between NFC was prevented. Larsson *et al.* (2012) produced bionanocomposites by mixing NFC aqueous suspensions and PLA latex with further vacuum filtration and hot pressing. The addition of NFC enhanced the elastic modulus, tensile strength, and strain at break of the composites.

The reinforcing effect of CNC in latex matrices has been also investigated (Favier *et al.* 1995; Helbert *et al.* 1996; Ben Elmabrouk *et al.* 2009; Siqueira *et al.* 2009a; Pasquini *et al.* 2010; Ben Mabrouk *et al.* 2014). However, compared with CNC, the use of NFC in latex-based composites commonly results in a stronger material with higher elastic modulus and

lower elongation at break due to the capacity of NFC to form entanglements (Azizi *et al.* 2004; Malainine *et al.* 2005).

In the above works, NFC or CNC had, mainly, physical interactions with the polymer matrix. Ben Mabrouk *et al.* (2011) showed the production of polybutylmethacrylate latex *via* miniemulsion polymerization, containing cationic surfactant and negatively charged CNC (due to the presence of sulfate ester groups after sulfuric acid hydrolysis). It was reported that the electrostatic interactions between the positively charged particles and negatively charged CNC ensured the anchoring between these two components.

In this dissertation the above concept of ionic interactions between latex particles and nanocellulose filler is employed in order to produce NFC/latex composites. The latexes with positively and negatively charged particles were synthesized *via* miniemulsion polymerization, assisted by cationic and anionic surfactants. TEMPO-oxidized NFC (negatively charged due to the presence of carboxylate ions) was incorporated into the latex and the composite films were prepared by casting. The ensuing composites were characterized from the point of view of NFC dispersion in the latex and the reinforcing effect of the incorporated filler.

## 3.2 Experimental

### 3.2.1 Materials

Bleached softwood bisulfite pulp (Quality 2100) was obtained from Domsjö Fabriker AB, Sweden. The alpha-cellulose content of 93 % and the DP of 780 were specified by the supplier. The monomers of Styrene ( $\geq 99\%$ ) and 2-ethylhexyl acrylate (2-EHA, 98%) were obtained from Sigma-Aldrich and were further distilled under vacuum and kept refrigerated under nitrogen gas atmosphere. Luperox A75, containing 75% of benzoyl peroxide and the remainder water, TEMPO (98%), sodium bromide ( $\geq 99\%$ ), sodium hypochlorite solution (13%), myristyltrimethylammonium bromide (MTAB,  $\geq 99\%$ ), sodium dodecyl sulfate (SDS,  $\geq 99\%$ ), 1-Hexadecanol ( $\geq 99\%$ ) and Hydroquinone ( $\geq 99\%$ ) were the products of Sigma-Aldrich and were used without further purification.

### 3.2.2 Nanofibrillated cellulose production

TEMPO-oxidized NFC suspension was prepared as reported in Section 1.2. Briefly, bleached softwood bisulfite pulp was soaked in water for 4 h and dispersed in a standard disintegrator

according to ISO 5263-1:2004 standard. TEMPO-mediated oxidation was performed based on the method proposed by Saito *et al.* (2007). TEMPO/NaBr/NaClO (0.1/1/5 mmol/g of cellulose, respectively) system was used. TEMPO and NaBr were mixed with the cellulose suspension before the addition of NaClO water solution with the adjusted pH till 10 using HCl. For the pH adjustments, 3M HCl and 3M NaOH were used. The concentration of the obtained cellulose suspension was 1 wt.%. The reaction was performed at 25 °C. The pH of  $10 \pm 0.1$  was maintained during the reaction by the addition of NaOH. When the pH no longer decreased (indicating that no longer creation of carboxyl groups occurs) the reaction was quenched by lowering the pH till 7.

The TEMPO-oxidized cellulose was filtered on a Büchner funnel using a nylon sieve with a mesh size of 1  $\mu\text{m}$  and washed until the filtrate conductivity was below 5  $\mu\text{S cm}^{-1}$ . Finally, the oxidized cellulose was redispersed in deionized water at 1.50 wt.% and ground using Supermasscolloider for 60 passes.

### 3.2.3 Latex synthesis

Latex aqueous dispersions of poly[styrene-*co*-(2-ethylhexyl acrylate)], hereinafter referred to as P[S-*co*-(2-EHA)], with varying monomer ratios and cationic (MTAB) or anionic (SDS) surfactants, were synthesized in miniemulsion, as summarized in Table 3.1. Different batches were abbreviated (*e.g.*, C-8.23) starting from letters C (cationic) or A (anionic) according to the type of surfactant used and followed by the amount of styrene in the recipe. Since only the first sample was synthesized with different amount of initiator, its abbreviation contains also this information (C-8.23-0.75).

**Table 3.1** Formulations for the miniemulsion copolymerization of styrene and 2-ethylhexyl acrylate

Product	Role	Sample abbreviation and quantity (g)					
		C-8.23-0.75	C-8.23	C-7.66	C-6.53	C-5.40	A-8.23
MTAB	surfactant	0.20	0.20	0.20	0.20	0.20	–
SDS	surfactant	–	–	–	–	–	0.17
1-Hexadecanol	costabilizer	0.44	0.44	0.44	0.44	0.44	0.44
Water	medium	24.00	24.00	24.00	24.00	24.00	24.00
Styrene <sup>a</sup>	monomer	8.23	8.23	7.66	6.53	5.40	8.23
2-Ethylhexyl acrylate <sup>a</sup>	monomer	4.00	4.00	5.00	7.00	9.00	4.00
Luperox A75 <sup>b</sup>	initiator	0.75	1.00	1.00	1.00	1.00	1.00

<sup>a</sup> total molar quantity of two monomers in all the reactions is equal;

<sup>b</sup> Luperox A75 was used as a source of benzoyl peroxide (75%, remainder water).

First, a pre-emulsion of surfactant and costabilizer in water was prepared by heating the above components at 70 °C for 1 h under mild stirring. Then, monomers (Styrene and 2-EHA) were added and the resulting product was emulsified in an ice bath by ultrasound using Branson sonifier 250 for 5 min at a duty cycle of 70% and a micro tip limit of 4. The polymerization reaction was performed under inert nitrogen gas atmosphere by mixing the prepared emulsion with an initiator (benzoyl peroxide), stirring at 150 rpm and heating at 70 °C for a determined period of time (defined from the monomer to polymer conversion analysis). As a result of such reaction, statistical (random) copolymer is obtained. The chemical structure of the synthesized P[S-*co*-(2-EHA)], *i.e.* P[S-*stat*-(2-EHA)], is illustrated in Figure 3.2.

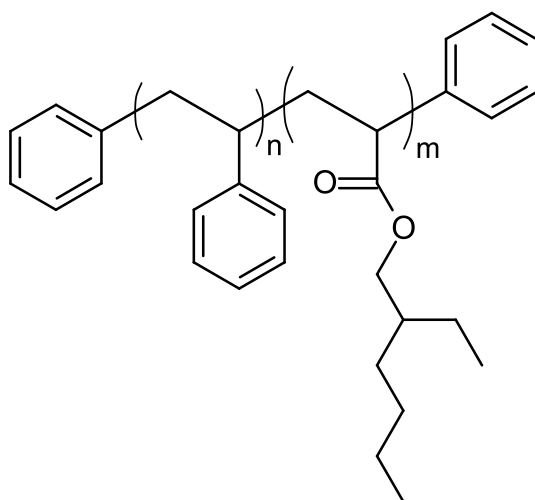


**Figure 3.2** Schematic diagram of the chemical structure of poly[styrene-*co*-(2-ethylhexyl acrylate)]

### 3.2.4 Composites fabrication

The TEMPO-oxidized NFC suspension, prepared as reported in Section 3.2.2, was degassed under atmospheric pressure of 5 kPa for 24 h to remove air trapped in the fibrous network. The composite dispersions of NFC and latex, with cellulose to polymer weight fraction ranging from 0 to 5%, were prepared by blending the above components at 200 rpm using 4-bladed stainless steel stirrer. Composite films were prepared by casting the prepared dispersions in Teflon molds for 48 h at 40 °C. Some samples were further hot pressed for 1 min at 1 bar and 90 °C.

For the production of composites, two synthesized latexes were used: C-8.23 and A-8.23. The schematic representation of ionic interactions between TEMPO-oxidized NFC, possessing carboxyl groups on its surface, and latex with cationic or anionic surfactant is shown in Figure 3.3.

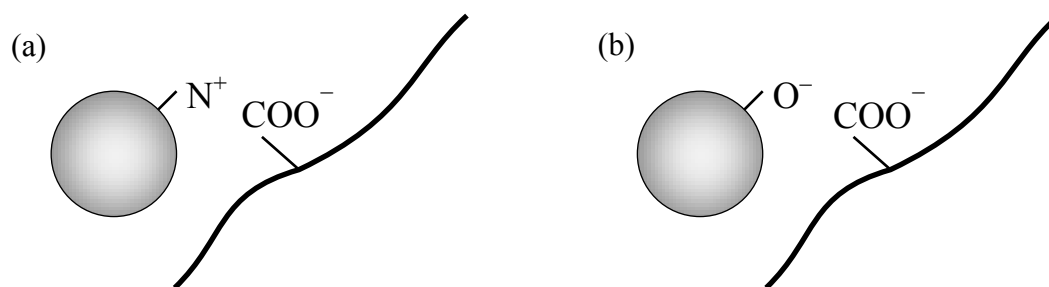


**Figure 3.3** Schematic representation of ionic interactions between synthesized latex particles and TEMPO-oxidized NFC

### 3.2.5 Characterization techniques

#### 3.2.5.1 Monomer to polymer conversion

Gravimetric method was used to determine the degree of monomer conversion within the reaction time. Latex samples of about 0.30 mL were withdrawn from the reaction mixture and the exact weight was measured thereafter. An exact amount of about 0.15 mL of hydroquinone aqueous solution (1 wt.%) was added immediately in order to stop the polymerization reaction. The samples were dried at ambient temperature until constant weight was reached. While drying, the monomers evaporate, while the polymer remains. The degree of monomer conversion was then calculated as follows:

$$\text{Conversion (\%)} = m_1/m_2 \times 100, \quad (3.1)$$

where  $m_1$  is the weight of the dried sample with subtracted amount of hydroquinone, surfactant and costabilizer, and  $m_2$  is the weight of monomers withdrawn from the reaction, calculated from the weight of the retrieved latex.

#### 3.2.5.2 Dynamic light scattering (DLS)

Z-average size of emulsion droplets and latex particles was determined by dynamic light scattering (DLS) technique using Vasco particle size analyzer (Cordouan Technologies, France). The measurements were performed at 25 °C using cumulant method. For each measurement, 7 acquisitions were performed.

#### 3.2.5.3 Size-exclusion chromatography (SEC)

Size-exclusion chromatography (SEC) was used to determine number-average molar mass ( $M_n$ ), weight-average molar mass ( $M_w$ ) and polydispersity index ( $M_w/M_n$ ) of the synthesized latexes. Dry latex films were dissolved in tetrahydrofuran (THF) overnight at room temperature and filtered through a 0.45  $\mu\text{m}$  PTFE filter before the injection into the SEC

system. The samples were eluted at a flow rate of 1 mL/min using a HPLC pump (Varian PLGel Mixed-B LS). Three SEC columns, preceded by a guard column, were connected in series. The molar mass distribution was determined using a di-angle laser light scattering (RALS-LALS) detector coupled with a concentration detector (RI) (VISCOTEK TDA-302). The graphs were normalized as a function of the surface under the curve.

#### **3.2.5.4 Optical microscopy**

The optical microscopy images of matrix and composite cross section and top surfaces were taken using Zeiss Stereo Discovery.V20 microscope equipped with AxioCam ICc 5 digital camera. For the cross section examination, the films were cut using a razor blade.

#### **3.2.5.5 Field emission gun scanning electron microscopy (FEG-SEM)**

The FEG-SEM was performed using a ZEISS Ultra 55 microscope, equipped with In-Lens secondary electron detector using an accelerating voltage of 1–5 kV. To analyze the film cross section, the samples were broken under liquid nitrogen and deposited on a double-sided adhesive carbon tape. The latex dispersions were diluted with distilled water till a polymer concentration of 0.1 wt.%, deposited on a double-sided adhesive carbon tape and lyophilized using Christ Alpha 2-4 LD plus Freeze Dryer. Before the analysis, samples were covered with Au/Pd layer of 3 nm by sputtering.

#### **3.2.5.6 Differential scanning calorimetry (DSC)**

Thermal analysis was conducted using DSC Q100 apparatus (TA Instruments, USA). The conditioned polymer films of around 10 mg were hermetically closed in aluminum pans and examined in the temperature range from –80 to 150 °C at a heating/cooling rate of 10 °C/min under nitrogen (50 mL/min). The first heating–cooling cycle was performed to erase the previous thermal history of the polymers. The glass transition temperature ( $T_g$ ) was determined from the second heating scan.

#### **3.2.5.7 Tensile testing**

The tensile mechanical properties of neat matrices and the composites were analyzed using RSA3 (TA Instruments, USA). Measurements were carried out with a crosshead speed of 0.1 mm/s at 23 °C. The samples were prepared by cutting rectangular strips from the films with a width of 5 mm. The distance between apparatus jaws was 10 mm. Five measurements were carried out for each sample and average values were calculated.

### 3.2.5.8 Proton nuclear magnetic resonance ( $^1\text{H}$ NMR)

$^1\text{H}$  NMR analysis was performed using Bruker Avance III HD spectrometer at a frequency of 400.15 MHz. For the analysis, dried latex films with the weight of 10 mg were solubilized in approximately 0.4 mL of solvent and were examined in their solubilized state. The chemical shift ( $\delta$ ) was measured in parts per million (ppm). Deuterated chloroform ( $\delta_{\text{H}} = 7.24$  ppm) was used as a solvent. Data treatment was conducted using TopSpin 3.2 and MestRe-C 2.3a software.

### 3.2.5.9 X-ray photoelectron spectroscopy (XPS)

The top and bottom surfaces of cast neat latex and composite films, the raw pulp after being treated in a standard disintegrator (according to ISO 5263-1:2004 standard) and the ensuing TEMPO-oxidized NFC were analyzed using XPS. The analysis was performed using XSAM800 (KRATOS) X-ray spectrometer operated in the fixed analyzer transmission (FAT) mode with a non-monochromatized Mg K $\alpha$  ( $h\nu = 1486.6$  eV) X-radiation and a pass energy of 20 eV. XPS Peak 4.1 software was used for peak fitting. The charge shift was corrected using the binding energy of 285 eV of carbon atoms bound to other carbons or hydrogens as a reference signal (Beamon and Briggs 1992). For quantification purposes, the sensitivity factors were 0.25 for C 1s, 0.66 for O 1s, 2.5 for Na 1s and 0.4 for S 2p.

## 3.3 Results and discussion

### 3.3.1 Synthesis of model latex

P[S-*co*-(2-EHA)] was synthesized as a model latex to study the interactions between NFC and polymer matrix and the quality of composite homogeneity. The latex samples were produced *via* miniemulsion polymerization, as described in Section 3.2.3.

Two emulsions with and without costabilizer were prepared according to C-8.23-0.75 recipe. Their droplet size evolution was monitored after ultrasound homogenization (before polymerization) as a function of storage time. The emulsions were stored at ambient temperature (23 °C) under nitrogen gas atmosphere covered with aluminum foil. Figure 3.4a shows the increase of the emulsion Z-average droplet size for the emulsions prepared without costabilizer, while the droplet size of the counterpart with costabilizer remains stable. The presence of surfactant in both emulsions is necessary to retard droplet coalescence. However, without costabilizer it is not sufficient to preserve the droplet size in such time scale. The growth

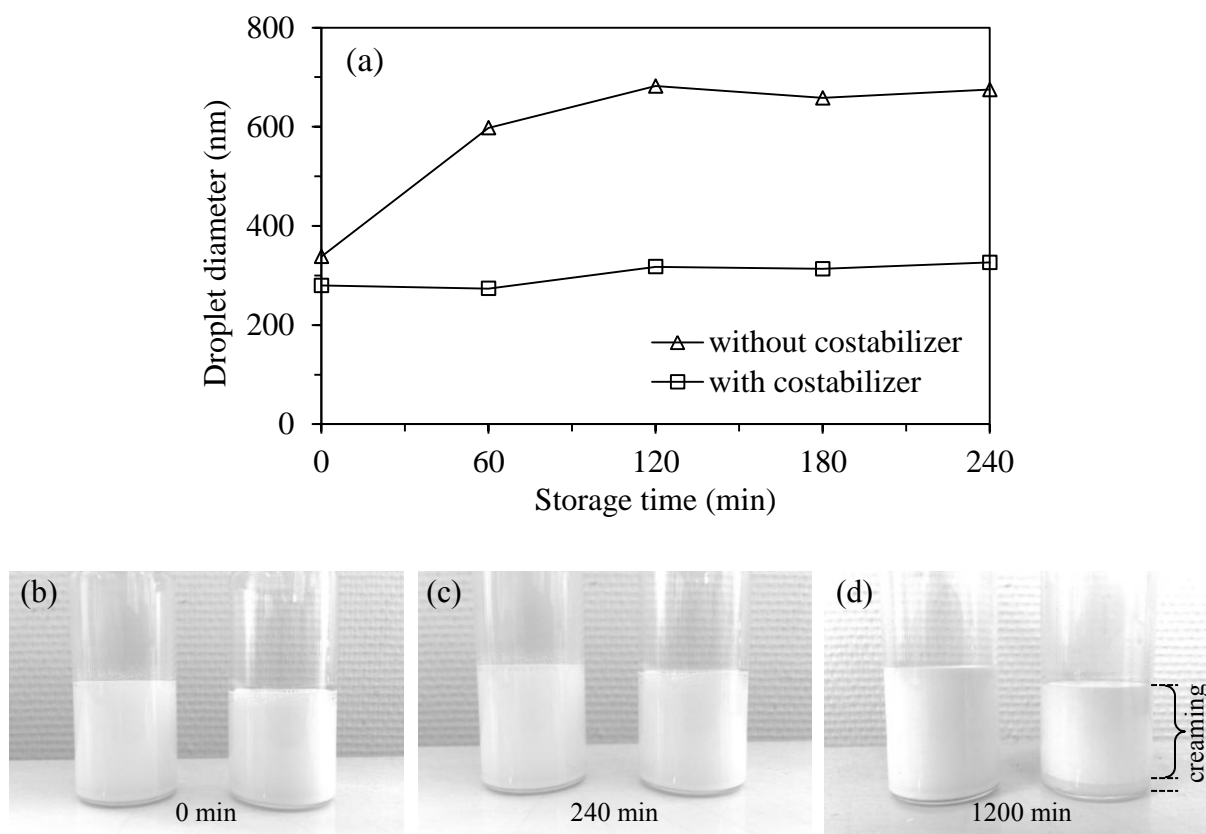


**Figure 3.4** Evolution of Z-average droplet diameter of C-8.23-0.75 emulsion prepared with and without costabilizer during storage (a) and visual appearance of the emulsions with costabilizer (*left*) and without costabilizer (*right*) after: 0 min (b), 240 min (c) and 1200 min (d) of storage

of droplet size occurs due to Ostwald ripening (monomer diffusion from the smaller droplets into the larger ones through aqueous medium). Figure 3.4b–d shows the visual appearance of the emulsions while storing. At higher time scale the creaming of the emulsion without costabilizer is observed as the droplet size becomes large enough to disobey Brownian motion. Thus, the use of costabilizer is necessary to prevent Ostwald ripening on time scale of hours.

Figure 3.5a shows the monomer conversion curves for polymerization reactions using varying amount of initiator. It is apparent that the conversion becomes faster when the initiator concentration increases. After 7 hours of the reaction, the degree of monomer conversion is 98% for C-8.23 sample, whereas for C-8.23-0.75 sample this value is 72%. Despite the faster reaction time, the increase of initiator concentration usually leads to lower DP of the synthesized latex and hence lower mechanical behavior, as well as lower  $T_g$ . The conversion within 7 hours was selected as reasonable reaction time for further experiments.

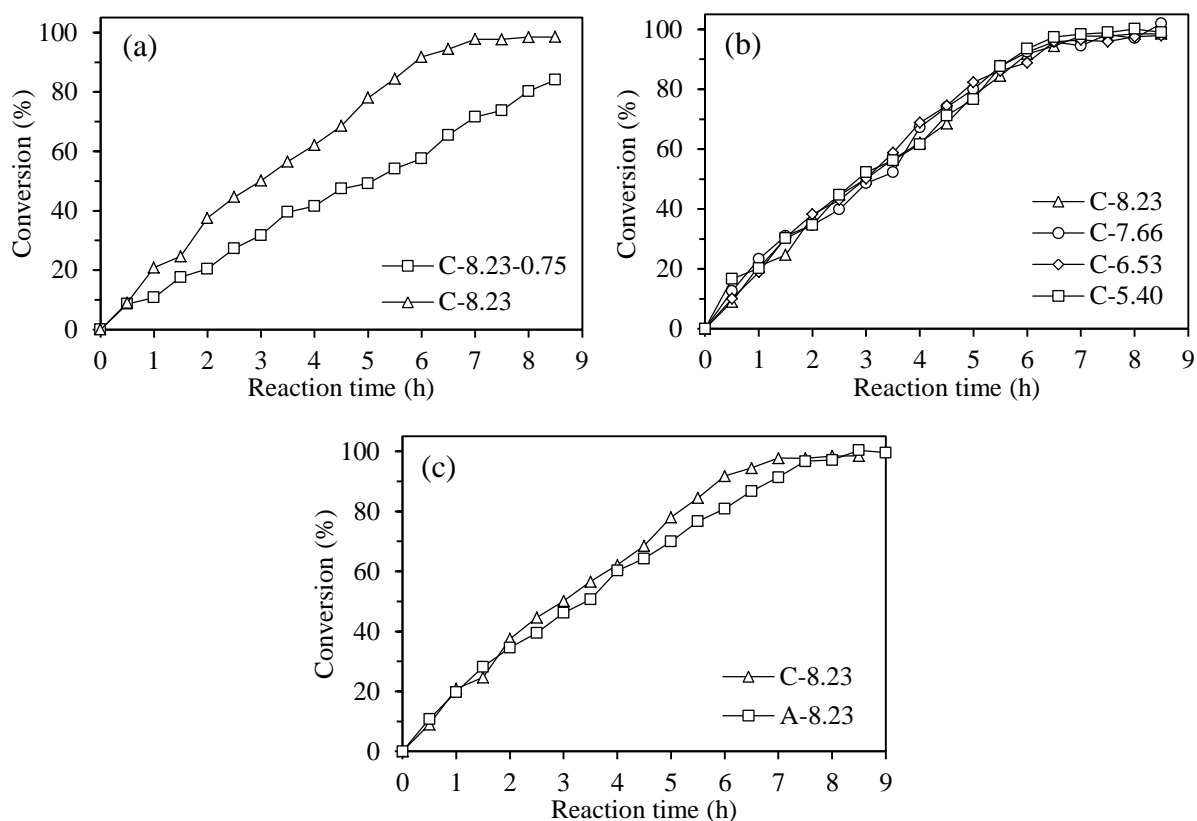


**Figure 3.5** Monomers conversion during miniemulsion polymerization reactions

The samples C-8.23, C-7.66, C-6.53 and C-5.40 were synthesized with different ratios of monomers, keeping equal their total molar quantity. The kinetics of monomer conversion for these samples is similar, as seen from Figure 3.5b. The copolymerization gives the possibility to produce a material with the properties intermediate between two homopolymers. 2-EHA has branched alkyl chains and possesses good film-forming properties (Haloi *et al.* 2012), while styrene shows high mechanical characteristics. Thus, by combining both and varying their concentrations, a copolymer with the desired properties can be obtained. A-8.23 sample was produced with similar recipe as C-8.23, but using SDS as a surfactant. Figure 3.5c shows that the monomer conversion for A-8.23 sample is slightly slower. It is probably associated with slight inaccuracies with the amount of components used in preparation of the recipe.

By increasing the amount of styrene ( $T_g \approx 100\text{ }^\circ\text{C}$ ) or decreasing the amount of 2-EHA ( $T_g \approx -50\text{ }^\circ\text{C}$ ), latexes with higher  $T_g$  can be obtained. Figure 3.6 shows the distinct average  $T_g$  of  $7\text{ }^\circ\text{C}$  and  $8\text{ }^\circ\text{C}$  for C-8.23 and A-8.23 samples, respectively. However, it is hard to detect a single slope having the onset and offset  $T_g$  for the other samples. This can be attributed to the difference of monomer reactivity ratios for styrene and 2-ethylhexylacrylate copolymer, which are determined as  $r_{\text{Styrene}} = 0.979$  and  $r_{2\text{-EHA}} = 0.292$ , respectively (Kavousian *et al.* 2004). Therefore, as the polymerization reaction starts, styrene monomers tend to react more

with themselves, rather with 2-EHA. It seems that in C-8.23 and A-8.23 samples all 2-EHA manages to react with styrene progressively within the reaction. However, in C-8.23, C-7.66, C-6.53 and C-5.40 samples, where higher concentrations of 2-EHA were used, the portion of unreacted 2-EHA will increase till the end of reaction; thus, it will react to a greater extent with itself. This will displace the type of copolymer from statistical towards block copolymer with wide or several  $T_g$ . Therefore, Figure 3.6e shows several shoulders (bends) for C-5.40 sample.

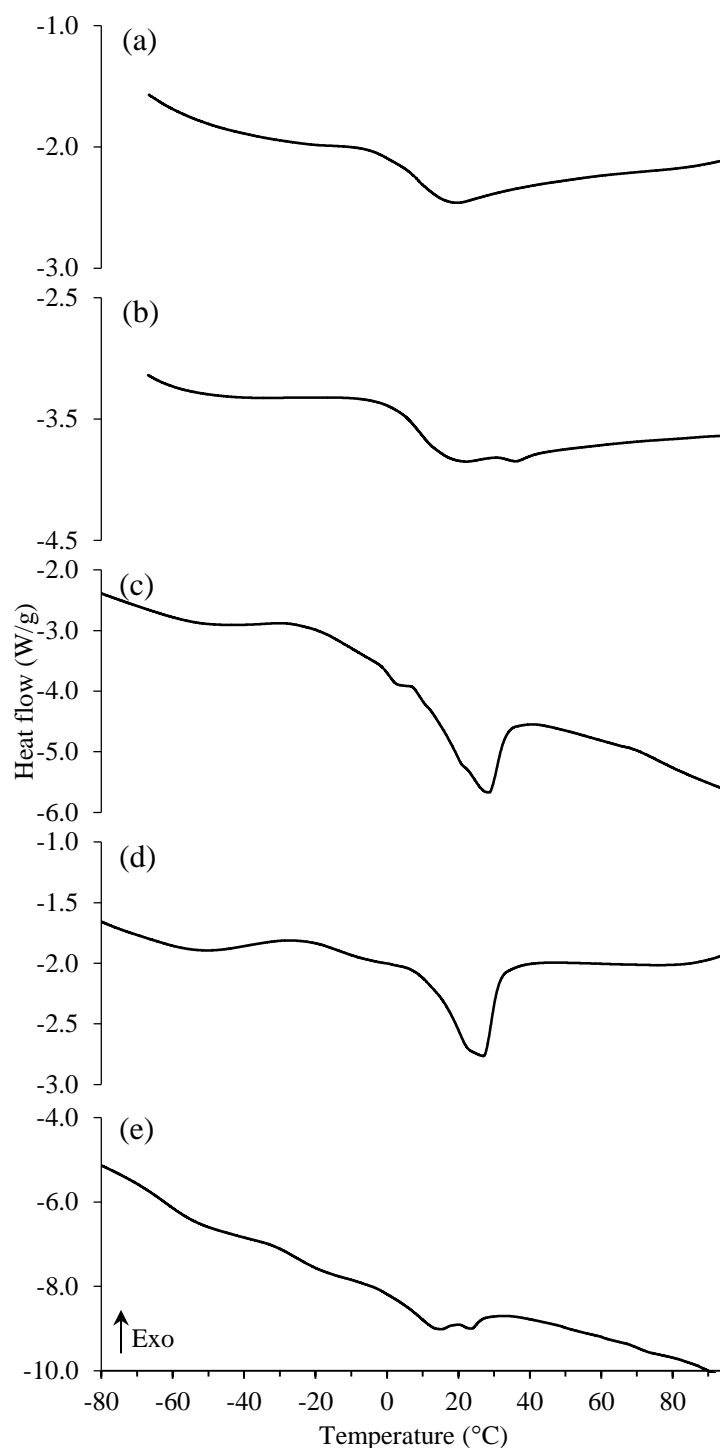


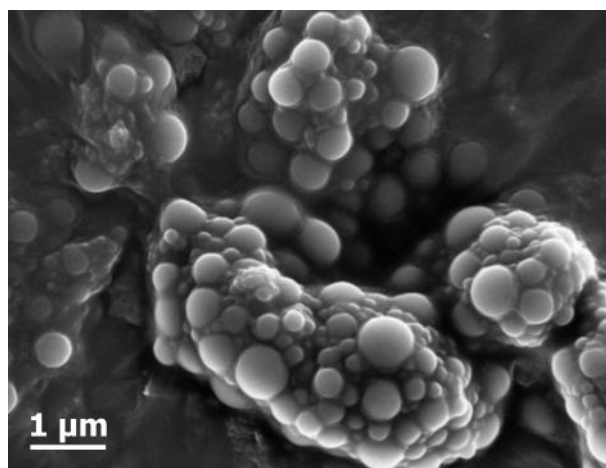
**Figure 3.6** DSC curves of latex samples: C-8.23 (a), A-8.23 (b), C-7.66 (c), C-6.53 (d), C-5.40 (e), synthesized *via* miniemulsion polymerization

C-8.23 and A-8.23 samples were used further as model waterborne latexes to study the interactions between TEMPO-oxidized NFC and the polymeric matrix in composites. Some measured properties of these latexes are summarized in Table 3.2. The particle size distribution graphs of C-8.23 and A-8.23 are shown in Figure D.1 and Figure D2, respectively, in Annex D. The particles size polydispersity of the synthesized latexes was also confirmed by FEG-SEM, as seen in Figure 3.7 for A-8.23 sample. Thus, particles with diameter in the nanometer and submicron scales are present. DLS measurements have shown the Z-average particle size of 385 and 271 nm for C-8.23 and A-8.23 latexes, respectively.

The chemical composition of the produced C-8.23 and A-8.23 latexes was analyzed using  $^1\text{H}$  NMR. The characteristic chemical shifts corresponding to styrene and 2-EHA were determined from NMR spectra, as shown in Figure 3.8. Two broad peaks at around 6.5–7.2 ppm, denoted as (I), represent the chemical shift of 5 protons in phenyl group of styrene repeating units. A well-defined triplet and a doublet peaks (the multiplicity was clearly seen from the enlarged spectra) at around 7.5–8.2 ppm have appeared, indicating the presence of: (i) some low molecular weight structures possibly in the form of biphenyls, which may be attributed to the tendency of radicals from oil-soluble initiators (*e.g.*, benzoyl peroxide) to recombine before initiating the polymerization (Schork *et al.* 2005), and (ii) phenyl groups at the end of polymer chains.

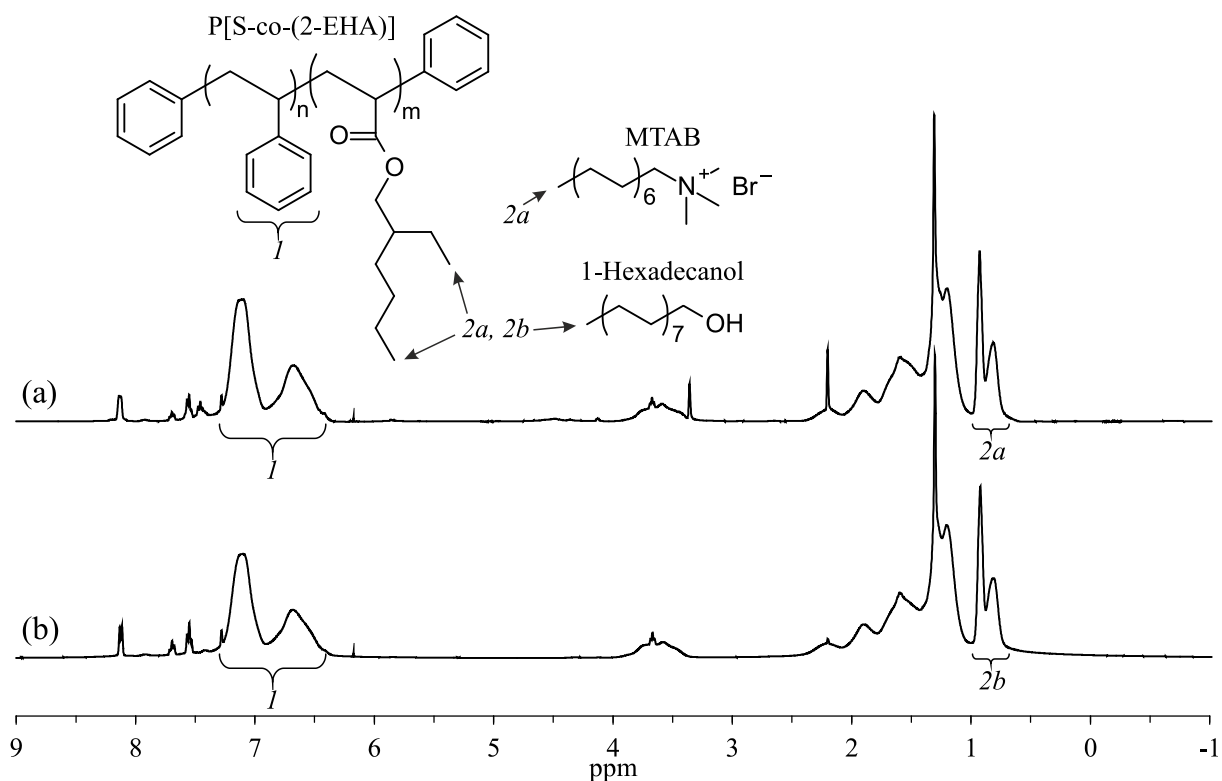
**Table 3.2** Some properties of the synthesized latexes C-8.23 and A-8.23

Sample	$T_g$ ( $^{\circ}\text{C}$ )	Z-average particle size (nm)	PDI	$M_w$ (Da)	$M_n$ (Da)	$M_w/M_n$
C-8.23	7	385	0.22	56218	26048	2.16
A-8.23	8	271	0.30	62512	28197	2.22



**Figure 3.7** FEG-SEM image of A-8.23 latex polymer particles

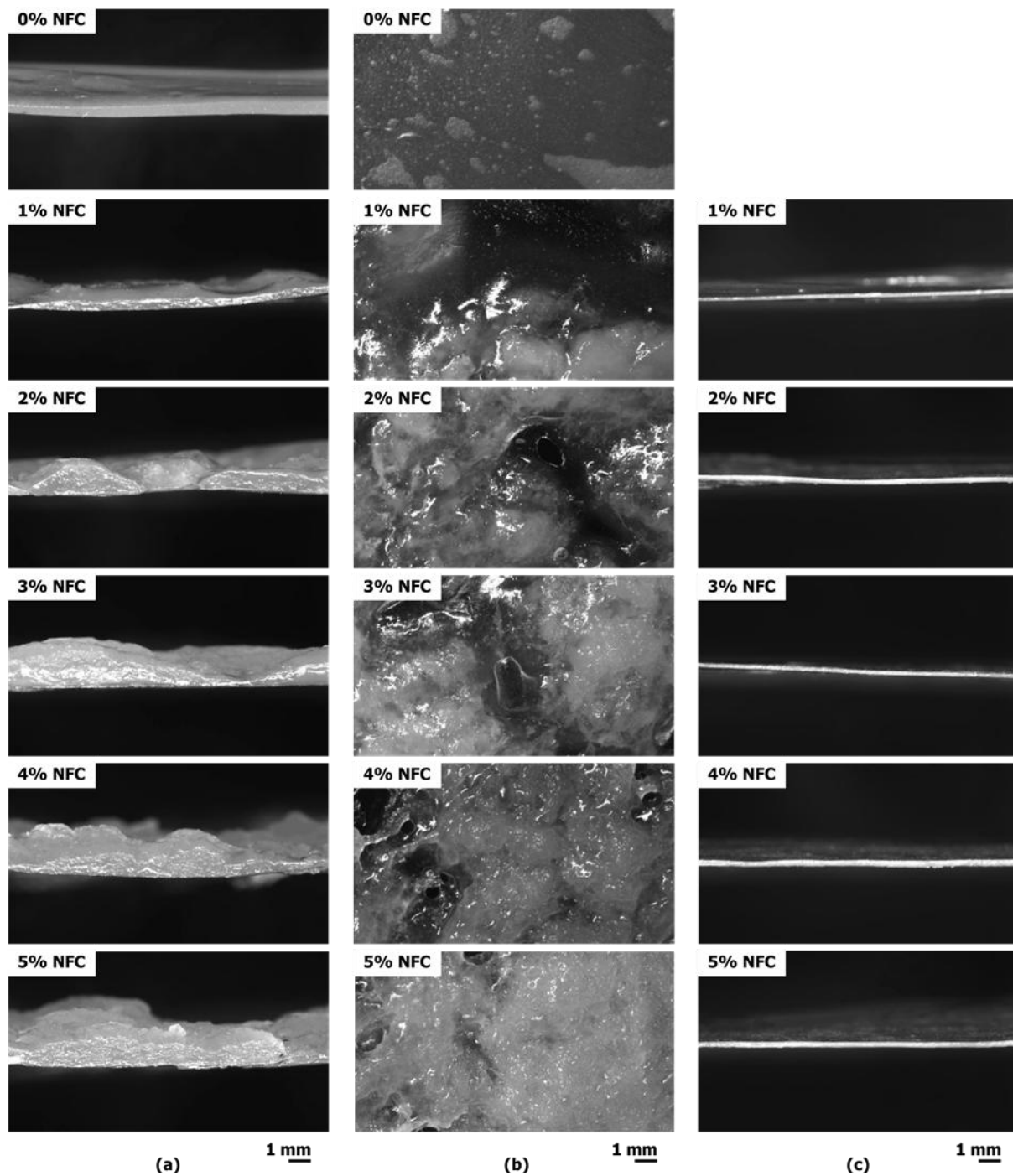
Two peaks at a chemical shift around 0.75–1.00 ppm, denoted as (2a) and (2b), originate from protons in methyl groups ( $-\text{CH}_3$ ) at the end of aliphatic chains of 2-EHA, 1-Hexadecanol and MTAB. Since SDS is not soluble in chloroform, used as deuterated solvent for NMR analysis, the spectrum of A-8.23 in Figure 3.8b does not display the contribution of the surfactant. Other two peaks at around 1.25 ppm represent the methylene groups ( $-\text{CH}_2-$ ) of the aliphatic chains in the system. By integrating the surfaces below the peaks, the ratios between two monomers in the synthesized polymer can be estimated. The peak (2a) contains the contribution of 6 protons from two methyl groups in 2-EHA, 3 protons from MTAB and 3 protons from 1-Hexadecanol. The peak (2b) comprises the same except 3 protons from MTAB. Knowing the molar quantities of all the components used in the polymerization reaction, and using the ratio between (2a) and (1) or (2b) and (1) peaks, the estimated molar ratios of Styrene/2-EHA in C-8.23 and A-8.23 samples were calculated as 3.1/1.0 and 2.5/1.0, respectively (the theoretic molar ratio is 3.6/1.0 for both samples).



**Figure 3.8**  $^1\text{H}$  NMR spectra of C-8.23 (a) and A-8.23 (b) synthesized latexes: (1) represents the chemical shift signal from 5 hydrogen protons in phenyl group of styrene repeating units; (2a) shows the chemical shift of protons from methyl groups present in 2-EHA repeating units, MTAB and 1-Hexadecanol; (2b) represents the chemical shift of protons in 2-EHA repeating units and 1-Hexadecanol

### 3.3.2 Composites production and characterization

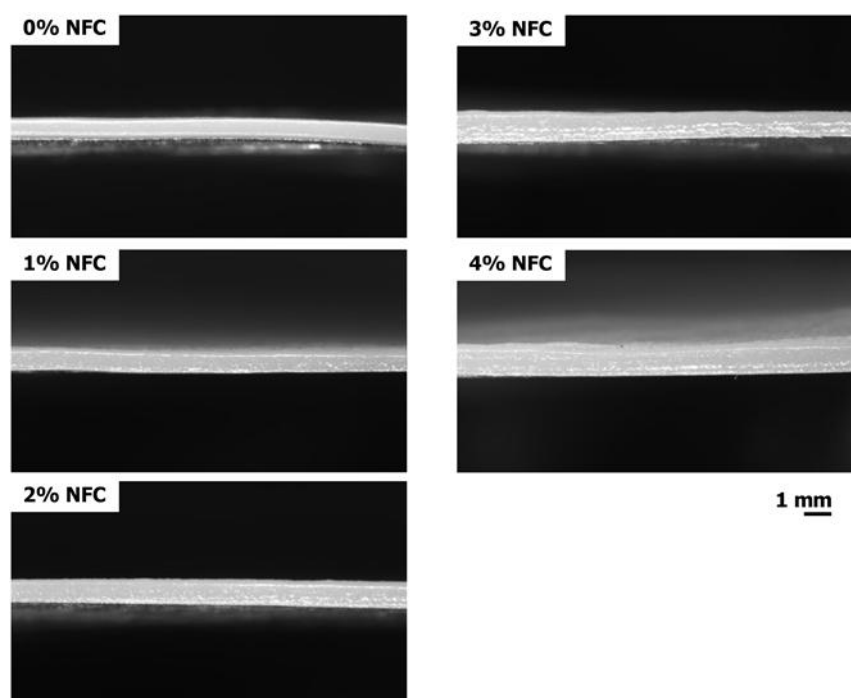
The preliminary experiments showed that it is necessary to degas the NFC suspension prior to mixing it with the matrix due to the presence of a high amount of air trapped in the fibrous network. Without the degassing operation, a high amount of air bubbles are present in the cast composite films.



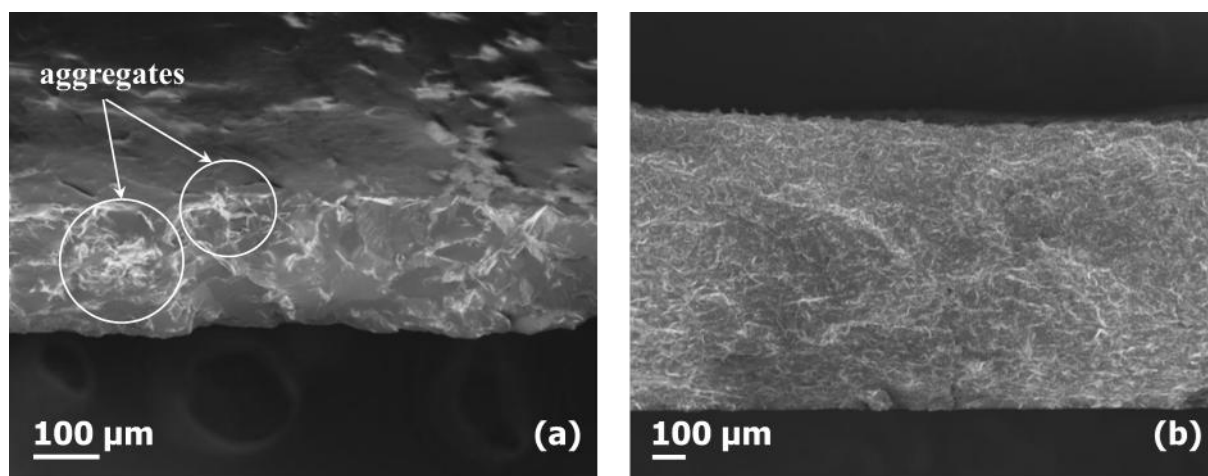
**Figure 3.9** Optical microscopy images of the neat matrix and composites prepared from C-8.23 latex and NFC: (a) cross section after casting; (b) top surface after casting and (c) cross section after casting and hot pressing

Figure 3.9a and b show the optical microscopy images of the cross section and top surface, respectively, of the neat matrix and composites prepared by casting the aqueous dispersions of the NFC compounded with C-8.23 latex. During mixing of the above components, the creation of aggregates was observed, resulting in non-homogeneous and non-stable aqueous dispersions. Furthermore, non-homogeneous composites were obtained as observed from the cross-sections and top surfaces of the cast films. On the contrary, Ben Mabrouk *et al.* (2011) reported the production of homogeneous latexes and the ensuing composites when using CNC and latex with cationic surfactant. It should be noted that NFC has much higher length and hence a single nanofibril can pass by tens of latex particles, whereas the length of a single cellulose nanocrystal is comparable with the diameter of one latex particle. Thus, the aggregation of NFC/latex system can be explained by cross-linking between nanofibers and polymer matrix particles through ionic interactions. To improve the homogeneity of the cast composites, they were hot pressed (as described in Section 3.2.4). Figure 3.9c shows that the obtained films have smooth surface.

The optical microscopy images of the composites produced from anionic latex A-8.23 and NFC by casting are shown in Figure 3.10. The ensuing composites have flat surface without visible heterogeneities at macroscopic level, comparing to the counterparts produced using cationic latex. The further characterization of the composite films C-8.23/NFC after casting and pressing and A-8.23/NFC after casting was performed using FEG-SEM. Figure 3.11a



**Figure 3.10** Optical microscopy images of the cross section of neat matrix and composites prepared from A-8.23 latex and NFC by casting



**Figure 3.11** FEG-SEM images of the freeze-fractured cross sections of the composites comprising 3 wt.% of NFC and: (a) C-8.23 latex, produced by casting and hot pressing and (b) A-8.23 latex, produced by casting

reveals the non-homogeneous distribution of NFC in C-8.23 matrix due to the presence of some aggregates. However, its counterpart with A-8.23 matrix (see Figure 3.11b) has much better homogeneity.

Tensile tests were performed on neat C-8.23 and A-8.23 latexes and those reinforced with NFC. Typical stress vs. strain curves are shown in Figure 3.12a and b for these samples. The curves indicate a typical ductile behavior with elastic, strain hardening and necking regions. Figure 3.12a shows the influence of NFC on the C-8.23-based composite mechanical properties. By increasing the filler content, the composite ultimate strength and elastic modulus increase progressively till 3 wt.% of NFC loading, above which there is no more enhancement of the mechanical properties. The visual observation of the experiment (see Figure 3.12c) reveals that such results originate from non-homogeneous distribution of NFC in the matrix, as also discussed above. Thus, the strain was accumulated in the composite regions, which were less filled with NFC. The elongation at break of > 1400% (see Table 3.3) for all the composites with C-8.23 matrix can be explained by the presence of such regions.

On the contrary, both the elastic modulus and ultimate strength values enhanced significantly while increasing the NFC content in A-8.23-based matrix composites, whereas the strain at break decreased (see Figure 3.12b), which is in agreement with the previous studies (Malainine *et al.* 2005; Chaker *et al.* 2013; Zhang *et al.* 2014). Despite the electrostatic repulsion between the filler and the matrix, the high reinforcement effect can be explained by percolation of the NFC, which forms a stiff continuous network of nanofibers linked to each other by hydrogen bonding. The elastic modulus, ultimate strength and elongation at break are collected in Table 3.3. The visual observation (see Figure 3.12d) revealed that the samples underwent an elongation without visible non-homogeneous zones.

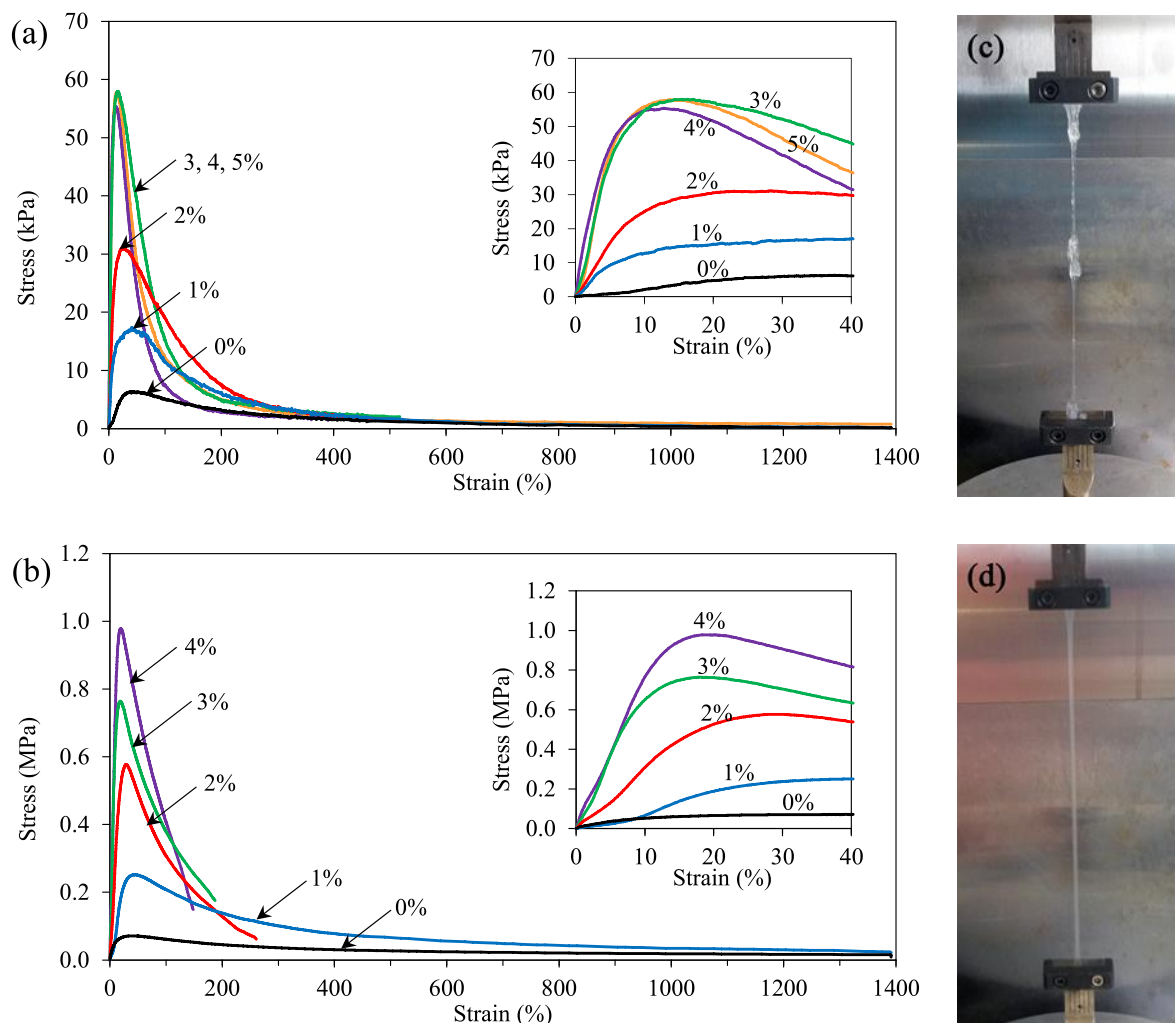


**Figure 3.12** Typical stress vs. strain curves for the films of: (a) cationic latex (C-8.23 sample) and (b) anionic latex (A-8.23 sample) at different loadings of TEMPO-oxidized NFC. The visual observation of the experiments for (c) C-8.23/3% NFC and (d) A-8.23/1% NFC samples

**Table 3.3** Mechanical properties of the neat latexes C-8.23 and A-8.23 and of the composites produced by incorporating the NFC

Sample	Elastic modulus (MPa)	Ultimate strength (kPa)	Elongation at break (%)
C-8.23	$0.034 \pm 0.003$	$7.0 \pm 0.02$	> 1400
C-8.23/1% NFC	$0.23 \pm 0.02$	$16.9 \pm 0.7$	> 1400
C-8.23/2% NFC	$0.34 \pm 0.01$	$33.4 \pm 3.6$	> 1400
C-8.23/3% NFC	$0.91 \pm 0.03$	$61.6 \pm 5.4$	> 1400
C-8.23/4% NFC	$0.79 \pm 0.07$	$50.5 \pm 6.4$	> 1400
C-8.23/5% NFC	$1.16 \pm 0.05$	$57.6 \pm 5.8$	> 1400
A-8.23	$0.37 \pm 0.03$	$66.5 \pm 4.4$	> 1400
A-8.23/1% NFC	$1.39 \pm 0.15$	$232 \pm 30$	> 1400
A-8.23/2% NFC	$5.06 \pm 0.16$	$594 \pm 67$	$336.7 \pm 77.1$
A-8.23/3% NFC	$6.47 \pm 0.20$	$763 \pm 84$	$180.6 \pm 14.9$
A-8.23/4% NFC	$7.27 \pm 0.13$	$965 \pm 117$	$161.9 \pm 23.1$

For the further application of such composites it is important to characterize their surface chemical composition on the top and bottom surface after drying, as well as the influence of incorporated NFC. Figure 3.13 shows XPS C 1s regions for raw pulp and the TEMPO-oxidized NFC. Each region can be fitted with four components for both samples. The component, centered at the binding energy of around 285.0 eV, is not representative of cellulose and is attributed to the binding energy of C 1s photoelectrons coming from a mixture of  $sp^2$  and  $sp^3$  carbon atoms bound to other carbons (C–C) and hydrogen atoms (C–H), which may originate from hemicellulose (*e.g.*, acetate groups of glucomannan), lignin or extractives (saturated and unsaturated fatty acids), since the cellulose content in the used pulp is just 93%.

The analyzed raw pulp has still higher component at  $(285.0 \pm 0.3)$  eV, comparing to the previous studies (Fardim *et al.* 2005; Pereira *et al.* 2013). This may be attributed to lubricants which may contaminate the pulp while using the machinery, in our case—standard disintegrator. The fatty acids from the lubricant tend to segregate on the surface of the material, thus they strongly influence the results. While disintegrating the oxidized fibers, cellulose can be contaminated during grinding operation, as well as the impurities can be liberated from the fibers and finally be concentrated on the surface of the dried NFC film. Moreover, it was reported that when NFC is dried directly from water it adsorbs a very high amount of non-cellulosic material on the surface, resulting in higher C–C carbon peak in XPS data (Johansson *et al.* 2011).

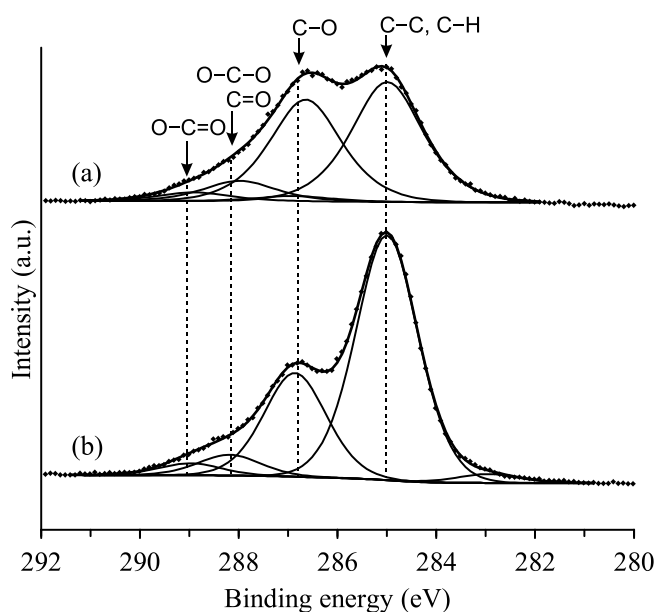


**Figure 3.13** XPS C 1s regions of: (a) the raw pulp and (b) the TEMPO-oxidized NFC

The fitted peaks, centered at  $(286.7 \pm 0.2)$  eV and  $(288.1 \pm 0.2)$  eV, correspond to C–O and O–C–O / C=O of cellulose, respectively. The component at  $(289.0 \pm 0.2)$  eV is assigned to O–C=O of cellulose. Table D.1 (see Annex D) presents the binding energies for all the fitted components obtained from XPS analysis. Quantitatively, the atomic ratios between O–C–O and C–O in the raw pulp and NFC are 0.19 and 0.20, respectively. Despite the presence of some impurities, these ratios are in a good agreement with the theoretical stoichiometric value of 0.20 in cellulose molecule. Figure 3.13b shows that the NFC has slightly higher O–C=O component, comparing to that of the raw pulp, which is explained by cellulose carboxylation while TEMPO-mediated oxidation. Despite the strong oxidation, proven by carboxylic content measurements (see Section 1.3.3), this is not much reflected by XPS, as reported previously (Karra-Châabouni *et al.* 2008; Orelma *et al.* 2012). It occurs most probably due to cellulose surface reconstruction while drying to minimize its surface free energy (Johansson *et al.* 2011).

Figure 3.14 shows C 1s regions of A-8.23 matrix and the composites produced by incorporating 3% of TEMPO-oxidized NFC. C–C component was fitted with two peaks: (i)  $sp^2$ , centered at 284.7 eV, representing the binding energy of carbon in aromatic ring and (ii)  $sp^3$ , located at 285.0 eV, representing the carbon in saturated aliphatic chains. Despite the complexity of the fitting of these two components due to the proximity of their location, the obtained fitting suggests the existence of common features at the top and at the bottom surfaces at this binding energy region. A-8.23 and A-8.23/3% NFC top surfaces are richer in saturated aliphatic chains, comparing to bottom ones, while the bottom surfaces have a higher component of carbon in aromatic rings, comparing to the top counterparts. This can be explained by the tendency of the surfactant to segregate on the top surface of the materials, which is also confirmed by the higher concentration of sulfur and sodium on the top surfaces, attributed to surfactant (SDS), as seen from Table 3.4. This surfactant layer attenuates the intensity of photoelectrons coming from latex.

The bottom surfaces of the matrix and composite have higher intensity of C–O and of O–C=O, centered at 286.5 eV and  $(288.9 \pm 0.1)$  eV, respectively, comparing to their top surface counterparts. This shows that the top surface has less acrylate, which also suggests the concentration of the surfactant on the top. Additionally, the composites top and bottom surfaces possess higher component of C–O, comparing to its matrix counterparts, which may originate from cellulose. The matrix and composite top surfaces also contain a peak centered at  $(287.3 \pm 0.1)$  eV, which most probably represent some C=O structures in extended delocalized  $\pi$  systems (*e.g.*, in benzophenone), that can result from recombined benzoyl

peroxide. All the above reveals the difference of the top and bottom surfaces of the cast composites, which can be important in the further utilization of such materials.

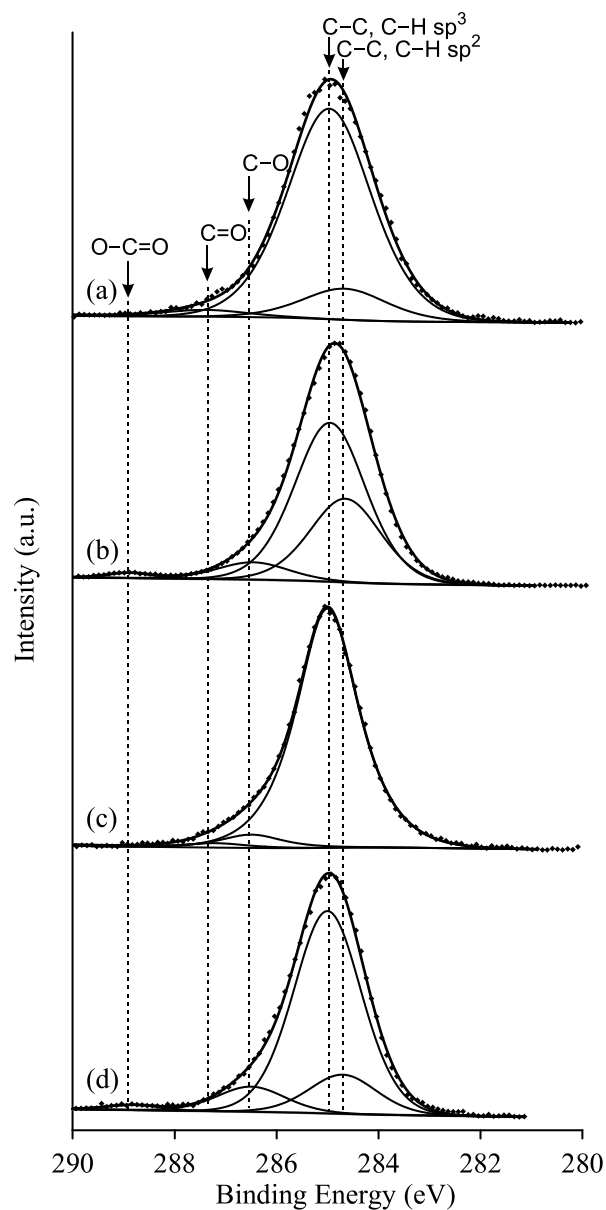


**Figure 3.14** XPS C 1s regions of: (a) A-8.23 top, (b) A-8.23 bottom, (c) A-8.23/3% NFC top and (d) A-8.23/3% NFC bottom surfaces

**Table 3.4** Atomic composition of the sample surface defined from XPS

Atoms	Atomic composition (%)			
	A-8.23 top	A-8.23 bottom	A-8.23/3% NFC top	A-8.23/3% NFC bottom
C	75.3	90.1	69.2	86.1
O	17.7	8.9	20.8	12.1
S	4.2	0.5	5.8	1.2
Na	2.8	0.5	4.2	0.6

## Conclusions

Two model latexes of poly[styrene-*co*-(2-ethylhexyl acrylate)] were synthesized *via* miniemulsion polymerization comprising cationic and anionic surfactants. The latexes were used further to study the interactions between their particles and TEMPO-oxidized NFC in composites. These interactions were examined by means of the homogeneity of NFC dispersion in the matrix and the ensuing composites mechanical properties.

Stable aqueous dispersions and homogeneous composites after casting were prepared when using latex with anionic surfactant and TEMPO-oxidized NFC. The good dispersion of the filler within the matrix was attributed to the electrostatic repulsion between the cellulose nanofibers and polymer particles. Despite these repulsive forces, the reinforcement effect was present in all the composites, comparing to the neat matrix. Both elastic modulus and ultimate strength increased progressively by incorporating the NFC into anionic latex, whereas the strain at break decreased. The reinforcement of the cast composites was achieved through hydrogen bonding of the percolated NFC network.

It was also shown that the use of cationic surfactant in latex for the purpose of enhancement of the interactions between the negatively charged NFC and positively charged matrix, and therefore the enhancement of the mechanical properties, resulted in non-homogeneous distribution of NFC within the matrix. It occurred due to aggregation through the creation of cross-linked structures between the NFC and latex particles, governed by ionic forces. XPS revealed the difference of the chemical composition at the top and bottom surfaces of the cast composite films which can have an influence in further applications of such materials.

## References

- Alemdar A, Sain M (2008) Biocomposites from wheat straw nanofibers: Morphology, thermal and mechanical properties. *Composites Science and Technology* 68:557–565. doi: 10.1016/j.compscitech.2007.05.044.
- Azizi SMA, Alloin F, Paillet M, Dufresne A (2004) Tangling Effect in Fibrillated Cellulose Reinforced Nanocomposites. *Macromolecules* 37:4313–4316. doi: 10.1021/ma035939u.
- Beamon G, Briggs D (1992) High resolution XPS of organic polymers. The Scienta ESCA300 Database, John Wileys & Sons.
- Ben Elmabrouk A, Wim T, Dufresne A, Boufi S (2009) Preparation of poly(styrene-co-hexylacrylate)/cellulose whiskers nanocomposites via miniemulsion polymerization. *Journal of Applied Polymer Science* 114:2946–2955. doi: 10.1002/app.30886.
- Ben Mabrouk, A., Ferraria, A. M., Rego, A. M. B. do, & Boufi, S. (2013). Highly transparent nanocomposite films based on polybutylmethacrylate and functionalized cellulose nanocrystals. *Cellulose*, 20(4), 1711–1723. <http://doi.org/10.1007/s10570-013-9916-4>.
- Ben Mabrouk A, Rei Vilar M, Magnin A, Belgacem MN, Boufi S (2011) Synthesis and characterization of cellulose whiskers/polymer nanocomposite dispersion by mini-emulsion polymerization. *Journal of Colloid and Interface Science* 363:129–136. doi: 10.1016/j.jcis.2011.07.050.
- Ben Mabrouk A, Salon MCB, Magnin A, Belgacem MN, Boufi S (2014) Cellulose-based nanocomposites prepared via mini-emulsion polymerization: Understanding the chemistry of the nanocellulose/matrix interface. *Colloid Surf A-Physicochem Eng Asp* 448:1–8. doi: 10.1016/j.colsurfa.2014.01.077.
- Bhatnagar A, Sain M (2005) Processing of Cellulose Nanofiber-reinforced Composites. *Journal of Reinforced Plastics and Composites* 24:1259–1268. doi: 10.1177/0731684405049864.
- Boissard CI, Bourban P-E, Plummer CJG, et al (2012) Cellular biocomposites from polylactide and microfibrillated cellulose. *Journal of Cellular Plastics* 48:445–458. doi: 10.1177/0021955X12448190.

- Bruce DM, Hobson RN, Farrent JW, Hepworth DG (2005) High-performance composites from low-cost plant primary cell walls. *Composites Part A: Applied Science and Manufacturing* 36:1486–1493. doi: 10.1016/j.compositesa.2005.03.008.
- Bunker S, Staller C, Willenbacher N, Wool R (2003) Miniemulsion polymerization of acrylated methyl oleate for pressure sensitive adhesives. *International Journal of Adhesion and Adhesives* 23:29–38. doi: 10.1016/S0143-7496(02)00079-9.
- Chaker A, Mutje P, Vilaseca F, Boufi S (2013) Reinforcing potential of nanofibrillated cellulose from nonwoody plants. *Polym Compos* 34:1999–2007. doi: 10.1002/pc.22607.
- Chakraborty A, Sain M, Kortschot M (2005) Cellulose microfibrils: A novel method of preparation using high shear refining and cryocrushing. *Holzforschung* 59:102–107.
- Chakraborty A, Sain M, Kortschot M, Cutler S (2007) Dispersion of Wood Microfibers in a Matrix of Thermoplastic Starch and Starch–Polylactic Acid Blend. *Journal of Biobased Materials and Bioenergy* 1:71–77. doi: 10.1166/jbmb.2007.008.
- Dalmas F, Cavallé J-Y, Gauthier C, Chazeau L, Dendievel R (2007) Viscoelastic behavior and electrical properties of flexible nanofiber filled polymer nanocomposites. Influence of processing conditions. *Composites Science and Technology* 67:829–839. doi: 10.1016/j.compscitech.2006.01.030.
- Dufresne A (2008) Cellulose-Based Composites and Nanocomposites. In: Belgacem MN and Gandini A (ed) *Monomers, Polymers and Composites from Renewable Resources*. Elsevier, Amsterdam, pp 401–418.
- Dufresne A, Dupeyre D, Vignon MR (2000) Cellulose microfibrils from potato tuber cells: Processing and characterization of starch–cellulose microfibril composites. *J Appl Polym Sci* 76:2080–2092. doi: 10.1002/(SICI)1097-4628(20000628)76:14<2080::AID-APP12>3.0.CO;2-U.
- Dufresne A, Vignon MR (1998) Improvement of Starch Film Performances Using Cellulose Microfibrils. *Macromolecules* 31:2693–2696. doi: 10.1021/ma971532b.
- Fardim P, Gustafsson J, von Schoultz S, Peltonen J, Holmbom B (2005) Extractives on fiber surfaces investigated by XPS, ToF-SIMS and AFM. *Colloids and Surfaces A: Physicochemical and Engineering Aspects* 255:91–103. doi: 10.1016/j.colsurfa.2004.12.027.

- Favier V, Canova GR, Cavaillé JY, Chanzy H, Dufresne A, Gauthier C (1995) Nanocomposite materials from latex and cellulose whiskers. *Polym Adv Technol* 6:351–355. doi: 10.1002/pat.1995.220060514.
- Fernandes SCM, Freire CSR, Silvestre AJD, et al (2010) Transparent chitosan films reinforced with a high content of nanofibrillated cellulose. *Carbohydrate Polymers* 81:394–401. doi: 10.1016/j.carbpol.2010.02.037.
- Fernández A, Sánchez MD, Ankerfors M, Lagaron JM (2008) Effects of ionizing radiation in ethylene-vinyl alcohol copolymers and in composites containing microfibrillated cellulose. *J Appl Polym Sci* 109:126–134. doi: 10.1002/app.27709.
- Gällstedt M, Hedenqvist MS (2006) Packaging-related mechanical and barrier properties of pulp–fiber–chitosan sheets. *Carbohydrate Polymers* 63:46–53. doi: 10.1016/j.carbpol.2005.07.024.
- George J, Sreekala MS, Thomas S (2001) A review on interface modification and characterization of natural fiber reinforced plastic composites. *Polym Eng Sci* 41:1471–1485. doi: 10.1002/pen.10846.
- Haloi DJ, Ata S, Singha NK, et al (2012) Acrylic AB and ABA Block Copolymers Based on Poly(2-ethylhexyl acrylate) (PEHA) and Poly(methyl methacrylate) (PMMA) via ATRP. *ACS Appl Mater Interfaces* 4:4200–4207. doi: 10.1021/am300915j.
- Helbert W, Cavaillé JY, Dufresne A (1996) Thermoplastic nanocomposites filled with wheat straw cellulose whiskers. Part I: Processing and mechanical behavior. *Polymer Composites* 17:604–611. doi: 10.1002/pc.10650.
- Henriksson M, Berglund LA (2007) Structure and properties of cellulose nanocomposite films containing melamine formaldehyde. *J Appl Polym Sci* 106(4):2814–2817. doi: 10.1002/app.26946.
- Hietala M, Mathew AP, Oksman K (2013) Bionanocomposites of thermoplastic starch and cellulose nanofibers manufactured using twin-screw extrusion. *European Polymer Journal* 49:950–956. doi: 10.1016/j.eurpolymj.2012.10.016.
- Hosokawa J, Nishiyama M, Yoshihara K, Kubo T (1990) Biodegradable film derived from chitosan and homogenized cellulose. *Ind Eng Chem Res* 29:800–805. doi: 10.1021/ie00101a015.

- Hubbe MA, Rojas OJ, Lucia LA, Sain M (2008) Cellulosic Nanocomposites: A Review. *BioResources* 3:929–980.
- Iwamoto S, Nakagaito AN, Yano H, Nogi M (2005) Optically transparent composites reinforced with plant fiber-based nanofibers. *Appl Phys A* 81:1109–1112. doi: 10.1007/s00339-005-3316-z.
- Iwatake A, Nogi M, Yano H (2008) Cellulose nanofiber-reinforced polylactic acid. *Composites Science and Technology* 68:2103–2106. doi: 10.1016/j.compscitech.2008.03.006.
- Johansson L-S, Tammelin T, Campbell JM, Setälä H, Österberg M (2011) Experimental evidence on medium driven cellulose surface adaptation demonstrated using nanofibrillated cellulose. *Soft Matter* 7:10917. doi: 10.1039/c1sm06073b.
- Kalia S, Boufi S, Celli A, Kango S (2014) Nanofibrillated cellulose: surface modification and potential applications. *Colloid Polym Sci* 292:5–31. doi: 10.1007/s00396-013-3112-9.
- Kalia S, Kaith BS, Kaur I (2009) Pretreatments of natural fibers and their application as reinforcing material in polymer composites—A review. *Polym Eng Sci* 49:1253–1272. doi: 10.1002/pen.21328.
- Karra-Châabouni M, Bouaziz I, Boufi S, Botelho do Rego AM, Gargouri Y (2008) Physical immobilization of *Rhizopus oryzae* lipase onto cellulose substrate: Activity and stability studies. *Colloids and Surfaces B: Biointerfaces* 66:168–177. doi: 10.1016/j.colsurfb.2008.06.010.
- Kavousian A, Ziaee F, Nekoomanesh MH, Leamen MJ, Penlidis A (2004) Determination of monomer reactivity ratios in styrene/2-ethylhexylacrylate copolymer. *J Appl Polym Sci* 92:3368–3370. doi: 10.1002/app.20338.
- Larsson K, Berglund LA, Ankerfors M, Lindström T (2012) Polylactide latex/nanofibrillated cellulose bionanocomposites of high nanofibrillated cellulose content and nanopaper network structure prepared by a papermaking route. *J Appl Polym Sci* 125:2460–2466. doi: 10.1002/app.36413.
- Leitner J, Hinterstoisser B, Wastyn M, et al (2007) Sugar beet cellulose nanofibril-reinforced composites. *Cellulose* 14:419–425. doi: 10.1007/s10570-007-9131-2.
- Lee K-Y, Tammelin T, Schulfte K, et al (2012) High Performance Cellulose Nanocomposites: Comparing the Reinforcing Ability of Bacterial Cellulose and

Nanofibrillated Cellulose. ACS Appl Mater Interfaces 4:4078–4086. doi: 10.1021/am300852a.

Lönnerberg H, Fogelström L, Berglund L, et al (2008) Surface grafting of microfibrillated cellulose with poly( $\epsilon$ -caprolactone) – Synthesis and characterization. European Polymer Journal 44:2991–2997. doi: 10.1016/j.eurpolymj.2008.06.023

López-Rubio A, Lagaron JM, Ankerfors M, et al (2007) Enhanced film forming and film properties of amylopectin using micro-fibrillated cellulose. Carbohydrate Polymers 68:718–727. doi: 10.1016/j.carbpol.2006.08.008.

Lu J, Wang T, Drzal LT (2008) Preparation and properties of microfibrillated cellulose polyvinyl alcohol composite materials. Composites Part A: Applied Science and Manufacturing 39:738–746. doi: 10.1016/j.compositesa.2008.02.003.

Malainine ME, Mahrouz M, Dufresne A (2005) Thermoplastic nanocomposites based on cellulose microfibrils from *Opuntia ficus-indica* parenchyma cell. Composites Science and Technology 65:1520–1526. doi: 10.1016/j.compscitech.2005.01.003

Masoodi R, El-Hajjar RF, Pillai KM, Sabo R (2012) Mechanical characterization of cellulose nanofiber and bio-based epoxy composite. Materials & Design 36:570–576. doi: 10.1016/j.matdes.2011.11.042.

Mathew AP, Chakraborty A, Oksman K, Sain M (2006) The structure and mechanical properties of cellulose nanocomposites prepared by twin screw extrusion. In: Oksman K, Sain M (eds) Cellulose nanocomposites: processing, characterization, and properties. American Chemical Society, Washington DC 938:114–131. doi: 10.1021/bk-2006-0938.ch009.

Miao C, Hamad WY (2013) Cellulose reinforced polymer composites and nanocomposites: a critical review. Cellulose 20:2221–2262. doi: 10.1007/s10570-013-0007-3.

Missoum K, Bras J, Belgacem MN (2012) Water Redispersible Dried Nanofibrillated Cellulose by Adding Sodium Chloride. Biomacromolecules 13:4118–4125. doi: 10.1021/bm301378n.

Mittal V (2010) Miniemulsion Polymerization: An Overview. In: Mittal V (ed) Miniemulsion Polymerization Technology. John Wiley & Sons, Inc., pp 1–23. doi: 10.1002/9780470922354.ch1

- Mondragón M, Arroyo K, Romero-García J (2008) Biocomposites of thermoplastic starch with surfactant. *Carbohydrate Polymers* 74:201–208. doi: 10.1016/j.carbpol.2008.02.004.
- Moon RJ, Martini A, Nairn J, et al (2011) Cellulose nanomaterials review: structure, properties and nanocomposites. *Chem Soc Rev* 40:3941–3994. doi: 10.1039/C0CS00108B.
- Nakagaito AN, Fujimura A, Sakai T, et al (2009) Production of microfibrillated cellulose (MFC)-reinforced polylactic acid (PLA) nanocomposites from sheets obtained by a papermaking-like process. *Composites Science and Technology* 69:1293–1297. doi: 10.1016/j.compscitech.2009.03.004.
- Nakagaito AN, Nogi M, Yano H (2010) Displays from Transparent Films of Natural Nanofibers. *MRS Bulletin* 35:214–218. doi: 10.1557/mrs2010.654.
- Nakagaito AN, Yano H (2004) The effect of morphological changes from pulp fiber towards nano-scale fibrillated cellulose on the mechanical properties of high-strength plant fiber based composites. *Appl Phys A* 78:547–552. doi: 10.1007/s00339-003-2453-5.
- Nakagaito AN, Yano H (2008) Toughness enhancement of cellulose nanocomposites by alkali treatment of the reinforcing cellulose nanofibers. *Cellulose* 15:323–331. doi: 10.1007/s10570-007-9168-2.
- Nogi M, Yano H (2008) Transparent Nanocomposites Based on Cellulose Produced by Bacteria Offer Potential Innovation in the Electronics Device Industry. *Adv Mater* 20:1849–1852. doi: 10.1002/adma.200702559.
- Nordqvist D, Idermark J, Hedenqvist MS, Gällstedt M, Ankerfors M, and Lindström T (2007) Enhancement of the Wet Properties of Transparent Chitosan–Acetic-Acid–Salt Films Using Microfibrillated Cellulose. *Biomacromolecules* 8:2398–2403. doi: 10.1021/bm070246x.
- Okubo K, Fujii T, Yamashita N (2005) Improvement of Interfacial Adhesion in Bamboo Polymer Composite Enhanced with Micro-Fibrillated Cellulose. *JSME International Journal Series A Solid Mechanics and Material Engineering* 48:199–204. doi: 10.1299/jsmea.48.199.
- Okahisa Y, Abe K, Nogi M, et al (2011) Effects of delignification in the production of plant-based cellulose nanofibers for optically transparent nanocomposites. *Composites Science and Technology* 71:1342–1347. doi: 10.1016/j.compscitech.2011.05.006

- Oksman K, Mathew AP, Bondeson D, Kvien I (2006) Manufacturing process of cellulose whiskers/polylactic acid nanocomposites. *Composites Science and Technology* 66:2776–2784. doi: 10.1016/j.compscitech.2006.03.002.
- Orelma H, Filpponen I, Johansson L-S, Österberg M, Rojas OJ, Laine J (2012) Surface Functionalized Nanofibrillar Cellulose (NFC) Film as a Platform for Immunoassays and Diagnostics. *Biointerphases* 7:61. doi: 10.1007/s13758-012-0061-7.
- Pasquini D, Teixeira E de M, da Silva Curvelo AA, Belgacem MN, Dufresne A (2010) Extraction of cellulose whiskers from cassava bagasse and their applications as reinforcing agent in natural rubber. *Ind Crop Prod* 32:486–490. doi: 10.1016/j.indcrop.2010.06.022.
- Pereira PHF, Voorwald HJC, Cioffi MOH, Silva MLCPDa, Rego AMB, Ferraria F, Pinho MNDe (2013) Sugarcane bagasse cellulose fibres and their hydrous niobium phosphate composites: synthesis and characterization by XPS, XRD and SEM. *Cellulose* 21:641–652. doi: 10.1007/s10570-013-0113-2.
- Plackett D, Anturi H, Hedenqvist M, Ankerfors M, Gällstedt M, Lindström T, Siró I (2010) Physical properties and morphology of films prepared from microfibrillated cellulose and microfibrillated cellulose in combination with amylopectin. *J Appl Polym Sci* 117:3601–3609. doi: 10.1002/app.32254.
- Qing Y, Sabo R, Wu Y, Cai Z (2012) High-performance cellulose nanofibrils composite films. *BioResources* 7:3064–3075. doi: 10.15376/biores.7.3.3064-3075.
- Qing Y, Sabo R, Cai Z, Wu Y (2013) Resin impregnation of cellulose nanofibril films facilitated by water swelling. *Cellulose* 20:303–313. doi: 10.1007/s10570-012-9815-0.
- Saheb DN, Jog JP (1999) Natural fiber polymer composites: A review. *Adv Polym Technol* 18:351–363. doi: 10.1002/(SICI)1098-2329(199924)18:4<351::AID-ADV6>3.0.CO;2-X.
- Saito T, Kimura S, Nishiyama Y, Isogai A (2007) Cellulose nanofibers prepared by TEMPO-mediated oxidation of native cellulose. *Biomacromol* 8:2485–2491. doi:10.1021/bm0703970.
- Savadekar NR, Mhaske ST (2012) Synthesis of nano cellulose fibers and effect on thermoplastics starch based films. *Carbohydrate Polymers* 89:146–151. doi: 10.1016/j.carbpol.2012.02.063.

- Schork FJ, Luo Y, Smulders W, Russum JP, Butté A, Fontenot K (2005) Miniemulsion Polymerization. In: Okubo M (ed) *Polymer Particles*. *Adv Polym Sci* 175:129–255. doi: 10.1007/b100115.
- Shimazaki Y, Miyazaki Y, Takezawa Y, Nogi M, Abe K, Ifuku S, Yano H (2007) Excellent thermal conductivity of transparent cellulose nanofiber/epoxy resin nanocomposites. *Biomacromolecules* 8(9):2976–2978. doi: 10.1021/bm7004998.
- Siqueira G, Abdillahi H, Bras J, Dufresne A (2009a) High reinforcing capability cellulose nanocrystals extracted from *Syngonanthus nitens* (Capim Dourado). *Cellulose* 17:289–298. doi: 10.1007/s10570-009-9384-z.
- Siqueira G, Bras J, Dufresne A (2009b) Cellulose Whiskers versus Microfibrils: Influence of the Nature of the Nanoparticle and its Surface Functionalization on the Thermal and Mechanical Properties of Nanocomposites. *Biomacromolecules* 10:425–432. doi: 10.1021/bm801193d.
- Siqueira G, Bras J, Dufresne A (2010) Cellulosic Bionanocomposites: A Review of Preparation, Properties and Applications. *Polymers* 2:728–765. doi: 10.3390/polym2040728.
- Siró I, Plackett D (2010) Microfibrillated cellulose and new nanocomposite materials: a review. *Cellulose* 17:459–494. doi: 10.1007/s10570-010-9405-y.
- Srithep Y, Turng L-S, Sabo R, Clemons C (2012) Nanofibrillated cellulose (NFC) reinforced polyvinyl alcohol (PVOH) nanocomposites: properties, solubility of carbon dioxide, and foaming. *Cellulose* 19:1209–1223. doi: 10.1007/s10570-012-9726-0.
- Srithep Y, Ellingham T, Peng J, Sabo R, Clemons C, Turng L-S, Pilla S (2013) Melt compounding of poly (3-hydroxybutyrate-co-3-hydroxyvalerate)/nanofibrillated cellulose nanocomposites. *Polymer Degradation and Stability* 98:1439–1449. doi: 10.1016/j.polymdegradstab.2013.05.006.
- Suryanegara L, Nakagaito AN, Yano H (2009) The effect of crystallization of PLA on the thermal and mechanical properties of microfibrillated cellulose-reinforced PLA composites. *Composites Science and Technology* 69:1187–1192. doi: 10.1016/j.compscitech.2009.02.022.

- Svagan AJ, Azizi SMA, Berglund LA (2007) Biomimetic Polysaccharide Nanocomposites of High Cellulose Content and High Toughness. *Biomacromolecules* 8:2556–2563. doi: 10.1021/bm0703160.
- Svagan AJ, Hedenqvist MS, Berglund L (2009) Reduced water vapour sorption in cellulose nanocomposites with starch matrix. *Composites Science and Technology* 69:500–506. doi: 10.1016/j.compscitech.2008.11.016.
- Tanpichai S, Sampson WW, Eichhorn SJ (2012) Stress-transfer in microfibrillated cellulose reinforced poly(lactic acid) composites using Raman spectroscopy. *Composites Part A: Applied Science and Manufacturing* 43:1145–1152. doi: 10.1016/j.compositesa.2012.02.006.
- Takagi H, Asano A (2008) Effects of processing conditions on flexural properties of cellulose nanofiber reinforced “green” composites. *Composites Part A: Applied Science and Manufacturing* 39:685–689. doi: 10.1016/j.compositesa.2007.08.019.
- Trovatti E, Fernandes SCM, Rubatat L, et al (2012) Pullulan–nanofibrillated cellulose composite films with improved thermal and mechanical properties. *Composites Science and Technology* 72:1556–1561. doi: 10.1016/j.compscitech.2012.06.003.
- Uetani K, Yano H (2011) Nanofibrillation of Wood Pulp Using a High-Speed Blender. *Biomacromolecules* 12:348–353. doi: 10.1021/bm101103p.
- Virtanen S, Vuoti S, Heikkinen H, Lahtinen P (2014) High strength modified nanofibrillated cellulose-polyvinyl alcohol films. *Cellulose* 21:3561–3571. doi: 10.1007/s10570-014-0347-7.
- Wang B, Sain M (2007a) Dispersion of soybean stock-based nanofiber in a plastic matrix. *Polym Int* 56:538–546. doi: 10.1002/pi.2167.
- Wang B, Sain M (2007b) Isolation of nanofibers from soybean source and their reinforcing capability on synthetic polymers. *Composites Science and Technology* 67:2521–2527. doi: 10.1016/j.compscitech.2006.12.015.
- Wang B, Sain M (2007c) The effect of chemically coated nanofiber reinforcement on biopolymer based nanocomposites. *BioResources* 2:371–388. doi: 10.15376/biores.2.3.371-388.
- Zhai T, Zheng Q, Cai Z, Turng L-S, Xia H, Gong S (2015) Poly(vinyl alcohol)/Cellulose Nanofibril Hybrid Aerogels with an Aligned Microtubular Porous Structure and Their

Composites with Polydimethylsiloxane. *ACS Appl Mater Interfaces* 7:7436–7444. doi: 10.1021/acsami.5b01679.

Zhang C, Zhai T, Sabo R, Clemons C, Dan Y, Turng L-S (2014) Reinforcing Natural Rubber with Cellulose Nanofibrils Extracted from Bleached Eucalyptus Kraft Pulp. *Journal of Biobased Materials and Bioenergy* 8:317–324. doi: 10.1166/jbmb.2014.1441.

Zimmermann T, Pöhler E, Geiger T (2004) Cellulose Fibrils for Polymer Reinforcement. *Adv Eng Mater* 6:754–761. doi: 10.1002/adem.200400097.



# General conclusions

This doctoral dissertation was focused on the development of bionanocomposites from nanofibrillated cellulose and latex. The main target of this study was to elaborate new composite materials with improved mechanical properties and acquire the homogeneous dispersion of hydrophilic cellulose in the hydrophobic polymer matrix. In this context, several objectives were established:

- (i) NFC extraction from wood pulp. Emphasis has been placed on the use of activation methods based on enzymatic hydrolysis and oxidation combined with mechanical treatment in order to facilitate the delamination of the nanofibrils and to reduce energy consumption during the production process;
- (ii) rheological and structural characterization of NFC aqueous suspensions. NFC is typically extracted into water medium, which loosens the hydrogen bonding between the nanofibrils and prevents their reverse coagulation, the resulting material appears as a viscous gel at low solids content (1–2 wt.%). Therefore, the rheological properties become a major issue since the flow is involved in the production process and can affect the performance of the NFC-based products;
- (iii) latex synthesis *via* miniemulsion polymerization with subsequent incorporation of NFC and film casting. The use of cationic and anionic surfactants was examined in order to have a clear-cut evidence of the homogeneity of the NFC dispersion in the latex and the quality of NFC/matrix interactions after film casting.

The NFC suspensions were successfully produced from dry bleached bisulfite softwood pulp using enzymatic and TEMPO-oxidation pretreatments followed by wet grinding in Supermasscolloider grinder (Masuko Sangyo Co. Ltd., Japan). The enzymatic pretreatment using cellulase solution (Celluclast 1.5 L) and monocomponent endoglucanase solution (FiberCare R) was compared in terms of nanofibrils isolation.

The endoglucanase solution was found to be more favourable for the NFC production since it led to lower depolymerization with better dissociation of the nanofibrils comparing to cellulase solution. Grinding of TEMPO-oxidized suspensions produced nanofibrils with lower lateral dimensions, as well as reduced length, comparing to that associated with enzymatically prehydrolyzed pulp. All the enzymatically treated NFC samples possessed highly entangled flocculated structures.

The concentration and the type of applied enzymes had an influence on the rheological behavior of the produced NFC suspensions. The dynamic moduli as well as the apparent viscosity and shear stress decreased with the increase of enzymatic charge which is likely to occur due to cellulose saccharification together with nanofibrils separation. The higher viscoelastic properties were found for endoglucanase-hydrolyzed suspensions. The NFC obtained from TEMPO-mediated oxidation resulted into stronger fibrous network.

As far as the authors of this work are aware, it is the first study devoted to the investigation of the flow instabilities in NFC suspensions using visualization approach. A slippage on the edge of geometry tools and suspension (wall-slip) as well as the flow localization within a specific volume of the sample (shear banding) were explored. These phenomena introduce an error into the rheological measurements. It was shown that the flow behavior depends strongly on the used rheometer geometry at low shear rates, where the wall-slip plays a significant role. However, at high shear rates the influence of the used geometry is neutralized, resulting in similar values of shear stress. The roughening of the geometry tools was proposed to overcome this problem and was shown to improve the measured response of the suspension for TEMPO-oxidized NFC.

SAXS was used to study the structural properties of NFC in aqueous medium. The scattering signal of the NFC was modeled using unified fit function (Beaucage) approach. It allowed to distinguish the scattering signal from individual nanofibers and their aggregates or residual non-fibrillated fibers, which can give a perspective for further studies in the field of MFC/NFC fractionation. The average diameter of nanofibrils swollen in water was also determined based on the unified fit function approach.

Finally, two model latexes of poly[styrene-*co*-(2-ethylhexyl acrylate)] were synthesized *via* miniemulsion polymerization comprising cationic and anionic surfactants. TEMPO-oxidized NFC suspensions were incorporated in these latexes and the composites were obtained by casting. The good dispersion of the NFC within anionic latex was attributed to the electrostatic repulsion between the cellulose nanofibers and polymer particles. Despite these repulsive forces, the reinforcement effect was found for the composites, comparing to the neat matrix. Both elastic modulus and ultimate strength increased progressively, whereas the strain at break decreased. The reinforcement of the cast composites was achieved through hydrogen bonding of the percolated NFC network.

The use of cationic latex and TEMPO-oxidized NFC resulted in non-homogeneous distribution of NFC within the matrix. It occurred due to aggregation through the creation of

cross-linked structures between the NFC and latex particles, governed by ionic forces. The increase of the composite mechanical properties was observed with an increase of NFC content till a specific concentration, beyond which the enhancement of elastic modulus and ultimate strength was not observed. This occurred due to non-homogeneous distribution of NFC within the matrix which was also proved by non-uniform elongation during the tensile tests.



# Résumé substantiel (Extended Summary)

Le développement de matériaux composites biosourcés pour différentes applications industrielles est aujourd'hui un sujet de recherche fréquent. Un grand nombre d'études ont été effectuées sur l'utilisation de fibres naturelles dans les matériaux composites comme une alternative à des charges organiques et inorganiques synthétiques (ex. de l'aramide, du carbone ou des fibres de verre), qui sont largement utilisées pour renforcer des matrices thermoplastiques. Par rapport à des composites classiques les matériaux nanocomposites ont un certain nombre d'avantages, comme par exemple des meilleures propriétés thermiques, mécaniques et barrière à faible teneur en charges, ainsi que leur faible poids et la transparence (en l'absence de chromophores dans sa structure chimique).

En raison des propriétés spécifiques de nanocellulose, comme par exemple haute rigidité, faible densité, matières premières abondantes, propriétés optiques, biodégradabilité et renouvellement, cette famille de nanomatériaux biosourcés offre un potentiel de développement économique important pour son utilisation comme charge dans des composites polymères.

Cette thèse a pour but le développement de matériaux composites à base de nanofibrilles de cellulose (NFC) et de latex. Les principaux objectifs de ce travail étaient d'élaborer de nouveaux matériaux composites avec des propriétés mécaniques améliorées et d'obtenir une dispersion homogène de la cellulose hydrophile dans la matrice polymère hydrophobe. Dans ce contexte, plusieurs objectifs ont été fixés:

- (i) l'extraction des NFC à partir de pâte de bois. L'accent a été mis sur l'utilisation de méthodes d'activation sur la base de traitements chimiques et enzymatiques combinés avec un traitement mécanique afin de faciliter la délamination des NFC et réduire la consommation d'énergie pendant le processus de production;
- (ii) la caractérisation rhéologique et structurelle de suspensions aqueuses de NFC. Les NFC étant extraites dans l'eau, ce qui réduit l'énergie de liaison hydrogène et empêche leur réaggrégation. Le matériau produit après traitement apparaît comme un gel visqueux à faible teneur en solides (1–2 % en poids). Par conséquent, maîtriser les propriétés rhéologiques de ces suspensions devient un enjeu majeur, car l'écoulement est impliqué dans le processus de production et peut influencer fortement les performances des produits à base de NFC;

(iii) la synthèse de latex par polymérisation en miniémulsion avec incorporation des NFC puis la mise en forme des films par coulée-évaporation. L'utilisation de tensioactifs cationiques et anioniques a été évaluée afin de mettre en évidence clairement l'homogénéité de la dispersion de NFC dans le latex et la qualité de l'interaction NFC/matrice après la coulée des films.

Cette thèse comporte trois chapitres décrivant en détails les objectifs présentés ci-dessus, les résultats, les analyses effectuées et les conclusions obtenues.

## Chapitre 1 Production et propriétés des nanofibrilles de cellulose

Dans ce chapitre, l'influence de la déstructuration mécanique, combinée à un traitement enzymatique ou d'oxydation, sur la capacité à atteindre une séparation optimale des nanofibrilles de cellulose a été analysée.

Les principales sources de cellulose actuellement sont les plantes et le bois. Outre la cellulose ces matières végétales contiennent également des hémicelluloses et de la lignine, une très faible teneur en matières extractibles et des substances minérales. La cellulose possède une architecture bien organisée d'éléments fibrillaires composant les cellules (voir

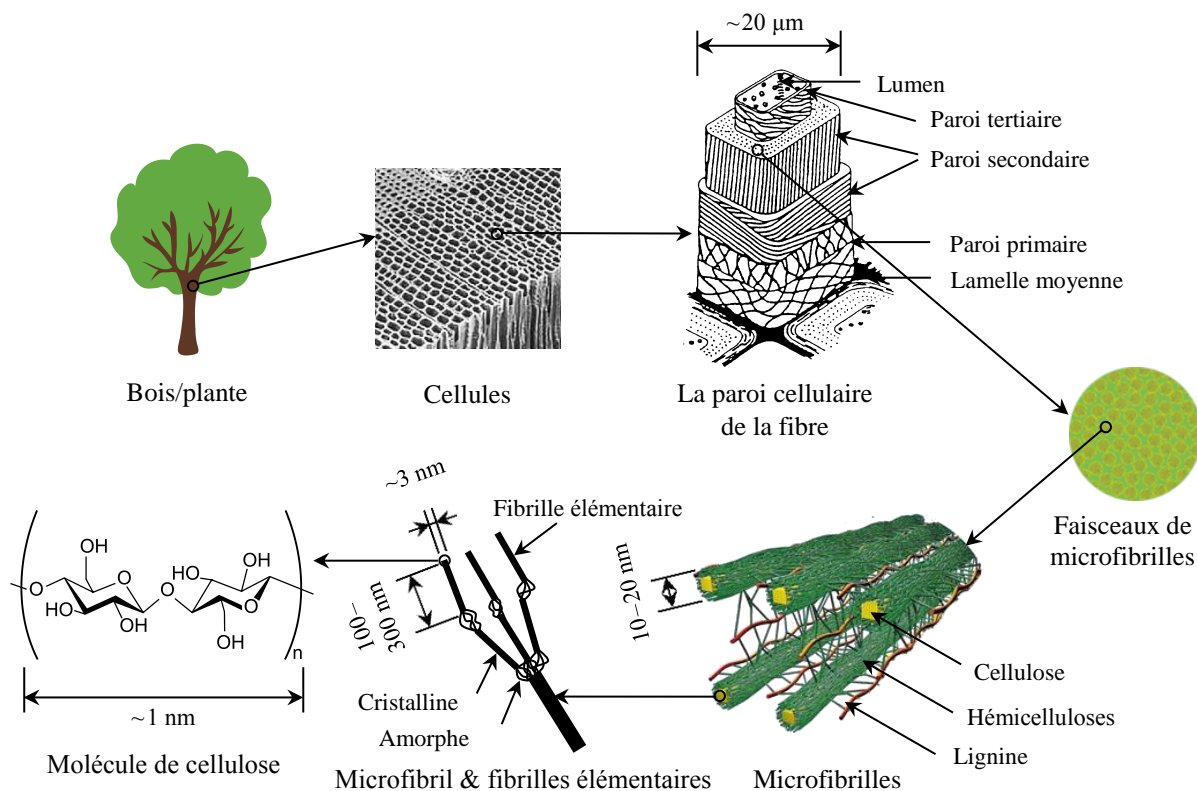


**Figure 1** Schéma de la composition structurelle de bois d'épicéa

Figure 1). La cible principale de la production des NFC est leur extraction à partir de microfibrilles. Pour atteindre cet objectif, différents prétraitements biochimiques ont été utilisés.

Dans cette thèse, l'hydrolyse de la cellulose a été effectuée en utilisant: (i) une solution de cellulase (Celluclast 1.5 L), avec une activité principale d'endoglucanase et exoglucanase, et (ii) une solution d'endoglucanase monocomposant (FiberCare R). Ces deux types de traitement ont été comparés en termes de capacité à l'isolement des nanofibrilles. Par ailleurs, l'oxydation de la cellulose par l'agent 2,2,6,6-tetramethylpiperidine-1-oxyl (TEMPO) en utilisant de l'hypochlorite de sodium a été étudiée.

Les suspensions de NFC ont été produites à partir de la pâte sèche de résineux blanchie au bisulfite en utilisant les prétraitements enzymatiques et TEMPO suivis par broyage humide. L'augmentation de la concentration enzymatique conduit à une hydrolyse plus forte et par conséquent à une plus grande efficacité de défibrillation, qui s'est accompagnée d'une diminution du degré de polymérisation (DP) et d'une augmentation de l'indice de cristallinité (IC).

Il a été démontré que l'hydrolyse enzymatique en utilisant la solution d'endoglucanase (FiberCare R) est plus favorable pour la production de NFC car elle a conduit à une dépolymérisation plus faible avec une meilleure séparation des nanofibrilles comparativement à la solution de cellulase (Celluclast 1.5 L), qui entraîne une activité plus grande de l'endoglucanase et d'exoglucanase. Le broyage de suspensions oxydées par TEMPO produit les nanofibrilles les plus fines avec des dimensions latérales inférieures, ainsi qu'une longueur réduite, en comparaison à celles préparées à partir de la pâte préhydrolysée par voie enzymatique. Tous les échantillons de NFC traités par voie enzymatique possèdent des structures flocculées très enchevêtrées.

Les NFC produites par oxydation TEMPO et broyage ont un diamètre de  $4 \pm 2$  nm, mesuré par microscope à force atomique (AFM) (voir Figure 2), et la teneur en carboxyle est de  $1,75 \pm 0,05$  mmol/g, déterminée selon la méthode de titrage conductimétrique. Ces NFC ont été utilisés par la suite pour l'incorporation dans les matrices polymères.

Il a également été montré que la morphologie des suspensions de NFC produites dépend des conditions de traitement appliquées, qui ont des conséquences ensuite sur les propriétés du matériau. Une fibrillation plus intensive aboutit à des nanofibrilles de tailles inférieures. Par conséquent, différents grades de NFC peuvent être produits. Les conditions exactes de traitement doivent être adaptées selon les exigences de l'application spécifique. La consommation

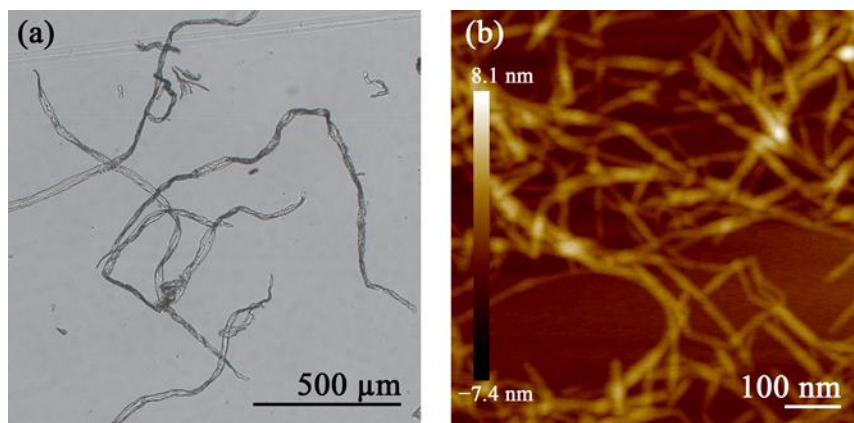


**Figure 2** L'image de microscopie optique de pâte de cellulose (a) et l'image du capteur de hauteur de microscope à force atomique pour NFC TEMPO-oxydé (b)

d'énergie la plus réduite et la plus efficace lors de la production de NFC est toujours une question importante pour leur industrialisation.

## **Chapitre 2 Propriétés rhéologiques et structurales de suspensions de nanofibrilles de cellulose**

Les NFC sont généralement fabriquées sous la forme de suspensions aqueuses. La rhéologie de ces suspensions devient alors une question clé, car l'écoulement est impliqué dans le processus de production et peut affecter les propriétés du produit final. Par conséquent, la maîtrise des propriétés d'écoulement de ces suspensions est nécessaire pour améliorer les performances de leur mise en forme et la qualité des matériaux composites fabriqués. En outre, les propriétés rhéologiques donnent des informations sur l'organisation structurale de ces matériaux complexes biphasiques. Une analyse plus approfondie des propriétés structurales des suspensions de NFC peut être effectuée en utilisant des techniques de diffusion, comme par exemple la diffusion de rayons X aux petits angles (SAXS).

Dans ce chapitre, le comportement rhéologique de suspensions aqueuses de NFC hydrolysées par voie enzymatique et oxydées par TEMPO est étudié. Les problèmes d'instabilités d'écoulement (glissement à la paroi et bandes de cisaillement), qui introduisent une erreur dans la mesure rhéométrique de la suspension mesurée, ont été mis en évidence. Ces phénomènes ont été étudiés par une technique de visualisation en utilisant différentes géométries d'écoulement. SAXS a été utilisée pour fournir des informations supplémentaires sur l'organisation structurale de NFC en milieu aqueux. Le diamètre moyen statistique a été déterminé pour les NFC hydratées à partir des données de SAXS et utilisant l'approche de Beaucage qui a développé une fonction d'ajustement unifiée de l'intensité diffusée.

Une étude rhéologique complète des suspensions de NFC en cisaillement harmonique et en régime d'écoulement permanent a été effectuée. Toutes les suspensions de type gel ont des propriétés rhéo-fluidifiantes. Il a été montré que la concentration et le type d'enzymes appliquées ont une influence sur le comportement rhéologique des suspensions testées. Les modules visco-élastiques ainsi que la viscosité et la contrainte de cisaillement apparente diminuent avec l'augmentation de la concentration enzymatique, ce qui était attendu en raison de la saccharification de la cellulose avec une séparation de nanofibrilles. Les NFC obtenues à partir de l'oxydation TEMPO ont formé un réseau fibreux plus résistant, associé à un meilleur raffinement des microfibrilles et des dimensions de nanofibrilles obtenues plus petites, comme observé par microscopie (Chapitre 1).

A notre connaissance, c'est la première étude consacrée à l'investigation des phénomènes de glissement à la paroi et bandes de cisaillement dans les suspensions de NFC par une approche de visualisation. Les systèmes de visualisation pour étudier le comportement rhéologique ont été construits comme représenté sur les Figures 2 et 3.

En utilisant la géométrie cône-plan lisse, des instabilités d'écoulement ont été détectées. Le glissement à la paroi a été mis en évidence sur une large gamme de gradients de cisaillement pour les deux types de suspensions de NFC produites : en utilisant soit des prétraitements enzymatiques soit le prétraitement d'oxydation TEMPO. Par conséquent, les valeurs obtenues sont considérés comporter une erreur, introduite par le glissement à la paroi.

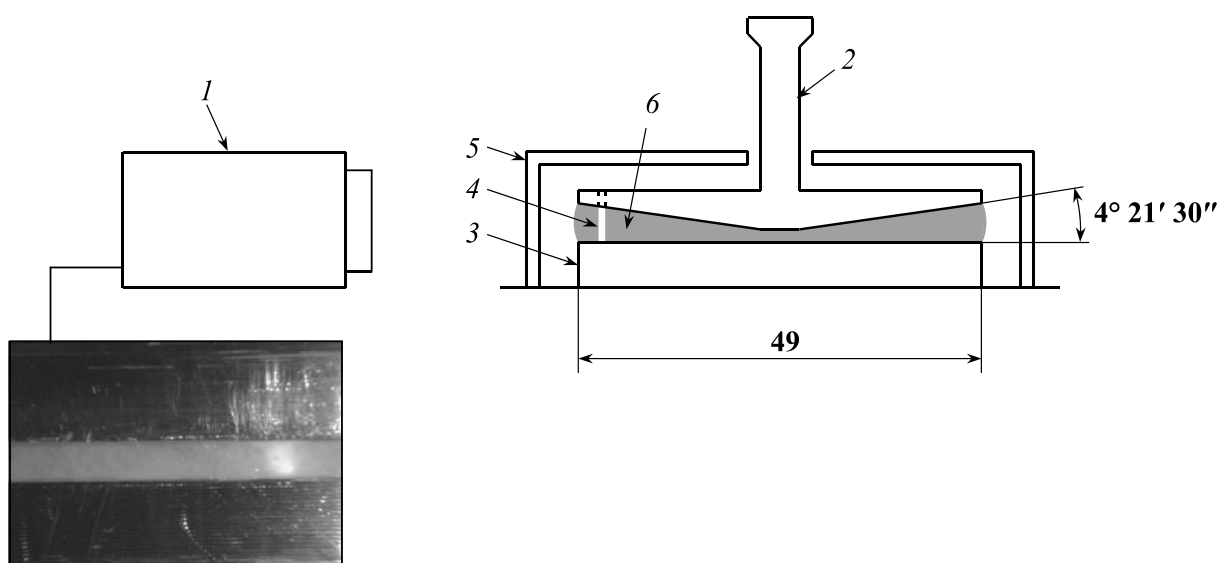


**Figure 2** Schéma de configuration cône-plan pour les mesures rhéologiques combinées avec la visualisation de la déformation de l'échantillon : (1) caméra vidéo ; (2) cône tronqué ; (3) plan ; (4) un filament de suspension de NFC, coloré par dioxyde de titane ; (5) couvercle transparent pour éviter l'évaporation de l'eau ; (6) suspension de NFC étudié. Les dimensions (mm) sont indiquées en gras

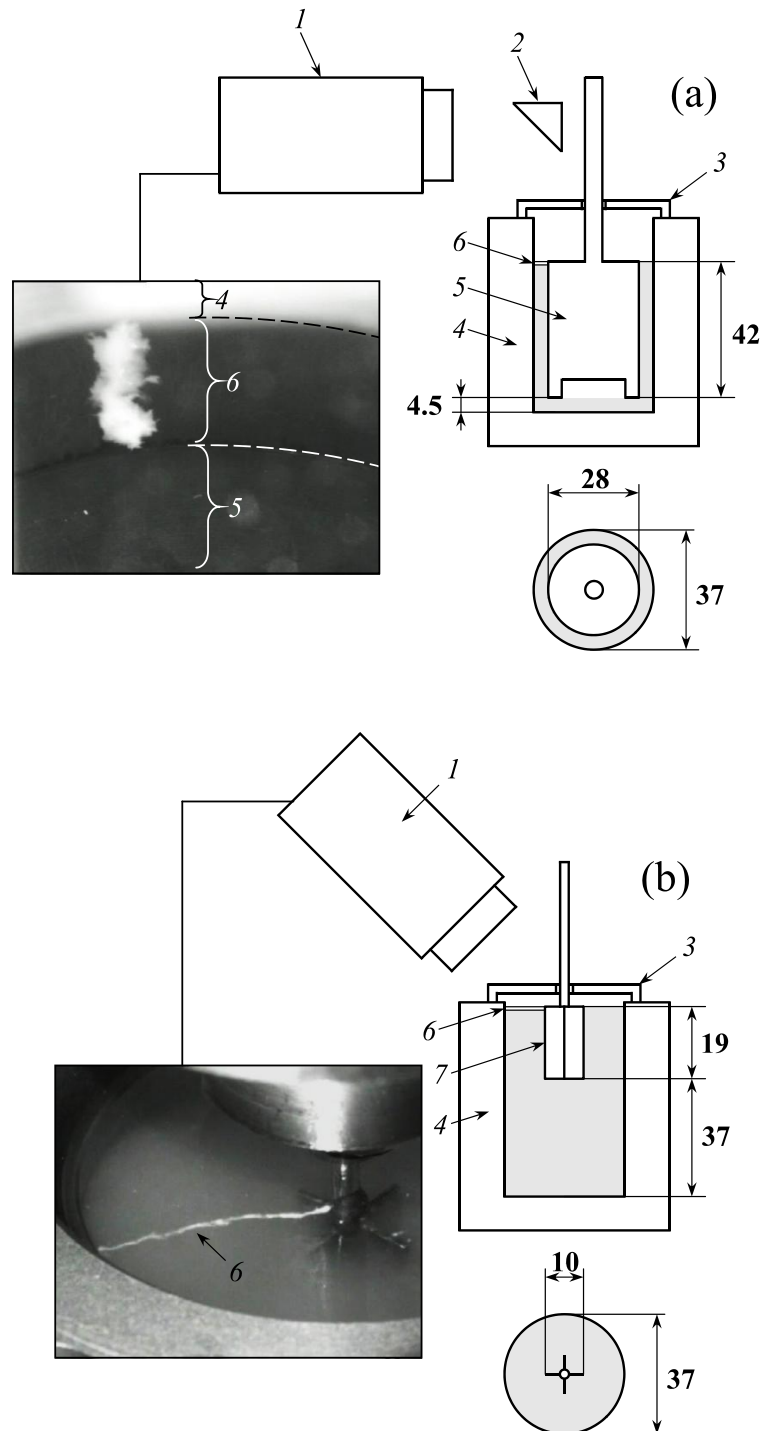


**Figure 3** Schémas de systèmes de Couette (a) et les pales dans une cuve (b) pour les mesures rhéologiques combinées avec la visualisation de la déformation de l'échantillon : (1) caméra vidéo ; (2) miroir ; (3) couvercle transparent pour éviter l'évaporation de l'eau ; (4) cuve ; (5) barrique ; (6) un filament de suspension de NFC, coloré par dioxyde de titane ; (7) pales. Les dimensions (mm) sont indiquées en gras

Pour éviter ce phénomène, les surfaces des outils ont été rendues rugueuses. Cela abouti à des mesures plus précises pour les suspensions de NFC oxydé par TEMPO. Cependant, l'utilisation d'outils rugueux n'a pas réussi à empêcher le glissement à la paroi pour les suspensions de NFC obtenues par prétraitement enzymatique.

Les suspensions de NFC obtenues par prétraitement d'oxydation TEMPO ont été étudiées par rhéométrie et SAXS à différentes concentrations. Les instabilités d'écoulement ont été observées pour des géométries Couette et de scissomètre (pales croisées dans une cuve) lors de l'utilisation de la technique de visualisation. Les expériences réalisées avec la géométrie Couette ont montré que l'utilisation de surfaces rugueuses est nécessaire pour réduire le glissement à la paroi, mais il ne suffit pas à l'empêcher complètement. Ces résultats ont été comparés à d'autres données précédemment obtenues avec une géométrie cône-plan. L'utilisation des pales croisées (scissomètre) provoque une fracture de la suspension à leur bord ressemblant à du glissement. Il est évident, que le glissement est plus crucial avec une augmentation de la concentration en fibres dans la suspension. Le comportement de l'écoulement dépend fortement de la géométrie utilisée à des taux de cisaillement faibles, où le glissement à la paroi joue un rôle important. Cependant, à des taux de cisaillement élevés l'influence de la géométrie utilisée est réduite, ce qui conduit à des valeurs identiques des contraintes de cisaillement. La géométrie Couette rugueuse est apparue comme la géométrie la plus appropriée (parmi les différentes étudiées) pour caractériser les propriétés d'écoulement des suspensions de NFC.

La polydispersité de NFC a été confirmée par l'analyse SAXS. Trois niveaux structuraux ont été déterminés à partir des données de diffusion expérimentales (voir Figure 4), résultant : soit (i) des surfaces de nanofibrilles, soit (ii) des nanofibrilles individuelle et soit (iii) des fibres partiellement désintégrées ou d'enchevêtrements des nanofibrilles. Il a été montré que l'approximation de Guinier n'est pas efficace pour extraire les caractéristiques de taille. Cependant, le diamètre moyen de nanofibrilles hydratées a été déterminé sur la base des données de diffusion en utilisant l'approche de Beaucage et la fonction d'ajustement unifiée (voir Figure 5).

### **Chapitre 3 Production de composites à partir de nanofibrilles de cellulose et de latex**

Deux types de latex de poly[styrène-co-(acrylate de 2-éthylhexyle)] ont été synthétisés par polymérisation en miniémulsion, comprenant des agents tensioactifs cationique (échantillon C-8.23) et anionique (échantillon A-8.23). Certaines propriétés mesurées de ces latex sont résumées dans le Tableau 1. Les températures de transition vitreuse ( $T_g$ ) ont été déterminées à partir des courbes de calorimétrie différentielle à balayage et étaient similaires (7–8 °C) pour les deux échantillons. Les tailles moyennes des particules de 385 et 271 nm ont été déterminées pour les échantillons C-8.23 et A-8.23, respectivement, à partir de mesures dynamiques de diffusion de la lumière. La chromatographie d'exclusion de taille a été utilisée pour déterminer une masse molaire moyenne en nombre ( $M_n$ ), une masse molaire moyenne en

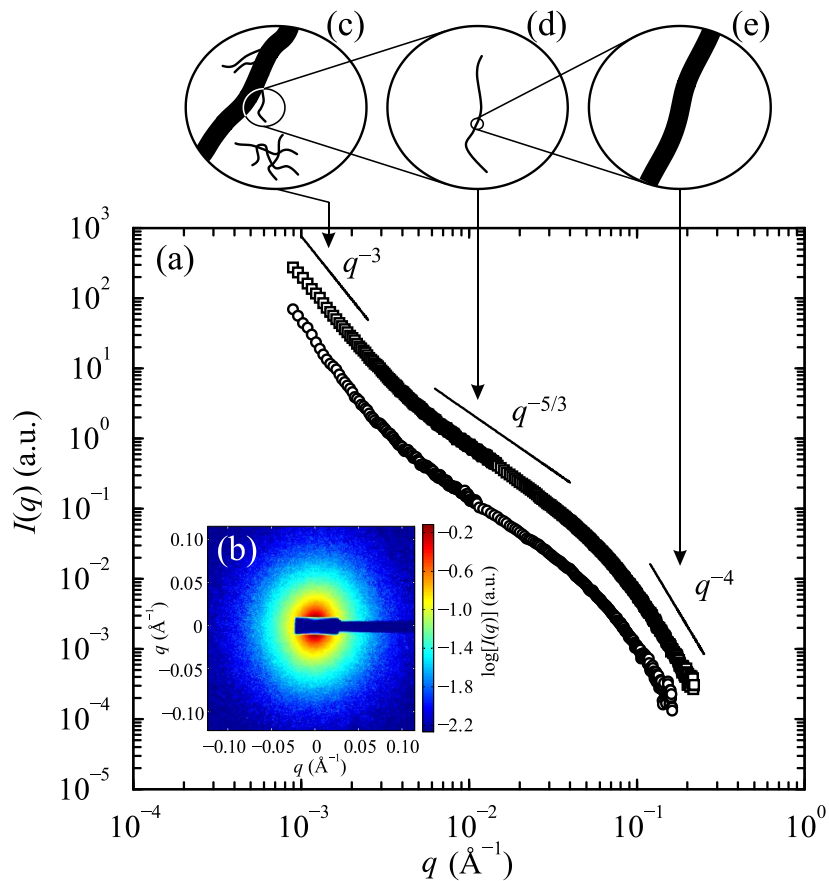


**Figure 4** Caractérisation par SAXS des suspensions de NFC TEMPO-oxydé : (a) intensité diffusée en fonction du vecteur de diffusion pour les suspensions à des concentrations de : 0.5 % en poids ( $\square$ ) et 0.1 % en poids ( $\circ$ ) ; (b) spectre de diffusion typique de suspensions de NFC ; (c-e) représentation schématique des structures produisant l'intensité diffusée

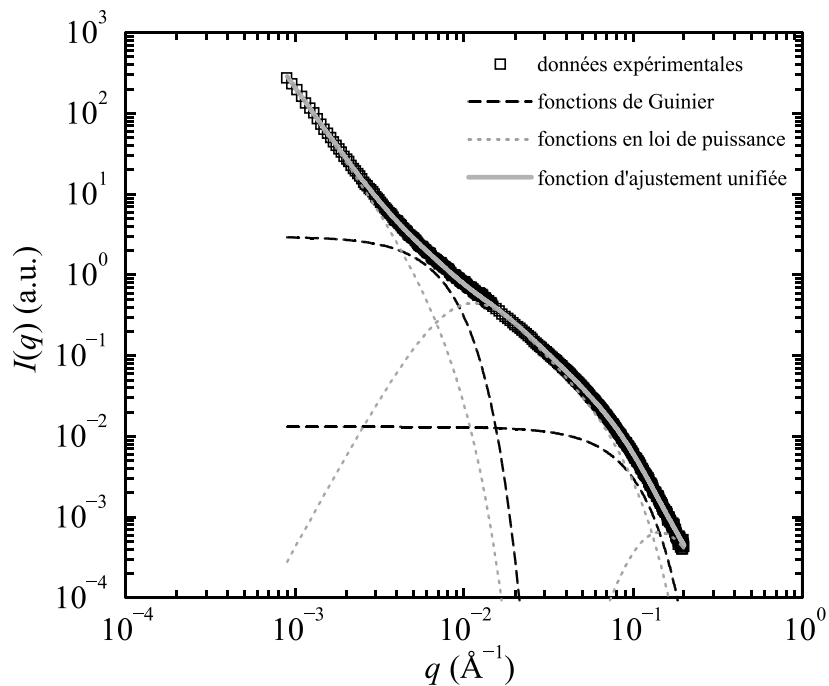


**Figure 5** Modélisation du comportement de diffusion de NFC utilisant la fonction d'ajustement unifiée (*trait plein gras*) selon les données de diffusion expérimentale ( $\square$ ) des suspensions de NFC à la concentration de 0.5 % en poids et les lois de diffusion locales (*traits pointillés*)

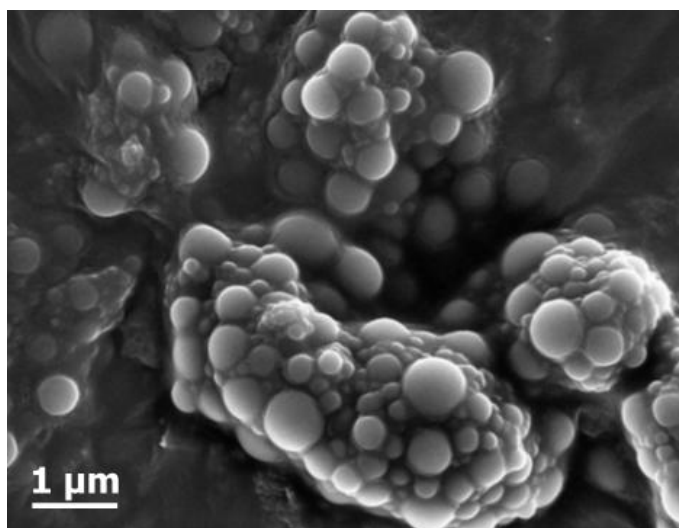


**Figure 6** Image FEG-SEM de particules de latex A-8.23

**Table 1** Certaines propriétés des C-8.23 et A-8.23 latex synthétisés

Échantillon	$T_g$ (°C)	Taille moyenne des particules (nm)	PDI	$M_w$ (Da)	$M_n$ (Da)	$M_w/M_n$
C-8.23	7	385	0.22	56218	26048	2,16
A-8.23	8	271	0.30	62512	28197	2,22

poinds ( $M_w$ ) et une polydispersité ( $M_w/M_n$ ) des latex synthétisés. La polydispersité en taille des particules a également été confirmée par FEG-SEM, comme on le voit sur la Figure 6 pour l'échantillon A-8.23. Des particules d'un diamètre à l'échelle nanométrique et submicronique sont présentes.

Les latex ont été utilisés par la suite pour étudier les interactions entre ses particules et les NFC TEMPO-oxydées dans les composites. Ces interactions ont été étudiées au travers de : (i) l'homogénéité de dispersion de NFC dans la matrice et (ii) des propriétés mécaniques des matériaux composites fabriqués.

L'utilisation de tensio-actif cationique dans le latex, dont le but initial est de renforcer l'interaction entre NFC chargé négativement et la matrice chargée positivement, et donc d'amélioration des propriétés mécaniques, a entraîné une distribution non homogène de NFC à l'intérieur de la matrice (voir Figure 7a). Ce comportement a eu lieu en raison de l'agrégation entre les particules de latex et NFC au travers de la création de structures réticulées régies par des forces ioniques.

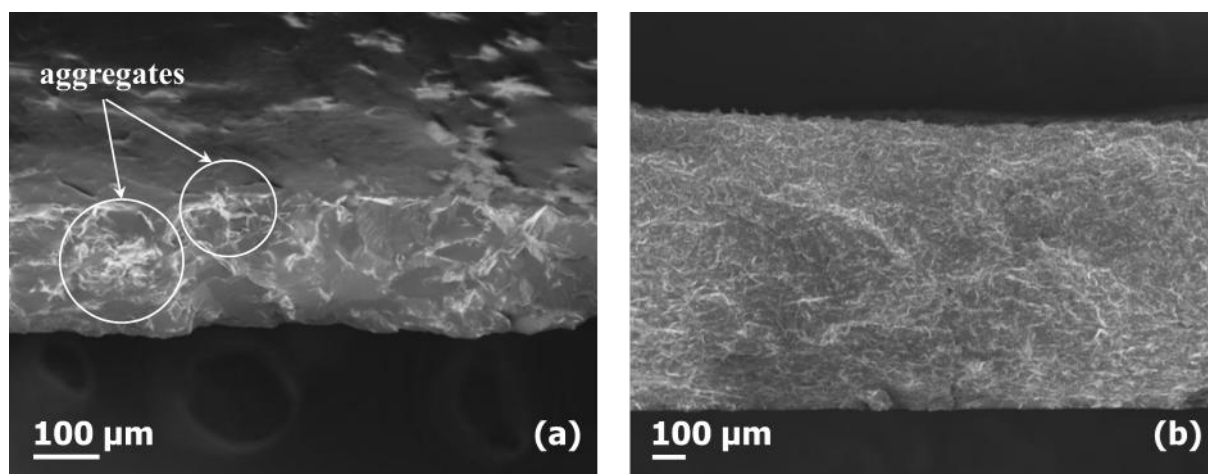


**Figure 7** Images FEG-SEM de sections transversales des composites cryo-fracturés contenant 3% en poids de NFC et : (a) latex C-8.23, produit par coulage et pressage à chaud et (b) latex A-8.23, produit par coulage

Des dispersions aqueuses stables et des composites homogènes ont été préparés lors de l'utilisation de latex avec un tensioactif anionique et NFC TEMPO-oxydé (voir Figure 7b). La bonne dispersion de la charge dans la matrice a été attribuée à la répulsion électrostatique entre les nanofibres de cellulose et les particules de polymère. En dépit de ces forces de répulsion, l'effet de renforcement a été déterminé pour tous les composites, en comparant à la matrice pure. Les deux modules d'élasticité et de résistance à la traction ont augmenté progressivement en intégrant les NFC dans le latex anionique, tandis que la déformation à la rupture a diminué, comme illustré dans la Figure 8. Le renforcement des composites obtenus par coulage, est ainsi obtenu grâce aux liaisons hydrogènes du réseau percolé de NFC.

La spectroscopie photoélectronique des rayons X révèle la différence de composition chimique sur les surfaces supérieures et inférieures des films composites coulés qui peuvent avoir une influence lors d'applications industrielles ultérieures de ces matériaux.

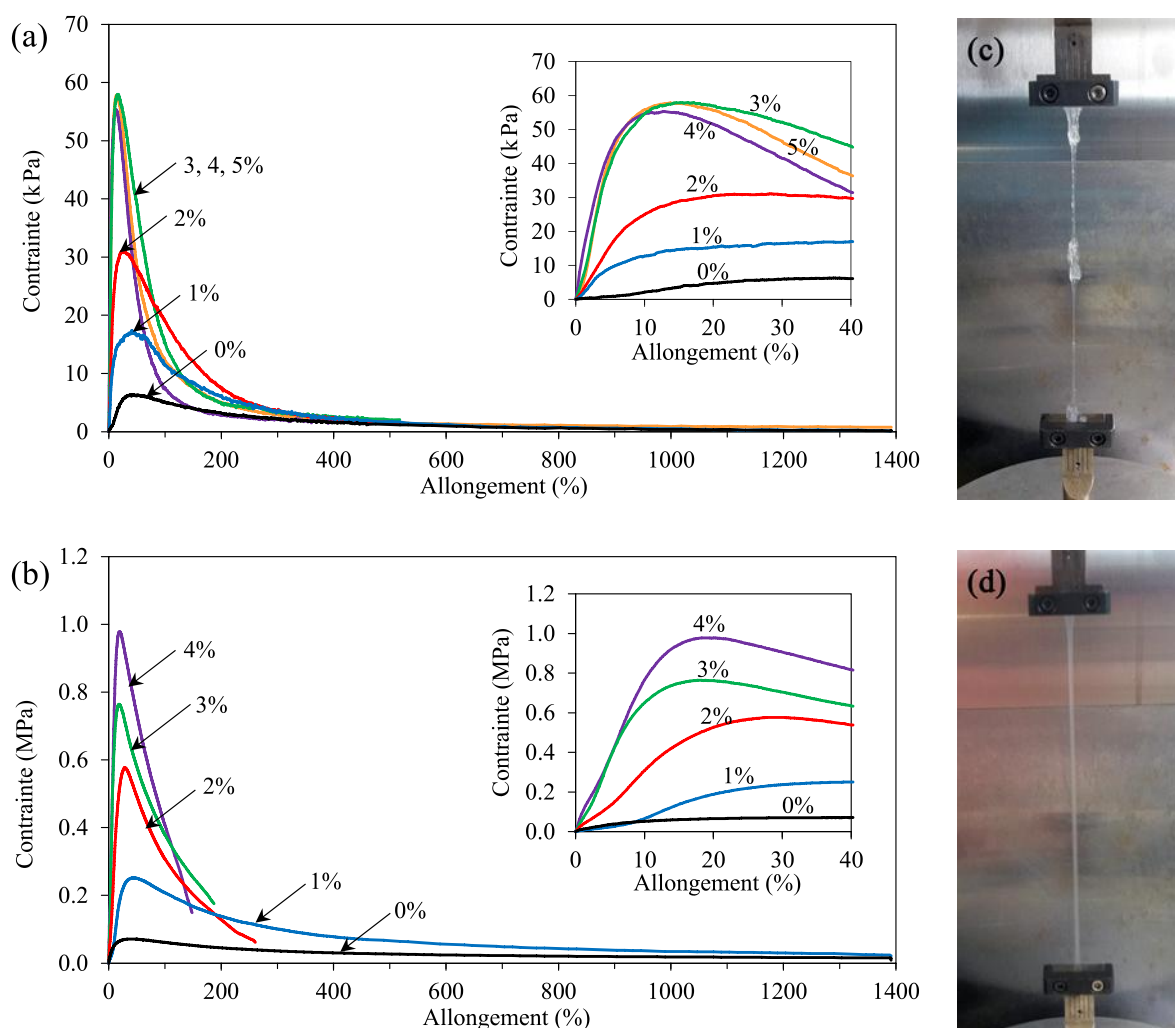


**Figure 8** Courbes contrainte-allongement typique pour les films de : (a) latex cationique (C-8.23) et (b) latex anionique (A-8.23) à différentes charges de NFC TEMPO-oxydé. L'observation visuelle des expériences pour les échantillons de (c) C-8.23/3% NFC et (d) A-8.23/1% NFC



## Annex A. Supplementary material for Chapter 1

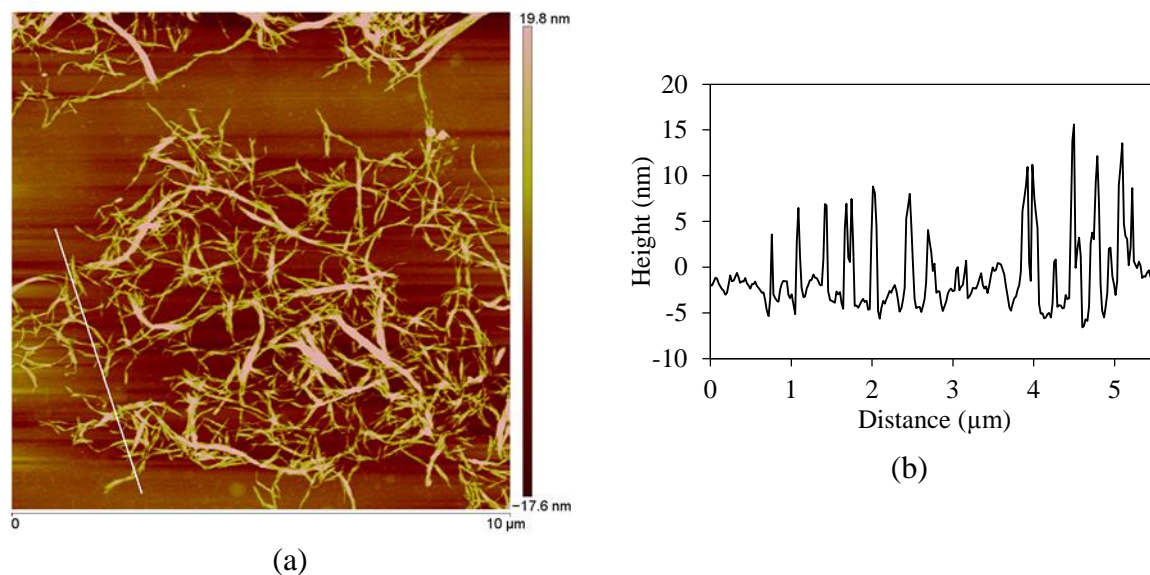


**Figure A.1** AFM height sensor image of enz-F210 NFC sample (a) and the corresponding height profile (b). The white bar in (a) shows the related profile position

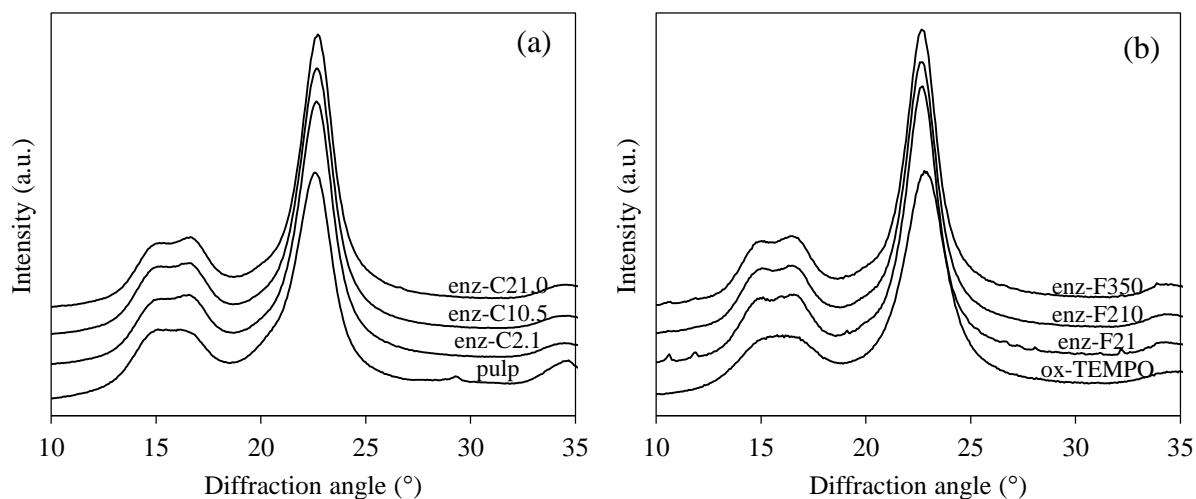


**Figure A.2** X-ray diffraction patterns of: the raw pulp and NFC produced using cellulase solutions (a); NFC produced using endoglucanase solutions and TEMPO-mediated oxidation (b)

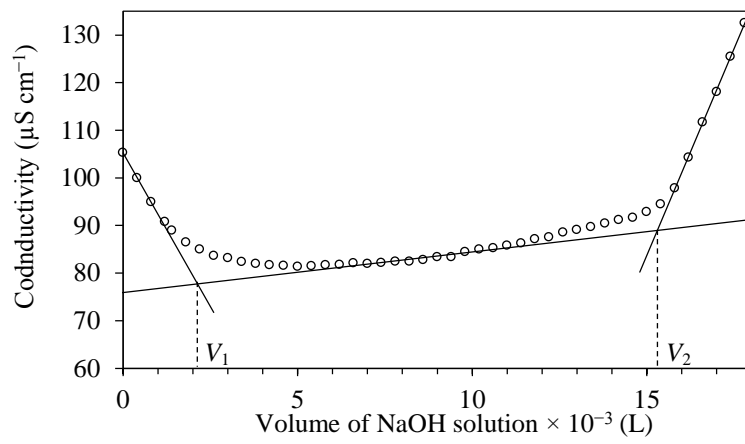


**Figure A.3** Conductometric titration curve of ox-TEMPO NFC for determination of cellulose carboxylic charge

# Annex B. Cellulose oxidation by oxygen, catalyzed by N-hydroxyphthalimide (NHPI)

## B.1 Introduction

Selective oxidation of cellulose primary hydroxyl groups was reported in the presence of TEMPO, which is the source of persistent nitroxyl radicals that mediate the oxidation (see Section 1.1.3.3). Coseri *et al.* (2009) reported the use of non-persistent nitroxyl radicals for cellulose oxidation, which can be generated from hydroxyl precursors such as N-hydroxyphthalimide (NHPI), N-hydroxybenzotriazole, violuric acid using a co-catalyst, *e.g.*, cerium (IV) ammonium nitrate or anthraquinone. The reported selective oxidation of cellulose (Coseri *et al.* 2009) was performed in the presence of NHPI, metallic or metal-free co-catalysts, NaBr and NaClO. The mechanism of oxidation using non-persistent phthalimide-N-oxyl (PINO) radical generated *in situ* from NHPI is the same as for TEMPO radical (Biliuta *et al.* 2013).

A process of cellulose mild oxidation using N-hydroxyphthalimide (NHPI) as catalyst and oxygen as ultimate oxidizing agent was recently reported by Biliuta *et al.* (2011). During such a process PINO radical, generated *in situ* from NHPI using anthraquinone, is able to withdraw hydrogen atom from cellulose, to form a carbon centered radical, which eventually is trapped by oxygen (see Figure B.1).

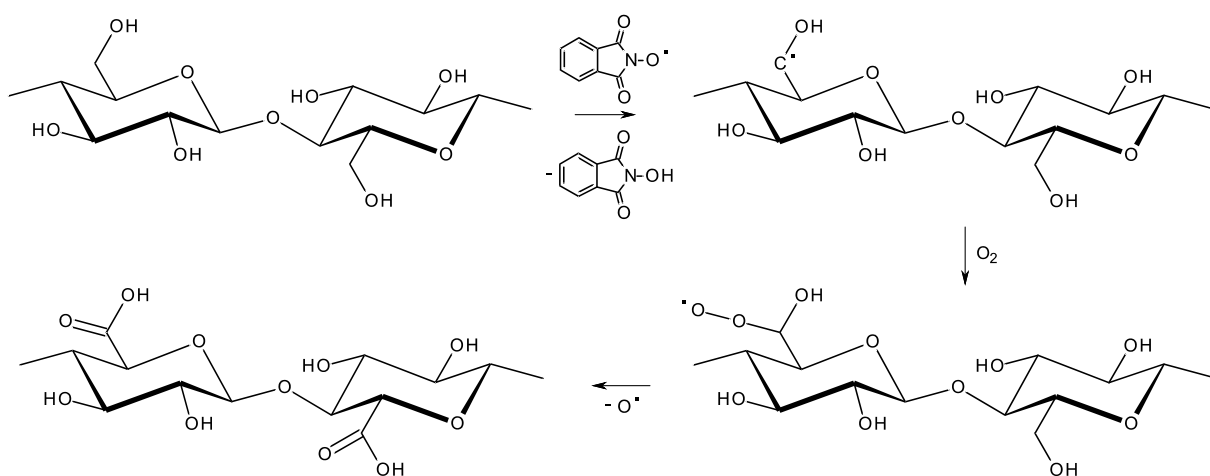


**Figure B.1** Schematic diagram of cellulose oxidation performed by oxygen, catalyzed by NHPI (adapted from Biliuta *et al.* 2011)

When the reaction was carried out at room temperature in water:acetonitrile (6:1 v/v) medium (to solubilize the anthraquinone), at neutral pH for 5 days, viscose with carboxylic charge of 0.0375 mmol/g was obtained (Biliuta *et al.* 2011). Such carboxylate content can be considered as too low comparing with TEMPO-mediated oxidation, where carboxylate content typically reaches 1.5 mmol/g (Saito *et al.* 2007). In the present work cellulose oxidation in the presence of NHPI, catalyzed by anthraquinone (in water/acetonitrile) or its water-soluble form: sodium anthraquinone-2-sulfonate (in water), and oxygen was performed at elevated pressure and temperature aiming at increasing the oxidation level. The reaction is performed as an alternative to TEMPO-mediated oxidation to promote the further disintegration of cellulose fibers to NFC.

## B.2 Materials and methods

Bleached softwood bisulfite pulp (Quality 2100, Domsjö Fabriker AB, Sweden) was used as a source of cellulose. NHPI, anthraquinone, sodium anthraquinone-2-sulfonate, acetonitrile and other chemicals were of laboratory grade and used without further purification.

For the cellulose oxidation two different essays were performed. For both, 16 g of cellulose was soaked in 1.2 L of deionized water for 4 hours and dispersed further using a disintegrator as described in ISO 5263-1:2004. The obtained suspension was placed into a steel reactor of 3.8 L volume together with 0.5220 g of N-hydroxyphthalimide. In the first assay (N1), 0.20 L of acetonitrile and 0.6662 g of anthraquinone were added (see Table B.1). The reactor was sealed and filled with O<sub>2</sub> till a pressure of 5 bars. The reaction was carried out at 80 °C under stirring for 6 hours. In the second assay (N2), water-soluble sodium anthraquinone-2-sulfonate (0.993 g) was used; thereby, acetonitrile was replaced with the same quantity of water. The reactor was filled with O<sub>2</sub> till a pressure of 10 bars and kept under stirring at 80 °C for 48 hours. Finally, for both essays, the reactor was cooled and the reaction quenched by the addition of 100 mL of ethanol. Cellulose suspensions were filtered on a

**Table B.1** Receipt for cellulose oxidation in the presence of NHPI and oxygen

Product	Quantity	
	N1	N2
Cellulose pulp	16.000 g	16.000 g
NHPI	0.522 g	0.522 g
Anthraquinone	0.666 g	–
Sodium anthraquinone-2-sulfonate	–	0.993 g
Water	1.2 L	1.4 L
Acetonitrile	0.2 L	–

Büchner funnel using a nylon sieve with mesh size of 1  $\mu\text{m}$  and washed until the filtrate conductivity reached values below 5  $\mu\text{S}/\text{cm}$ . For the first assay, cellulose was washed with hot ethanol to remove anthraquinone. The cellulose oxidation level was characterized using conductometric titration and FTIR, as described in Sections 1.2.3.8 and 1.2.3.9, respectively.

### B.3 Results and discussion

FTIR absorbance spectra of pulp reacted in N1 and N2 assays is compared with that of the raw pulp in Figure B.2. The peaks corresponding to C=O stretching vibrations in its carboxylate and carboxylic acid forms are located at 1743  $\text{cm}^{-1}$  and 1608  $\text{cm}^{-1}$  positions, respectively (Awada *et al.* 2012, Leppänen *et al.* 2013, Sadeghifar *et al.* 2011). The peak at 1608  $\text{cm}^{-1}$  is not detected in Figure B.2 and may overlap with the absorbed water band at 1638  $\text{cm}^{-1}$ , observed on the spectra. The pulp, oxidized in the presence of NHPI, anthraquinone and acetonitrile (N1), compared to initial pulp, bears a slight increase of absorbance at 1743  $\text{cm}^{-1}$ . It seems that sodium anthraquinone-2-sulfonate does not act similarly to anthraquinone, thereby yielding lower signal at this wavenumber.

The carboxylic charge of the raw pulp, as well as that resulted from N1 and N2 assays, was lower than 0.020 mmol/g, as determined from conductometric titration. Obviously, when passing the oxidized samples through the grinder, no distinct facilitation of the disintegration was observed, comparing to the raw pulp.

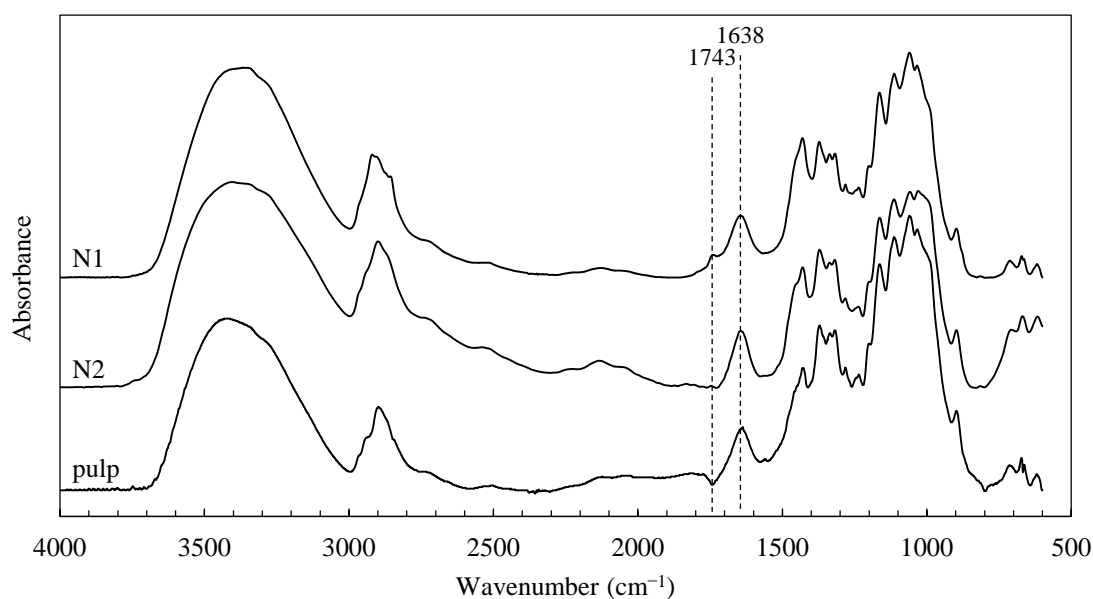


**Figure B.2** FTIR absorbance spectra of raw bisulfite pulp and recovered after oxidation reactions with NHPI and oxygen

## B.4 Conclusions

The oxidation reactions at elevated pressure and temperature comparing to those reported by Biliuta *et al.* (2011) did not increase significantly the oxidation level of the treated pulp. Thus, it was not efficient to promote the nanofibrils delamination. Probably, longer reaction time is required to achieve such a purpose.

## B.5 References

- Awada H, Montplaisir D, Daneault C (2012) Growth of polyelectrolyte on lignocellulosic fibres: study by zeta potential, FTIR, and XPS. *BioResources* 7:2090–2104. doi: 10.15376/biores.7.2.2090-2104
- Biliuta G, Fras L, Drobotă M, Persin Z, Kreze T, Stana-Kleinschek K, Ribitsch V, Harabagiu V, Coseri S (2013) Comparison study of TEMPO and phthalimide-N-oxyl (PINO) radicals on oxidation efficiency toward cellulose. *Carbohydr Polym* 91:502–507. doi: 10.1016/j.carbpol.2012.08.047
- Biliuta J, Fras L, Harabagiu V, Coseri S (2011). Mild oxidation of cellulose fibers using dioxygen as ultimate oxidizing agent. *Digest Journal of Nanomaterials and Biostructures*. Vol. 6, No 1, January-March 2011, p. 291- 297
- Coseri S, Biliuta G, Simionescu BC, Stana-Kleinschek K, Ribitsch V, Harabagiu V (2013) Oxidized cellulose—Survey of the most recent achievements. *Carbohydr Polym* 93:207–215. doi: 10.1016/j.carbpol.2012.03.086.
- Coseri S, Nistor G, Fras L, Strnad S, Harabagiu V, Simionescu BC (2009) Mild and Selective Oxidation of Cellulose Fibers in the Presence of N-Hydroxyphthalimide. *Biomacromol* 10:2294–2299. doi: 10.1021/bm9004854
- Leppänen A-S, Xu C, Eklund P, Lucenius J, Österberg M, Willför S (2013) Targeted functionalization of spruce O-acetyl galactoglucomannans—2,2,6,6-tetramethylpiperidin-1-oxyl-oxidation and carbodiimide-mediated amidation. *Journal of Applied Polymer Science* 130:3122–3129. doi: 10.1002/app.39528.
- Sadeghifar H, Filpponen I, Clarke SP, Brougham DF, Argyropoulos DS (2011) Production of cellulose nanocrystals using hydrobromic acid and click reactions on their surface. *J Mater Sci* 46:7344–7355. doi: 10.1007/s10853-011-5696-0
- Saito T, Kimura S, Nishiyama Y, Isogai A (2007) Cellulose nanofibers prepared by TEMPO-mediated oxidation of native cellulose. *Biomacromol* 8:2485–2491. doi:10.1021/ bm0703970.

## Annex C. Supplementary material for Chapter 2

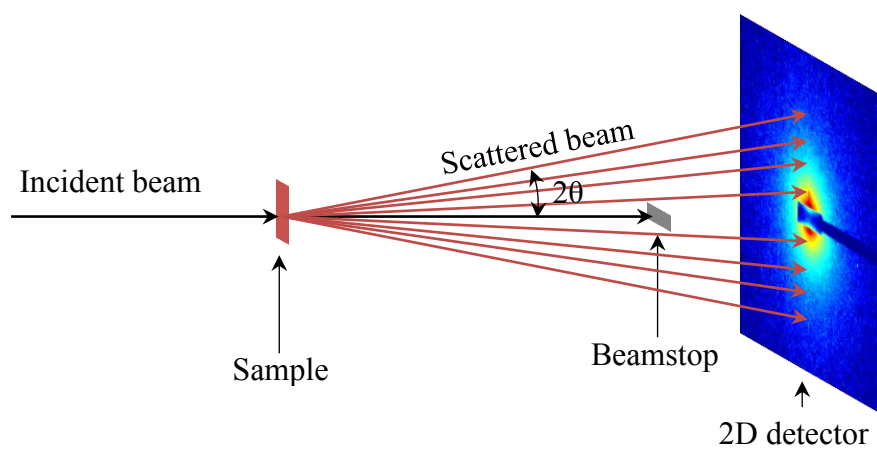


**Figure C.1** Schematic diagram of small-angle X-ray scattering measurements



**Figure C.2** The photograph of DHR-3 rheometer equipped with serrated (roughened) Couette geometry manufactured by gluing the sandpaper to the available Couette with smooth surfaces



## Annex D. Supplementary material for Chapter 3

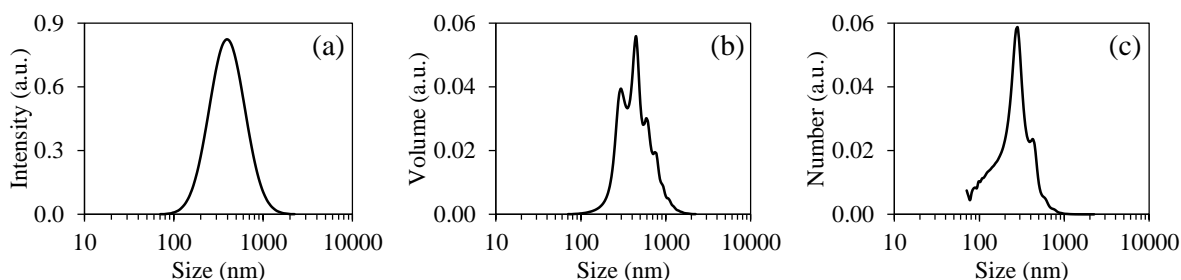


**Figure D.1** Particle size distribution of C-8.23 latex sample by (a) intensity; (b) volume and (c) number

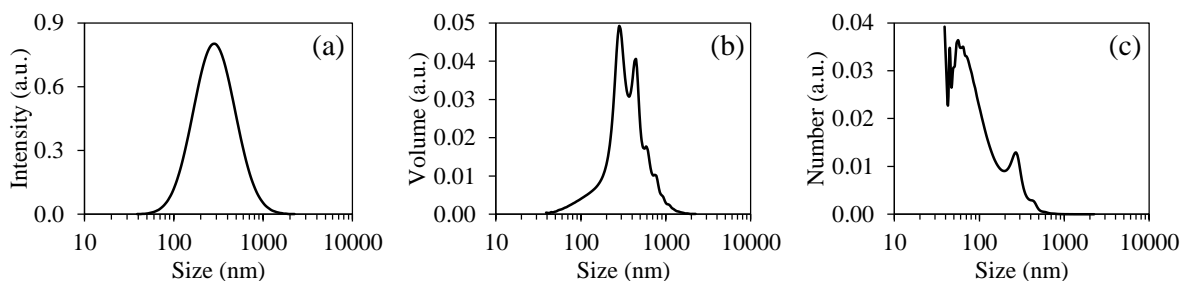


**Figure D.2** Particle size distribution of A-8.23 latex sample by (a) intensity; (b) volume and (c) number

**Table D.1** Corrected binding energies ( $\pm 0.2$  eV) and assignments for the components of the XPS regions

Component	Binding energies (eV)						Assignment
	pulp	TEMPO-NFC	matrix <sup>a</sup> top	matrix bottom	composite <sup>b</sup> top	composite bottom	
C 1s 1	–	–	284.7	284.7	–	284.7	C–C, C–H sp <sup>2</sup>
C 1s 2	285.0	285.0	285.0	285.0	285.0	285.0	C–C, C–H sp <sup>3</sup>
C 1s 3	286.9	286.6	286.5	286.5	286.5	286.5	C–O
C 1s 4	–	–	287.4	–	287.2	–	C=O in extended delocalized $\pi$ systems
C 1s 5	288.0	288.2	–	–	–	–	O–C–O / C=O
C 1s 6	288.9	289.0	–	288.9	–	288.8	O–C=O
C 1s 7	–	–	291.5	291.5	290.9	291.4	$\pi$ – $\pi^*$ in delocalized $\pi$ systems
O 1s 1	532.7	532.4	532.4	532.3	532.3	532.3	C–O–H
O 1s 2	533.3	533.6	533.4	533.5	533.4	533.6	C–O–C
S 2p <sub>3/2</sub>	–	–	169.6	169.9	169.3	169.8	–O–SO <sub>3</sub> <sup>–</sup>
S 2p <sub>1/2</sub>	–	–	170.8	171.1	170.5	171.0	
Na 1s	–	–	1072.1	1072.5	1071.7	1072.3	Na <sup>+</sup>

<sup>a</sup> A-8.23 sample;

<sup>b</sup> A-8.23/3% NFC sample

## **Résumé**

Un des principaux challenges dans le contexte du développement des matériaux biocomposites est de remplacer les matières plastiques à base de pétrole par des matériaux biosourcés. En raison de leurs origines naturelles, d'une résistance relativement élevée et de leur capacité à former des produits transparents, les nanofibres de cellulose possèdent un grand potentiel d'applications dans les matériaux composites. Dans ce travail des résultats ont été apportés premièrement sur l'optimisation des procédés de productions de nanofibres de cellulose par des traitements biochimiques et mécaniques, deuxièmement sur leurs propriétés rhéologiques et structurelles en milieu aqueux et troisièmement sur la production de composites à matrice de latex. Les questions de dispersions homogènes de nanofibres de cellulose dans la matrice et des interactions entre ces composants à des fins de renforcement des bio-composites ont été étudiés en détails.

## **Abstract**

One of the main challenges in the context of biocomposites development is to replace petroleum-based materials with bio-based. Because of their natural origin, relatively high strength and the ability to form transparent products, cellulose nanofibers have a large potential for application in the composite materials. This work was focused primarily on the optimization of cellulose nanofiber production methods using biochemical and mechanical treatments, secondly on their rheological and structural properties in an aqueous medium and thirdly on the production of latex-based composites. The questions of homogeneous dispersion of cellulose nanofibers in the matrix and the interactions between these components for the purpose of matrix reinforcement were particularly addressed.